Origin and Evolution of Large-scale Magnetic Fields

David J. Barnes

Thesis submitted for the degree of

Doctor of Philosophy

of

University College London

Mullard Space Science Laboratory

Department of Space and Climate Physics

University College London

September 2014

I, David Barnes, confirm that the work presented in this thesis is my own. Where information has been derived from other sources, I confirm that this has been indicated in the thesis.

Signed: _____

Date: _____

Abstract

Magnetic fields are ubiquitous at all scales in the Universe and have been observed in galaxies and clusters of galaxies via observations of diffuse radio emission and Faraday Rotation Measures. Despite the observations, the origin and impact of the magnetic fields in these systems is poorly understood. In this thesis we develop a state of the art cosmological Smoothed Particle Magnetohydrodynamics code, GCMHD+, to enable the study of the magnetic fields of the largest bound structures in the Universe. Using a wide range of idealized test problems, we justify our choice of free parameters and demonstrate the performance of the code relative to analytical solutions and the results produced by a grid based MHD scheme.

We then used the code to investigate the evolution of a seed magnetic field due to the formation of structure. By varying the numerical scheme, we demonstrate that the growth of magnetic fields in galaxy clusters are very sensitive to the growth of numerical divergence of the magnetic field. We find that amplitude and topology of the cluster magnetic field are insensitive to the mass or formation history of the cluster. Using high resolution simulations, we show that a primordial seed magnetic field is capable of reproducing a wide range of observations of large-scale magnetic fields in galaxy clusters.

Additionally, we examine the impact of the formation of spiral structure in a disc galaxy on the galactic magnetic field. We find that the numerical scheme can become unstable unless the divergence cleaning scheme is limited. We find that the rotation of the galaxy produces a disc orientated magnetic field with a spiral structure and large-scale field reversals. The formation of spiral arms amplifies the ambient μG magnetic field to $\sim 20\,\mu$G, in agreement with the observations of spiral galaxies. We conclude that additional physics is required to produce a more realistic galactic magnetic field.

Acknowledgements

First, I would like to thank my supervisors Prof. Kinwah Wu and Dr. Daisuke Kawata for their support, encouragement and patience over the course of my PhD. I have been very lucky to have two supervisors with such physical insight and passion for science.

Next, I would like to thank my office mates Alivna On and Idunn Jacobson for their help, countless useful discussions, maintaining my perspective and sharing the journey of obtaining our PhDs together. I would also like to thank Dr. Curtis Saxton, Dr. Ziri Younsi, Dr. Rob Grand, Dr. Stefano Pasetto, Dr. Jason Rawlings, Jason Hunt, Megan Whewell and the rest of the MSSL astrophysics group for their insight, fascinating world views and making my time spent at MSSL more enjoyable. I gratefully acknowledge the financial support of a PhD studentship awarded by the UK Science & Technology Facilities Council (STFC) that enabled me to undertake this research.

I would like to thank my parents for their love and encouragement at all stages during my education.

Most of all, I would like to thank Amy for her endless love, continual encouragement and support through all the ups and downs of my PhD. She is my inspiration and I dedicate this thesis to her.

Contents

List of Figures

List of Tables

Chapter 1

A Magnetized Universe

Pertinent observations of the Universe show that magnetic fields are ubiquitous to systems of all scales. They are found to be present in the solar system, in stars and molecular clouds, in the Milky Way, in low and high redshift galaxies, in groups and clusters of galaxies, in super clusters and even in cosmological filaments and voids. The largely accepted idea for gravitationally bound structures is that their observed magnetic field was produced, and where necessary is maintained, by a dynamo mechanism (Jones 2011; Ossendrijver 2003; Kulsrud 2011). However, any dynamo requires the presence of an initially non-zero "seed" magnetic field upon which it can act. The magnetic fields present on scales larger than bound objects, i.e. in cosmological voids, could be relics of the magnetic fields that initially seeded the Universe or they may simply be magnetic fields that have been ejected from structures at a later epoch (Widrow 2002), a pointer to the location of the baryons that appear to be missing from these structures. How the Universe became seeded with magnetic fields at all scales is an open question in astrophysics and understanding its answer, along with understanding how these magnetic fields evolved, could allow detailed observations of the large-scale magnetic fields in the Universe to be used as a probe of physics in the early Universe and of physics beyond the standard model.

Magnetic fields are known to be critical to the behaviour of many astrophysical systems. The Earth's magnetic field deflects the charged particles of the solar wind, preventing the atmosphere of the planet from being stripped

away. The magnetic field of the Sun drives activity at the solar surface and is critical to the production of solar flares and coronal mass ejections. Although the exact mechanism is still not absolutely certain, magnetic fields are essential to the launching of astrophysical jets that are commonly observed to emanate from compact systems and active galactic nuclei (AGN). In star forming molecular clouds, magnetic fields are known to be critically important as they are able to transport angular momentum away from collapsing protostars. Cosmic rays would not exist in the Universe without a magnetic field to mediate their acceleration and the background of lower energy cosmic rays observed on Earth is confined by the galactic magnetic field.

However, an increase in the size of the system corresponds to decrease in the comprehension of the origin, evolution and impact of the magnetic field inhabiting the system. At the galactic scale, magnetic fields are believed to be seeded at high redshift, with one possible mechanism being supernovae, and then dynamo processes, driven by turbulence and the large-scale rotation of the galaxy, amplify and shape the magnetic field to the observed one. This theory is supported by observations of high redshift galaxies ($z = 1.3$) showing magnetic field strengths comparable to galaxies at the current epoch (Bernet et al. 2008). Although the magnetic energy density is only $\approx 1\%$ of the kinetic energy density of a galaxy, it is roughly equal in strength to the turbulent energy density and an order of magnitude greater than the thermal energy density of the gas of the interstellar medium (ISM). Therefore, it should play a role in the structural evolution of a galaxy. However, in galactic modeling and numerical simulations the magnetic field is often neglected. Beyond the galactic scale, the understanding of the origin and role of magnetic fields in these systems is even more limited.

1.1 Magnetic Fields and the Formation of the Universe

Galaxy clusters are the largest virialized systems in the Universe, consisting of hundreds to thousands of galaxies clustered together. The intra-cluster medium (ICM) is the low-density gas that is present between the galaxies of a cluster and contains the majority of the baryons. Magnetic fields of micro-

Gauss (μG) amplitude have been observed to permeate the ICM (Carilli and Taylor 2002), but their origin is uncertain. Beyond the cluster scale, there is growing evidence of truly cosmological, coherent magnetic fields inhabiting super clusters and cosmological voids (Neronov and Vovk 2010; Tavecchio et al. 2011; Takahashi et al. 2013). The theories of magnetogenesis on the largest scales fall into two broad categories, those generated in the early Universe and those generated after recombination. If magnetic fields were generated on the largest scales in the early Universe, with sufficient strength, they could have potentially impacted processes critical to the formation of the Universe (see Widrow 2002).

1.1.1 Cosmic Microwave Background

The cosmic microwave background (CMB) is relic radiation whose last interaction occurred before recombination, when the protons and electrons cooled sufficiently to form neutral atoms. There are several magnetogenesis theories that produce magnetic fields on the large scales before the CMB is generated (Ichiki et al. 2007; Kandus et al. 2011). A spatially coherent, sufficiently strong magnetic field would generate an anisotropic stress term that would non-negligibly affect the geometry of the Universe, causing it to expand more slowly in one direction, as it works against the magnetic tension force, and more quickly in another, as it is aided by the additional pressure the magnetic field exerts. This anisotropic expansion would be visible as anisotropies in the CMB (Durrer 2007). Even if the magnetic field is stochastic, its coupling to the electron-proton plasma prior to recombination will lead to Alfv́en wave perturbations in the plasma velocity that produce vector anisotropies in the CMB (Durrer et al. 1998). The highly detailed maps of the CMB produced by the WMAP (Bennett et al. 2003) and Planck (Tauber et al. 2010) experiments allow a search for these anisotropies, with the vectorial anisotropies capable of placing a stringent limit on the strength of any magnetic field present at this epoch.

Prior to recombination, the electrons in the plasma of the Universe existed as free electrons and were able to continually scatter the photons of the CMB. As the CMB photons are scattered, they are polarized. Scalar perturbations

in the CMB, such as temperature variations, naturally produce "E-mode" polarization patterns and these were detected in 2002 (Kovac et al. 2002). If a magnetic field were present during this epoch it would have polarized the electrons in the plasma, leading to a rotation of the CMB polarization. This rotation converts E-mode polarized photons to "B-mode" polarized photons, making it possible to explain the recently observed B-mode polarization of the CMB with a primordial magnetic field (Bonvin et al. 2014).

1.1.2 Nucleosynthesis

A sufficiently strong magnetic field in the early Universe would have altered the formation and ratio of the primordial elements (hydrogen, deuterium, helium and lithium). A magnetic field present at this epoch will introduce two competing effects. First, the magnetic field will contribute to the energy density of the Universe (Greenstein 1969). Neglecting any cosmological term and curvature effects, the expansion rate of the Universe is given by

$$\frac{\dot{a}}{a} = \left(\frac{8\pi G\rho_E}{3}\right)^{1/2} , \tag{1.1}$$

where a is the scale factor of the universe, $\dot{a}$ is the rate of change of the scale factor, G is the gravitational constant and ρ_E is the energy density of the Universe. The presence of a magnetic field increases the energy density of the Universe, leading to an increase in the expansion rate of the Universe and altering the temperature at which the neutron-proton ratio of the Universe becomes fixed. Unbound, free neutrons are not stable and, via beta decay, begin to decay to protons, having a half-life of roughly ten minutes. Increasing the expansion of the Universe reduces the time over which nucleosynthesis can occur and so reduces the time free neutrons have to decay. This effect will boost the abundance of ^{4}He.

The second effect is the influence of the magnetic field on the beta decay rate of neutrons. The magnetic field increases the available phase-space for the electron wave function, which in turn significantly increases the beta decay rate (Matese and O'Connell 1969). Once the neutrons freeze out of the initial plasma of the Big Bang, and the proton-neutron ratio is set, it takes time for the neutrons to become bound into composite nuclei. During this period the

unbound neutrons are free to decay, and they decay faster due to the presence of the magnetic field. This results in a lower abundance of ^{4}He. When these two effects are carefully considered it is found that the magnetic field's contribution to the energy density of the Universe, and the more rapid expansion, is greater than its contribution to the neutron decay rate. Therefore, the abundance of ^{4}He in the Universe at the present epoch is dependent on the amplitude of any magnetic field present at the epoch of nucleosynthesis. A full review of these two competing effects can be found in Grasso and Rubinstein (2001)

1.1.3 Formation of the First Structures and Reionization

After recombination, the Universe was neutral and the only light was the slowly fading CMB. As the first stars and galaxies formed, they began to emit ultraviolet (UV) photons that where energetic enough to reionize the Universe. Large-scale magnetic fields present at the onset of the formation of structure can, if sufficiently strong, effect the properties and statistics of the large-scale structure of the Universe and the observational signals of the reionization. A magnetic field can effect the abundance of galaxy clusters, modifying the Sunyaev-Zeldovich effect on the CMB (Tashiro and Sugiyama 2011). A large-scale magnetic field would provide an additional contribution to the pressure support of gravitationally collapsing objects, producing an increase in their Jeans mass. This would effectively act to suppress the formation of small-scale structures. As it is thought that the small-scale structures are responsible for the majority of ionizing radiation in the Universe, the presence of a magnetic field during this epoch would delay the onset, and increase the duration of, reionization. However, the Lorentz force that couples the magnetic field to the fluid of the Universe would induce additional baryonic perturbations that can be transferred to the dark matter. This would enhance the formation of small structures, causing reionization to start sooner and occur more rapidly (Sethi and Subramanian 2005). The balance between these two competing factors will effect the reionization of the Universe.

Additionally, magnetic fields will input heat into the Universe via ambipolar diffusion and the decay of magnetic turbulence, altering the 21 cm emission

signal during reionization. Without a magnetic field the gas temperature is closely coupled to the CMB by Compton-scattering, until at low redshifts this becomes inefficient and the gas cools adiabatically. The presence of a magnetic field during this epoch causes the gas to decouple from the CMB earlier, resulting in a larger difference between the gas and radiation temperatures. This change in temperature will alter the 21 cm line emission signal. If the magnetic field is weak then the heating is negligible and the gas temperature remains colder than the CMB leading to a 21 cm line absorption signal at $z = 20$. However, if the magnetic field is sufficiently strong then the gas is heated more strongly, leading to it being warmer than the CMB and a 21 cm line emission signal at much higher redshift. Current and future radio telescopes such as LOFAR, 21CMA, MWA, LWA and SKA may be able to find this signature of the presence of magnetic fields at the epoch of reionization, placing constraints on them at this epoch (Schleicher et al. 2009).

1.1.4 Constraining magnetic fields in the early Universe

The presence of a magnetic field in the early Universe could have impacted on processes that are critical to the formation of the Universe. Hence, observations of these processes can place limits on the parameters of any magnetic field present during this epoch. Current observations place upper limits on the strength of magnetic fields in the early Universe, while future observational facilities will attempt to distinguish the relic magnetic fields of the early Universe from other sources of magnetism and measure their properties.

Magnetic fields present at recombination and the production of the CMB would have left observable anisotropies in the CMB. The non-observations of these anisotropies in the CMB yields an upper limit amplitude for magnetic fields coherent on megaparsec (Mpc) scales of $B \lesssim 5 \times 10^{-9}\,\mathrm{G}$ for a range of magnetic field power law spectrums (Barrow et al. 1997; Paoletti and Finelli 2011). Measurements of the Helium abundance in the Universe can place a limit of the strength of magnetic fields during nucleosynthesis. Careful observations place an upper limit on the root mean squared amplitude of a magnetic field, coherent on Mpc scales, of $B \lesssim 1 \times 10^{-9}\,\mathrm{G}$ during the epoch of nucleosynthesis (Grasso and Rubinstein 2001). The onset and duration of

reionization can be altered by a sufficiently strong magnetic field, due to its influence on the formation of small-scale structure. Using the optical depth of the WMAP 7 year data release to reproduce the observed Thompson optical depth and solving for the ionization fraction of the Universe, Schleicher and Miniati (2011) found that to fully reionize the Universe by $z = 7$ places an upper limit of $B \lesssim 2 \times 10^{-9}$ G on the magnetic field strength during this period. Combining the limits placed on magnetic fields in the early Universe with the observations of magnetic fields at the current epoch constrains the possible magnetogenesis mechanisms.

1.2 Observations of Galactic and Extragalactic Magnetic Fields

The knowledge that magnetic fields exist on all scale in the Universe was obtained by the observations made of the astrophysical systems they inhabit. Magnetic fields are observable through the physical processes that they trigger when present in a system, allowing the properties of the magnetic field to be inferred. However, there are inherent uncertainties in their properties due to complexity of the astrophysical system being observed. Here the observational techniques used to study magnetic fields on the largest-scales in the Universe are reviewed.

1.2.1 Polarization of Starlight

Polarized starlight was first observed by Hall (1949) and Hiltner (1949). It was found that polarization levels for some stars was as high as 10% and that the degree of polarization of the starlight correlated with position on the sky. At the same time, Alfvén (1949) proposed the existence of a galactic magnetic field to confine the propagation of cosmic rays and reproduce the observed cosmic ray population. Davis and Greenstein (1951) first made the connection between the polarization of the starlight and the magnetic field of the Milky Way.

Dust grains in the Galaxy align themselves so that one of their short axes aligns with the Galactic magnetic field. For optical starlight, the dust grains then preferentially absorb light that is polarized along their longest

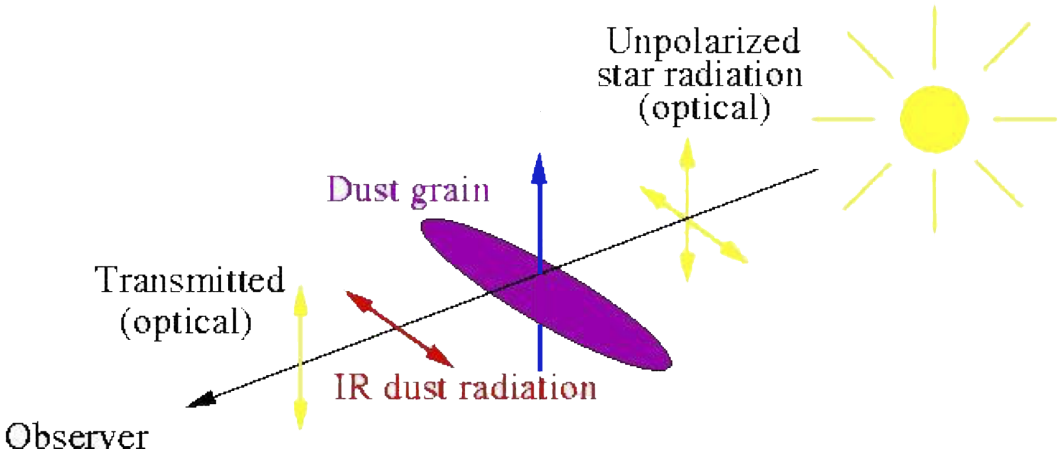

Fig. 1.1: Diagram demonstrating the polarization of optical (yellow arrow) and infrared photons (red arrow) due to dust grains (purple) aligning with the local magnetic field (blue arrow) of the Galaxy. Image credit: Rainer Beck, IAC winter school 2013.

axis. This results in optical starlight that is polarized in the direction parallel to the galactic magnetic field and perpendicular to the long axis of the dust grains. The absorption of starlight heats the dust grains and they release this energy by emitting infrared photons. As the dust grains are aligned to the local magnetic field this submillimeter wavelength emission is intrinsically polarized, but, as shown in Fig. 1.1, the polarization is perpendicular to the optical photons. The optical starlight in the Galaxy and the diffuse starlight in nearby galaxies can be used to infer the presence and trace the topology of a galactic magnetic field. Polarized infrared photons can be used to trace the magnetic field in dense concentrations of dust grains, such as in molecular clouds (Tang et al. 2009).

An advantage of using polarized starlight is that it provides complementary information to other observing techniques. However, both optical and infrared observations are limited by several issues. First, the exact mechanism of alignment for the dust grains is uncertain. The paramagnetic relaxation proposed by Davis and Greenstein (1951) is a very slow way of aligning the dust grains and it is uncertain whether the observations support this mechanism (Kim and Martin 1995; Lazarian 1997). The radiative torque alignment proposed by Hoang and Lazarian (2008) may help to remedy the theory of grain

alignment with the observations. Additionally, anisotropic scattering in the inter stellar medium can mimic grain alignment and produce polarized starlight. Another issue is that the polarization of the starlight is self-obscuring. For every 3% of polarization that is generated there is approximately a one order of magnitude of extinction in the visible light and a polarization of 10% must be coupled with a 20× reduction in the luminosity of the starlight. Tracing molecular clouds via infrared polarized emission requires very high angular resolutions as molecular clouds are small objects compared to the scale of the galaxy. This means that this technique requires bright sources and is limited to providing magnetic field information about the local Universe only.

1.2.2 Zeeman Splitting

Zeeman splitting is a quantum effect, where the electron energy levels of an atom separate due to the presence of a magnetic field. The field lifts the degeneracy of the levels by picking out a particular direction in space and a spread in the energy levels occurs due to the orientation of the angular momentum, **J**, of a level with respect to this direction. If the total angular momentum is **J**, then there will be $2j+1$ levels, where j is the associated quantum number. The levels are split by an energy difference $\Delta E = g\mu_B B$, where g is the Lande factor, μ_B is the Bohr magneton and B is the strength of the magnetic field. Zeeman splitting provides an *in situ* measure of the magnetic field, without any further assumptions, and was first used in an astrophysical context to discover the magnetic fields of sunspots by Hale (1908).

However, in large-scale astrophysical systems Zeeman splitting is incredibly difficult to detect due to the magnetic fields being very weak. For the most common lines in astrophysics, the 21cm hyperfine transition line and the 18cm OH line of molecular clouds, the frequency shift due to Zeeman splitting, $\Delta\nu/\nu \simeq 10^{-9} g (B/10^{-6}\,\mathrm{G})$, is orders of magnitude smaller than the thermal Doppler broadening of the line, $\Delta\nu/\nu \simeq 6\times10^{-7}(T/100\,\mathrm{K})^{1/2}$ where T is the mean temperature. Zeeman splitting is observed as an atypically shaped thermally broadened line and is most easily detected in cold regions with a strong magnetic field.

Despite these difficulties, Zeeman splitting has been used to measure the

magnetic field of the Galaxy. Reid and Silverstein (1990) used observations of a range OH masers lines to map the large-scale galactic magnetic field and found a structure consistent with other observational techniques. Although there have been claims of extra-galactic measurements of magnetic fields using Zeeman splitting (Kazes et al. 1991), these results have been disputed (Verschuur 1995) and the measurements of astrophysical magnetic fields via Zeeman splitting are limited to the Milky Way.

1.2.3 Synchrotron Emission

The motion of a single charged particle in a magnetic field $\mathbf{B}$ is given by

$$\frac{d(\gamma m\mathbf{v})}{dt} = \frac{q}{c}(\mathbf{v}\times\mathbf{B})\,, \tag{1.2}$$

where q is the particle's charge, m is the particle's mass, $\mathbf{v}$ is the particle's velocity and $\gamma = (1 - v^2/c^2)^{-1/2}$ is the Lorentz factor, where $v = |\mathbf{v}|$ and c is the speed of light. For an electron, its motion will be a helix, as there is no acceleration parallel to the magnetic field, and its gyration frequency is given by

$$\nu_{\rm g} = \frac{eB}{2\pi\gamma m_e c}\,, \tag{1.3}$$

where e is the electron charge and m_e is the electron mass. From equation (1.3), the acceleration perpendicular to the magnetic field is by $a_\perp = 2\pi\nu_{\rm g} v\sin\theta$, where θ is the angle between the velocity and magnetic field and is more commonly known as the pitch angle. The total power emitted by an accelerated relativistic electron is given by

$$P = \frac{2}{3} r_0^2 \beta^2 \gamma^2 B^2 \sin^2\theta\,, \tag{1.4}$$

where $r_0 = e^2/m_e c^2$ is the classical electron radius and $\beta = v/c$. Due to the motion of the charged particle being relativistic, the radiation is concentrated in a narrow cone. If an observer's line of sight intersects with the emission cone then they will see a spectrum of emission, at large γ, that peaks in energy, E, at the critical frequency

$$\nu_c = \frac{3eB\sin\theta}{4\pi m_e c}\left(\frac{E}{m_e c^2}\right)^2\,. \tag{1.5}$$

The power emitted by a single electron per unit frequency interval is then given by

$$P(E,\nu) = \frac{\sqrt{3}e^3 B\sin\theta}{m_e c^2} F\left(\frac{\nu}{\nu_c}\right) , \tag{1.6}$$

and the function F is defined by

$$F(x) = x\int_x^\infty K_{5/3}(\xi)d(\xi) , \tag{1.7}$$

where $K_{5/3}(\xi)$ is the modified Bessel function of order 5/3. Hence, the total power emitted at all frequencies by an electron is found by integrating $P(E,\nu)$ over ν. For an ensemble of electrons, the number density, n_e, with an energy between E_1 and $E_2 = E_1 + dE$ is given by $n_e(E)dE$ and the power emitted as a function of frequency is

$$P(\nu) = \int_{E_1}^{E_2} P(E,\nu)n_e(E)dE . \tag{1.8}$$

If the electrons have a power law distribution of energies, such a distribution can be generated via a shock, then the number density as a function of energy is given by $n_e(E)dE = CE^{-p}dE$, where C and p are constants. Defining $x = \nu/\nu_c$ the power emitted by an ensemble of electrons at frequency ν is given by

$$P(\nu) = \frac{\sqrt{3}e^3}{2m_e c^2}\left(\frac{3e}{4\pi m^3 c^5}\right)^{(p-1)/2} C\,(B\sin\theta)^{(p+1)/2}\,\nu^{-(p-1)/2} G(x_1,x_2,p) , \tag{1.9}$$

where

$$G(x_1,x_2,p) = \int_{x_1}^{x_2} x^{(p-3)/2}F(x)dx , \tag{1.10}$$

where x_1 and x_2 correspond to the critical frequencies at energy E_1 and E_2 respectively. It is clear from equation (1.9) that the emitted spectrum has a simple power law of the form

$$P(\nu) \propto \nu^{-\alpha} , \tag{1.11}$$

where the spectral index of the emission $\alpha = (p-1)/2$. Equation (1.9) allows the synchrotron emission of a system to be related to the amplitude of the magnetic field and the energy density of the relativistic electrons in the system. In order to say anything about the magnetic field the bulk properties of the relativistic electrons must be known. In order to proceed, the assumption of

minimizing the total energy of the electrons with respect to the magnetic field is made. By integrating over a fixed energy interval, $E_1 < E < E_2$, the energy density of the relativistic electrons is given by

$$\begin{aligned} \varepsilon_{\rm re} &= \int_{E_1}^{E_2} E n_e(\nu_c) d\nu_c \\ &\propto B^{\alpha} \Theta^2 S_{\nu} \, , \end{aligned} \tag{1.12}$$

where S_ν is the total flux density, Θ is the angular size of the source. Re-arranging this equation, a minimum energy estimate for the magnetic field strength of the system is obtained

$$B_{\rm eq} \propto S_{\nu}^{-2/(p-5)} \Theta^{-4/(p-5)} \, . \tag{1.13}$$

Due to their low self-absorption in the ISM, intergalactic medium (IGM) and ICM, the majority of the emitted synchrotron photons will travel until they are detected, making it an invaluable tool for studying extragalactic magnetic fields. It has been used to study the magnetic fields of external galaxies, finding μG amplitude magnetic fields in many spiral galaxies, such as M31 (Beck 1982) and M51 (Fletcher et al. 2011). Diffuse synchrotron emission, known as a "radio halo", has been found in the IGM of groups and the ICM of clusters of galaxies, demonstrating the presence of volume filling magnetic fields in these objects. These radio halos have a steep spectral index and are consistent synchrotron emission due to μG amplitude magnetic fields. There is a strong correlation between the X-ray and radio surface brightness and the X-ray and radio halo luminosity, see Fig. 1.2, of galaxy clusters (Govoni et al. 2001). A review of the properties of the magnetic fields in these large-scale systems is given in Carilli and Taylor (2002).

At some level the minimum energy assumption will be incorrect, due to the interactions between relativistic particles, shock fronts and magnetic fields redistributing the energy of the cosmic rays and the magnetic field. In the case of a galaxy, it has been argued that to achieve discrepancies as large as an order of magnitude between the estimated value under the minimum energy condition and the true value of the magnetic field would require extreme conditions (Duric 1990). Lower values of the magnetic field would require a

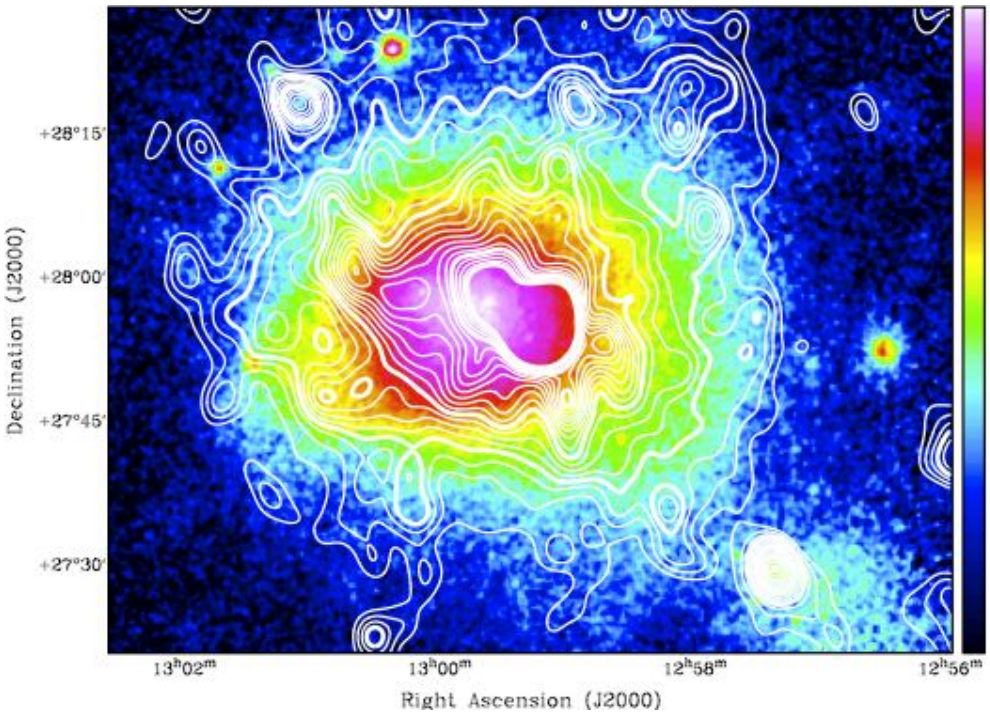

Fig. 1.2: A colour map of the X-ray emission from the Coma galaxy cluster. Overlaid are contours of synchrotron emission that demonstrate the presence of a diffuse radio halo, whose morphology is similar to the X-ray morphology. Image credit: Brown and Rudnick (2011).

significantly higher energy population of particles to explain the emission. This would imply larger propagation lengths and an extended radio halo, which is inconsistent with the observations (Beck and Hoernes 1996). Higher values would imply shorter correlation lengths, again in conflict with the observational evidence. The minimum energy assumption can be tested in the Milky Way as the cosmic-ray electron density and the cosmic-ray proton density, via continuum γ-rays, can be independently measured. The result of this test yields a value in excellent agreement with the equipartition value (Beck 2002).

Synchrotron emission from an ensemble of relativistic electrons is linearly polarized. The degree of linear polarization, Π, for a regular magnetic field and a power-law distribution of electrons is fixed by the spectral index of the electron distribution, p, and is given by

$$\Pi = \frac{p+1}{p+7/3} \,, \tag{1.14}$$

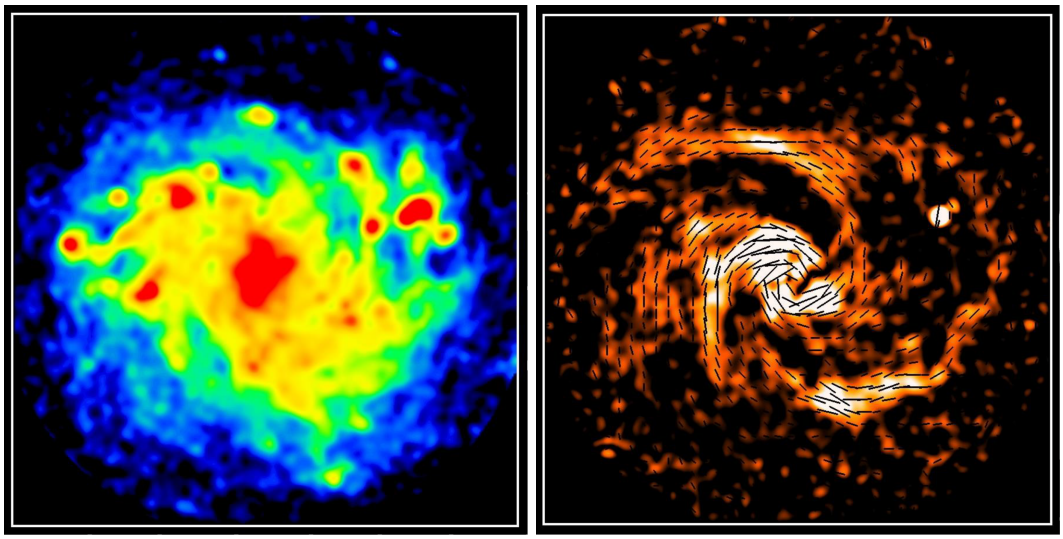

Fig. 1.3: Plot of the total (left panel) and linearly polarized (right panel) synchrotron intensity of the intermediate spiral galaxy NCG6946. The black lines in the polarized panel show the orientation of the magnetic field in the galaxy. Image credit: Beck and Hoernes (1996).

in the optically thin limit (see Rybicki and Lightman 1979). The degree of polarization measures the ratio of the intensity of linearly polarized photons to the total synchrotron intensity of the source. For typical values of p for a spiral galaxy this should yield a linear polarization fraction of $\Pi = 0.72 - 0.74$. However, the observed value is $\Pi = 0.1 - 0.2$ for an average spiral galaxy. The polarization of synchrotron radiation is a measure of how ordered the magnetic field is in the system and provides the orientation of the magnetic field in the system, see Fig. 1.3. Fluctuations in the magnetic field, inhomogeneities in the electron density, beaming smearing and Faraday depolarization will all lead to a reduction in fraction of polarized emission.

1.2.4 Faraday Rotational Measure

A linearly polarized electromagnetic wave can be considered as being made up of left handed and right handed circularly polarized components traveling with the same phase velocity. When passing through a medium that contains both a magnetic field and free electrons, such as a magnetized plasma, these two components will see a different refractive index for the medium. This will

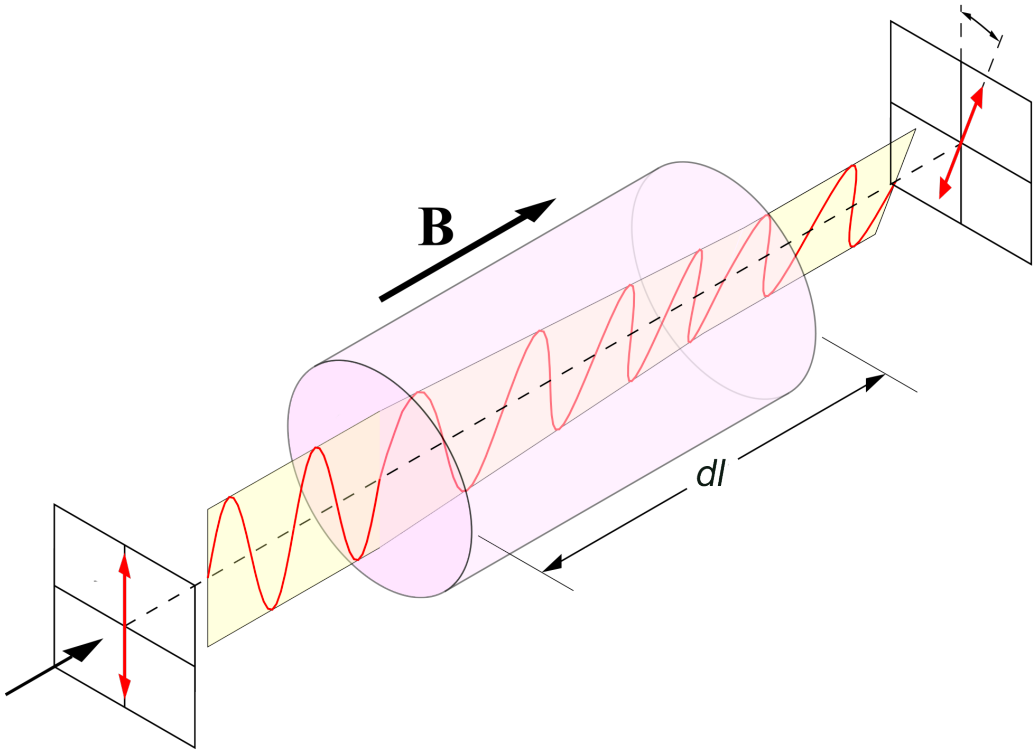

Fig. 1.4: Diagram showing the Faraday effect on a linearly polarized electromagnetic wave passing through a medium containing both free electrons and a magnetic field. The rotation of the polarization angle can be used to obtain a measure of the magnetic field along the line of sight.

cause the them to travel with different phase velocities through the medium, leading to a change in their relative phases. This is known as the Faraday effect and it leads to a rotation in the plane of the polarization of the wave relative to its orientation when it entered the medium, see Fig. 1.4. For a wave with an initial polarization angle Φ_0, the change in angle, neglecting absorption and scattering, is given by

$$\Phi = \Phi_0 + \frac{e^3\lambda^2}{2\pi m_e^2 c^4}\int_0^{l_s} n_e(l)B_{\parallel}(l)dl = \Phi_0 + (RM)\lambda^2 \,, \qquad (1.15)$$

where e is the electron charge, m_e is the electron mass, c is the speed of light and λ is the wavelength of the wave. The change in angle of the polarization is dependent on the thermal electron distribution, $n_\mathrm{e}(l)$, and the magnetic field, $B_{\parallel}(l)$, parallel to the line of sight, l, from the observer at $l = 0$ to the source at $l = l_s$. This can be written more succinctly as the rotation measure RM

of the polarization, which on large scales can be expressed in terms of radians per square meter via

$$RM \simeq 812 \frac{\mathrm{rad}}{\mathrm{m}^2} \int_0^{l_s} \left(\frac{n_e}{\mathrm{cm}^{-3}}\right) \left(\frac{B_\parallel}{\mu\mathrm{G}}\right) \left(\frac{dl}{\mathrm{kpc}}\right) . \tag{1.16}$$

The RM can be deduced from multiwavelength observations, where the several different wavelengths enable the $\Phi \pm n\pi$ ambiguity to be resolved. These measurements are typically done at radio wavelengths. By convention a positive/negative RM is for a magnetic field that is orientated towards/away from the observer. For an extended source, Faraday rotation will vary across the source due to variation in the source properties. If these variations are smaller than the beam size used to observe the source there will be vector addition of differently rotated beams, leading to a reduction in the observed polarized flux (see Sokoloff et al. 1998).

The RM of pulsars and extragalactic radio sources have been used to constrain the structure of the magnetic field in the disk of the Milky Way. It was found that the Galaxy has a bi-symmetric spiral con uration that is strong in the interarm regions and reverses in the arm regions. The strength of the galactic magnetic field was found to be $B = 1.4\,\mu$G (Han and Qiao 1994). A study of the RMs of polarized sources at higher latitudes suggests that the magnetic field does not reverse across the mid plane of the galaxy and that the azimuthal magnetic field has an amplitude of $B = 1.4\,\mu$G between $0.8-2.0\,$kpc above the galactic disk (Mao et al. 2012). Faraday RMs have been used to map the magnetic field strength of the Coma galaxy cluster. They found a radially decreasing magnetic field profile that peaks with a central amplitude of $B = 4.7\,\mu$G (Bonafede et al. 2010).

The RM will contain contributions from every magnetized region along the line of sight from the source. If the source itself is magnetized this will contribute to the RM and the Galaxy contains a magnetic field that will contribute as a foreground source to the RM. These contributions contaminate the RM signal and to obtain a true measure of the magnetic field in the system of interest these signals must be separated. This can be achieved using the Faraday RM synthesis technique, first presented by Burn (1966) and extended

and implemented by Brentjens and de Bruyn (2005). The different RM line of sight contributions can be found by using the RM transfer function to convert the complex polarized intensity to the Faraday spectrum. The spectrum enables different contributions to the Faraday depth to found, isolating the individual contributions and obtaining a more accurate value of the magnetic field in the system of interest.

1.2.5 TeV Blazar Emission

Blazars are AGN where the orientation of their jet is closely aligned along the line of sight. The $0.1 - 10\,\mathrm{TeV}$ γ-rays that they emit enable us to probe magnetic fields on scales beyond the largest gravitationally bound objects in the Universe. TeV photons will interact with homogeneous and isotropic Extragalactic Background Light (EBL) photons, which have energies of $0.1 - 10\,\mathrm{eV}$ (Gould and Schréder 1966). EBL photons are produced by stars and star formation in galaxies. The mean free path of a TeV γ-ray in the EBL photon field is on the order of $100\,\mathrm{Mpc}$ and decreases as the energy of the γ-ray increases (Kneiske 2008), as the higher energy photons can interact with the increasingly more abundant lower energy photons of the EBL. The interaction of the very high energy γ-rays with the EBL photons results in the production of a cascade of electron-positron pairs in the IGM. These pairs are relativistic and propagate along the initial γ-ray beam. However, these electron-positron pairs rapidly lose energy via inverse Compton scattering with CMB photons. All of the energy of the original TeV γ-ray is very quickly converted from the electron-positron pairs into inverse Compton γ-rays. This mechanism produces a cascade of secondary γ-rays, with energies ranging from $< 1\,\mathrm{GeV}$ to $> 100\,\mathrm{GeV}$, that can, in principle, be separated from the intrinsic source contribution by their extended distribution on the sky in comparison to the point like blazar emission. A thorough review of this process is given in Durrer and Neronov (2013).

The magnetized IGM will leave an imprint on the secondary electrons. The pair produced electrons and positrons are deflected and travel on curved trajectories through the IGM, leading to a displacement in the production of the secondary γ-rays (Neronov et al. 2010). Additionally, lower energy pairs

are more highly deflected leading to a time delay in the cascade signal of the secondary electrons. Hence, the angular size of the secondary emission and the time delay of the emission is dependent on the amplitude and coherence length of the magnetic fields permeating the IGM. Observations made using the Fermi γ-ray telescope (Atwood et al. 2009) by Neronov and Vovk (2010) and Tavecchio et al. (2011) set a lower bound magnetic field strength of $B \gtrsim 3 \times 10^{-16}$ G in the IGM. Takahashi et al. (2013) using Fermi, with additional data from the ARGO-YBJ experiment (Aloisio et al. 2001), set a lower limit amplitude of $B \gtrsim 3 \times 10^{-21}$ G for a magnetic field permeating a cosmological void of the Universe.

The biggest uncertainty in the lower bound for the IGM magnetic field derived from γ-ray observations is mainly caused by the uncertainty in the measurement of the EBL. The ratio of secondary to primary γ-rays has an exponential dependence on the EBL density, so a factor of two uncertainty in the EBL density will result in an order of magnitude uncertainty in the derived lower limit of the magnetic field. However, recent measurements of the EBL by the HESS experiment (Abramowski et al. 2012) have significantly reduced this uncertainty. If the extended emission around a TeV source could be measured to obtain an energy dependent morphology then the magnetic field could be directly measured, instead of obtaining a lower bound for it. However, this has not yet been achieved. The presence of coherent magnetic fields on scales beyond the largest bound structure of the Universe presents significant challenges for the theory of their generation.

1.3 The Origin of Large-scale Magnetic fields

The generation of magnetic fields on Mpc scales and beyond is still not well understood. On stellar scales the accretion disk that forms around protostars is capable of seeding the magnetic field that permeates these systems and their stellar winds, outflows and supernovae can provide seed magnetic fields on the galactic scale (Hanasz et al. 2009). However, at the Mpc scale the diffusion time-scale for a supernovae is too large to explain the presence of magnetic fields in clusters, superclusters and cosmological voids. The theory of magne-

togenesis for the very largest systems in the Universe is split into two broad categories, those that occur in the very early Universe before recombination and those that occur during the formation of structure.

1.3.1 Generation via Inflation

Inflation provides a viable mechanism to produce scale free energy density perturbations, making it an attractive candidate as the magnetogenesis mechanism for the Universe. During inflation the size of the observable Universe, roughly the age of the Universe multiplied by the speed of light, is approximately constant while length scales are stretched beyond it, causing them to become horizon scaled at the current epoch. Therefore, a magnetic field generated by primordial fluctuations before inflation could seed the entire observable Universe after inflation. However, electromagnetic fields are conformally coupled to gravity and so, in a Friedmann-Robertson-Walker framework, as the Universe expands the energy density of the magnetic fluctuation decreases as a^{-4}, where a is the scale factor of Universe. Hence for a length scale of 1 Mpc and an energy scale of inflation of 10^{15} GeV, in the most optimistic case the co-moving magnetic field strength after inflation is $B \sim 10^{-49}$ G (Martin and Yokoyama 2008; Subramanian 2010). This value is far too small to explain the large-scale magnetic field observed in the Universe, even with dynamo amplification.

To generate meaningful magnetic fields during inflation either the conformal invariance of the magnetic field or the gauge invariance must be broken. This has been studied by many authors (Turner and Widrow 1988; Ratra 1992; Kunze 2010; Kandus et al. 2011; Jain and Sloth 2012) and any mechanism to brake conformal or gauge invariance requires additional physics that is beyond the standard model. However, once the invariance is broken, inflation can generate magnetic fields with a co-moving amplitude up to $B \sim 10^{-9}$ G on cosmologically relevant scales. An inflationary magnetogenesis mechanism would naturally explain the presence of coherent magnetic fields in cosmological voids and could seed the dynamos of bound systems. Void magnetic fields would then be a relevant tool for studying the physics of inflation and physics beyond the standard model.

1.3.2 Phase Transitions in the early Universe

In the standard model of the formation of the Universe there are phase transitions that break the symmetries of the early Universe, leading to the separation of the fundamental forces. The standard model predicts that these transitions are not true phase transitions, associated with discontinuities in the free energy, but are simply crossovers where the Universe changes from one behaviour to another (Csikor et al. 1998; de Forcrand and Philipsen 2003). If this is the case, the amplitude strength of a magnetic field generated on large-scales by these transitions is negligible. However, there are many modifications to the standard model that predict these transitions are first order and associated with a discontinuity in the free energy (Grojean et al. 2005; Huber et al. 2007; Schwarz and Stuke 2009).

The first phase transition the Universe undergoes is the electroweak transition. This is where a symmetry of the early Universe breaks and the weak and electromagnetic forces become separate and distinct. The second phase transition is the QCD transition. Before this transition the quarks and gluons of the Universe behave like free particles in a quark-gluon plasma. At the phase transition the strong force dominates and locks the charged quarks into neutral hadrons. Under the assumption that these transitions are first order, the co-moving amplitude of the magnetic field can be calculated. On a 1 Mpc scale, the co-moving magnetic field strength generated by the electroweak transition is $B \sim 1 \times 10^{-29}$ G and the QCD transition is $B \sim 1 \times 10^{-23}$ G (Kahniashvili et al. 2013). In a first order phase transition, bubbles of matter in the new phase appear, grow and then merge. The coherence length of the relic magnetic fields generated by phase transitions is the size of the largest bubbles that form, which is a few parsecs for the electroweak transition and on the order of a kiloparsec for the QCD transition (Huber and Konstandin 2008). The discovery of magnetic fields coherent on these scales inhabiting cosmological voids would enable the use of magnetic fields as a probe of physics beyond the standard model.

1.3.3 Density Perturbations

In the early Universe photons, protons and electrons are tightly coupled by very efficient Compton and Coulomb interactions, allowing them to be considered as a single fluid. However, photons preferentially scatter off electrons, leading to differences in the velocities of protons and electrons. This difference in velocities leads to the generation of electric currents, and these currents seed the Universe with magnetic fields (Lesch and Chiba 1995). The electric currents generated are associated with the density perturbations of the photons and so the magnetic fields must be associated with temperature fluctuations of the CMB.

The generation of magnetic fields during the epoch of recombination is governed by three main factors: the baryon-photon slip, the vorticity difference and the anisotropic pressure. These can be derived from the fact that the photons exert a force on the electrons via Compton scattering when there is anisotropic pressure from the photons. These terms were calculated by Ichiki et al. (2006) and used to derive the power spectrum of the magnetic fields induced by density perturbations in the early Universe. They found that the generated magnetic fields increased monotonically with decreasing scale. At Mpc scales they found that density perturbations would generate a magnetic field amplitude of $B \sim 8 \times 10^{-25}\,\mathrm{G}$. At the comoving scale of 0.1 kpc they found a field strength of $B \sim 2 \times 10^{-13}\,\mathrm{G}$, enabling the magnetic field to trigger the magneto-rotational instability in the accretion discs of the first stars. This allows angular momentum to be transported out of the disc and is critical to their formation, causing magnetic fields to be a vital ingredient of the formation of structure at high redshift.

1.3.4 Reionization

As the first stars and galaxies begin to form they emit UV photons that begin to reionize the Universe. Ions and electrons in the ionized material around the emitting object interact with radiation according to a scattering cross section that varies as $\sigma_T \propto \mathrm{mass}^{-2}$. Due to the difference in mass between the electrons and ions, the radiation drags experienced by them are different and this leads to a local separation of charge. For a medium that is inhomogeneous,

such as one collapsing to form structure, this charge separation will lead to the generation of electric fields that vary, which in turn will generate magnetic fields (Langer et al. 2003).

Initially, the electron-ion collision frequency is greater than the cyclotron frequency and the magnetic field grows. Once the magnetic field is strong enough, so that the cyclotron frequency is greater than the electron-ion frequency, the back reaction of the magnetic field becomes important and the magnetic field reaches saturation. At the beginning of reionization the average source separation is $\sim 2\,\mathrm{Mpc}$ and so on megaparsec scales radiation drag leads to magnetic fields with an amplitude of $B \approx 4 \times 10^{-20}\,\mathrm{G}$ (Langer et al. 2005). These magnetic fields are strong enough to seed dynamos that will amplify them to the values observed in systems at the current epoch. However, these magnetic fields are only generated where material is collapsing to form structure, hence an additional mechanism is required to explain the presence of magnetic fields in cosmological voids.

1.3.5 Biermann Battery in Large-scale Collapsing Structure

As the fluid of the Universe collapses to form structure it generates vorticity. However, it is impossible to produce vorticity purely by gravitational collapse and its generation must be the result of baryonic processes. Second order fluctuations in the density and pressure will produce misaligned density and pressure gradients in the fluid, leading to the generation of vorticity. After the reionization of the Universe, the generation of vorticity in a plasma will drive an electric current that, in turn, will generate a magnetic field. This magnetogenesis mechanism is commonly known as the Biermann battery (Biermann 1950). This will seed magnetic field in the large gravitating systems according to

$$\frac{d\mathbf{B}}{dt} = \frac{m_{\mathrm{p}} c}{e\,(1+\chi)} \frac{\nabla\rho \times \nabla P}{\rho^2}\,, \tag{1.17}$$

where m_{e} is the electron mass, e is the electron charge, c is the speed of light, P is the pressure and ρ is the density and a full derivation of this term can be found in Appendix A. The generation of a magnetic field is due to the difference in mass between the ions and the electrons of the plasma. The

differing masses cause them to experience a different amount of acceleration for a given force, leading to a charge separation that is eventually balanced by an induced electrostatic field. However, when the gradients are no longer parallel an equilibrium between the separated charges and the electrostatic field is no longer possible and a current is generated.

This magnetogenesis mechanism has been tested in laboratory plasmas. Gregori et al. (2012) used high powered lasers focused onto a carbon rod in an interaction chamber filled with Helium gas to generate the crossed density and pressure gradients. They measured a magnetic field of $10 - 30\,\mathrm{G}$. By scaling their set up to an astrophysical sized system, they predicted that collapsing structure could generate a seed magnetic field of $B \approx 1 \times 10^{-21}\,\mathrm{G}$ on Mpc scales via the Biermann battery mechanism. This would be sufficient to seed the dynamos of large-scale astrophysical systems, but would struggle to produce coherent magnetic fields in cosmological voids.

1.3.6 Stellar and Galactic Outflows

The first stars that form in the Universe will be magnetized, even if no significant field develops before their formation. Material accreting on to a protostar will form an accretion disc. The differential rotation of the disc, temperature gradients in the disc and the presence of an ionizing source at the centre of the disc mean that seed magnetic fields can be generated in the accretion disc by both the Biermann battery mechanism and the radiation drag mechanism. These initial seeds are then amplified by dynamo mechanisms in the accretion disc and in the star. During their lifetime stars eject material into their surrounding medium, via winds, outflows and supernovae, and, as their material is magnetized, they "pollute" the surrounding medium with magnetic fields. Within a galaxy, the magnetic fields ejected by many stars are amplified by the small-scale dynamo, driven by the turbulence of the ISM, and made coherent by the large-scale dynamo, which is driven by the large-scale rotation of the galaxy. The large-scale structure of the Universe can then be polluted by magnetic material removed from galaxies. Material can be stripped from galaxies by ram pressure as they fall into larger objects such as groups and clusters. Additionally, intense bursts of star formation can drive winds in galaxies that

pollute the IGM with the magnetized material of the galaxy, such as the observed super wind of M87. Pollution of a galaxy cluster by galactic winds was studied by Donnert et al. (2009). After seeding the galaxies at $z = 4.1$ with a magnetic field of $B = 5 \times 10^{-9}$ G they used a semi-analytic model of starburst driven outflows to pollute the ICM. The magnetic field is then further amplified by shear flows and turbulent motions induced by the formation of the cluster. They found that they could pollute the entire volume of the ICM by the current epoch and that the magnetic fields have the observed micro-Gauss strength.

The super massive black holes at the centre of galaxies provide another way to magnetize the large-scale structure of the Universe, even if no significant magnetic fields were generated before structure formation. Material accreting onto the black hole forms an accretion disc, which can generate seed magnetic fields via the Biermann battery and radiation drag mechanisms. Initial seed magnetic fields are then amplified by a dynamo mechanism in the accretion disc and by the extreme physics close to the black hole. These magnetic fields are then transported out into the large-scale structure of the Universe by the relativistic jets that are seen emanating from AGN. Xu et al. (2010) studied the magnetic pollution of a galaxy cluster by material released by AGN jets. By modeling the amount of magnetic energy injected by many different AGNs as the cluster forms, they were able to reproduce the observed magnetic field amplitude in galaxy clusters. They found that if the majority of the energy is injected at a high enough redshift then the magnetic field will pollute the entire cluster volume.

Magnetized material thrown out into the large-scale structure of the Universe by stars and galaxies can easily seed galaxy groups and clusters with magnetic fields with sufficient amplitude to explain the observations of these systems. However, it is very difficult to reconcile them with the observed coherent magnetic fields in low-density cosmological structures, i.e. cosmological voids. However, magnetogenesis mechanisms are not mutually exclusive and it is more than likely that several mechanisms could seed the Universe with magnetic fields at different scales. To determine the dominant mechanisms

that seed the largest structures in the Universe the initial seed magnetic fields must be evolved to the current epoch, allowing a comparison with the observations. This is not a trivial process as the magnetic fields undergo significant compressional and shear motions as the structure of the Universe forms. To understand how to transform a seed field to an observable field the equations of electromagnetism and the equations of fluid dynamics must be solved simultaneously.

1.4 Magnetohydrodynamics

On the very largest scales in the Universe the magnetic energy density is significantly weaker than the kinetic energy density. Therefore, any seed magnetic field, regardless of its generation mechanism, is effectively "frozen" into the gaseous fluid from which the Universe forms. As this gas collapses to form galaxies and clusters of galaxies, the magnetic field will be dragged with it and undergo compressional and shearing motions. This will significantly alter the initial seed magnetic fields and will amplify them to the magnetic fields observed in the large-scale structures of the Universe. To gain a deeper understanding of the magnetic fields that permeate the largest structures in the Universe the evolution of a seed field, due to the formation of structure, must be correctly modeled.

By treating the gas as a fluid, the evolution of a seed magnetic field from its generation to the current epoch is the interaction of a fluid with a magnetic field. Following Spitzer (1962), the ohmic resistive timescale of large-scale systems in the Universe can be estimated. Using typical values for the temperature and size of a galaxy cluster ($T \sim 10^7\,\mathrm{K}$, $L \sim 1\,\mathrm{Mpc}$) the resistive timescale is found to be $\tau \sim 1.91 \times 10^{39}\,\mathrm{yrs}$, which is significantly longer than the current age of the Universe. Therefore, the large-scale structure of the Universe can effectively be considered as a perfect conductor. The negligible resistive dissipation of large-scale structure and the fact that the sound speed in these systems is non-relativistic allows the use of the magnetohydrodynamic (MHD) single fluid approximation.

1.4.1 The Equations of MHD

Magnetohydrodynamics describes the interaction between an electromagnetic field and a conducting fluid. It combines the equations of fluid dynamics with Maxwell's equations. The equations of fluid dynamics are

$$\frac{d\rho}{dt} + \rho\nabla \cdot \mathbf{v} = 0 \,, \tag{1.18}$$

$$\frac{d\mathbf{v}}{dt} + \frac{\nabla P}{\rho} = \mathbf{F} \,, \tag{1.19}$$

$$\frac{du}{dt} + \frac{P}{\rho}\nabla \cdot \mathbf{v} = 0 \,, \tag{1.20}$$

where the ρ is the density, $\mathbf{v}$ is the velocity, u is the internal specific energy, $\mathbf{F}$ is any force acting on the fluid and, in the absence of a magnetic field, the pressure $P = P_{\rm gas} = (\gamma - 1)\rho u$ for an ideal fluid, where γ is the adiabatic index. These equations are expressions of mass, momentum and energy conservation respectively. In a magnetized plasma $P = P_{\rm gas} + P_{\rm mag}$ and $\mathbf{F} = (\mathbf{J} \times \mathbf{B})/\rho$ is the Lorentz force. In MHD, the fluid equations need to incorporate Maxwell's equations, which in c.g.s. units take the form

$$\nabla \cdot \mathbf{E} = 4\pi\rho_c \,, \tag{1.21}$$

$$\nabla \cdot \mathbf{B} = 0 \,, \tag{1.22}$$

$$\nabla \times \mathbf{E} = -\frac{1}{c}\frac{\partial \mathbf{B}}{\partial t} \,, \tag{1.23}$$

$$\nabla \times \mathbf{B} = \frac{4\pi}{c}\mathbf{J} + \frac{1}{c}\frac{\partial \mathbf{E}}{\partial t} \,, \tag{1.24}$$

where $\mathbf{E}$ is the electric field, $\mathbf{B}$ is the magnetic field, ρ_c is the charge density, c is the speed of light and $\mathbf{J}$ is the current density. The current density can be related to the electric and magnetic fields via Ohm's law, such that $\mathbf{J} = \sigma[\mathbf{E} + (\mathbf{v} \times \mathbf{B})/c]$, where σ is the conductivity of the fluid. One of the assumptions of MHD is that the timescale of the system considered is very large in comparison to the interaction timescale and this allows the second right

hand side term of Ampere's law, equation (1.24), to be neglected. Substituting Ohm's law for the current density into Ampere's law produces

$$\mathbf{E} = \frac{c}{4\pi\sigma}\nabla \times \mathbf{B} - \left(\frac{\mathbf{v}}{c} \times \mathbf{B}\right) , \tag{1.25}$$

where the equation has been rearranged to find an expression for the electric field. Substituting equation (1.25) into Faraday's law, equation (1.23), gives

$$\frac{\partial \mathbf{B}}{\partial t} = \nabla \times (\mathbf{v} \times \mathbf{B}) - \frac{c^2}{4\pi\sigma}\nabla \times \nabla \times \mathbf{B} . \tag{1.26}$$

Using vector identities for $\nabla \times (\mathbf{v} \times \mathbf{B})$ and $\nabla \times \nabla \times \mathbf{B}$ this expression can be rearranged to obtain

$$\frac{\partial \mathbf{B}}{\partial t} + (\mathbf{v}\cdot\nabla)\mathbf{B} = \mathbf{v}(\nabla\cdot\mathbf{B}) - \mathbf{B}(\nabla\cdot\mathbf{v}) + (\mathbf{B}\cdot\nabla)\mathbf{v} - \frac{c^2}{4\pi\sigma}(\nabla(\nabla\cdot\mathbf{B}) - \nabla^2\mathbf{B}). \tag{1.27}$$

This equation simplifies using the definition of a total derivative and the solenoidal constraint of the magnetic field, equation (1.22), to yield the induction equation, which defines the evolution of the magnetic field with time as

$$\frac{d\mathbf{B}}{dt} = (\mathbf{B} \cdot \nabla)\mathbf{v} - \mathbf{B}(\nabla \cdot \mathbf{v}) - \eta\nabla^2\mathbf{B} , \tag{1.28}$$

where $\eta = -c^2/4\pi\sigma$ is the resistivity. The third term on the right hand side represents the large scale diffusion of the magnetic field. Due to the size of the system, the timescale for this diffusion is very large in comparison to the age of the Universe and the third term can be neglected to obtain

$$\frac{d\mathbf{B}}{dt} = (\mathbf{B} \cdot \nabla)\mathbf{v} - \mathbf{B}(\nabla \cdot \mathbf{v}) . \tag{1.29}$$

This is the induction equation and it is the continuity equation for the magnetic field. The first term on the right hand side will enhanced/diluted the magnetic field parallel to the fluid flow when it is compressed/rarified and shows that an acceleration of the flow produces an increase in the magnetic field perpendicular to the flow. The second term will enhance or dilute the magnetic field where flows converge or diverge respectively.

The addition of a magnetic field to the system leaves the mass and energy equations, equations (1.18) and (1.20), unchanged. The momentum equation

gains additional terms, due to the need to include the Lorentz force, and becomes

$$\frac{d\mathbf{v}}{dt} = -\frac{\nabla P}{\rho} + \frac{\mathbf{J}\times\mathbf{B}}{\rho} + \frac{\mathbf{B}\nabla\cdot\mathbf{B}}{4\pi\rho}\,, \tag{1.30}$$

where the current density $\mathbf{J} = (\nabla\times\mathbf{B})/4\pi$. As magnetic monopoles do not seem to exist, equation (1.22), this equation reduces to

$$\frac{d\mathbf{v}}{dt} = -\frac{\nabla P}{\rho} + \frac{\mathbf{J}\times\mathbf{B}}{\rho}\,. \tag{1.31}$$

Equations (1.18), (1.31), (1.20) and (1.29) are the mass, momentum, energy and magnetic field equations of ideal MHD. An additional complexity introduced in a magnetized fluid is the speed at which information can propagate through the fluid.

1.4.2 Waves in an MHD system

In an unmagnetized fluid, information can travel through the system as a wave, moving at the sound speed. For an ideal fluid the adiabatic sound speed is given by

$$c_s = \sqrt{\frac{\gamma P}{\rho}}\,, \tag{1.32}$$

and the waves travel through the system as compressions and rarefactions. However, with the introduction of a magnetic field the situation becomes more complicated. This is demonstrated by perturbing the system according to

$$\rho = \rho_0 + \delta\rho\,, \tag{1.33}$$

$$\mathbf{B} = \mathbf{B}_0 + \delta\mathbf{B}\,, \tag{1.34}$$

$$\delta P = c_s^2\delta\rho\,, \tag{1.35}$$

and for simplicity setting $\delta\mathbf{v} = \mathbf{v}$. If only linear perturbation terms are considered, the MHD equations are given by

$$\frac{d(\delta\rho)}{dt} = -\rho_0(\nabla\cdot\mathbf{v})\,, \tag{1.36}$$

$$\frac{d\mathbf{v}}{dt} = -\frac{c_s^2\nabla(\delta\rho)}{\rho_0} - \frac{\mathbf{B}_0\times(\nabla\times\delta\mathbf{B})}{4\pi\rho_0}\,, \tag{1.37}$$

$$\frac{d(\delta\mathbf{B})}{dt} = (\mathbf{B}_0 \cdot \nabla)\mathbf{v} - \mathbf{B}_0(\nabla \cdot \mathbf{v}) \,. \tag{1.38}$$

Without losing generality, a plane wave solution can be taken, which has the form

$$\delta\rho = Re^{i(\mathbf{k}\cdot\mathbf{x}-\omega t)} \,, \tag{1.39}$$

$$\mathbf{v} = \mathbf{v}e^{i(\mathbf{k}\cdot\mathbf{x}-\omega t)} \,, \tag{1.40}$$

$$\delta\mathbf{B} = \mathbf{b}e^{i(\mathbf{k}\cdot\mathbf{x}-\omega t)} \,, \tag{1.41}$$

and so equations (1.36), (1.37) and (1.38) respectively become

$$-\omega R = -\rho_0(\mathbf{v} \cdot \mathbf{k}) \,, \tag{1.42}$$

$$-\omega\mathbf{v} = -c_s^2\frac{R\mathbf{k}}{\rho_0} - \frac{1}{4\pi\rho_0}[(\mathbf{B}_0 \cdot \mathbf{b})\mathbf{k} - (\mathbf{B}_0 \cdot \mathbf{k})\mathbf{b}] \,, \tag{1.43}$$

$$-\omega\mathbf{b} = (\mathbf{B}_0 \cdot \mathbf{k})\mathbf{v} - \mathbf{B}_0(\mathbf{k} \cdot \mathbf{v}) \,. \tag{1.44}$$

Considering the plane wave in only the x-direction, i.e. $\mathbf{k} = (k_x, 0, 0)$, and that $b_x = 0$ as $\nabla \cdot \mathbf{B} = 0$, equation (1.42) can be rearranged in terms of R and substituted into equation (1.43) to obtain

$$v_x\left(\nu - \frac{c_s^2}{\nu}\right) = \left(\frac{B_{0,y}b_y + B_{0,z}b_z}{4\pi\rho_0}\right) \,, \tag{1.45}$$

$$v_y\nu = -\frac{B_{0,x}b_y}{4\pi\rho_0} \,, \tag{1.46}$$

$$v_z\nu = -\frac{B_{0,x}b_z}{4\pi\rho_0} \,, \tag{1.47}$$

where the phase speed is defined as $\nu = \omega/k$. Substituting into equation (1.44) produces

$$b_y\nu = -B_{0,x}v_y + B_{0,y}v_x \,, \tag{1.48}$$

$$b_z\nu = -B_{0,x}v_z + B_{0,z}v_x \,. \tag{1.49}$$

Solving for the perturbation amplitudes $v_{x,y,z}$ and $b_{y,z}$, substituting those solutions into equation (1.45) and dropping the subscript 0 produces an expression for the wave speed

$$(\nu^2 - \frac{B_x^2}{4\pi\rho}) \left[\nu^4 - \nu^2 \left(c_s^2 + \frac{|\mathbf{B}|}{4\pi\rho} \right) + \frac{c_s^2 B_x^2}{4\pi\rho} \right] = 0 \,. \tag{1.50}$$

This demonstrates that information can propagate at three different speeds in a magnetized fluid. The first solution to this equation is

$$\nu^2 = \frac{B_x^2}{4\pi\rho} \,, \tag{1.51}$$

which is a wave travelling at Alfvén speed along the field lines. The other two solutions can be found by solving the quadratic equation in ν^2 and produces

$$\nu^2 = \frac{1}{2} \left[\left(c_s^2 + \frac{|\mathbf{B}|^2}{4\pi\rho} \right) \pm \sqrt{\left(c_s^2 + \frac{|\mathbf{B}|^2}{4\pi\rho} \right)^2 - \frac{c_s^2 B_x^2}{\pi\rho}} \right] \,, \tag{1.52}$$

where the positive solution is the fast magnetoacoustic wave speed and the negative solution is the slow magnetoacoustic wave speed. To study how seed fields evolve to the magnetic fields observed, and their impact on the formation of the Universe, the equations of MHD must be solved either analytically or numerically, and the additional speeds at which information can propagate taken into account.

1.5 Summary

This chapter reviews the observations, the theoretical origins and the potential impact of the magnetic fields observed to permeate the largest structures in the Universe. First, the potential impact of sufficiently strong large-scale magnetic fields on processes that occur in the early Universe was examined. How these processes would have been affected by the presence of a magnetic field was discussed and upper limits on the amplitude of any magnetic field present in the early Universe, derived from observations of these processes, were presented.

The methods used to observe magnetic fields in galactic and extragalactic systems were reviewed. For each technique, the physical mechanism that allows the presence of a magnetic field to be inferred and its properties to be

studied was examined and the strength and weaknesses of each observational method were discussed. For each technique, observational results of magnetic fields in the Universe were presented, with a focus on magnetic fields in the largest systems.

The theory of the generation of magnetic fields for the largest structures in the Universe was introduced. The underlying physical mechanism that leads to the generation of a seed magnetic field was introduced and how these seeds go on to permeate the large-scale structure of the Universe. The advantages and disadvantages of each magnetogenesis mechanism compared to the observations was discussed.

Finally, the equations of fluid dynamics and the equations of electromagnetism were introduced. It was shown that, for large-scale astrophysical systems, assumptions can be made that simplify these two sets of equations to the equations magnetohydrodynamics. The induction equation, showing the change of the magnetic field with time, was derived and the additional terms required in the equation of motion for the fluid were presented. This system of equations was perturbed to demonstrate the additional speeds at which information can propagate through a fluid when a magnetic field is introduced.

Chapter 2

Smoothed Particle Magnetohydrodynamics

Cosmological magnetic fields, whether generated in the early Universe or via baryonic processes driven by the formation of structure at a later epoch, will undergo significant evolution due to the formation of large-scale structure in the Universe. To accurately capture the formation of structure, and the resulting seed field evolution, the equations of MHD must be reliably solved. The need to model multiple magnetogenesis mechanisms, the highly dynamic nature of structure formation and the complex interaction between the magnetic field and formation processes of the Universe make numerical simulations the only tractable approach to producing solutions to these equations. The standard approach adopted in solving this problem is to discretize the system on to a regular spatial grid, defining the fluid quantities, such as mass and pressure, for each cell of the grid and calculating their derivatives via a finite difference or finite volume scheme. However, in astrophysical fluid dynamics problems the spatial, temporal and density scales change by many orders of magnitude and the fixed grid approach is too restrictive. To overcome this limitation, techniques such as adaptive mesh refinement (AMR) have been developed to provide additional spatial refinement in locations of physical interest within the simulations. These methods are still not perfect, as astrophysical problems are commonly highly asymmetric, resulting in significant numerical diffusion when calculating derivatives and errors in the solution due to the failure to

maintain Galilean invariance (Robertson et al. 2010; Springel 2010).

An alternative to the discretization of the system by its space, is to discretize it by mass. This results in interpolation points, commonly known as 'particles', of set mass that follow the flow of the mass in the system and, therefore, are inherently spatially adaptive. The quantities of the fluid are carried by the particles and the derivatives of the fluid quantities are calculated either by interpolation over the neighbouring particles, known as the particle method, or by interpolation to a mesh generated from the particles themselves at each time-step. The particle method of solving the equations of fluid dynamics is known as Smoothed Particle Hydrodynamics (SPH) and was introduced by Lucy (1977) and Gingold and Monaghan (1977) and reviews are given in Monaghan (1992) and Springel et al. (2001).

SPH has found widespread use in astrophysics and is conceptually simple, with all of the equations self-consistently derivable from simple physical principles. Its Lagrangian nature automatically accounts for changes in flow and density, while minimizing the computational resources wasted on regions of empty space in the simulations. It easily deals with free boundaries that can cause issues in grid-based codes and no fluid is lost from the simulations. SPH naturally couples to commonly used N-body techniques, such as tree-codes to construct neighbours lists, allowing the self-gravity of the fluid to be easily incorporated.

The inclusion of a magnetic field in SPH produces Smoothed Particle Magnetohydrodynamics (SPMHD). An additional equation is required to follow the evolution of the magnetic field and additional terms in existing equations to allow the field to act back on the fluid and to conserve the total energy when magnetic energy is dissipated. The presence of a magnetic field introduces additional complexities to the simulations. First, the presence of a magnetic field can lead to the 'tensile' instability that can cause the particles to clump together when the magnetic pressure dominates, leading to incorrect solutions. Second, the ideal formulation for the resistive dissipative terms, enabling discontinuities in the magnetic field to be correctly resolved and accurately captured, is an active area of research. The final complexity is

maintaining the solenoidal constraint of the magnetic field, $\nabla \cdot \mathbf{B} = 0$. Physically this naturally occurs, equation (1.22), however, numerically this is not the case due to numerical integration and round-off errors. Demonstrated below are improvements to the standard implementation that produces a reliable and stable SPMHD formulation.

This chapter provides an overview of the SPMHD method, including improvements from the basic scheme that can resolve the problems that the addition of a magnetic field introduces. Section 2.1 introduces the basic numerical concepts required and section 2.2 derives the basic equations of SPH from the Lagrangian of the fluid. Section 2.3 examines the requirement for viscosity and how discontinuities in the fluid can be captured. How to include the self-gravity of the fluid, which is critical for many astrophysical problems, is shown in section 2.4. Section 2.5 introduces the SPMHD equation for the evolution of the magnetic field and derives the conservative magnetic stress tensor, allowing the magnetic field to act back on the fluid. How to deal with the instabilities this formulation produces is shown. Finally, a formulation for capturing discontinuities in the magnetic field and a scheme for maintaining the solenoidal constraint is introduced.

2.1 Basic Interpolant Formalism

The basis of the SPH approach is the trivial identity

$$A(\mathbf{x}) = \int A(\mathbf{x}')\delta(|\mathbf{x} - \mathbf{x}'|)d\mathbf{x}' \,, \tag{2.1}$$

where A is a quantity defined on the spatial coordinates $\mathbf{x}$ and δ is the Dirac delta function. Replacing the delta function with a smoothing kernel W of characteristic width of h, where h is commonly known as the smoothing length, produces

$$\lim_{h\to 0} W(|\mathbf{x} - \mathbf{x}'|, h) = \delta(|\mathbf{x} - \mathbf{x}'|) \,, \tag{2.2}$$

and the integral can be approximated such that

$$A(\mathbf{x}) = \int A(\mathbf{x}')W(|\mathbf{x} - \mathbf{x}'|, h)d\mathbf{x}' + O(h^2) \,. \tag{2.3}$$

The kernel function is normalized to unity via

$$\int W(|\mathbf{x} - \mathbf{x}'|, h)d\mathbf{x}' = 1 \,. \tag{2.4}$$

To make equation (2.3) computationally tractable it must be discretized for a finite set of interpolation points. This is achieved by replacing the integral over the fluid mass element, $\rho d\mathbf{x}$, by a summation over the particle masses, m, so that the fluid quantity at a particle is given by

$$\begin{aligned} A(\mathbf{x}) &= \int \frac{A(\mathbf{x}')}{\rho(\mathbf{x}')} W(|\mathbf{x}-\mathbf{x}'|,h)\rho(\mathbf{x}')d\mathbf{x}' + O(h^2)\,, \\ &\approx \sum_{j=1}^{N} m_j \frac{A_j}{\rho_j} W(|\mathbf{x}_i-\mathbf{x}_j|,h_i)\,, \end{aligned} \tag{2.5}$$

where the fluid quantity for particle i is evaluated using the fluid quantity at a different particle, j. This interpolation of the fluid quantities via summation is the basis of all SPH methods. The gradient of this quantity can be obtained by taking the analytic derivative of equation (2.5),

$$\begin{aligned} \nabla A(\mathbf{x}) &= \frac{\partial}{\partial \mathbf{x}} \int \frac{A(\mathbf{x}')}{\rho(\mathbf{x}')} W(|\mathbf{x}-\mathbf{x}'|,h)\rho(\mathbf{x}')d\mathbf{x}' + O(h^2)\,, \\ &\approx \sum_{j} m_j \frac{A_j}{\rho_j} \nabla_i W_{ij}(h_i)\,, \end{aligned} \tag{2.6}$$

where $\nabla_i \equiv \partial/\partial \mathbf{x}_i$, $W_{ij}(h_i) \equiv W(|\mathbf{x}_i-\mathbf{x}_j|,h_i)$ and it should be noted that $\nabla_i W_{ij} \sim (\mathbf{x}_{ij}/|\mathbf{x}_{ij}|) \times \partial W_{ij}$, so that the derivative is only dependent on the chosen kernel and the smoothing length. It is clear from both equations (2.5) and (2.6) that the step from continuous integral to discrete sum will introduce errors into the formulation. For those interested in the calculation of the errors introduced, and their correction terms, see Price (2004) and Monaghan (2005). As the magnetic field is a vector field, it is important to define estimates for the derivatives of vector quantities. The divergence and curl of a vector field are given by

$$(\nabla \cdot \mathbf{A})_i \approx -\sum_j m_j \frac{(\mathbf{A}_i - \mathbf{A}_j)}{\rho_i} \cdot \nabla_i W_{ij}(h_i)\,, \tag{2.7}$$

$$(\nabla \times \mathbf{A})_i \approx -\sum_j m_j \frac{(\mathbf{A}_i - \mathbf{A}_j)}{\rho_i} \times \nabla_i W_{ij}(h_i)\,. \tag{2.8}$$

Note that the divergence of a vector field can also be estimated via

$$(\nabla \cdot \mathbf{A})_i \approx \rho_i \sum_j m_j \left(\frac{\mathbf{A}_i}{\rho_i^2} + \frac{\mathbf{A}_j}{\rho_j^2} \right) \cdot \nabla_i W_{ij}(h_i)\,, \tag{2.9}$$

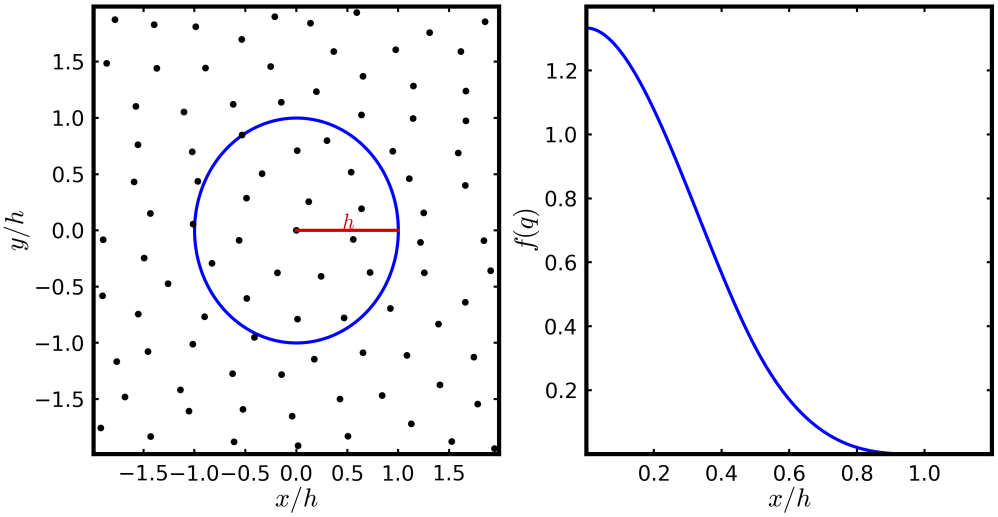

Fig. 2.1: The left panel shows the finite extent of the B_2-spline kernel. The right panel shows the weighting given to neighbour particles as a function of their distance.

however, this formulation is sensitive to the disorder of the particles (Price 2012). This is a numerical artefact that produces an incorrect value of the divergence of a vector quantity, such as the divergence of the magnetic field, and should be avoided where possible. To estimate a fluid quantity, and its derivatives, the smoothing kernel must first be specified.

2.1.1 Smoothing Kernel

The choice of function for the smoothing kernel must satisfy the limit of a Dirac delta function as h tends to zero, equation (2.2), and must normalize according to equation (2.4). The simplest function that satisfies these constraints is a Gaussian. The advantage of a Gaussian is that it is infinitely differentiable and, therefore, numerically stable. However, it has infinite extent and so quickly becomes computationally intractable. Therefore, smoothing kernels with finite extent (compact support) that approximate a Gaussian are used and traditionally produce the best results (Fulk and Quinn 1996). The most commonly used kernel function is the B_2-spline (Monaghan and Lattanzio 1985), commonly known as the cubic spline, that in 3-D, approximates

a Gaussian function via

$$W(\mathbf{x}, h) = \frac{8}{\pi h^3} \begin{cases} 1 - 6q^2 + 6q^3 & \text{if } 0 \leq q \leq 0.5\,, \\ 2(1-q)^3 & \text{if } 0.5 \leq q \leq 1\,, \\ 0 & \text{if } 1 \leq q\,, \end{cases} \tag{2.10}$$

where $q = \mathbf{x}/h$. As shown in Fig. 2.1, the kernel above is finite at $x = h$, not $2h$ as is common in many SPH implementations. The kernel estimation of a fluid quantity is subject to random error due to the disorder of the particles, but this is significantly less than the expected Poisson error as the random fluctuations are limited by the available energy. The use of higher order splines to reduce this error have been investigated, but they show no significant improvement and are far more computationally expensive (Rosswog 2009). Recently, different classes of kernel functions have been proposed that significantly reduce the random errors due to particle disorder and improve the convergence rate of SPH (Read et al. 2010; Dehnen and Aly 2012). However, all of the results presented in this thesis use the standard cubic spline. With a form for the smoothing kernel chosen, the discrete equations of fluid dynamics can be derived.

2.2 Equations of Smoothed Particle Hydrodynamics

SPH is a Lagrangian numerical method and for a perfect fluid system, that neglects external forces and gravity, its Lagrangian is given by

$$L = \int \rho \left(\frac{\mathbf{v}^2}{2} - u(\rho, s) \right) dV\,, \tag{2.11}$$

where ρ is the mass per unit volume, $\mathbf{v}$ is the fluid velocity, u is the internal energy, s is the entropy per unit mass and dV is the volume element (Eckart 1960). This is simply the kinetic energy of the system minus its internal energy. The Lagrangian must possess the correct symmetries of the system to ensure that it conserves the correct physical quantities. To make equation (2.11) computationally viable the fluid must be discretized. This is done in SPH by replacing the integral over the volume element, $\int \rho dV$, by a sum over the masses of the particles, $\sum m$. For particles of equal mass this is effectively

a sum over the total number of particles in the system. The discretized SPH Lagrangian for particle i is then given by

$$L_{\mathrm{SPH},i} = \sum_j m_j \left(\frac{\mathbf{v}_j^2}{2} - u_j(\rho_j, s_j) \right) , \tag{2.12}$$

where the quantities with indices are the value of that quantity at the position of particle j (Price and Monaghan 2004a). It is now possible to specify all of the particle's quantities in terms of its position, which is treated as the canonical variable. Specifying all of the quantities as a function of position and the Lagrangian's invariance to transformations ensures that the conservation laws are automatically satisfied, and the equation of motion for the discretized fluid is obtained via the Euler-Lagrange equations

$$\frac{d}{dt}\left(\frac{\partial L_{\mathrm{SPH},i}}{\partial \mathbf{v}_i} \right) - \frac{\partial L_{\mathrm{SPH},i}}{\partial \mathbf{x}_i} = 0 , \tag{2.13}$$

where $\mathbf{x}_i$ is the position of particle i. Inserting equation (2.12) into this equation, assuming that the entropy is a function of density, produces

$$m_i \frac{d\mathbf{v}_i}{dt} + \sum_j m_j \frac{\partial u_j(\rho_j, s_j)}{\partial \mathbf{x}_i} = 0 , \tag{2.14}$$

where the fact that $\partial A_j / \partial A_i$ is equal to zero unless $i = j$ has been used. For an adiabatic case, the first law of thermodynamics is given by

$$\partial u_i = \frac{P_i}{\rho_i^2} \partial \rho_i , \tag{2.15}$$

and allows the expansion of the second term in equation (2.14) such that

$$m_i \frac{d\mathbf{v}_i}{dt} + \sum_j m_j \frac{\partial u_j}{\partial \rho_j} \frac{\partial \rho_j}{\partial \mathbf{x}_i} = 0 , \tag{2.16}$$

$$m_i \frac{d\mathbf{v}_i}{dt} + \sum_j m_j \frac{P_j}{\rho_j^2} \frac{\partial \rho_j}{\partial \mathbf{x}_i} = 0 . \tag{2.17}$$

This trivially rearranges to produce the equation of motion for the discretized fluid

$$m_i \frac{d\mathbf{v}_i}{dt} = - \sum_j m_j \frac{P_j}{\rho_j^2} \frac{\partial \rho_j}{\partial \mathbf{x}_i} . \tag{2.18}$$

By differentiating equation (2.15) with respect to time an equation for the evolution of the internal energy of the discretized fluid is obtained

$$\frac{du_i}{dt} = \frac{P_i}{\rho_i^2} \frac{d\rho_i}{dt} . \tag{2.19}$$

The energy equation is naturally derived in the Lagrangian approach and there is a choice of what to integrate. The simplest approach is to integrate the total energy, but this can result in unphysical negative thermal energies due to round off. Another approach is to integrate the internal energy of the particle and though this provides excellent conservation of energy, it fails to conserve the entropy of the fluid. Therefore, following Springel and Hernquist (2002) the entropy of a particle is defined in terms of an entropic function, $A(s)$, via

$$P = A(s)\rho^{\gamma} \,, \tag{2.20}$$

where γ is the adiabatic index and $A(s) = P/\rho^{\gamma}$. This is related to the internal energy via

$$u_i = \frac{\rho_i^{\gamma-1}}{\gamma - 1} A_i(s) \,. \tag{2.21}$$

In the absence of dissipation terms $dA(s)/dt = 0$, $A(s)$ is constant and integrating the entropy is equivalent to integrating the internal energy, providing excellent energy conservation. However, at discontinuities in the fluid where dissipative terms are required, the entropy can be directly controlled and guaranteed to only increase, see section 2.3.1. Thus, the scheme provides excellent energy conservation and entropy conservation.

To obtain specific forms of equations (2.18) and (2.19) a form for the density must be specified. Using equation (2.5) for the fluid quantity at a particle, the density is defined as

$$\rho_i = \sum_j m_j W_{ij}(h_i) \,, \tag{2.22}$$

and its derivatives with respect to space and time are given, respectively, by

$$\frac{\partial \rho_i}{\partial \mathbf{x}_i} = \sum_j m_j \nabla_i W_{ij}(h_i) \,, \tag{2.23}$$

$$\frac{d\rho_i}{dt} = \sum_j m_j (\mathbf{v}_i - \mathbf{v}_j) \cdot \nabla_i W_{ij}(h_i) \,. \tag{2.24}$$

Converting equation (2.24) back from its discrete form to a continuous one reveals that it, and therefore equation (2.22), is an expression of mass continuity. This demonstrates the self-consistent nature of the SPH formalism.

The smoothing length of the particle, h, determines the radius over which it interacts. Allowing the smoothing length of a particle to vary according to the local density of particles greatly increases the spatial resolution of the simulation (Herquist and Katz 1989; Benz 1990). In most SPH implementations, in 3-D it varies according to

$$h_i = \nu \left(\frac{m_i}{\rho_i} \right)^{1/3} , \tag{2.25}$$

where the constant ν is typically in the range 2.4 to 3.0. Now the density is dependent on the smoothing length, and vice versa, in a non-linear equation where h evolves in time according to

$$\frac{dh_i}{dt} = -\frac{h_i}{3\rho_i} \frac{d\rho_i}{dt} . \tag{2.26}$$

A self-consistent solution for the density and the smoothing length is found using the Newton-Raphson iteration method (Price and Monaghan 2012). The density as a function of the smoothing length can be written as

$$f(h_i) = \rho_i(h_i) - \rho_{\rm sum}(h_i) = 0 , \tag{2.27}$$

where ρ_i is the density consistent with the smoothing length, h_i, calculated from equation 2.25 and $\rho_{\rm sum}$ is the density is calculated, using h_i, by summing over the particles. The new smoothing length is found via

$$h_i^{\rm new} = h_i - \frac{f(h_i)}{f'(h_i)} , \tag{2.28}$$

where

$$f'(h_i) = \frac{\partial \rho_i}{\partial h_i} - \sum_j m_j \frac{\partial W_{ij}(h_i)}{\partial h_i} . \tag{2.29}$$

During the iteration, convergence is determined via $|h_i^{\rm new} - h_i^{\rm prev}|/h_i^0 < \xi$, where h_i^0 is the smoothing length at the start of the iteration and $\xi = 10^{-3}$ is the convergence criteria. If found in this manner for particles of equal mass, then the smoothing length is simply dependent on the number density of the particles. However, to be fully self-consistent, the use of variable smoothing lengths requires additional terms in the energy and momentum equations, involving the derivative of the smoothing length. These additional terms were

derived in Springel and Hernquist (2002) and modify equations (2.23) and (2.24) to

$$\frac{\partial \rho_i}{\partial \mathbf{x}_i} = \frac{1}{\Omega_i} \sum_j m_j \nabla_i W_{ij}(h_i) \,, \tag{2.30}$$

$$\frac{d\rho_i}{dt} = \frac{1}{\Omega_i} \sum_j m_j (\mathbf{v}_i - \mathbf{v}_j) \cdot \nabla_i W_{ij}(h_i) \,, \tag{2.31}$$

where

$$\Omega_i \equiv 1 - \frac{\partial h_i}{\partial \rho_i} \sum_j m_j \frac{\partial}{\partial h_i} W_{ij}(h_i) \,. \tag{2.32}$$

With a definition for the density and its derivatives, exact forms for the equation of motion of the fluid and the evolution of fluid's energy can be given. The partial differential term in equation (2.18) can be expanded (Knight 2013) to

$$\frac{\partial \rho_j}{\partial \mathbf{x}_i} = \frac{\delta t}{\delta \mathbf{x}_i} \frac{\delta \rho_j}{\delta t} \,. \tag{2.33}$$

Using this expansion, that $\mathbf{v}_i = \delta \mathbf{x}_i / \delta t$ and the fact that $\partial A_j / \partial A_i$ is equal to zero unless $i = j$, allows the substitution of equation (2.31) into equation (2.18) to obtain the SPH equation of motion

$$\frac{d\mathbf{v}_i}{dt} = -\sum_j m_j \left(\frac{P_i}{\Omega_i \rho_i^2} \nabla_i W_{ij}(h_i) + \frac{P_j}{\Omega_j \rho_j^2} \nabla_i W_{ij}(h_j) \right) \,, \tag{2.34}$$

where the identity $\nabla_i W_{ij} = -\nabla_i W_{ji}$ has been used. The equation for the evolution of the internal energy can be found by substituting equation (2.31) into equation (2.19)

$$\frac{du_i}{dt} = \frac{1}{\Omega_i} \frac{P_i}{\rho_i^2} \sum_j m_j (\mathbf{v}_i - \mathbf{v}_j) \cdot \nabla_i W_{ij}(h_i) \,. \tag{2.35}$$

Equations (2.31), (2.34) and (2.35) are the discretized versions of the fluid dynamic equations (1.18), (1.19) and (1.20) and are sufficient to produce solutions for a smooth and continuous fluid. However, many astrophysical fluids are not smooth and contain discontinuities. In these fluids additional techniques are required to produce a physically meaningful solution.

2.3 Fluid Discontinuities

The SPH method is completely free of numerical dissipation of any kind. This was initially thought of as a significant advantage of the technique. However,

the lack of dissipation means that instabilities are not regularized and that sharp physical discontinuities in the fluid are not properly handled. Numerical simulations of shocks without dissipation produce unphysical oscillations behind the shock front. The cause of these oscillations is that the fluid quantities were assumed to vary smoothly on the scale of the smoothing length, h, and this is no longer valid at a discontinuity. Shocks are ubiquitous in astrophysical systems and treating them correctly is critical to the behaviour of many systems.

A solution to this problem is to introduce a small amount of 'artificial' viscosity to the simulations. This spreads the discontinuity out allowing it to be sufficiently resolved and correctly captured (Neumann and Richtmyer 1950; Richtmyer and Morton 1967). This is what physically occurs in nature, however, the scale at which this process occurs is much smaller than currently achievable in numerical simulations. Artificially inducing viscosity everywhere in the simulation leads to excessive heating in areas where it is not required, such as away from discontinuities. This heating problem can be overcome by introducing a switch that reduces the viscosity away from discontinuities.

2.3.1 Artificial Viscosity

Artificial viscosity is simple to incorporate into the numerical scheme and is widely used in many Lagrangian schemes. It is formulated in an analogous way to a 1-D Riemann solver, with the two particles being regarded as the left and right states (Monaghan 1997). The addition of viscosity introduces an additional term into the equation of motion

$$\left(\frac{d\mathbf{v}_i}{dt}\right)^{\text{diss}} = -\sum_j m_j Q_{ij} \overline{\nabla_i W_{ij}}\,, \tag{2.36}$$

where

$$Q_{ij} = \begin{cases} \dfrac{\alpha_{ij}^{\text{AV}}(t) v_{\text{sig}} \mathbf{v}_{ij} \cdot \hat{\mathbf{x}}_{ij}}{\rho_{ij}} & \text{if } \mathbf{v}_{ij} \cdot \hat{\mathbf{x}}_{ij} < 0\,, \\ 0 & \text{otherwise}\,, \end{cases} \tag{2.37}$$

and the strength of the applied viscosity is controlled by the parameter α_{ij}^{AV}, $\rho_{ij} = (\rho_i + \rho_j)/2$, $\mathbf{v}_{ij} = \mathbf{v}_i - \mathbf{v}_j$, $\hat{\mathbf{x}}_{ij} = (\mathbf{x}_i - \mathbf{x}_j)/|\mathbf{x}_i - \mathbf{x}_j|$, the kernel gradient

is given by

$$\overline{\nabla_i W_{ij}} = \frac{1}{2}\left(\frac{1}{\Omega_i}\nabla_i W_{ij}(h_i) + \frac{1}{\Omega_j}\nabla_i W_{ij}(h_j)\right) , \tag{2.38}$$

and $v_{\rm sig}$ is the signal speed. Information propagates between particles i and j at the signal speed and in the hydrodynamic case this is simply given by

$$v_{sig} = \frac{c_i + c_j - \beta^{AV}\mathbf{v}_{ij}\cdot\hat{\mathbf{x}}_{ij}}{2} , \tag{2.39}$$

where $c_i = \sqrt{\gamma P_i/\rho_i}$ is the sound speed at particle i and the constant is set such that $\beta^{AV} = 3$. This addition to the equation of motion smooths the discontinuity allowing it to be resolved and correctly captured. However, it introduces viscosity away from shocks where it is not required. To minimize the viscosity where it is not required, $\alpha_{ij}^{\rm AV}$ can be implemented so that it varies spatially and temporally (Rosswog and Price 2007). This allows viscosity to be targeted at discontinuities and quickly reduced to some minimum value away from them. The $\alpha_{ij}^{\rm AV}$ parameter takes the form

$$\alpha_{ij}^{\rm AV} = \frac{1}{4}\left[(\alpha_i^{\rm AV}(t) + \alpha_j^{\rm AV}(t))(f_i + f_j)\right] , \tag{2.40}$$

where f_i is the Balsara switch that suppresses the effects of artificial viscosity in pure shear flows (Balsara 1995). This effectively amounts to an average viscosity felt by particle i and j, ensuring that momentum is conserved. Without the Balsara switch artificial viscosity can lead to spurious forces and an incorrect solution in shear flows. It takes the form of

$$f_i = \frac{|\nabla\cdot\mathbf{v}|_i}{|\nabla\cdot\mathbf{v}|_i + |\nabla\times\mathbf{v}|_i + 10^{-4}c_i\rho_i/h_i} , \tag{2.41}$$

where the third term in the denominator is present to prevent the switch from diverging when both $|\nabla\cdot\mathbf{v}|_i$ and $|\nabla\times\mathbf{v}|_i$ tend to zero. Individual particles evolve their own viscosity coefficients, $\alpha_i^{\rm AV}$, according to

$$\frac{d\alpha_i^{\rm AV}}{dt} = -\frac{\alpha_i^{\rm AV} - \alpha_{\rm min}^{\rm AV}}{\tau} + S_i , \tag{2.42}$$

where $\tau = h_i/0.2c_i$ is a decay constant that determines how quickly the viscosity returns to the minimum value, $\alpha_{\rm min}^{\rm AV}$ is the minimum level of applied viscosity and $S_i = \max(-\nabla\cdot\mathbf{v}, 0)(2 - \alpha_i^{\rm AV})$ is the viscosity source term (Morris and Monaghan 1997). With the chosen value for τ the viscosity of the fluid

decays away to a minimum value over approximately five smoothing lengths and grows in areas of fluid compression. Even with a switch controlled artificial viscosity, SPH still struggles to regulate instabilities, such as the Kelvin-Helmholtz and Rayleigh-Taylor instabilities (Agertz et al. 2007). Switches to target the application of viscosity is currently an active area of research and recent implementations have shown significant improvement in the treatment of instabilities, the minimization of viscosity away from discontinuities and improvement in convergence with increasing resolution (Cullen and Dehnen 2010; Read and Hayfield 2012; Tricco and Price 2013a). However, all results presented here use the above implementation for the artificial viscosity. The artificial viscosity smooths the discontinuity and dissipates the kinetic energy of the particles as heat. Viscosity generates entropy according to

$$\frac{dA_i(s)}{dt} = -\frac{1}{2}\frac{\gamma-1}{\rho_i^{\gamma-1}}\sum_j m_j Q_{ij}(\mathbf{v}_{ij}\cdot\mathbf{x}_{ij})\mathbf{x}_{ij}\cdot\nabla_i W_{ij}(h_i)\,, \tag{2.43}$$

which produces an increase in the internal energy of the particle according to

$$\left(\frac{du_i}{dt}\right)^{\text{diss}} = -\frac{1}{2}\sum_j m_j Q_{ij}(\mathbf{v}_{ij}\cdot\mathbf{x}_{ij})\mathbf{x}_{ij}\cdot\nabla_i W_{ij}(h_i)\,, \tag{2.44}$$

ensuring that the change in total energy is zero and that energy is conserved.

2.3.2 Artificial Thermal Conductivity

In those systems that exhibit large gradients in the thermal energy it is useful to add artificial thermal conductivity to the simulation to produce more accurate results. Without conductivity, the thermal energy at contact discontinuities can be significantly over estimated (Noh 1987). In most cases, large gradients in the internal energy are accompanied by large gradients in other fluid quantities. In these cases the use of artificial viscosity to smooth the discontinuity will smooth the thermal energy gradient. A contact discontinuity is a special case where the pressure and velocity are constant across a density change and internal energy change, and so viscosity is not required. Therefore, artificial thermal conductivity is required at this type of discontinuity to smooth gradients in the thermal energy. It is formulated in a similar way to artificial viscosity and included as an additional term in the energy equation

of the form

$$\left(\frac{du_i}{dt}\right)^{\rm cond} = -\sum_j m_j \frac{v_{sig}\alpha_{ij}^{\rm AC}(u_i - u_j)}{\rho_{ij}} |\overline{\nabla_i W_{ij}}| \,, \tag{2.45}$$

where $\alpha_{ij}^{\rm AC} = (\alpha_i^{\rm AC} + \alpha_j^{\rm AC})/2$ and $\alpha_i^{\rm AC}$ is a coefficient determining the strength of the thermal conductivity at particle i. To ensure that the conductivity only occurs where required, the particle's coefficient is evolved according to

$$\frac{d\alpha_i^{\rm AC}}{dt} = -\frac{\alpha_i^{\rm AC}}{\tau} + S_i^{\rm AC} \,, \tag{2.46}$$

where the decay constant is given by $\tau = h_i/0.2c_i$ and the source term is defined as $S_i^{\rm AC} = 0.1h_i|\nabla^2 u_i|$ (Rosswog and Price 2007). Second order derivatives estimated in the standard SPH way are very noisy and sensitive to particle disorder. Therefore, it is better to approximate it using first order derivatives of the kernel in a Brookshaw-type second derivative (Brookshaw 1985), which takes the form

$$(\nabla^2 u)_i = 2\sum_j m_j \frac{u_i - u_j}{\rho_j} \frac{|\overline{\nabla_i W_{ij}}|}{r_{ij}} \,. \tag{2.47}$$

With the addition of artificial viscosity and conductivity the implementation is capable of resolving discontinuities in the fluid and producing physically meaningful solutions with the correct pre- and post-shock values of the fluid. In many astrophysical problems the self-gravity of the fluid must be included to capture the correct behaviour of the fluid.

2.4 Gravity

If the fluid of the Universe did not feel its own gravity then stars, galaxies and clusters of galaxies would not exist. In most astrophysical systems of interest, and especially in structure formation, the self-gravity of the fluid is critical. Self-gravity is included in SPH via a modification to the Lagrangian, such that $L_{{\rm SPH},i} = L_{{\rm SPH},i} + L_{{\rm grav},i}$ where

$$L_{{\rm grav},i} = -\sum_i m_i \Phi_i \,, \tag{2.48}$$

and Φ_i is the gravitational potential at particle i (Monaghan and Price 2001). The potential at particle i is related to the density via Poisson's equation,

$\nabla^2\Phi = 4\pi G\rho$. The total potential is found by summing over all of the particles in the system and is given by

$$\Phi_i(\mathbf{x}) = -G\sum_j m_j \phi_{ij}(|\mathbf{x}_i - \mathbf{x}_j|, h_i)\,, \tag{2.49}$$

where G is the gravitational constant, h_i is the smoothing length of particle i and ϕ_{ij} is the gravitational softening kernel. The inclusion of self-gravity directly into the Lagrangian allows the introduction of a variable softening length. The relationship between the smoothing kernel and the softening kernel is found by substituting equation (2.22) for the density and equation (2.49) for the gravitational potential into Poisson's equation, which produces

$$W_{ij}(h_i) = -\frac{1}{4\pi}\frac{\partial}{\partial \mathbf{x}}\left[\mathbf{x}^2 \frac{\partial}{\partial \mathbf{x}}\phi_{ij}(h_i)\right]\,. \tag{2.50}$$

This relation between the smoothing and softening lengths ensures that the implementation is consistent. The inclusion of the self-gravity of the particle introduces an additional term in the equation of motion that can be found by applying the Euler-Lagrange equations, equation (2.13), to equation (2.48) and takes the form of

$$\begin{aligned}\left(\frac{d\mathbf{v}_i}{dt}\right)^{\text{grav}} =& -G\sum_j m_j \left[\frac{\phi'_{ij}(h_i) + \phi'_{ij}(h_j)}{2}\right]\hat{\mathbf{x}}_{ij} \\ & -\frac{G}{2}\sum_j m_j \left[\frac{\zeta_i}{\Omega_i}\nabla_i W_{ij}(h_i) + \frac{\zeta_j}{\Omega_j}\nabla_i W_{ij}(h_j)\right]\,,\end{aligned} \tag{2.51}$$

where $\phi'_{ij} = \partial\phi_{ij}/\partial\mathbf{x}_{ij}$. The first term on the right hand side is the standard gravitational force between the particles and the second term is due to gradients in the smoothing length. The second term arises because the softening length is variable and, therefore, a function of the particle's position. It is required to ensure that the system is conservative when allowing softening lengths to vary. This additional term looks like a pressure gradient term and acts against the gas pressure of the system to increase the force due to gravity, as ζ_i takes the form

$$\zeta_i \equiv \frac{\partial h_i}{\partial \rho_i}\sum_j m_j \frac{\partial \phi_{ij}(h_i)}{\partial h_i}\,, \tag{2.52}$$

and is definite negative. Gravity is a long range force, to directly sum the force on all the particles due to all the other particles in the simulation is an

N^2 calculation. This quickly becomes unfeasible for $N > 100,000$ and is an inefficient use of computational resources. For the astrophysical simulations presented in this work the gravitational force is calculated using a tree method. This improves the calculations to $N\log(N)$, while maintaining greater accuracy over other methods. The reader is referred to Appendix B for further details on this method. The methods described in this chapter so far lay the foundations for a full SPH code capable of investigating many astrophysical problems. A magnetic field is now incorporated into the fluid.

2.5 Magnetohydrodynamics

The incorporation of MHD into SPH has been attempted since its inception (Gingold and Monaghan 1977) and a variety of techniques have been used. Magnetic fields have been updated on a grid and interpolated to the particles (Habe et al. 1991; Murray et al. 1996; Mac Low et al. 1999). Non-conservative formulations of the $\mathbf{J} \times \mathbf{B}$ force were found to always be stable, however, they perform poorly in problems involving shocks (Meglicki 1994; Byleveld and Pongracic 1996; Hosking 2002). Conservative formulations produced a better performance in shock problems, but were shown to be unstable to the clumping of SPH particles (Phillips 1985). Therefore, despite the relative simplicity of the MHD equations, there are significant technical issues with their implementation into an SPH code.

The first consideration is scaling between the physical units and the simulation units of the magnetic field. The unit scaling for a hydrodynamic numerical system can be defined by choosing values for the mass, length and time. The choice of these values then determines the scaling for others, such as the energy or velocity. The magnetic field has dimensions

$$[\mathbf{B}] = \frac{[\text{Mass}]}{[\text{Time}][\text{Charge}]} , \tag{2.53}$$

and the permeability of free space has dimensions

$$[\mu_0] = \frac{[\text{Mass}][\text{Length}]}{[\text{Charge}]^2} . \tag{2.54}$$

Choosing $\mu_0 = 1$ defines the unit of charge in the simulation and the scaling

of the magnetic field is then set by

$$\mathbf{B}_{\text{physical}} = \left(\frac{\mu_0[\text{Mass}]}{[\text{Length}][\text{Time}]^2}\right)^{1/2} \mathbf{B}_{\text{numerical}} \,. \tag{2.55}$$

To develop a stable SPMHD formulation, an SPH expression for the evolution of the magnetic field with time must be obtained. A thorough review of the SPMHD method is given in Price (2012).

2.5.1 The Induction Equation

The induction equation describes the evolution of a magnetic field with time and is derived from Maxwell's equations, producing equation (1.29). The continuum form of the equation can be converted to a discrete SPH form using the same approximation that was made in the hydrodynamic case. Using the same approximation ensures that there is consistency throughout the implementation. Making the summation approximation for the spatial derivatives in equation (1.29) produces

$$\frac{d\mathbf{B}_i}{dt} = \frac{1}{\Omega_i \rho_i} \sum_j m_j \left[\mathbf{B}_i(\mathbf{v}_{ij} \cdot \nabla_i W_{ij}(h_i)) - \mathbf{v}_{ij}(\mathbf{B}_i \cdot \nabla_i W_{ij}(h_i))\right] \,, \tag{2.56}$$

where $\mathbf{B}_i$ is the magnetic field at particle i. The induction equation shows how the flow of the fluid affects the magnetic field present in it. However, MHD is the interaction of a magnetic field and a fluid, so the field must be able to act back on the fluid. This back reaction can be derived from the Lagrangian of the fluid using variational principles, with the induction equation providing a constraint.

2.5.2 The Lorentz Force

The back-reaction of the magnetic field on the fluid can be derived by variational principles (Newcomb 1962; Henyey 1982; Oppeneer 1984; Price and Monaghan 2004b), where an additional term is included in the Lagrangian of the system that takes the form

$$L = \int \rho \left(\frac{\mathbf{v}^2}{2} - u(\rho, s) - \frac{\mathbf{B}^2}{8\pi\rho}\right) dV \,. \tag{2.57}$$

This is converted to the SPMHD Lagrangian by replacing the integral over the volume by a sum over the masses of the particles, yielding

$$L_{\text{SPMHD}} = \sum_j m_j \left(\frac{\mathbf{v}_j^2}{2} - u_j(\rho_j, s_j) - \frac{\mathbf{B}_j^2}{8\pi\rho_j}\right) \,. \tag{2.58}$$

Under the assumption that $\mathbf{B}_i = \mathbf{B}_i(\mathbf{x}_i)$, the equation of motion for the system can be found by substituting this equation into the Euler-Lagrange equations, equation (2.13), giving

$$m_i \frac{d\mathbf{v}_i}{dt} + \sum_j m_j \left(\frac{\partial u_j}{\partial \mathbf{x}_i} + \frac{\mathbf{B}_j^2}{8\pi\rho_j^2} \frac{\partial \rho_j}{\partial \mathbf{x}_i} + \frac{\mathbf{B}_j}{4\pi\rho_j} \frac{\partial \mathbf{B}_j}{\partial \mathbf{x}_i} \right) = 0 \,, \tag{2.59}$$

where the fact that $\partial A_j / \partial A_i$ is zero unless $i = j$ has been used. This equation can be expanded using the first law of thermodynamics, equation (2.15), expanding the partial differential of the density according to equation (2.33) (Knight 2013) and, in a similar manner, expanding the partial differential of the magnetic field according to

$$\frac{\partial \mathbf{B}_j}{\partial \mathbf{x}_i} = \frac{\delta \mathbf{B}_j}{\delta \mathbf{x}_i} \frac{\delta t}{\delta t} = \frac{\delta t}{\delta \mathbf{x}_i} \frac{\delta \mathbf{B}_j}{\delta t} \,. \tag{2.60}$$

Equation (2.31) for the derivative of the density with respect to time and equation (2.56) for the derivative of the magnetic field with respect to time can then be substituted into the expanded equation. Expressing the velocities as $\mathbf{v}_i = \delta \mathbf{x}_i / \delta t$ and rearranging gives

$$\begin{aligned} \frac{d\mathbf{v}_i}{dt} = &- \sum_j m_j \left(\frac{P_i}{\Omega_i \rho_i^2} \nabla_i W_{ij}(h_i) + \frac{P_j}{\Omega_j \rho_j^2} \nabla_i W_{ij}(h_j) \right) \\ &- \frac{1}{8\pi} \sum_j m_j \left(\frac{\mathbf{B}_i^2}{\Omega_i \rho_i^2} \nabla_i W_{ij}(h_i) + \frac{\mathbf{B}_j^2}{\Omega_j \rho_j^2} \nabla_i W_{ij}(h_j) \right) \\ &+ \frac{1}{4\pi} \sum_j m_j \left(\frac{\mathbf{B}_i}{\Omega_i \rho_i^2} (\mathbf{B}_i \cdot \nabla_i W_{ij}(h_i)) + \frac{\mathbf{B}_j}{\Omega_j \rho_j^2} (\mathbf{B}_j \cdot \nabla_i W_{ij}(h_j)) \right) \,, \end{aligned} \tag{2.61}$$

where $\nabla_i W_{ij} = -\nabla_i W_{ji}$ has been used. The first term on the right hand side of this equation is the standard hydrodynamic pressure term. The second term is another pressure term, analogous to the first, and is produced by the magnetic field. The final term is a tension term that is produced by the magnetic field to prevent the fluid from moving perpendicular to the field lines and bending them. This equation can be significantly simplified by the introduction of the conservative magnetic stress tensor, which takes the form

$$M^{ab} \equiv - \left(P + \frac{\mathbf{B}}{8\pi} \right) \delta^{ab} + \frac{B^a B^b}{4\pi} \,, \tag{2.62}$$

where the co-ordinate indices a and b are summed over. The equation of motion of particle i then simplifies to

$$\frac{dv_i^a}{dt} = \sum_j m_j \left(\frac{M_i^{ab}}{\Omega_i \rho_i^2} \nabla_i^b W_{ij}(h_i) + \frac{M_j^{ab}}{\Omega_j \rho_j^2} \nabla_i^b W_{ij}(h_j) \right) . \tag{2.63}$$

For an infinite number of particles, this equation conserves both linear momentum and angular momentum (Price 2004). Although the use of a finite number of particles will introduce errors, these are very small in practice. The considerable problem with using this equation of motion is that it is unstable. It is clear from the equation above that when the magnetic energy density dominates the thermal energy density the stress can become negative between two particles (Phillips 1985). This leads to particle clumping know as the "tensile" instability. This instability can be fatal to SPMHD calculations and must be accounted for to produce physically meaningful solutions.

2.5.3 Maintaining Stability

The tensile instability can be catastrophic for SPMHD simulations and suppressing it is a basic requirement of any SPMHD implementation. The source of this error can be found in equation (1.27) and its impact can be seen in equation (1.30). In the derivation of the induction equation the first right hand side term of the equation was neglected, as the solenoidal constraint of the magnetic field, equation (1.22), implies that this term should be zero. However, numerically the solenoidal condition is not guaranteed, therefore the induction equation should contain this additional term. The use of the conservative stress tensor will then introduce an additional term into the equation of motion that takes the form of the third right hand side term of equation (1.30). This term leads to an additional force, parallel to the magnetic field lines, that causes the particles to stick together and the onset of the tensile instability. The additional force is unphysical, a result of the choice of numerical implementation, and must be minimized to produce physically meaningful solutions.

Various methods have been proposed to deal with the tensile instability. Phillips (1985) proposed an additional sweep over the particles to calculate the maximum negative stress, which could then be subtracted from the equation

of motion to counter the instability. The problems with this approach are that it fails to conserve total energy, can produce unphysical effects and it is computationally costly to implement an additional sweep. Morris (1996) proposed adopting a more accurate derivative estimate for the anisotropic term. This approach fails to conserve both momentum and total energy, but the errors due to non-conservation are generally very small. The issue with this approach is that it cannot be turned "off" and the non-conservation of momentum can accumulate, leading to a loss of symmetry in simulations that run for a long period of time. Monaghan (2000) suggested the addition of a short range force that would counteract this unphysical attractive force. However, it was found to be problematic in highly compressible simulations with smoothing lengths that had large variations (Price 2004).

Børve et al. (2001) suggested a method that used the conservative stress tensor and directly subtracted the contribution of any non-zero divergent magnetic field terms. This subtraction introduces a correction term into the momentum equation of the form

$$\left(\frac{d\mathbf{v}_i}{dt}\right)^{\text{corr}} = -\frac{\hat{\beta}}{4\pi}\sum_j m_j \left(\frac{\mathbf{B}_i}{\Omega_i\rho_i^2}\nabla_i W_{ij}(h_i) + \frac{\mathbf{B}_j}{\Omega_j\rho_j^2}\nabla_i W_{ij}(h_j)\right) , \qquad (2.64)$$

where $\hat{\beta}$ is a constant controlling the strength of the correction. Børve et al. (2004) argued that $\hat{\beta} = 0.5$ was sufficient to suppress the tensile instability and maintain the stability of the implementation, however, Tricco and Price (2012) demonstrated that in certain circumstances this can fail to achieve stability and recommend $\hat{\beta} = 1.0$. The key point of this correction term is that the discretization is identical to that of the divergence term in the force equation. The addition of this term does lead to the violation of exact energy and momentum conservation, but only when the divergence of the magnetic field is non-zero. This correction term has the advantage that it switches off in regions where the divergence of the magnetic field is zero (Børve et al. 2006).

In many astrophysical problems, the magnetic field is so weak that it never becomes the dominant term in the equation of motion and it is possible to run simulations without the correction term (Dolag et al. 1999). However, the inclusion of this correction term successfully stabilizes the SPMHD imple-

mentation when the magnetic field is the dominant force, and has a negligible impact in simulations where it is not required but still included. It is therefore included in all simulations presented here.

2.5.4 Artificial Resistivity

In section 1.4.1, it was demonstrated that a galaxy cluster can effectively be considered as a perfectly conducted fluid and so resistivity is not required when simulating them. Resistivity is included in the simulations because it is numerically required, in a similar way to artificial viscosity and conductivity. Failure to include resistivity will result in unphysical oscillations of the post-shock magnetic field value. Although some discontinuities in the magnetic field will be smoothed by the application of artificial viscosity, discontinuities in the magnetic field can occur without discontinuities in other fluid quantities. Therefore, it is important to include artificial resistivity in the numerical implementation to smooth discontinuities in the magnetic field, allowing them to be resolved and the correct pre- and post-shock values of the field to be obtained.

As noted in section 1.4.2, the introduction of a magnetic field to the fluid enables information to propagate at the Alfvén, slow and fast magnetoacoustic wave speeds. This means that shocks in a magnetized fluid are significantly more complex as information can now propagate at three different speeds. The signal velocity must be modified to account for the fastest possible speed at which information can propagate in the fluid. The natural generalization is to replace the signal velocity defined in equation (2.39) by

$$v_{\rm sig} = \frac{v_i^M + v_j^M - \beta^{\rm AV}\mathbf{v}_{ij}\cdot\hat{\mathbf{x}}_{ij}}{2}\,, \tag{2.65}$$

where

$$v_i^M = \frac{1}{\sqrt{2}}\left[\left(c_i^2 + \frac{\mathbf{B}_i^2}{4\pi\rho_i}\right) + \sqrt{\left(c_i^2 + \frac{\mathbf{B}_i^2}{4\pi\rho_i}\right) - \frac{c_i^2(\mathbf{B}_i\cdot\mathbf{x}_{ij}/|\mathbf{x}_{ij}|)^2}{\pi\rho_i}}\right]^{1/2}\,, \tag{2.66}$$

is the fastest magnetoacoustic wave speed at particle i. As already mentioned, the divergence of the magnetic field is not exactly zero numerically and non-zero divergence is often created at discontinuities where the fluid quantities

are rapidly changing. With the failure to maintain the solenoidal condition of the magnetic field, components of the magnetic field parallel to and, as a consequence, velocity components perpendicular to the line joining the two interacting particles are now able to change. This is most likely to occur at a discontinuity in the magnetic field. Therefore, an artificial resistivity scheme based on the jump of the total magnetic field energy is found to perform better in practice than one based only on the magnetic field components parallel to the line joining the two particles (Price and Monaghan 2005). Analogous to artificial viscosity, the artificial resistivity term is defined according to

$$\left(\frac{d\mathbf{B}_i}{dt}\right)^{\text{resis}} = \rho_i \sum_j m_j \frac{\alpha_{ij}^{\text{B}} v_{\text{sig}}}{\rho_{ij}^2} (\mathbf{B}_i - \mathbf{B}_j)\hat{\mathbf{x}}_{ij} \cdot \nabla_i W_{ij}(h_i) \,, \tag{2.67}$$

where

$$v_{\text{sig}} = \begin{cases} \dfrac{v_i^{\text{M}} + v_j^{\text{M}} - \beta^{\text{AV}} \mathbf{v}_{ij} \cdot \hat{\mathbf{x}}_{ij}}{2} & \text{if } \mathbf{v}_{ij} \cdot \hat{\mathbf{x}}_{ij} < 0 \,, \\ 0 & \text{otherwise} \,, \end{cases} \tag{2.68}$$

and

$$\alpha_{ij}^{\text{B}} = \frac{(\alpha_i^{\text{B}} + \alpha_j^{\text{B}})}{2} \,, \tag{2.69}$$

is an averaged coefficient that controls the strength of the dissipation. The resistivity coefficients are averaged to ensure that momentum is conserved. To ensure that total energy is conserved, this resistivity term will generate entropy according to

$$\left(\frac{dA_i}{dt}\right)^{\text{resis}} = \frac{\gamma - 1}{\rho_i^{\gamma - 1}} \frac{\alpha_{ij}^{\text{B}}}{8\pi} \sum_j \frac{m_j v_{\text{sig}}}{\rho_{ij}} (\mathbf{B}_i - \mathbf{B}_j)^2 \hat{\mathbf{x}}_{ij} \cdot \overline{\nabla_i W_{ij}} \,. \tag{2.70}$$

This term introduces artificial resistivity everywhere in the simulation. Away from discontinuities in the magnetic field, this term leads to excessive dissipation of the magnetic field. This smooths out small scale features of the magnetic field and reduces the magnitude of the field, especially in cosmological MHD simulations. In a similar approach to artificial viscosity, a switch for the resistivity that targets its application to discontinuities can be introduced.

The formulation of a switch to make the application of resistivity targeted at shocks is an active area of research. Two different formulations of a resistivity switch in the implementation are included and their impact on ideal test

cases, section 3.2.4, and astrophysical problems, sections 4.3, is examined. The first switch implemented is similar to the switch for artificial viscosity (Price and Monaghan 2005), where each particle evolves its own resistivity coefficient according to

$$\frac{d\alpha_i^{\rm B}}{dt} = -\frac{(\alpha_i^{\rm B} - \alpha_{\rm min}^{\rm B})}{\tau} + S_i^{\rm B} \,, \tag{2.71}$$

where $\alpha_{\rm min}^{\rm B}$ is the minimum applied resistivity and $\alpha_i^{\rm B}$ varies in the range $[0.0, 2.0]$, $S_i^{\rm B}$ is a source term and τ controls the decay timescale of the dissipation according to

$$\tau = \frac{h_i}{C v_{\rm sig}} \,, \tag{2.72}$$

where the constant $C = 0.2$, so that the resistivity decays to the minimum value within five smoothing lengths. While a value of $\alpha_{\rm min}^{\rm B} = 0.05 - 0.1$ produces a better solution to the ideal test cases, it was found to produce excessive dissipation of the magnetic field in cosmological applications, see section 4.1. A value of $\alpha_{\rm min}^{\rm B} = 0.0$ removes this excessive dissipation and still produces acceptable solutions to the range of ideal test cases that were used to validate the implementation. The source term takes the form

$$S_i^{\rm B} = \max\left(\frac{|\nabla \times \mathbf{B}_i|}{\sqrt{4\pi\rho_i}}, \frac{|\nabla \cdot \mathbf{B}_i|}{\sqrt{4\pi\rho_i}}\right) . \tag{2.73}$$

From now on, this switch is referred to as the PM05 switch. This switch targets the application of resistivity at discontinuities and works satisfactorily for many problems. However, it is obvious from equation (2.73) that the size of the resistivity coefficient calculated by this switch, and hence the strength of the applied resistivity, is directly proportional to the magnitude of the magnetic field. This potentially leads to a situation where $\alpha_i^{\rm B}$ remains small even at large discontinuities and it does not sufficiently resolve them, producing an incorrect solution. Tricco and Price (2013b) demonstrated that this switch fails to correctly increase the strength of the resistivity applied in a mach 10 MHD turbulence simulation with a weak magnetic field leading to an incorrect result.

Tricco and Price (2013b) have proposed a new resistivity where the strength of the applied resistivity is not dependent on the magnitude of the

magnetic field. Following this, a second resistivity switch has been implemented that directly sets the resistivity coefficient of each particle to the dimensionless quantity

$$\alpha_i^{\mathrm{B}} = \frac{h_i |\nabla \mathbf{B}_i|}{|\mathbf{B}_i| + \vartheta} \,, \tag{2.74}$$

where $\nabla \mathbf{B}_i$ is the 3×3 gradient matrix of $\mathbf{B}_i$, α_i^{B} is restricted to $[0, 1]$ and $\vartheta = 10^{-3}$ is a small constant that prevents the incorrect behaviour of $\alpha_i^{\mathrm{B}} \to 1$ as $|\mathbf{B}_i| \to 0$. By normalizing the gradient of the magnetic field by its magnitude the dependence of the applied resistivity strength on the magnitude of the magnetic field is removed. This switch should apply resistivity appropriate to the size of the discontinuity encountered and be negligible away from discontinuities. The individual terms of the gradient matrix are calculated using the standard first derivative estimator

$$\nabla \mathbf{B}_i \equiv \frac{\partial B_i^a}{\partial x_i^b} \approx -\frac{1}{\Omega_i \rho_i} \sum_j m_j (B_i^a - B_j^a) \nabla_i^b W_{ij}(h_i) \,. \tag{2.75}$$

The norm of the gradient of the magnetic field is then calculated using the 2-norm via

$$|\nabla \mathbf{B}_i| \equiv \sqrt{\sum_a \sum_b \left| \frac{\partial B_i^a}{\partial x_i^b} \right|^2} \,, \tag{2.76}$$

where the indices a and b are summed over for the three co-ordinate directions. From now on, this switch is referred to as the TP13 switch. Neither of these switches were specifically designed for studying the evolution of seed magnetic fields during the formation of structure. Both are implemented into the SPMHD code and their performance examined in idealized test cases and in realistic astrophysical problems, such as structure formation. The final part of our numerical method is the implementation of a scheme to minimize the violation of the solenoidal condition of the magnetic field.

2.5.5 Maintaining the Solenoidal Condition

A key issue in numerical magnetohydrodynamics is maintaining the solenoidal condition of the magnetic field, $\nabla \cdot \mathbf{B} = 0$. As demonstrated in section 2.5.3, violation of this condition results in a spurious unphysical force parallel to the magnetic field that leads to incorrect solutions and the onset of the tensile

instability. When running MHD simulations of a magnetic field that is amplified, such as a seed field during structure formation, the failure to maintain the solenoidal condition leads to an additional term in the induction equation. As demonstrated in section 4.3, this leads to the amplification of both the true magnetic field and the unphysical divergent magnetic field producing a magnetic field that is orders of magnitude larger than one where the violation of the solenoidal condition is minimized. The divergence error, Σ_B, present in the simulation is measured at particle i according to the dimensionless quantity

$$\Sigma_{B,i} = \log_{10}\left(\frac{h_i|\nabla \cdot \mathbf{B}_i|}{|\mathbf{B}_i|}\right) . \tag{2.77}$$

A range of methods have been developed to try and prevent the growth of the numerical divergence of the magnetic field. In grid based codes these schemes include the projection method (Brackbill and Barnes 1980), constrained transport (Evans and Hawley 1988) and the eight wave approach (Powell et al. 1999) and a review of these techniques is provided in Tóth (2000). Most modern MHD grid codes use constrained transport, which minimizes the violation of the solenoidal constraint to machine precision. All of these schemes minimize the divergence only in their particular discretization and numerical artefacts may still be present.

In SPMHD several different methods have been used to minimize the divergence of the magnetic field. Enforcing the solenoidal constraint by construction has been attempted by formulating the magnetic field either in terms of the Euler potentials (Stern 1970) or the vector potential (Price 2010), however they both suffer from limitations. The Euler potentials cannot model winding motions past one rotation, as the field simply resets, and the set up of the initial field is non-trivial in more realistic problems. The vector potential method suffers from an unstable equation of motion and significant time evolution issues. As such, these approaches are not suitable. Another option is to clean the divergence from the simulation as it is generated. The artificial resistivity scheme will clean the divergence from the simulation, but it should not simply be increased to remove more divergence as this will weaken both the true magnetic field as well as the divergent field. A cleaning scheme that

has found widespread use in both grid and Lagrangian methods is the hyperbolic cleaning scheme proposed by Dedner et al. (2002). This scheme couples an additional scalar field to the magnetic field, allowing numerical divergence to be cleaned away. It has been successfully implemented for astrophysical problems in both SPMHD (Tricco and Price 2012; Stasyszyn et al. 2013) and a Lagrangian grid code (Pakmor et al. 2011).

The hyperbolic cleaning scheme introduces an additional scalar field, ψ, that couples to the magnetic field by introducing an additional term in the induction equation of the form

$$\left(\frac{d\mathbf{B}_i}{dt}\right)^{\text{clean}} = -\nabla\psi_i \,, \tag{2.78}$$

where ψ_i is the value of the scalar field at particle i. This scalar field evolves according to

$$\frac{d\psi_i}{dt} = -\left(v_i^M\right)^2 (\nabla\cdot\mathbf{B}_i) - \frac{\psi_i}{\tau} \,, \tag{2.79}$$

where v_i^M is the fastest magnetoacoustic wave at particle i and τ controls the timescale for the divergence to decay away. To understand how this scheme cleans the divergence of the magnetic field from the simulation, the gradient of equation (2.79) can be taken and used in equation (2.78) to eliminate $\nabla\psi_i$. Taking the divergence of the resulting equation produces

$$\frac{d^2(\nabla\cdot\mathbf{B}_i)}{dt^2} - \left(v_i^M\right)^2 \nabla^2(\nabla\cdot\mathbf{B}_i) + \frac{1}{\tau}\frac{d(\nabla\cdot\mathbf{B}_i)}{dt} = 0 \,, \tag{2.80}$$

where the vector identity $\nabla\cdot\nabla(\nabla\cdot\mathbf{B}_i) = \nabla^2(\nabla\cdot\mathbf{B}_i)$ has been used. Equation (2.80) is a damped wave equation and shows that the hyperbolic cleaning scheme spreads divergence away from a source like a wave, which dilutes it over a large area. This enables the decay term, $-\psi_i/\tau$, to further reduce the divergence of the magnetic field. The decay timescale, τ, is set equal to the dimensionless quantity

$$\frac{1}{\tau} \equiv \frac{\sigma v_i^M}{h_i} \,, \tag{2.81}$$

where σ is a dimensionless parameter that controls the strength of the damping. The choice of σ is critical to the performance of the scheme and should be set to maximize the dilution of the wave without the damping of the wave being too weak. In the literature, Price and Monaghan (2005) suggested that

$\sigma \in [0.4, 0.8]$, Tricco and Price (2012) suggest that for 2-D $\sigma \in [0.4, 0.8]$ and in 3-D $\sigma \in [0.8, 1.2]$, while Stasyszyn et al. (2013) suggested that $\sigma = 4$.

Tricco and Price (2012) argue that, from a total energy conservation viewpoint, equation (2.79) should contain an additional term that takes the form

$$\frac{d\psi_i}{dt} = -\left(v_i^M\right)^2 (\nabla \cdot \mathbf{B}_i) - \frac{\psi_i}{\tau} - \frac{\psi_i \nabla \cdot \mathbf{v}_i}{2} \,, \tag{2.82}$$

where the third term balances the energy associated with scalar field. Although the testing of the implementation found that this term produced a negligible change in the solutions for all idealized tests and astrophysical problems, it is included to help maintain total energy conservation. One of the critical choices for the cleaning scheme is the SPH estimator chosen for the divergence of the magnetic field. Under the assumption that energy of the magnetic field and scalar field is conserved

$$\frac{dE}{dt} = \sum_i m_i \left(\frac{\mathbf{B}_i}{4\pi\rho_i} \cdot \left(\frac{d\mathbf{B}_i}{dt} \right)_\psi + \frac{\psi_i}{4\pi\rho_i \left(v_i^M\right)^2} \frac{d\psi_i}{dt} \right) = 0 \,. \tag{2.83}$$

Choosing the difference estimator, equation (2.7), for the divergence of the magnetic field and substituting it into equation (2.82), in the absence of dissipation and neglecting the additional energy conservation term, produces

$$\frac{d\psi_i}{dt} = \frac{\left(v_i^M\right)^2}{\Omega_i \rho_i} \sum_j m_j (\mathbf{B}_i - \mathbf{B}_j) \cdot \nabla_i W_{ij}(h_i) \,, \tag{2.84}$$

and can be used to eliminate the time derivative of the scalar field in equation (2.83), yielding

$$\begin{aligned} \sum_i \frac{m_i}{4\pi\rho_i} \mathbf{B}_i \cdot \left(\frac{d\mathbf{B}_i}{dt} \right)_\psi = &- \sum_i \sum_j \frac{m_i m_j}{4\pi\Omega_i\rho_i^2} \psi_i \mathbf{B}_i \cdot \nabla_i W_{ij}(h_i) \\ &+ \sum_i \sum_j \frac{m_i m_j}{4\pi\Omega_i\rho_i^2} \psi_i \mathbf{B}_j \cdot \nabla_i W_{ij}(h_i) \,, \end{aligned} \tag{2.85}$$

where the right hand side has been rearranged to split the two terms. By swapping the summation indices of the second right hand term and making use of the fact $\nabla_i W_{ij} = -\nabla_j W_{ji}$ this expression can be simplified to

$$\left(\frac{d\mathbf{B}_i}{dt} \right)^{\text{clean}} = -\rho_i \sum_j \left(\frac{\psi_i}{\Omega_i \rho_i^2} \nabla_i W_{ij}(h_i) + \frac{\psi_j}{\Omega_j \rho_j^2} \nabla_i W_{ij}(h_j) \right) \,. \tag{2.86}$$

Hence, by choosing the difference estimator for the divergence of the magnetic field the choice of symmetric estimator has been enforced for $\nabla\psi_i$. This is a critical point for the implementation of a hyperbolic cleaning scheme because the use of this conjugate pair of estimators greatly improves the stability of the cleaning scheme. Even so, as demonstrated in chapter 5, in certain circumstances the cleaning is unstable and can lead to an exponentially increasing divergence error. To counter this, the influence of the cleaning on the magnetic field can be limited via

$$|\nabla\psi_i| < \frac{1}{2}\left|\frac{d\mathbf{B}_i}{dt}\right| , \tag{2.87}$$

so that the change in the magnetic field due to the cleaning scheme is less than half of the total change of the basic induction equation. This prevents the cleaning scheme becoming the dominant term and driving an instability in the field. Unless otherwise specifically stated, this limiter is turned off in all of the solutions presented here.

2.6 Time stepping

In order to produce solutions to the SPMHD equations presented above, they must be integrated with respect to time. The equation of motion, equation (2.63), is integrated using the leap-frog method. Each particle determines its own individual time-step, dt_i, and for a particle at a time-step, n, its position at the next time-step is given by

$$\mathbf{x}_i^{n+1} = \mathbf{x}_i^n + \mathbf{v}_i^{n+1/2} dt_i , \tag{2.88}$$

where the velocity, or the first derivative of $\mathbf{x}$, is updated at the half integer step according to

$$\mathbf{v}_i^{n+1/2} = \mathbf{v}_i^{n-1/2} + F(\mathbf{x}_i^n) dt_i , \tag{2.89}$$

where $F(\mathbf{x}_i^n)$ is the force acting on the particle at time-step n. For a constant time-step this method is second order accurate in time and has the advantages of being reversible in time and symplectic in nature, i.e. energy conserving. The use of individual and varying time-steps breaks the symmetry of the system and so the integration is no longer reversible in time. The limit of numerical precision means that the energy of the system is not strictly

conserved. However, due to the symplectic nature of the leap-frog method, any change in energy of the system occurs over very long timescales and any error remains roughly constant. This ensures that the system maintains the correct long-term behaviour.

The induction equation, equation (2.56), and the internal energy equation, equation (2.35), are integrated using the Euler method with the trapezoidal rule (also know as the Predict-Evaluate-Correct-Evaluate method). First, their values at the next time-step are predicted by

$$\tilde{A}_i^{n+1} = A_i^n + dt_i \frac{dA_i^n}{dt} \,, \tag{2.90}$$

$$\tilde{\mathbf{B}}_i^{n+1} = \mathbf{B}_i^n + dt_i \frac{d\mathbf{B}_i^n}{dt} \,, \tag{2.91}$$

and then improved from this initial guess using the trapezoidal rule to obtain a corrected value for the next time-step

$$A_i^{n+1} = A_i^n + \frac{1}{2} dt_i \left(\frac{dA_i^n}{dt} + \frac{d\tilde{A}_i^{n+1}}{dt} \right) \,, \tag{2.92}$$

$$\mathbf{B}_i^{n+1} = \mathbf{B}_i^n + \frac{1}{2} dt_i \left(\frac{d\mathbf{B}_i^n}{dt} + \frac{d\tilde{\mathbf{B}}_i^{n+1}}{dt} \right) \,. \tag{2.93}$$

In order to time step the equations the time-step, dt_i, must be defined. The particles evolve a variable time-step based on the criteria

$$dt_i = \min \left[C_{\rm CFL} \left(\frac{0.5 h_i}{v_{\rm dt}} \right) , C_{\rm DYN} \left(\frac{0.5 h_i}{|d\mathbf{v}_i/dt|} \right)^{1/2} \right] \,, \tag{2.94}$$

where $C_{\rm CFL} = 0.2$ and $C_{\rm DYN} = 0.2$ and $v_{\rm dt} = v_{\rm sig}$ if $\mathbf{v}_{ij} \cdot \hat{\mathbf{x}}_{ij} < 0$, otherwise $v_{\rm dt} = 0.5(v_i^M + v_j^M - \mathbf{v}_{ij} \cdot \hat{\mathbf{x}}_{ij})$. The first term on the right hand side is the Courant-Friedrichs-Lewy stability condition and is the condition that information does not propagate further than the smoothing length in one time step. The constant, $C_{\rm CFL}$, ensures that it takes roughly ten time steps for information to propagate a smoothing length. The second term is a constraint from the forces acting on a particle during a time-step.

The time-step limiter suggested by Saitoh and Makino (2009) is employed, so that for a particle, i, its time-step compared to those particles around it, j,

is limited by

$$\begin{aligned} dt_i &\leq 4dt_j \quad \text{and} \\ dt_j &\leq 4dt_i \,, \end{aligned} \tag{2.95}$$

which ensures that, in a strong shock, a particle's pre-shock time-step is shortened so that it responds correctly as the shock front approaches and passes its position. Additionally, the Fully Asynchronous Split Time-integrator (FAST) scheme (Saitoh and Makino 2010) is implemented, allowing the use of different time-steps for the integration of the magnetohydrodynamics and gravity. This significantly reduces the number of time-steps for the calculation of gravity interactions, reducing its computational requirements.

2.7 Summary

This chapter reviews the theory behind the smoothed particle method for solving the equations of magnetohydrodynamics. The basic interpolant approximation of a fluid quantity, the derivatives of that quantity and the smoothing kernel that makes the equations numerically computable were presented. The fluid equations were self-consistently derived, including variable smoothing length terms, from a variational principle. The inclusion of artificial viscosity and artificial conductivity schemes to ensure that shocks and discontinuities in the fluid are resolved were discussed. Their implementation and the use of switches to target their application to where they are required in the simulation was presented. How to included the self-gravity of the fluid, which is critical to many astrophysical problems, was shown.

The inclusion of a magnetic field in the simulations was discussed. The SPH version of the induction equation, to enable the evolution of a magnetic field with time, was shown. By including the magnetic field in the Lagrangian and using the continuity and induction equations to constrain it, the MHD equation of motion was derived and the conservative magnetic stress tensor defined. The origin of the tensile instability that plagues conservative MHD formulations was examined and it was demonstrated that the failure to maintain the solenoidal condition of the magnetic field was its source. Various methods for suppressing the onset of the instability and their strengths and

weaknesses were discussed. The inclusion of an artificial resistivity scheme, in a similar vein to the viscosity and conductivity schemes, to resolve discontinuities in the magnetic field was presented. Two different switches to control the application of resistivity were shown. A hyperbolic cleaning scheme for the divergence of the magnetic field was introduced and how the choice of divergence estimator is a critical factor in the design of the scheme was shown. It was then demonstrated how the scheme works to clean divergence from the simulation by spreading it away from the source as a wave and then damping that wave.

Finally, how to step the equations of MHD with time to produce solutions to them was shown. Additional constraints and algorithms that help to capture discontinuities were also shown.

Chapter 3

GCMHD+: An N-body/SPMHD code

The previous chapter presented the numerical theory for a gridless numerical method of producing solutions to the MHD equations. We highlighted the major technical issues and methods to overcome them. In order to study magnetic fields in the very largest structures in the Universe we implemented this theory in the N-body/SPMHD code GCMHD+. The hydrodynamic scheme and key parameters are summarized in Kawata and Gibson (2003); Kawata et al. (2013). The basic MHD addition and key parameter choices are summarized in Barnes et al. (2012). The choice of parameters associated with additional schemes to deal with some of the technical challenges of MHD are presented below.

To ensure that the results produced by the code are reliable, and to assess the performance of the code relative to other numerical methods of solving the MHD equations, we used a range of idealized test problems. These test cases are a standard set commonly used to validate the performance of grid-based MHD solvers. The results produced by our code are compared against analytical solutions, where they exist, and results produced by well known grid MHD codes. In all the results presented in this chapter we use particles of equal mass so that changes in density are simply changes in the spacing between the particles. We integrate the equation of motion (2.63), the entropy equation (2.43) and the induction equation (2.56). Unless otherwise indicated, artificial viscosity, conductivity and resistivity schemes are used and their application is controlled by the switches discussed in the previous chapter. The minimum

coefficient for the viscosity is set equal to $\alpha_{\rm min}^{\rm AV} = 0.5$. When the artificial resistivity scheme suggested by Price and Monaghan (2005) is used, the minimum coefficient for the resistivity is set to $\alpha_{\rm min}^{\rm B} = 0.0$. The tensile instability is suppressed using the direct subtraction method (Børve et al. 2001) with $\hat{\beta} = 1.0$. Unless otherwise stated, the hyperbolic cleaning scheme is included, using the difference estimator, equation (2.7), for the divergence of the magnetic field, and the decay term set by choosing $\sigma = 1.0$. These parameters represent the best compromise choice for producing results to both the idealized test cases and the more realistic astrophysical problems presented in subsequent chapters.

3.1 SPH Tests

To produce credible results for the MHD equations, the code must be able to produce reliable results for the hydrodynamic fluid equations. Poor solutions to the equations of fluid dynamics will produce incorrect interactions with the magnetic field, leading to significant errors that will be compounded when the magnetic field then acts back on the fluid. Therefore, we present results for a range of test problems that demonstrate the code's ability to solve the equations of fluid dynamics in different regimes and the magnetic implementation, and all associated algorithms, is neglected.

3.1.1 Sod Shock Tube

The shock tube test is a standard test of any compressible fluid dynamics code (Sod 1978). This test consists of a tube of gas split into two regions. The first region contains a high density, high pressure gas and is separated from the second region, containing a low density and low pressure gas, by a wall. At the start of the test the wall is removed and the discontinuity in the properties of the gas decays into two non-linear waves. A shock wave travels into the low density region, while a rarefaction wave moves into the high density region. In between these two waves a new contact discontinuity forms, across which the pressure is constant. This problem can be solved analytically and an exact solution for the spread of the two waves can be obtained. This allows us to examine our code's ability to handle discontinuities in the fluid quantities.

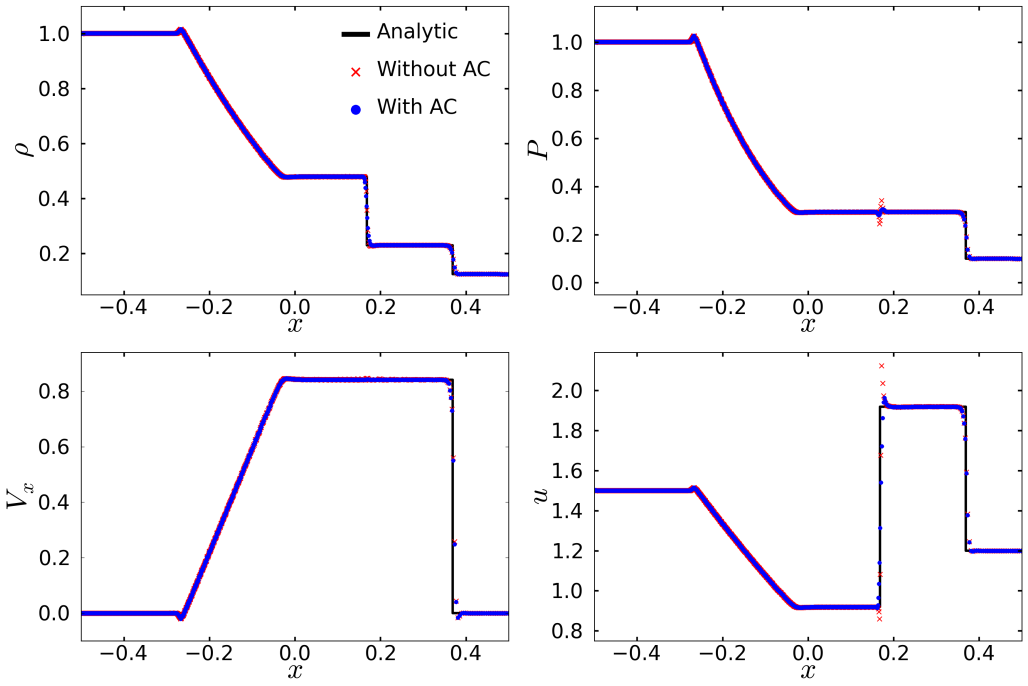

Fig. 3.1: Density (upper left), pressure (upper right), v_x (lower left) and internal energy (lower right) results produced by our implementation, with (blue points) and without (red crosses) artificial conductivity, for the Sod shock tube test compared to the analytic solution (black line). Without conductivity the change in internal energy at the contact discontinuity is not well captured, leading to a significantly greater pressure "glitch".

We set this test up in a 1-D tube of length unity. The high density region runs from $-0.5 < x_1 < 0.0$ and contains $n_1 = 960$ particles with a density $\rho_1 = 1$ and pressure $P_1 = 1$. The low density region runs from $0.0 < x_1 < 0.5$ and contains $n_2 = 120$ particles with a density $\rho_2 = 0.125$ and pressure $P_2 = 0.1$. We use an adiabatic equation of state with $\gamma = 5/3$. To demonstrate the need for artificial conductivity we run this test with and without it. As the system evolves a contact discontinuity, a shock wave and a rarefaction wave develop. A contact discontinuity is a transition layer where there is a discontinuity in the density and internal energy, but the velocity and pressure remain constant. At shock and rarefaction waves the density, internal energy, pressure and velocity can all change.

We evolve this system until $t = 0.2$ and Fig. 3.1 shows the density, pressure, x-direction velocity and internal energy results of our code with (blue

points) and without (red crosses) artificial conductivity (Sec. 2.3.2). Both results produced by the code show good agreement with the analytic solution (black line), with a small amount of smoothing visible at discontinuities. The need for artificial conductivity can be seen in the internal energy profile. Without it (red crosses), the large discontinuity at $x = 0.18$ in the internal energy is not properly resolved and the result overshoots either side of it. With the introduction of artificial conductivity the overshoot is significantly lessened and the result is much closer to the analytic solution. This test demonstrates that the code is capable of handling discontinuities in 1-D and we need to test its ability to handle 3-D discontinuities.

3.1.2 Sedov Blast Wave

The Sedov blast wave is a standard 3-D test used to validate many fluid dynamics codes (Sedov 1959). At $t = 0$, energy is injected into the center of the simulation volume resulting in a strong shock wave that propagates through the volume as the system is evolved. The blast wave test allows us to evaluate the code's ability to capture a discontinuity in the strong shock limit. The simulation results to this test can be compared to the analytic solution, which is found using Sedov-Taylor self-similarity.

In a periodic box of length unity, we set out the particles between $-0.5 < x < 0.5$ in a cubic lattice arrangement and we slightly offset the lattice to ensure that a particle is present at the origin. The particles are initially stationary with a uniform density $\rho = 1$ and pressure $P = 1$, and an adiabatic index $\gamma = 1.4$. The particle located at the origin of the box is then over pressured by a factor of a hundred so that $P = 100$. We run this test at 3 different resolutions of 32^3, 64^3 and 128^3 to enable us to investigate how our code's result changes as the resolution of the test increases.

The left panel of Fig. 3.2 shows the density as a function of radius for the three different resolutions and the analytic solution at $t = 0.04$. The results produced by the code tend towards the analytic solution as the resolution improves. The shock front is visibly smoothed by the application of artificial viscosity and the distance over which it is smoothed reduces with increasing resolution. The right panel shows a density slice through the xy plane of the

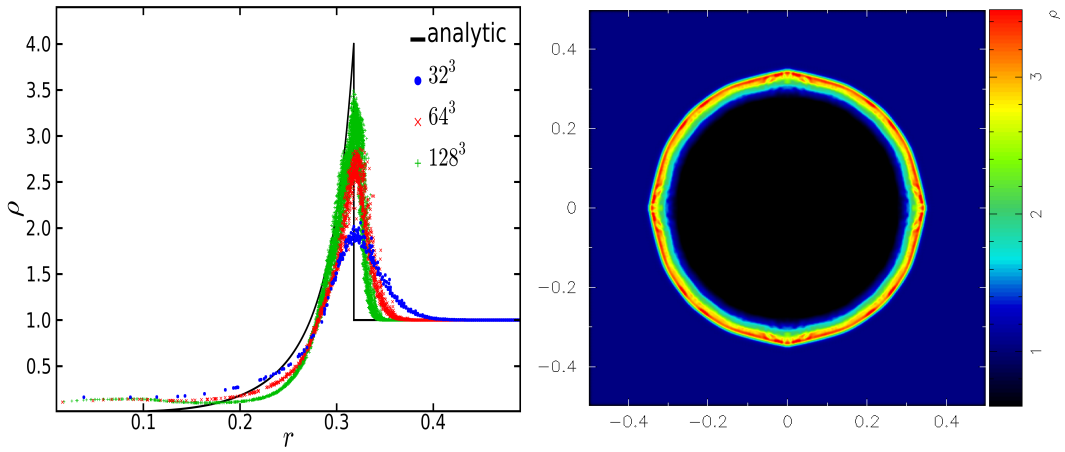

Fig. 3.2: The left hand panel shows the density as a function of radius for the 32^3 (blue points), 64^3 (red x's) and 128^3 (green crosses) resolution Sedov blast wave tests at $t = 0.04$. The result tends toward the analytic solution (black line) as the resolution increases. The right hand panel shows the density for a slice through the xy plane of the 128^3 test. Slight numerical artefacts, due to use of a square lattice, are visible.

128^3 simulation. The shock wave is not quite a perfect sphere, the imperfections are due to the initial layout of the particles on to a cubic grid. This test demonstrates that our code accurately captures strong discontinuities in three dimensions and the viscosity scheme reliably smooths them out so that they are resolved. We now look at a common test problem for astrophysical fluid codes.

3.1.3 Self-similar Collapse

The self-similar collapse test is the collapse of a gas and dark matter (DM) halo in an expanding flat universe, due to a centrally located overdense perturbation. An analytic solution to this system can be obtained under the assumption of self-similarity. Initially, the gas and DM expands with the expansion of the universe, but its own self-gravity will begin to decelerate it. Gas and DM closest to the perturbation decelerates more quickly and then falls back on to the central perturbation. This increases the density contrast, which increases the deceleration, causing more matter to collapse back on to the center. The self-similarity of the system arises because shells of gas and DM further from the initial perturbation take longer to decelerate and fall

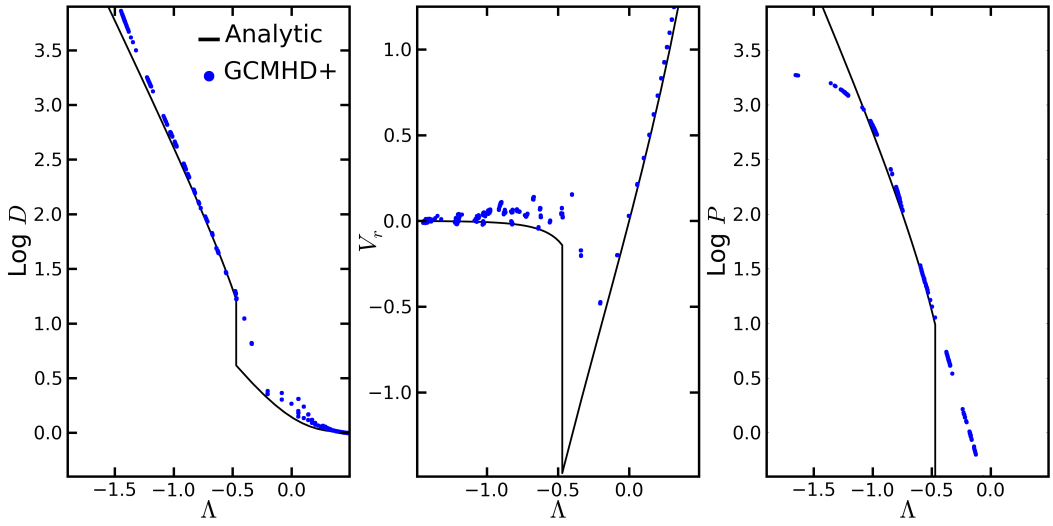

Fig. 3.3: Self-similar density (left), radial velocity (center) and pressure (right) results for the gas only simulation (blue points) against the analytic solution (black line). There is reasonable agreement between the two.

back. The time taken for this to occur provides a length scale for the system.

When a shell collapses on to the central perturbation it begins to cross other shells of mass and a shock wave develops that travels outward through the fluid. The density profile of a collapsing self-similar DM halo was found by Fillmore and Goldreich (1984) and this was extended by Bertschinger (1985) to include the treatment of gas. The radius of this shock, $r_{\rm sh}$, as a function of turnaround radius, $r_{\rm ta}$, is constant and given by $r_{\rm sh} = 0.34 r_{\rm ta}$. This solution allows us to test our implementation as the relation between the turnaround radius and turnaround time is given by

$$r_{ta}(t) = R_i \delta_i \left(\frac{4t}{3\pi t_i} \right)^{8/9} , \tag{3.1}$$

where R_i is the initial radius and δ_i is the initial overdensity of the perturbation at the initial time t_i. We can then define the fluid quantities $(r, \rho, v_r \text{and} P)$ as dimensionless constants

$$\Lambda(r,t) = \frac{r}{r_{ta}(t)} , \tag{3.2}$$

$$D(\Lambda) = \frac{\rho(r,t)}{\rho_H} , \tag{3.3}$$

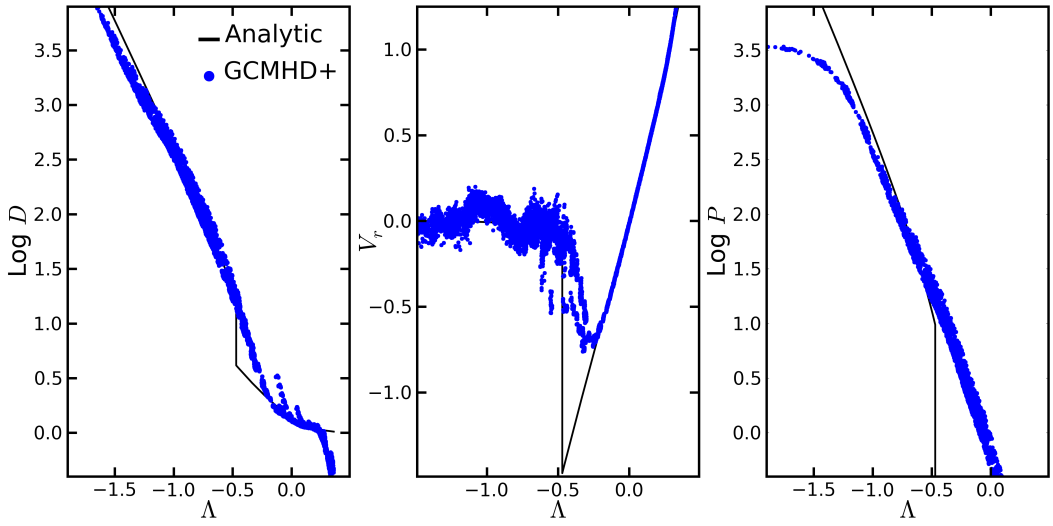

Fig. 3.4: Self-similar density (left), radial velocity (center) and pressure (right) results for the $n_R = 16$ gas and DM simulation (blue points) against the analytic solution (black line). The addition of DM to the simulation produces additional noise in the position of the gas particles.

$$V_r(\Lambda) = \frac{t}{r_{ta}(t)} v_r(r,t)\,, \tag{3.4}$$

$$P(\Lambda) = \left(\frac{t}{r_{ta}(t)}\right)^2 \frac{P(r,t)}{\rho_H}\,, \tag{3.5}$$

where $\rho_H = (6\pi G t_i^2)^{-1}$, with $G = 1$, is the density outside of the perturbation. Once we have chosen $\delta_i = 0.05 M_{\rm tot}$ for the mass and $R_i = 0.1 R_{\rm sim}$ for the size of the initial perturbation then this problem has no free parameters (Navarro and White 1993). We set up a sphere of radius $R_{\rm sim} = 1.0$ and place the gas particles so that $n_R = 16$, where n_R is the number of particles along the radial direction. Additionally, we set up a sphere of gas and dark matter particles with $n_R = 16$ and another sphere of gas and dark matter particles with $n_R = 32$. The DM particles have a mass five times that of the gas particles. The results obtained from the simulations are converted into self-similar values using equations (3.2-3.5).

The result of the gas only simulation is shown in Fig. 3.3. There is good agreement between the analytic solution and the self-similar fluid quantities

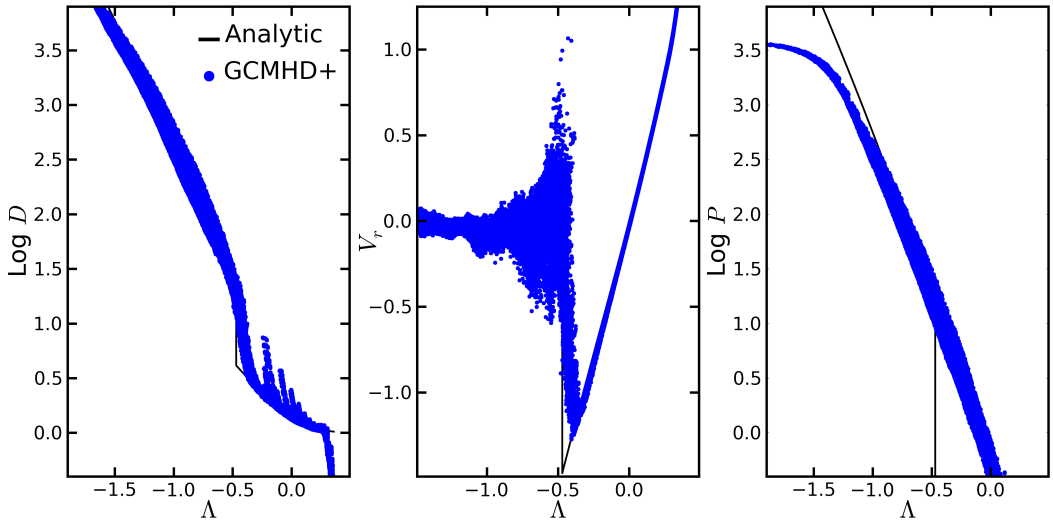

Fig. 3.5: Self-similar density (left), radial velocity (center) and pressure (right) results for the $n_R = 32$ gas and DM simulation (blue points) against the analytic solution (black line). As the resolution of the simulation increases the result produced by GCMHD+ tends to the analytic solution.

produced by the code. The shock front is smoothed out by our viscosity scheme ensuring that it is resolved and the correct pre- and post-shock fluid values are obtained. Fig. 3.4 shows the result of the $n_R = 16$ gas and DM simulation. The self-similar fluid quantities still show good agreement with the analytic solution, although the interaction of the gas particles with the DM particles introduces more noise to the simulation and the gas particles are now uniformly distributed as a function of radius and not grouped at particular radii, as they are in the previous figure. The result of the higher resolution gas and DM particle simulation, with $n_R = 32$, is shown in Fig. 3.5. The increase in resolution produces a clear improvement in the agreement between the analytic solution and the simulated result. The improved resolution reduces the length over which the shock front is smoothed.

Discretization of the mass of the system provides the SPH method with an inherent adaptability that allows it to naturally cope with the orders of magnitude change in scales that occur in many astrophysical systems. It is this property that makes SPH a suitable method for studying the formation of structure in the Universe. However, an issue for SPH is correctly capturing

mixing processes and this causes it to struggle when trying to resolve fluid instabilities.

3.1.4 Kelvin-Helmholtz Instability

The Kelvin-Helmholtz instability (KHI) test is a common test for both particle and grid methods to assess their ability to resolve and regulate the KHI. In a 2-D periodic box of length unity, we set up particles on a square lattice in the range $-0.5 < x < 0.5$ and $-0.5 < y < 0.5$. The box is split into a high density region, $\rho_h = 4$, that lies within $|y| < 0.25$ and a low density region, $\rho_l = 1$. As we use particles of equal mass, the high density region contains 512×256 particles and the low density region contains 256×128 particles. The two regions are in pressure equilibrium with $P_h = P_l = 2.5$ and we assume $\gamma = 5/3$. The particles in the high density region have a velocity $\mathbf{v}_h = (-0.5, 0.0, 0.0)$ and those in the low density region have a velocity $\mathbf{v}_h = (0.5, 0.0, 0.0)$. Additionally, we add sinusoidal perturbations to the y velocity component of the form $v_y(x) = \delta v_y \sin(\lambda 2\pi \mathrm{x})$, where we set $\delta v_y = 0.01$ and $\lambda = 1.0$. Following Price (2008), the timescale for the growth of the instability can be considered as

$$\tau_{\mathrm{KHI}} = 2\pi/\omega \,, \tag{3.6}$$

where

$$\omega = \frac{2\pi}{\lambda} \frac{(\rho_h \rho_l)^{1/2} |v_{x,h} - v_{x,l}|}{(\rho_h + \rho_l)} \,. \tag{3.7}$$

These initial conditions produce a KHI time scale of $\tau_{\mathrm{KHI}} = 2.5$. There is no analytic solution for this test. Therefore, we compare the result produced by our SPH code with the result produced by the publicly available mesh code ATHENA (Stone et al. 2008). We use the exact same initial conditions for the ATHENA run, with a resolution of 512×512 cells and we use the HLLC Riemann solver with third-order interpolation.

We evolve the system until $t = 3.75$ ($\tau_{KHI} = 1.5$) for both codes and the results are shown in Fig. 3.6. Although the KHI develops for both codes, the development of the instability is much faster for the grid code. At $t = 1.25$, the ATHENA result has many more small-scale features present in comparison to GCMHD+ and these develop into the larger features seen at later times.

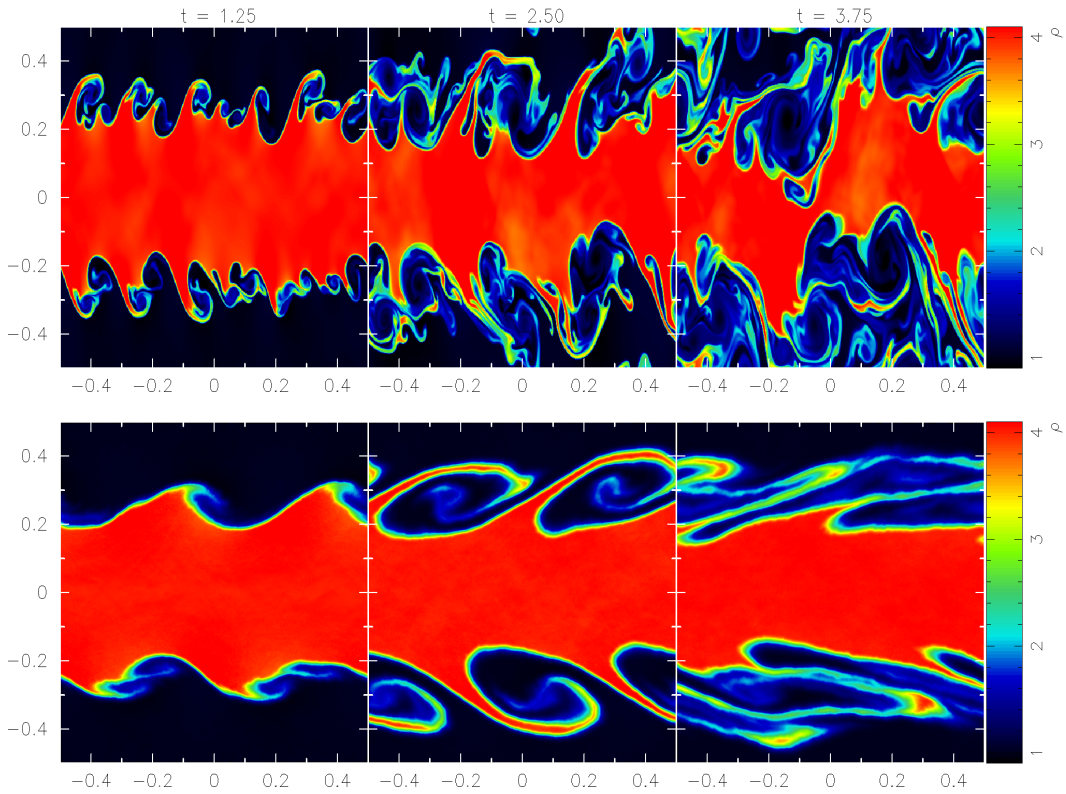

Fig. 3.6: Density results for the ATHENA grid code (upper row) and GCMHD+ (lower row) at $t = 1.25$ [$\tau_{\rm KHI} = 0.5$] (left column), $t = 2.50$ [$\tau_{\rm KHI} = 1.0$] (centre column) and $t = 3.75$ [$\tau_{\rm KHI} = 1.5$] (right column). Significantly more small-scale structure develops at early times for the ATHENA result, leading to significantly more mixing at late times.

Our numerical implementation is capable of resolving instabilities, such as the KHI, however, the timescale for their development is longer in comparison to other techniques.

GCMHD+ is capable of accurately solving the equations of fluid dynamics and can handle both weak and strong shocks. It can resolve and regulate the development of instabilities that many SPH codes fail to achieve. We now add a magnetic field to the fluid and examine our code's ability to solve the equations of magnetohydrodynamics.

3.2 SPMHD Tests

The addition of a magnetic field to the fluid introduces an additional level of complexity to the simulations. This complexity is both physical and numer-

ical in nature and makes analytical solutions to the equations of MHD very difficult. In order to demonstrate that our implementation produces reliable results, we present our code's results to a range of standard test problems used to assess the performance of grid-based MHD codes. These ideal test cases allow us to demonstrate how our additional algorithms improve the result and suppress the numerical issues presented in the previous chapter. Additionally, the fiducial values of the free parameters in the scheme, such as $\hat{\beta}$ and σ, can be found.

3.2.1 Shock Tube Tests

Shocks in magnetized fluids are complicated by the propagation of waves at multiple speeds and by magnetic field components parallel to and velocity components perpendicular to the discontinuity potentially varying due to the failure to maintain the solenoidal condition of the magnetic field. To demonstrate that our implementation can correctly resolve the various MHD shocks and obtain the correct pre- and post-shock values of the fluid, we run the full range of shock tube tests presented in Ryu and Jones (1995). These tests are 1-D and so the particles only move in the x-direction, however, we allow the velocity and magnetic field to vary in 3-D. This means that we evolve all of the components of the velocity, but the y and z components do not move the particles.

The set up of these eleven tests is presented in the table in Appendix C. As no analytic solutions to these tests are known, we compare the results produced by our implementation to those produced by the ATHENA code. We do not change the parameters from those provided with the ATHENA code. We use these simple tests to investigate the performance of the two resistivity switches, PM05 (equation 2.71) and TP13 (equation 2.74), we presented in the previous chapter, section 2.5.4.

The density, pressure, x-direction velocity and magnetic field y-component results for each test are presented in Figs. 3.7-3.17, with the ATHENA reference result shown by the black line, the GCMHD+ result using the PM05 switch shown by the blue points and the GCMHD+ result using the TP13 switch shown by the red crosses. Tests $1A$ and $1B$ demonstrate a strong and a

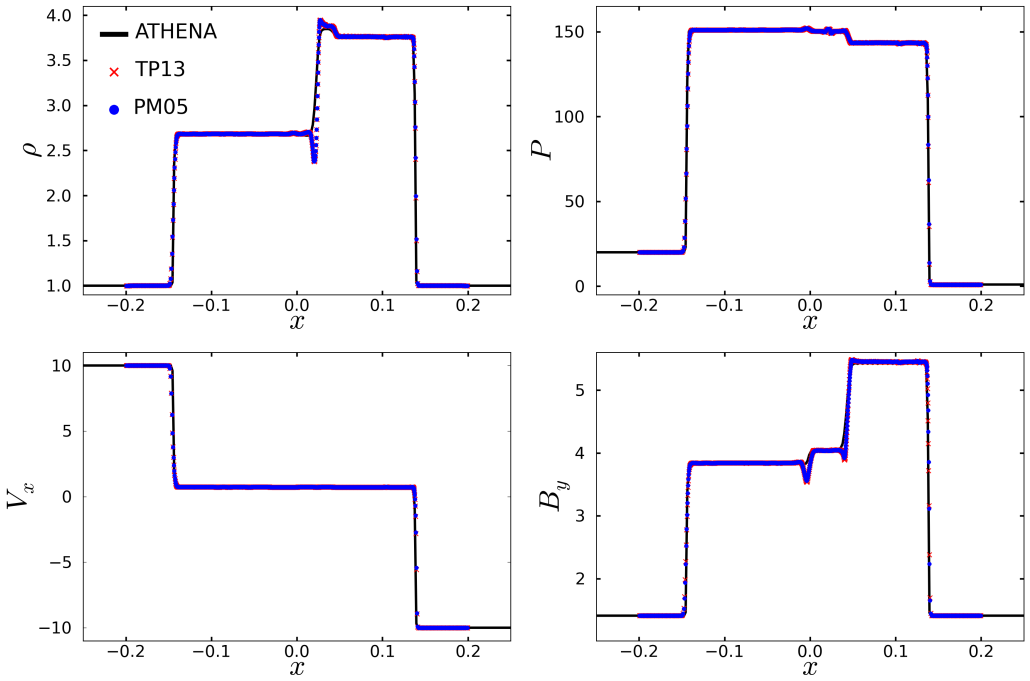

Fig. 3.7: Density (upper left), pressure (upper right), v_x (lower left) and B_y (lower right) results for magnetic shock tube 1A at $t = 0.03$, with the resistivity switches PM05 (blue points) and TP13 (red crosses), against a reference result (black line) provided by the ATHENA grid MHD code. Both switches produce slight glitches at the contact discontinuity.

weak shock respectively, with a constant magnetic field parallel to the shock. Rarefaction waves, shock waves and contact discontinuities develop in both tests (Figs. 3.7 and 3.8). Both results produced by GCMHD+ show reasonable agreement with the result produced by the ATHENA, with only a small overshoot in the density and magnetic field profiles.

Tests $2A$ (Fig. 3.9) and $2B$ (Fig. 3.10) have three dimensional velocity and magnetic field structures that allow a rotational discontinuity to develop, along with fast and slow shocks and a contact discontinuity. A rotational discontinuity is one where the thermodynamic quantities remain constant across the shock, but the magnetic field component tangential to the shock can "rotate" from one component to another. The results produced by GCMHD+ show good agreement with the result produced by ATHENA. There is some oscillation present around the rotational discontinuity in the magnetic field profile produced by the TP13 switch for test $2A$, suggesting that it is not

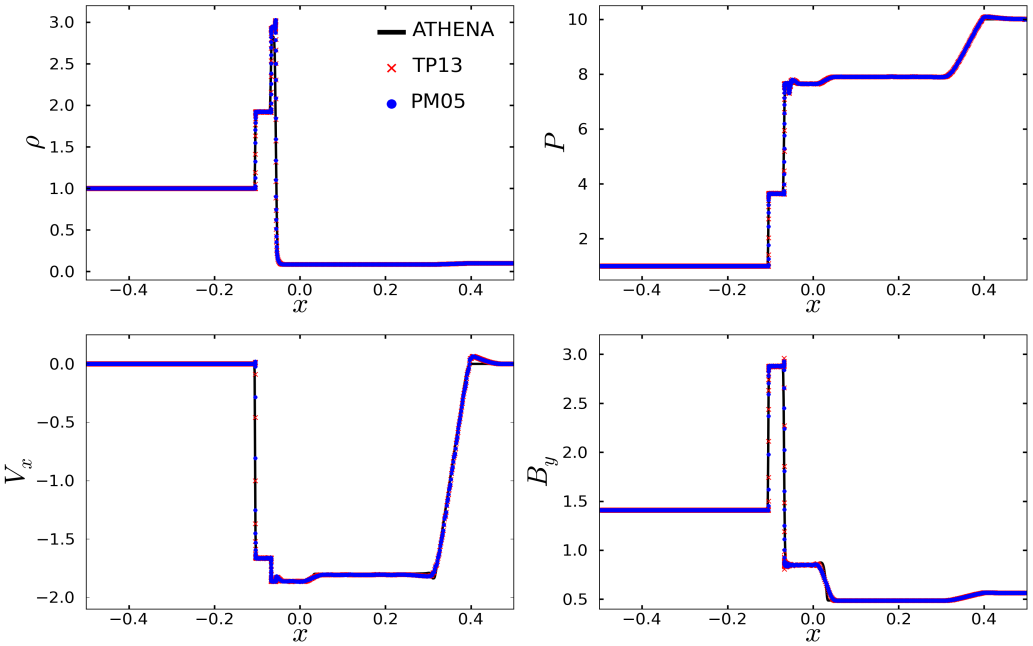

Fig. 3.8: The same fluid quantities as Fig. 3.7 for magnetic shock tube 1B at $t = 0.03$, with the same numerical schemes. There is good agreement between the different numerical techniques.

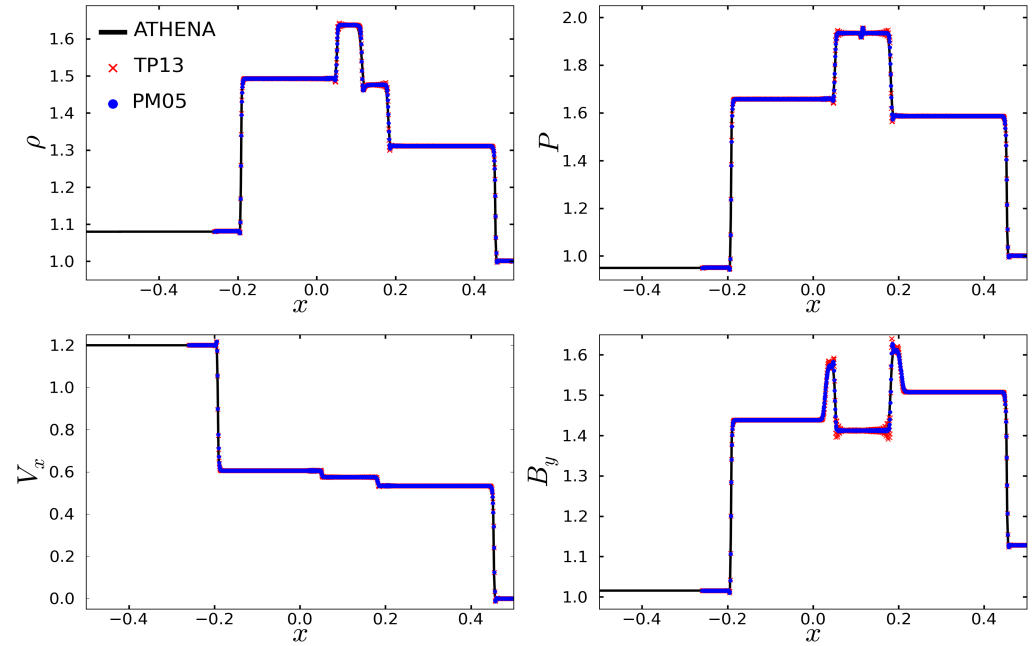

Fig. 3.9: The same fluid quantities as Fig. 3.7 for magnetic shock tube 2A at $t = 0.2$, with the same numerical schemes. Our results show good agreement with the reference result, although the TP13 switch shows some post shock oscillation in the magnetic field, pressure and density.

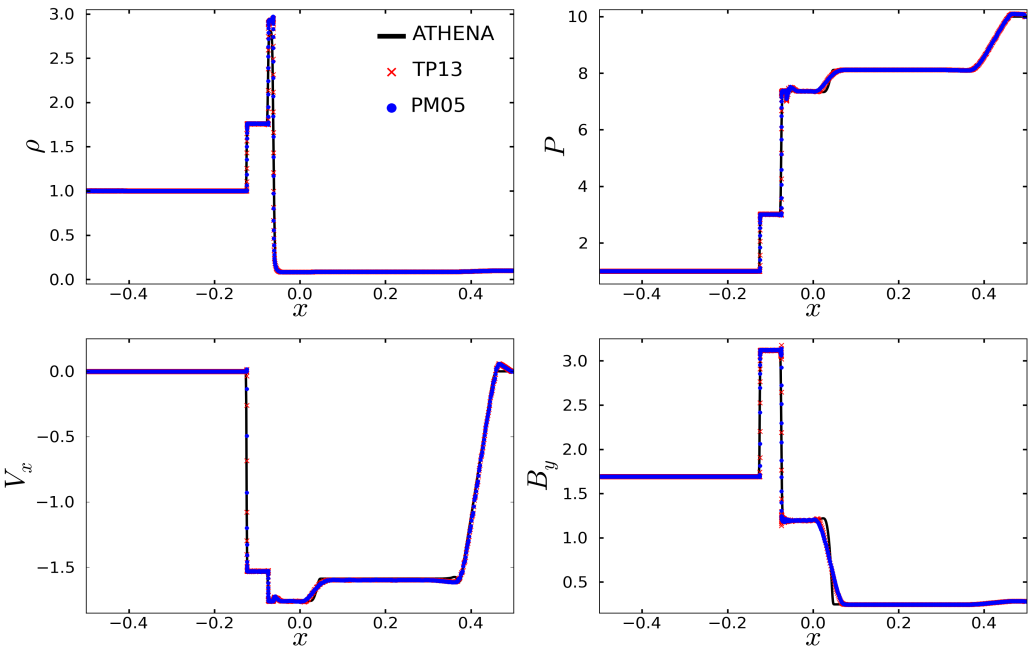

Fig. 3.10: The same fluid quantities as Fig. 3.7 for magnetic shock tube 2B at $t = 0.035$, with the same numerical schemes. There is good agreement between the reference result and the GCMHD+ results, with some intrinsic smoothing of the magnetic field.

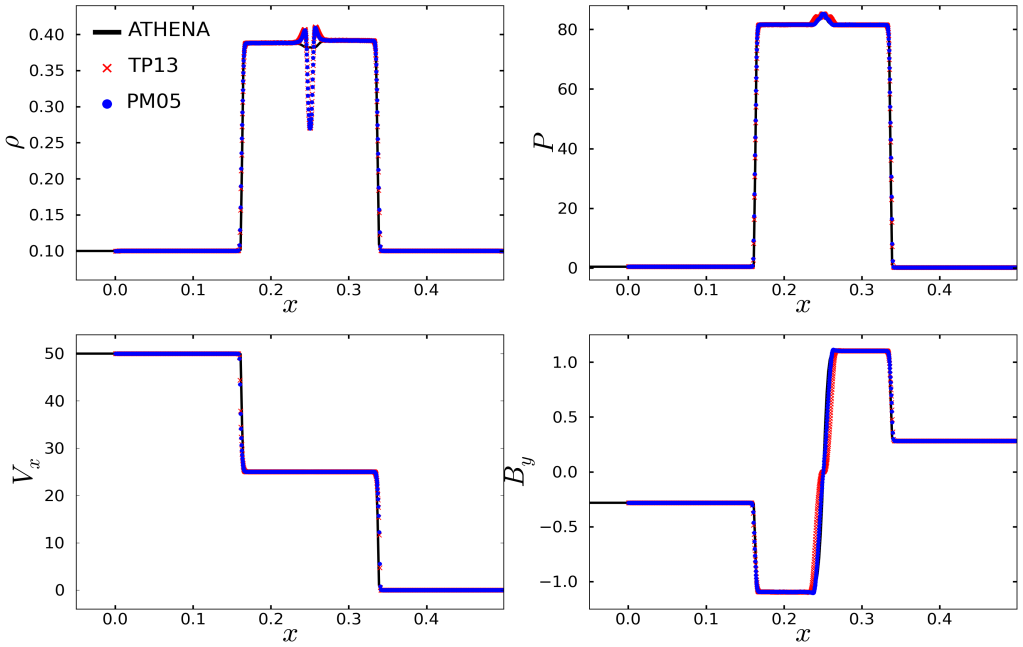

Fig. 3.11: The same fluid quantities as Fig. 3.7 for magnetic shock tube 3A at $t = 0.01$, with the same numerical schemes. Although most of the features are captured, our implementation experiences a wall heating error in the density results.

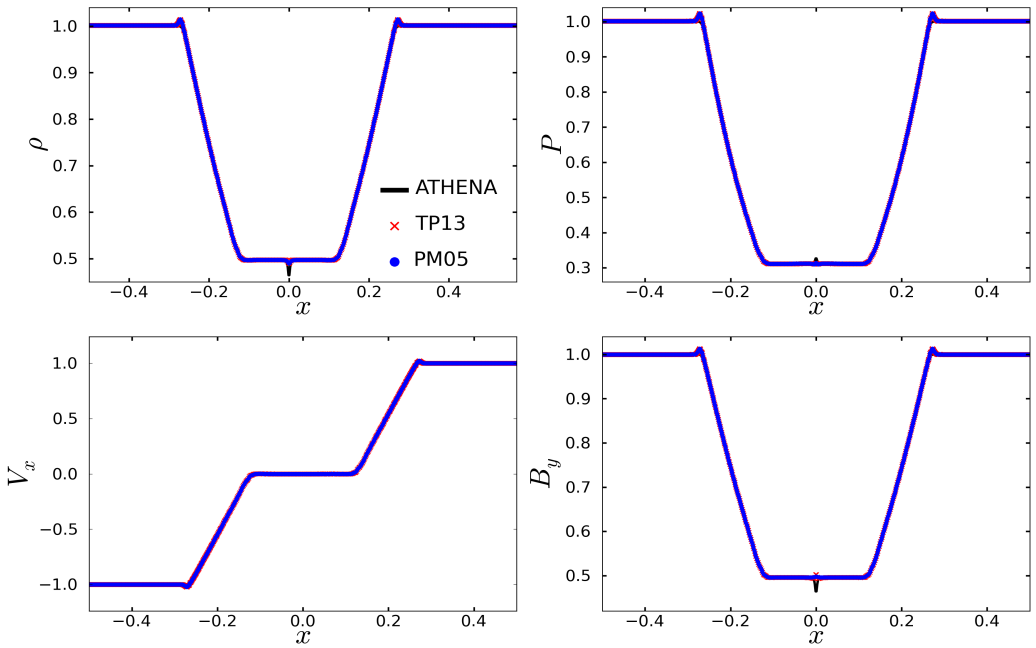

Fig. 3.12: The same fluid quantities as Fig. 3.7 for magnetic shock tube 3B at $t = 0.1$, with the same numerical schemes. There is excellent agreement between the results with the SPMHD results showing smaller central glitches compared to the grid result.

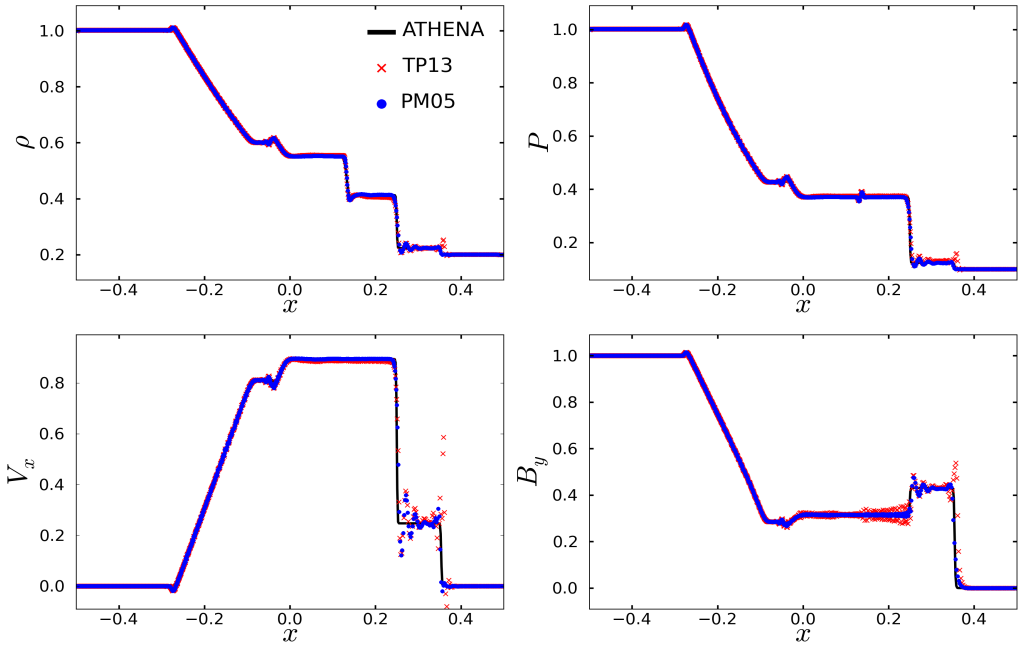

Fig. 3.13: The same fluid quantities as Fig. 3.7 for magnetic shock tube 4A at $t = 0.15$, with the same numerical schemes. There is some post switch-on shock oscillations for both GCMHD+ results, but the oscillations are smaller using the PM05 switch.

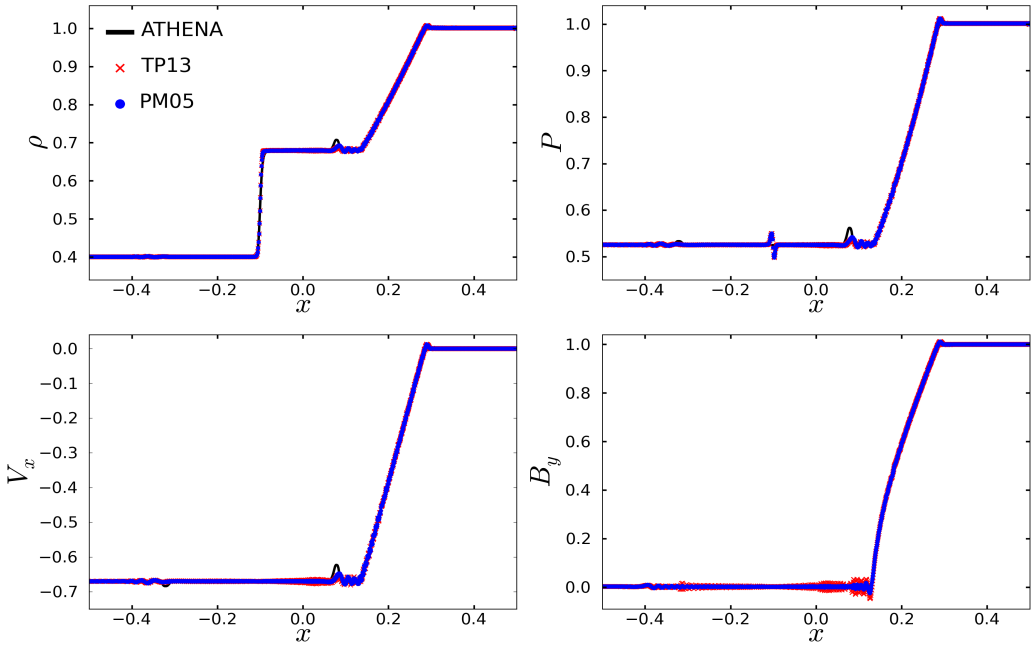

Fig. 3.14: The same fluid quantities as Fig. 3.7 for magnetic shock tube 4B at $t = 0.15$, with the same numerical schemes. There is good agreement between the reference result and the results produced by our implementation. The TP13 switch shows some post-shock oscillations.

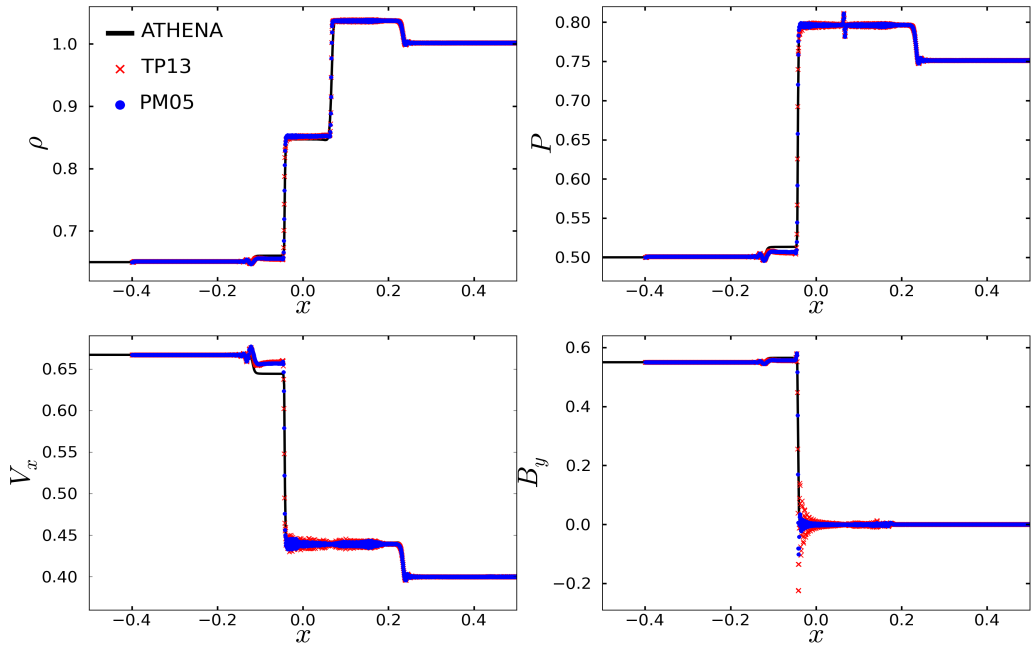

Fig. 3.15: The same fluid quantities as Fig. 3.7 for magnetic shock tube 4C at $t = 0.15$, with the same numerical schemes. There is reasonable agreement between the results and the reference result, with the PM05 resistivity switch showing significantly less oscillation.

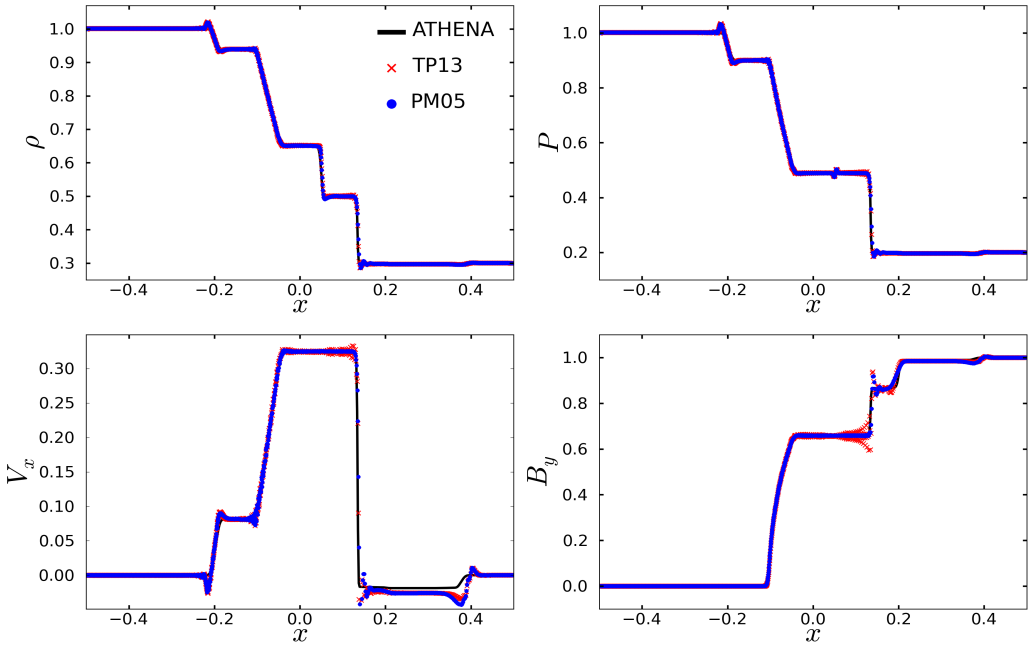

Fig. 3.16: The same fluid quantities as Fig. 3.7 for magnetic shock tube 4D at $t = 0.16$, with the same numerical schemes. There is good agreement between the GCMHD+ results and the ATHENA result, although the TP13 switch result shows post-shock oscillation.

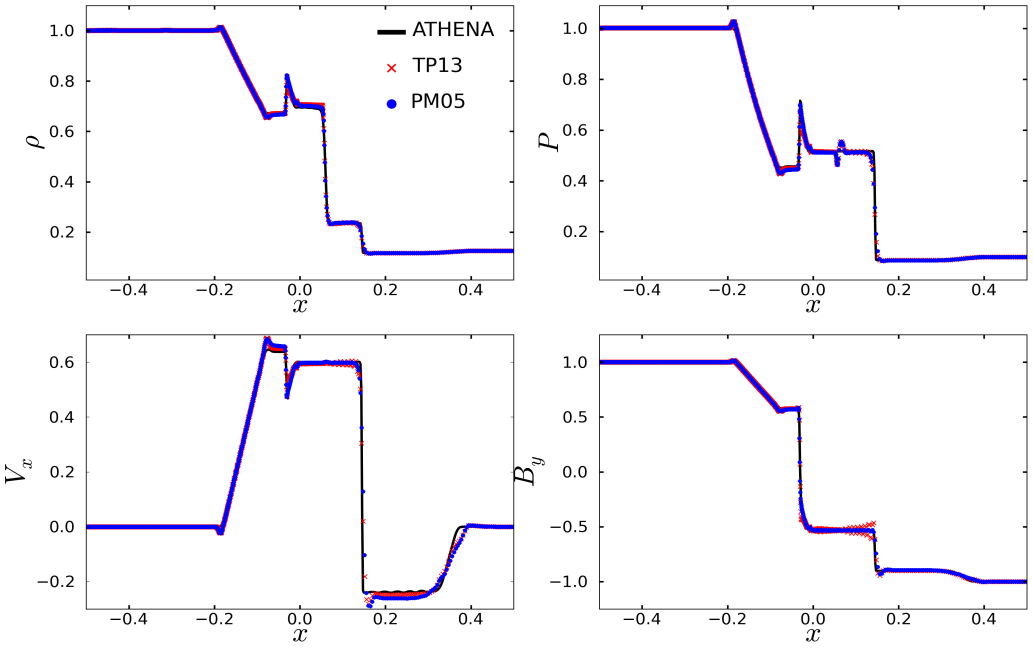

Fig. 3.17: The same fluid quantities as Fig. 3.7 for magnetic shock tube 5A at $t = 0.1$, with the same numerical schemes. The agreement between the reference result and the results produced by our code is excellent, with a small amount of post-shock oscillation in the TP13 switch result.

resolving the discontinuities as well as the PM05 switch. Both switches produce a slightly smoothed profile for the discontinuity in the magnetic field at $x = 0.05$ for test $2B$ in comparison with the ATHENA result.

The third set of tests, $3A$ and $3B$, demonstrate the code's ability to handle magnetosonic structures. The results produced by our implementation for test $3A$ (Fig. 3.11) show good agreement with the reference result produced by ATHENA, except for the density. The result for the density shows a large dip in comparison to the reference result and this is due to difficult hydrodynamical conditions of the test. Particles from the left hand side are colliding at high velocity with stationary particles and this produces a wall heating error. Due to the restriction of only being allowed to travel in one direction, the particles collide with the wall and oscillate back, resulting in the dip in the density. Grid based codes do not suffer from this issue and so no dip is seen in the reference result. The TP13 switch shows a slightly more smoothed magnetic profile in comparison to the PM05 switch. For $3B$, in Fig. 3.12, both GCMHD+ results show good agreement with the reference result for all of the profiles.

The fourth set of tests have special fast and slow structures, know as switch-on and switch-off structures. Behind shocks moving at the fast magnetoacoustic wave speed and rarefactions moving at the slow magnetoacoustic wave speed the tangential magnetic field is "switched-on", i.e. becomes non-zero. Behind fast rarefactions and slow shocks the field becomes negligible and is "switched-off". In test $4A$ a fast switch-on shock propagates from left to right (Fig. 3.13). The results produced by our implementation show good agreement with the result produced by ATHENA. However, there is some oscillation in the magnetic field result for both switches, which is driving the oscillation in the velocity, with the TP13 switch showing significantly more. Further, the oscillation in the PM05 result can be reduced by increasing the minimum applied resistivity, $\alpha^B_{\rm min}$, to a value of $\alpha^B_{\rm min} = 0.05 - 0.1$, without negatively affecting the other ideal test results. However, our implementation is tuned for cosmological simulations, see Chapter 4, and so $\alpha^B_{\rm min} = 0.0$ in this test.

Test $4B$ contains a switch-off rarefaction wave travelling from left to right

(Fig. 3.14). Both results produced by GCMHD+ show good agreement with the reference result, with a small amount of oscillation after the wave. In test $4C$ a slow switch-off shock is traveling through it (Fig. 3.15) and is essentially a hydrodynamic shock tube behind the switch-off shock. Both GCMHD+ results have some post shock oscillation in the magnetic field profile, with the TP13 oscillation being larger and the PM05 oscillation being reduced by increasing $\alpha^B_{\min}$. This oscillation drives the oscillation in the velocity. A slow switch-on rarefaction propagates from left to right in test $4D$ (Fig. 3.16). The results produced by our implementation show good agreement with the reference result, with the TP13 switch showing some oscillation in the magnetic field profile.

Test $5A$, Fig. 3.17, demonstrates our implementation's ability to deal with compound structures, where a shock and rarefaction of the same wave family move together. Both results produced by GCMHD+ show good agreement with the ATHENA result, with the TP13 switch showing some oscillation. The velocity result produced by GCMHD+ overshoots the reference result and can be improved by turning the Balsara switch, section 2.3.1, for the artificial viscosity off.

Overall, the code reproduces the same features for all of the tests as the grid-based ATHENA code. Some results show some post shock oscillation in the magnetic field profile and this is generally worse when using the TP13 switch. Regardless of whether it is in the strong or weak shock regime, the code captures all of the various fast and slow structures and their associated switch-ons or offs. However, in one dimension the divergence of the magnetic field is conserved because of the discretization. Therefore, to demonstrate the code's ability to handle the tensile instability and maintain the solenoidal condition of the magnetic field, we must test it in more than one dimension.

3.2.2 Divergence Advection

The divergence advection test is a simple ideal test that illustrates how the hyperbolic cleaning scheme, section 2.5.5, minimizes the divergence of the magnetic field and how the choice of σ affects the performance of the scheme. In a 2-D periodic box we set up 50×50 particles in a square lattice arrangement

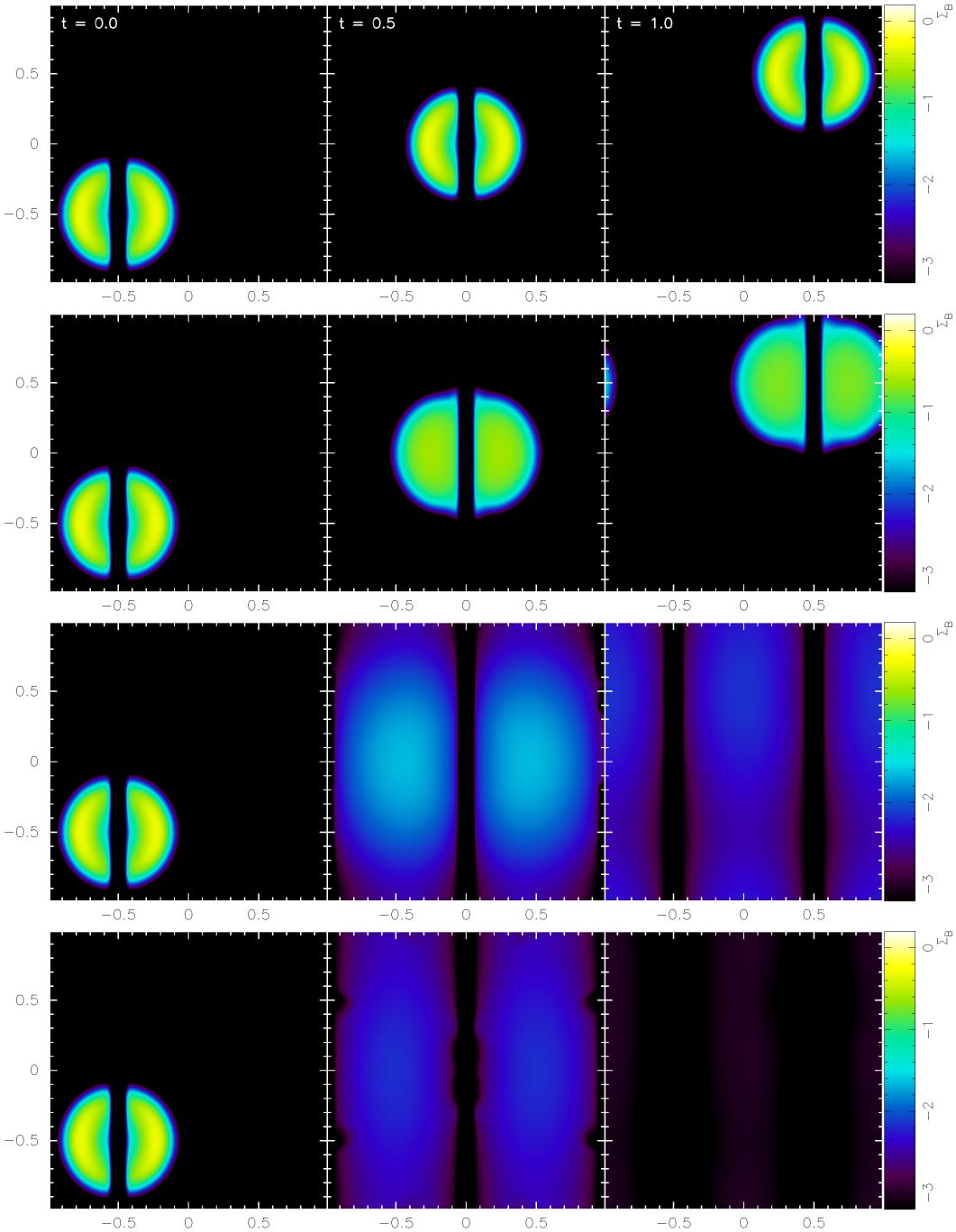

Fig. 3.18: The divergence error at $t = 0.0$ (left column), 0.5 (central column) and 1.0 (right column) for four GCMHD+ implementations: without artificial resistivity and hyperbolic cleaning (top row), with artificial resistivity and without hyperbolic cleaning (2nd row), with hyperbolic cleaning and without artificial resistivity (3rd row) and with hyperbolic cleaning and artificial resistivity (bottom row). The divergence perturbation is advected without either cleaning or resistivity, smoothed and slightly reduced by the resistivity and diluted and significantly reduced by the cleaning scheme.

in the range $x, y \in [-1.0, 1.0]$. The particles have a uniform density $\rho = 1$, a uniform pressure $P = 6$ and we use an adiabatic index $\gamma = 5/3$. The particles have a velocity $\mathbf{v}_i = (1, 1, 0)$ and a magnetic field $\mathbf{B}_i = (0, 0, 1/\sqrt{4\pi})$. To this set up we introduce a perturbation to the magnetic field of the form

$$B_i^x = \frac{1}{\sqrt{4\pi}} \left[(r_i/r_0)^8 - 2(r_i/r_0)^4 + 1 \right] \; ; \quad \text{for} \;\; r_i < r_0 \tag{3.8}$$

where $r_i = \sqrt{(x_i - 0.5)^2 + (y_i - 0.5)^2}$ and $r_0 = 1/\sqrt{8}$ is the radial extent of the perturbation. This perturbation makes the divergence non-zero. To demonstrate how our implementation minimizes the divergence of the magnetic field we evolve this initial set up to $t = 1.0$ with several different configurations of the code. First, we run the simulation with an implementation of the code where both the artificial resistivity scheme and the hyperbolic cleaning scheme (section 2.5.5) are turned off. We then run the simulation with just the artificial resistivity scheme, using the PM05 switch, and a third simulation where just the hyperbolic cleaning scheme, with $\sigma = 1.0$, is active. Finally, we evolve this simulation set up using the full code with both the artificial resistivity scheme, using the PM05 switch, and the hyperbolic cleaning scheme, with $\sigma = 1.0$.

Fig. 3.18 shows the divergence error, Σ_B (section 2.5.5), of the magnetic field at $t = 0.0$, $t = 0.5$ and $t = 1.0$ for these for simulations. With no cleaning and no resistivity the perturbation is transported by the fluid flow and remains unchanged otherwise. Our implementation with just resistivity acts to smooth the perturbation and reduces its magnitude moderately. The cleaning scheme dilutes the perturbation throughout the simulation and by $t = 1.0$ has reduced the divergence of the magnetic field to less than 0.1% throughout the simulation. The combination of the artificial resistivity and hyperbolic cleaning schemes produces a similar effect.

To demonstrate how the choice of σ impacts the performance of the hyperbolic cleaning scheme we use the same initial conditions and run the simulation with GCMHD+ including the cleaning scheme and the resistivity scheme with the PM05 switch. We run four tests with four different values of $\sigma = 0.25, 0.5, 1.0, 2.0$ and evolve the set up to $t = 0.1$. The result of these

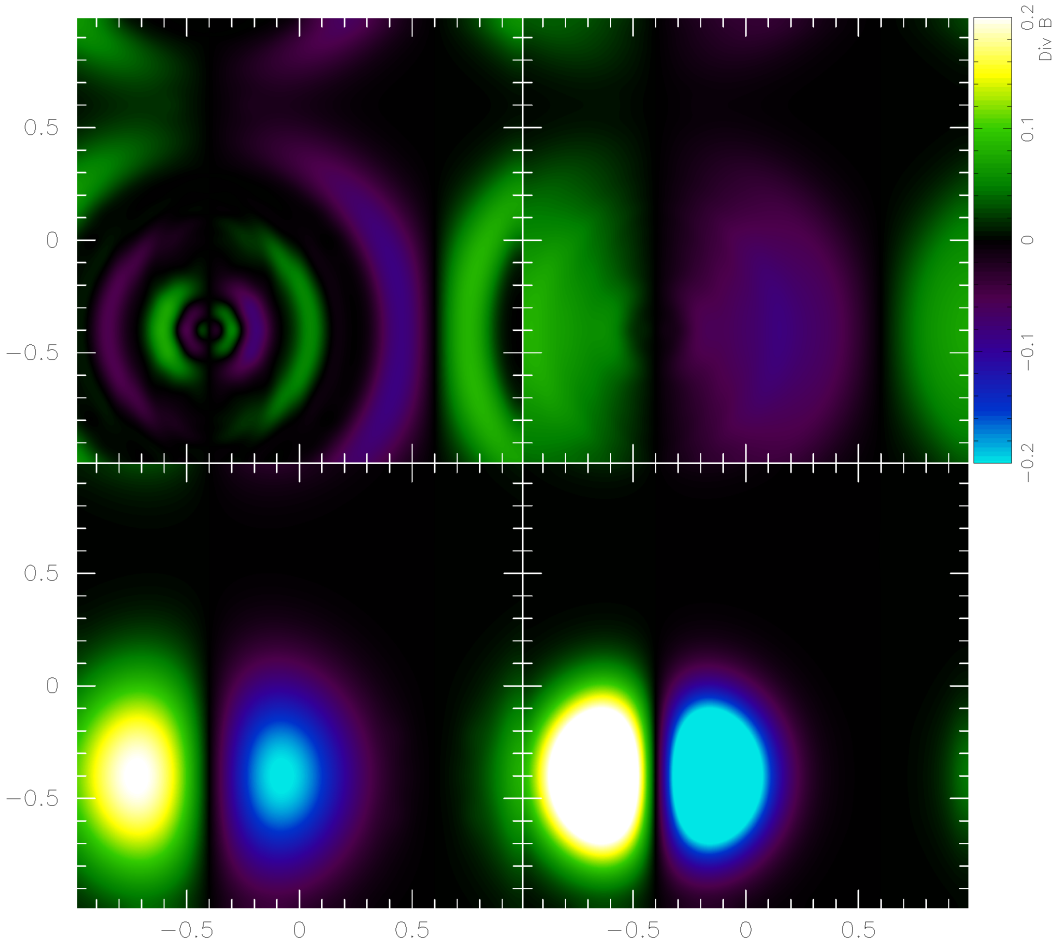

Fig. 3.19: Result of the divergence advection test at $t = 0.1$ for $\sigma = 0.25$ (upper left), 0.5 (upper right), 1.0 (lower left) and 2.0 (lower right). Too small a value causes divergence waves to propagate through the simulation, while too high a value causes the divergence to decay at a slower rate.

four simulations is shown in Fig. 3.19. With $\sigma = 0.25$ it is clear that the initial perturbation is diluted throughout the simulation volume in a wave like manner, and that the wave is damped on shorter length scales as the value of σ increases. However, from $\sigma = 1.0$ to $\sigma = 2.0$ the spatial extent of the perturbation is similar. As the perturbation is diluted over a smaller area, its strength increases as sigma increases. The strength of the perturbation in the $\sigma = 2.0$ case is significantly greater than the $\sigma = 1.0$ case, despite the dilution area being similar. We believe that the $\sigma = 2.0$ case is effectively over damping the wave and so it will take longer for the divergence wave to decay away.

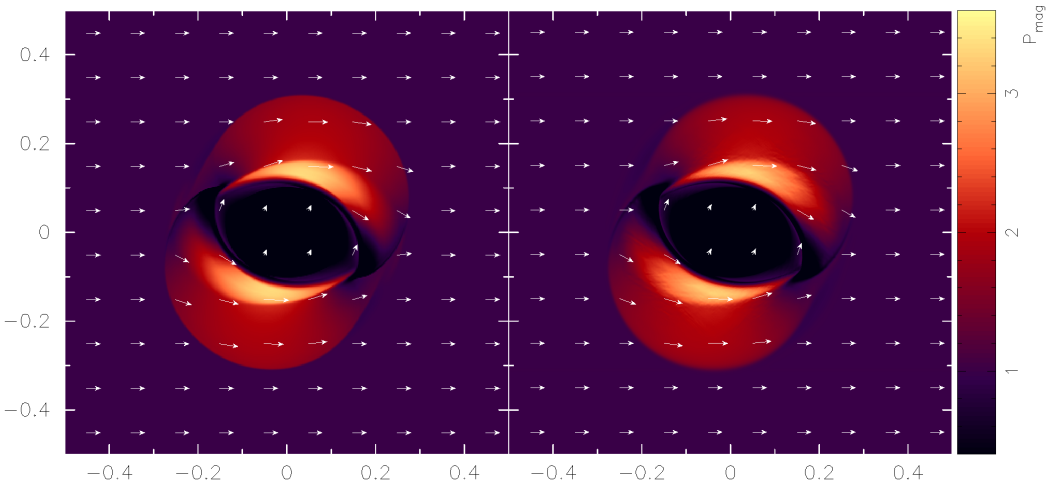

Fig. 3.20: Magnetic pressure results of the fast rotor test at $t = 0.1$ for the ATHENA code (left) and our implementation (right), where the arrows denote the magnetic field in the xy plane. Some intrinsic smoothing at the edge of the propagating fast mangetoacoustic wave is visible in the GCMHD+ result.

In more realistic astrophysical simulations a divergence numerical error can be generated throughout the simulation volume at any time and allowing the wave to spread throughout the simulation will no longer dilute the divergence as effectively. The wave should, therefore, be damped as quickly as possible. Unless otherwise stated, all simulations presented here use a value of $\sigma = 1.0$ as this damps the wave without it travelling throughout the simulation, but it does not over damp the wave and produce a longer decay timescale. We now demonstrate the performance of our code in more strenuous tests.

3.2.3 Fast Rotor

The fast rotor test is commonly used to validate the results produced by MHD implementations. This 2-D test consists of a dense rotating disk embedded in a static, low density ambient medium, with a uniform magnetic field throughout the simulation. As this initial set up evolves, the disk is thrown out into the ambient medium and constrained by the magnetic field. In a 2-D periodic square box of length unity we set up particles on a hexagonal lattice. We set up 400 particles along the x-axis producing a resolution of 400×460 particles for the background ambient medium in the range $x, y \in [-0.5, 0.5]$. The

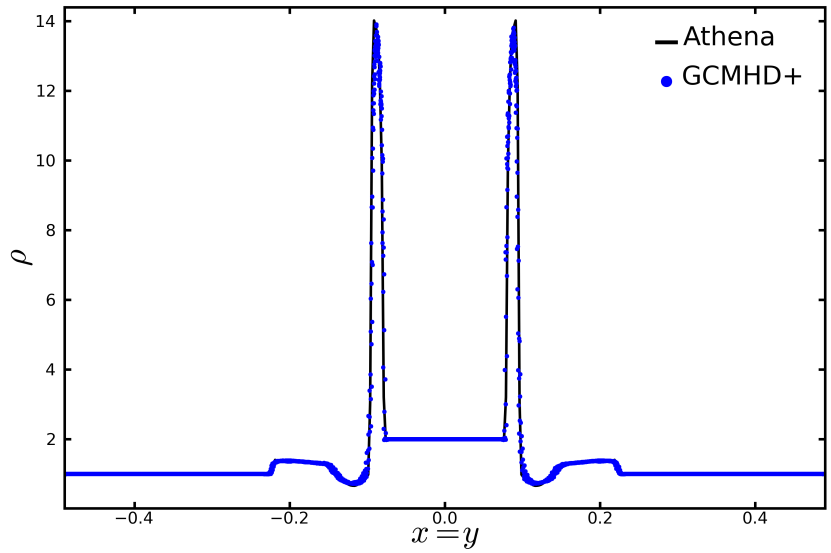

Fig. 3.21: A cut along $x = y$ of the density results produced by our code (blue points) and the ATHENA grid code (black line) at $t = 0.1$, enabling a quantitative comparison. Our code correctly reproduces all the features at the correct magnitude in comparison to the reference result.

ambient medium has a density $\rho = 1$, a pressure $P = 1$ and is static, i.e. $\mathbf{v}$=(0,0,0). A constant magnetic field of $\mathbf{B} = (2.5/\sqrt{\pi}, 0, 0)$ is applied to all particles in the simulation and we use an adiabatic index $\gamma = 1.4$.

The rotating disc has a radius $r_0 = 0.1$ and is centred on the origin. One way to produce the density contrast is to give the particles inside this radius a larger mass, but this can result in unphysical spurious forces. Instead, we apply the same mass to all the particles and place ten times more particles in the disc region. So we first place the ambient medium and remove particles that fall inside r_0. We then place a second hexagonal lattice with a reduced particle spacing in a region $2r_0 \times 2r_0$ centred on the origin and remove particles that fall outside r_0. The use of a hexagonal lattice reduces any discontinuities between the ambient medium and the disc. All particles in the disc have a density $\rho = 10$, pressure $P = 1$ and a velocity $\mathbf{v}_i = (-2(y_i)/r_0, 2(x_i)/r_0, 0)$. Our set up results in a total of $236,626$ particles in the simulation.

We evolve this initial configuration, with PM05 resistivity and the cleaning scheme, to $t = 0.1$ and the result can be seen in Fig. 3.20. As no analytic

solution to this test exists, we compare the result produced by our implementation with that produced by the ATHENA code using 400×400 cells. The results qualitatively agree well with all of the features in the ATHENA result produced by our implementation, with some slight intrinsic smoothing. To give a quantitative comparison between the two results we make a cut through the simulation along $x = y$, which is shown in Fig. 3.21. The result produced by GCMHD+ exactly reproduces all of the features of the reference result and reproduces the correct peak value for the central density features. We use the next idealized test case to show the impact of the artificial resistivity scheme and the hyperbolic cleaning scheme on the result produced by our implementation.

3.2.4 Orszag-Tang Vortex

The compressible Orszag-Tang vortex was developed from a test problem in Orszag and Tang (1979) and is a common test of MHD codes. This test demonstrates the code's ability to handle the interaction between different classes of shocks and the transition to MHD turbulence. In a 2-D periodic square box of length unity we set up particles on a hexagonal lattice in the range $x, y \in [-0.5, 0.5]$. Using $\gamma = 5/3$, we set $B_0 = 1/\sqrt{4\pi}$ and the pressure of the medium $P = \gamma B_0^2$, to give a magnetic to thermal pressure ratio of $10/3$. We set $v_0 = 1.0$ and the density of the medium is set to $\rho = \gamma P / v_0$ to produce an average Mach number of unity. The initial magnetic field is set as $\mathbf{B}_i = (-B_0 \sin(2\pi y_i), B_0 \sin(4\pi x_i), 0.0)$ and the particles have an initial velocity $\mathbf{v}_i = (-v_0 \sin(2\pi y_i), v_0 \sin(2\pi x_i), 0.0)$. To demonstrate the effect of resolution on the result produced, we perform this simulation with three different resolutions: 256×294, 512×590 and 1024×1180.

We evolve this initial set up until $t = 1.0$ and a comparison of the density and the magnetic pressure results produced by the three different resolutions with the ATHENA reference result, using 600×600 cells, can be seen in Fig. 3.22 and Fig. 3.23 respectively. All three resolutions produce good agreement with the reference result for the large-scale structures and as resolution increases the complex interactions between the shock fronts becomes clearer with significantly more small-scale structure visible in the highest resolution

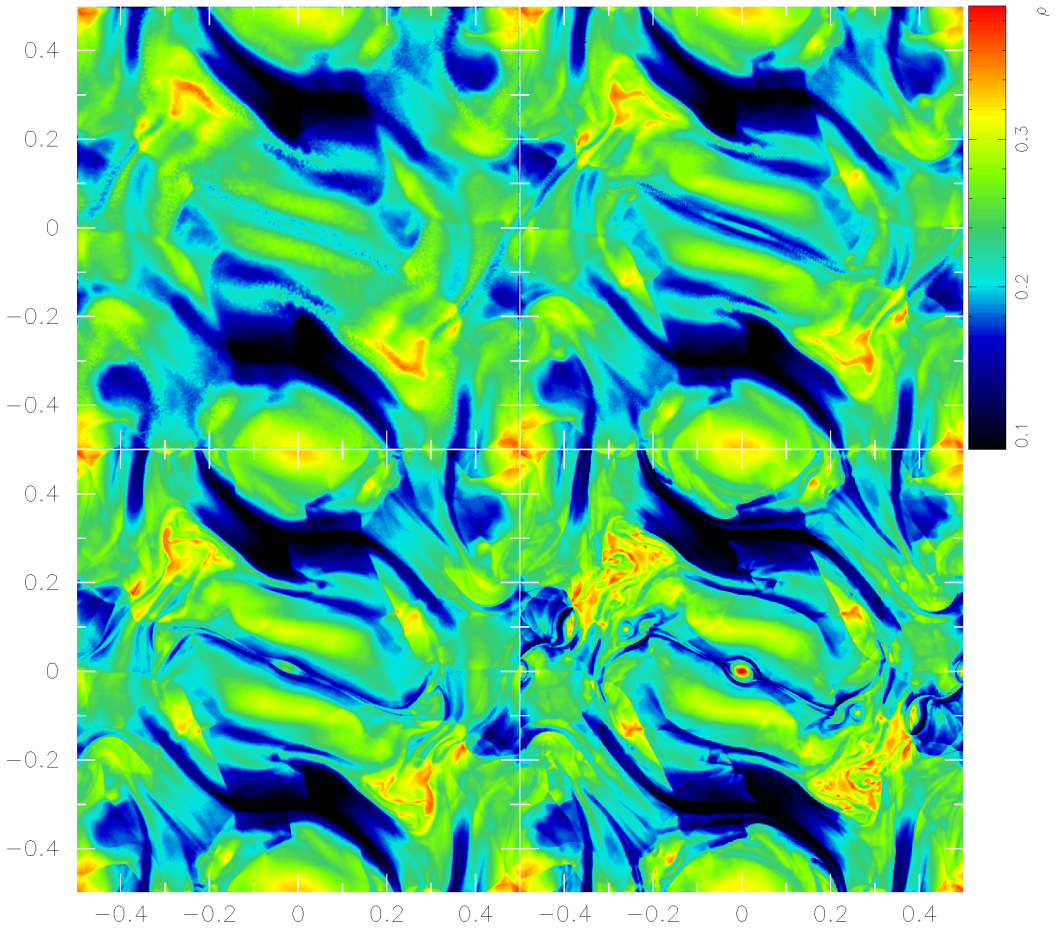

Fig. 3.22: Density results for the Orszag-Tang vortex, at $t = 1.0$, produced by our code at a resolution of 256×294 (upper left), 512×590 (upper right) and 1024×1180 (lower left) compared to a reference result produced by the ATHENA code (lower right) using 600×600 cells. The result produced by our code tends to the reference result as the resolution increases.

simulation. The lower resolution simulations fail to capture the very dense, very high magnetic pressure central island feature that forms in the reference result and even in the highest resolution simulation there is only a hint of this island.

To provide a quantitative comparison between the ATHENA result and the results produced by our implementation we make a cut through the simulation volume at $y = -0.1875$. We make this cut at $t = 0.5$ to allow comparison with other schemes that only evolve the Orszag-Tang vortex to this point (for

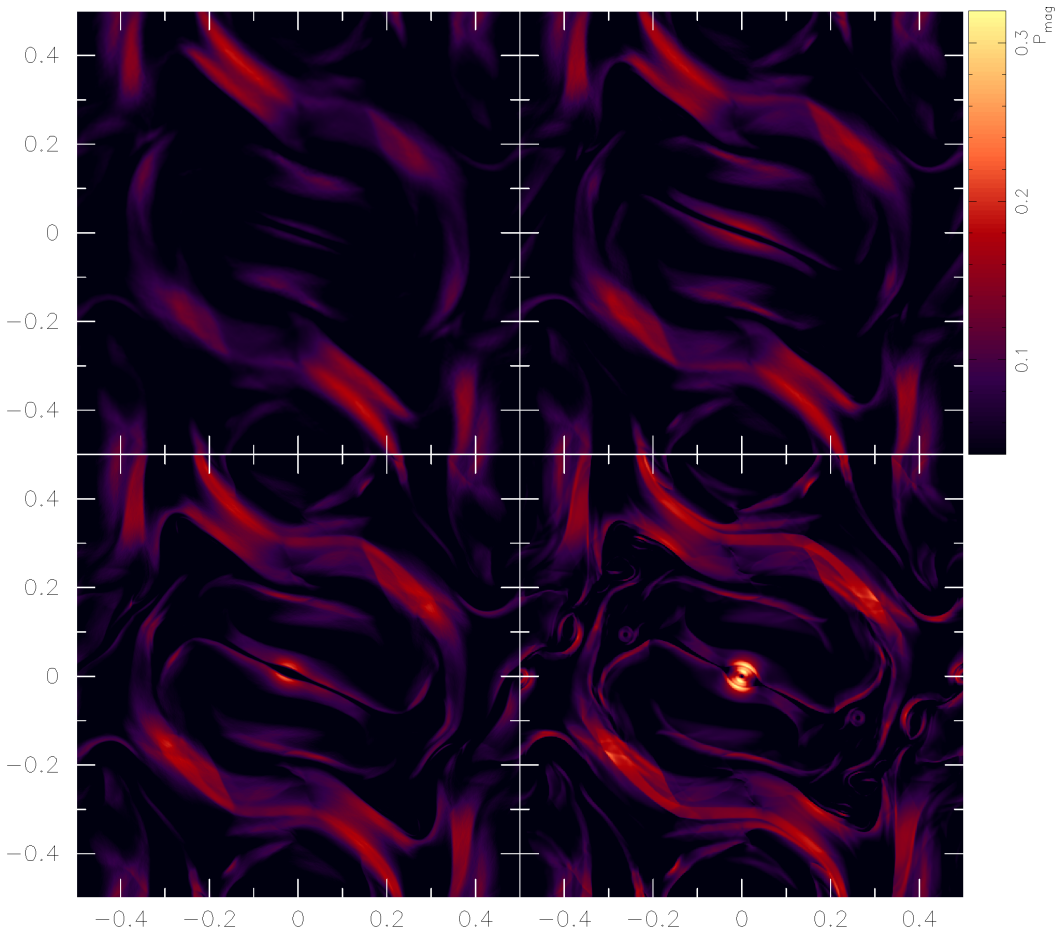

Fig. 3.23: Magnetic pressure results for the Orszag-Tang vortex, at $t = 1.0$, produced by our code at a resolution of 256×294 (upper left), 512×590 (upper right) and 1024×1180 (lower left) compared to a reference result produced by the ATHENA code (lower right) using 600×600 cells. The central density peak begins to form as the central magnetic pressure increases with resolution.

example Londrillo and Del Zanna 2000; Dolag and Stasyszyn 2009). The result of this cut can be seen in Fig. 3.24. It is again clear that all three GCMHD+ results reproduce the large-scale features of the ATHENA result. However, as the resolution increases our implementation begins to capture the smaller, sharper features, such as those at $x = -0.42$ and $x = -0.48$.

In this test the shock fronts become more and more complex as they interact during their evolution. This provides an excellent test of the artificial resistivity switch's ability to track this behaviour and to correctly apply resis-

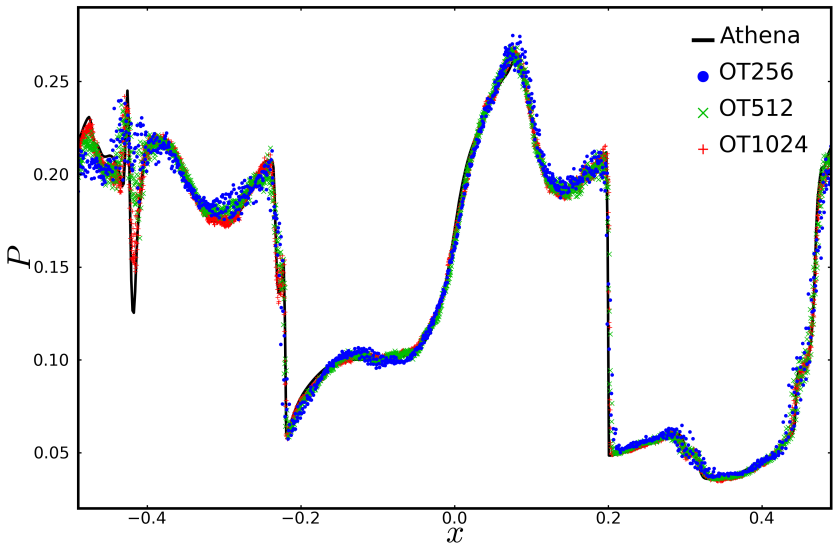

Fig. 3.24: A cut at $y = -0.1875$ through the pressure results of the Orszag-Tang vortex, at $t = 0.5$, to allow a comparison of the results produced by our implementation, at a resolution of 256×294 (blue points), 512×590 (green x's) and 1024×1180 (red crosses), with the reference result produced by ATHENA (black line).

tivity. We evolve the 1024×1180 resolution test with the PM05 switch and the TP13 switch to $t = 1.0$ to examine how the switches track the shocks as they become more complex. The result of this simulation is shown in Fig. 3.25. The density results produced by both switches show good agreement, with the exception of the formation of the central high density island, as seen in the ATHENA result in Fig. 3.22. The applied resistivity for the two switches is very different. The TP13 switch tracks the major shock fronts and applies the maximum resistivity to these shocks, whereas the PM05 switch applies significantly less resistivity to these shocks and applies more resistivity to the smaller features. The application of strong resistivity to the central feature smooths the magnetic field and reduces its strength. This reduction in strength reduces the magnetic pressure and prevents the central density feature from forming. The TP13 switch shows improved shock tracking ability in comparison to the PM05 switch, however, it applies too much resistivity to these shocks and smooths them too aggressively, leading to some sharp features being smoothed out and lost.

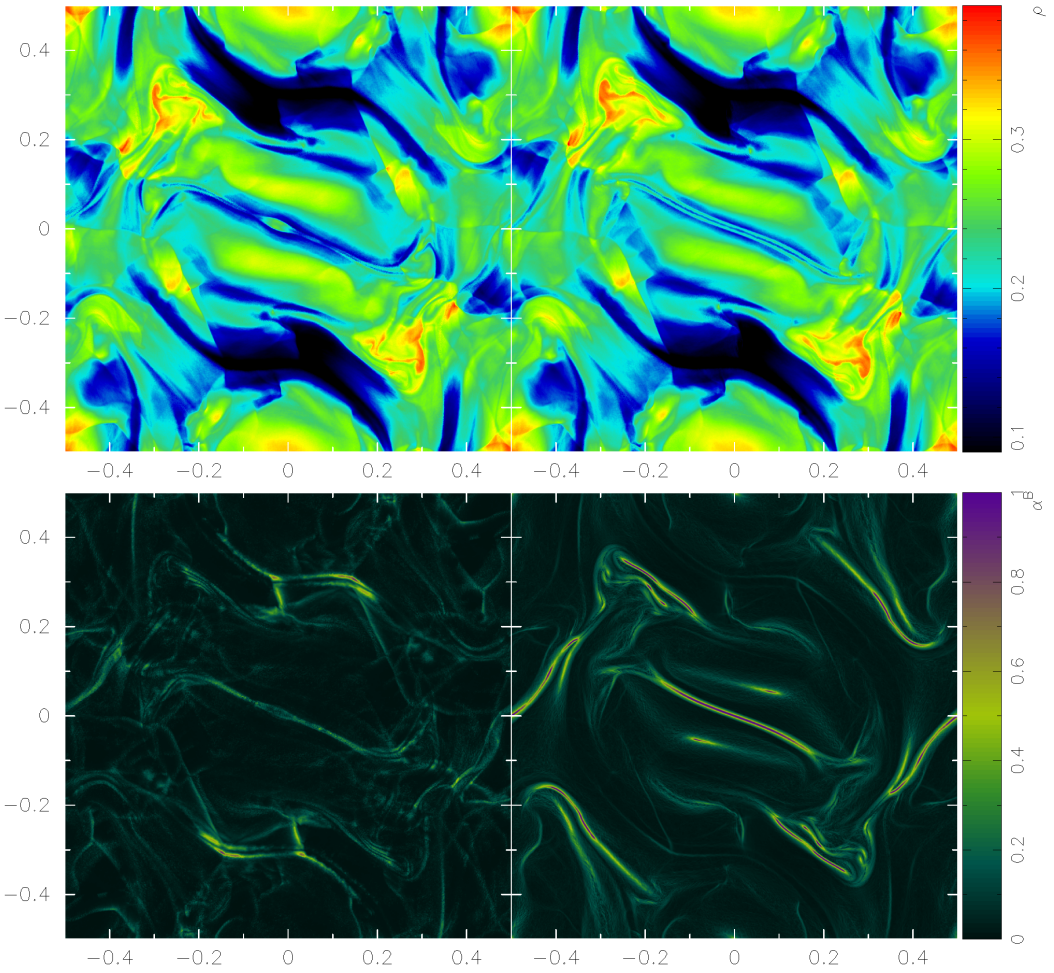

Fig. 3.25: Density (upper row) and resistivity (lower row) results to the Orszag-Tang vortex at $t = 1.0$ for our implementation using the PM05 (left column) and TP13 (right column) resistivity switches. The TP13 switch more accurately tracks the shock fronts, but it applies too much resistivity leading to some features being smoothed out.

The interacting shock fronts in this test produce a very rapidly varying magnetic field and this is a significant source of numerical divergence of the magnetic field. Therefore, we use this test to demonstrate the improvement the hyperbolic cleaning scheme brings to the growth of the divergence of the magnetic field. We evolve two 1024×1180 tests to $t = 1.0$ for an implementation with, and another without, the hyperbolic cleaning scheme, both using the PM05 resistivity switch. The divergence error, Σ_B, is shown for both implementations in Fig. 3.26. The hyperbolic cleaning scheme produces an order of magnitude reduction in the divergence error throughout the sim-

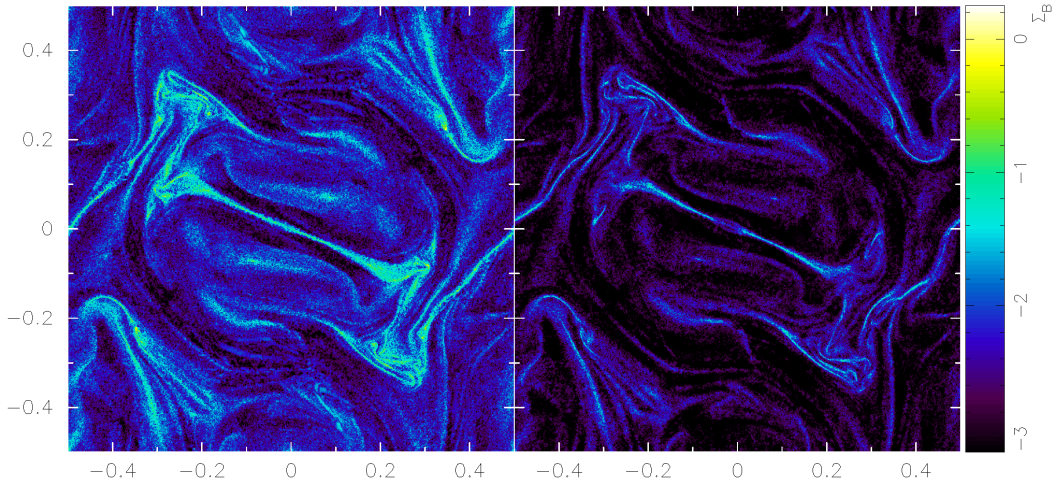

Fig. 3.26: Divergence error result for the Orszag-Tang vortex, at $t = 1.0$, produced by our implementation without (left) and with (right) the hyperbolic cleaning scheme. The incorporation of the cleaning scheme produces an order of magnitude reduction in the divergence error throughout the simulation.

ulation. With the scheme, the divergence of the magnetic field is kept below 1% of the magnetic field magnitude in the majority of the simulation and our implementation only fails to do this at the complex shock fronts, which are sources of divergence. We now test our implementation in a magnetic pressure dominated, strong shock regime to demonstrate our code's ability to handle this regime and demonstrate the effect of failing to adequately suppress the tensile instability.

3.2.5 Magnetized Blast Wave

The magnetized blast wave test is a common test of numerical MHD implementations. It consists of a point like explosion, similar to the Sedov blast wave test, expanding in a magnetized ambient medium. The magnetic pressure is significantly greater than the thermal pressure and so the blast is constrained perpendicular to the magnetic field by the magnetic tension force. We perform this test in two dimensions to maximize the spatial resolution of the test. In a periodic square box of length unity we set up 512×590 particles on a hexagonal lattice in the range $x, y \in [-0.5, 0.5]$. The particles have a density $\rho = 1$ and a pressure $P = 1$, using $\gamma = 1.4$. All of the particles are at rest and have an

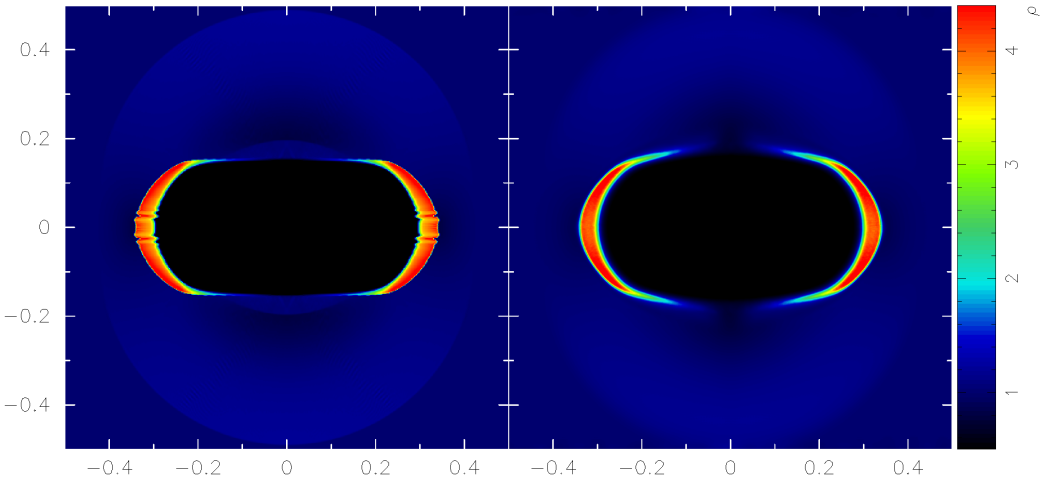

Fig. 3.27: Density results for the magnetized blast wave test, at $t = 0.03$, produced by ATHENA (left) and our code (right). Numerical artefacts are present in the shock front of the grid code result.

initially divergence free magnetic field of $\mathbf{B}_i = (10.0, 0.0, 0.0)$. Particles that fall within a radius of $r_i \leq 0.125$ from the origin had their pressure increased to $P = 100$.

We evolve this initial set up to $t = 0.03$ for both the ATHENA code and our implementation, using resistivity with the PM05 switch and the hyperbolic cleaning scheme using $\sigma = 1.0$, and the results are shown in Fig. 3.27. Both codes show a shock front that develops parallel to the magnetic field, but is suppressed perpendicular to it. There is a small amount of smoothing visible in our implementation's result in comparison to the ATHENA reference result, but the ATHENA result has significant numerical artefacts present in the shock fronts. It should be noted that if the magnetic field is oriented in the $x = y$ direction then these artefacts disappear and they are most likely caused by the grid discretization.

In this test the magnetic pressure is significantly greater than the thermal pressure, with a plasma beta of 0.02, and is therefore susceptible to the tensile instability. To prevent the onset of this instability we directly subtract any non-zero divergent magnetic field force terms from the equation of motion of the fluid. This correction term has a free parameter $\hat{\beta}$ that controls

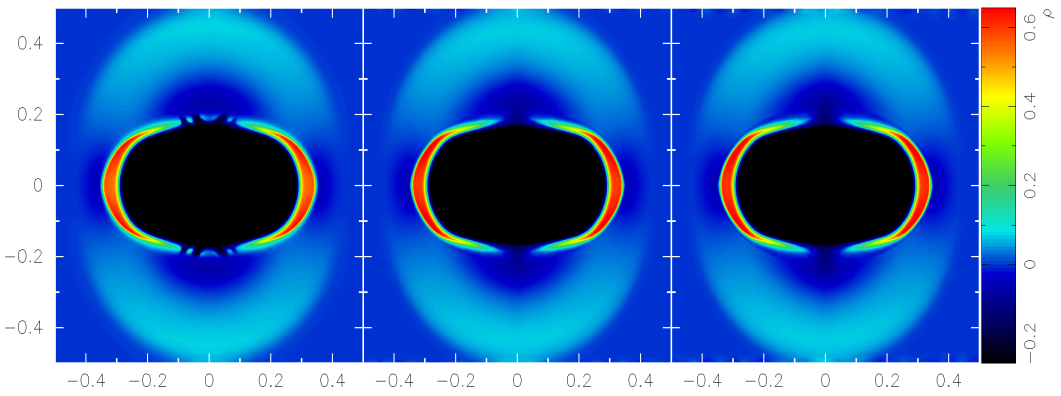

Fig. 3.28: Density results for the magnetized blast wave test, at $t = 0.03$, produced by our code with $\hat{\beta} = 0.50$, 0.75 and 1.00. Failure to suppress force terms due to numerical divergence of the magnetic field can lead to instabilities and numerical artefacts in the result.

the strength of the correction. Børve et al. (2004) argued that $\hat{\beta} = 0.5$ was sufficient to prevent the onset of the instability, while Tricco and Price (2012) argued that this value fails to achieve stability in certain circumstances, such as this test. To demonstrate why we choose $\hat{\beta} = 1.0$, we run the magnetized blast wave test with $\hat{\beta} = 0.5, 0.75$ and 1.0. The log of the density result produced by each parameter implementation is shown in Fig. 3.28. With $\hat{\beta} = 0.5$ instabilities develop where the development of the shock front is suppressed, but this does not occur for $\hat{\beta} = 0.75$ and 1.0. Therefore, to ensure stability in all circumstances we choose $\hat{\beta} = 1.0$. With the tensile instability suppressed with our choice of $\hat{\beta}$, we now examine our code's ability to capture magnetized instabilities.

3.2.6 Magnetized Kelvin-Helmholtz Instability

The magnetized KHI test is the same as the hydrodynamic KHI test with an initially uniform magnetic field applied in the x-direction. The addition of the magnetic field should lead to a suppression of the growth of perturbations perpendicular to the field, via the magnetic tension force, resulting in a slower growth of the instability. In a periodic square box of length unity we place particles on a square lattice in the range $x, y \in [-0.5, 0.5]$. The box is split into a region of high density, $\rho_h = 4.0$, that lies within $|y| < 0.25$ and a low density region, $\rho_l = 1.0$, outside of this. We use equal mass particles for both regions

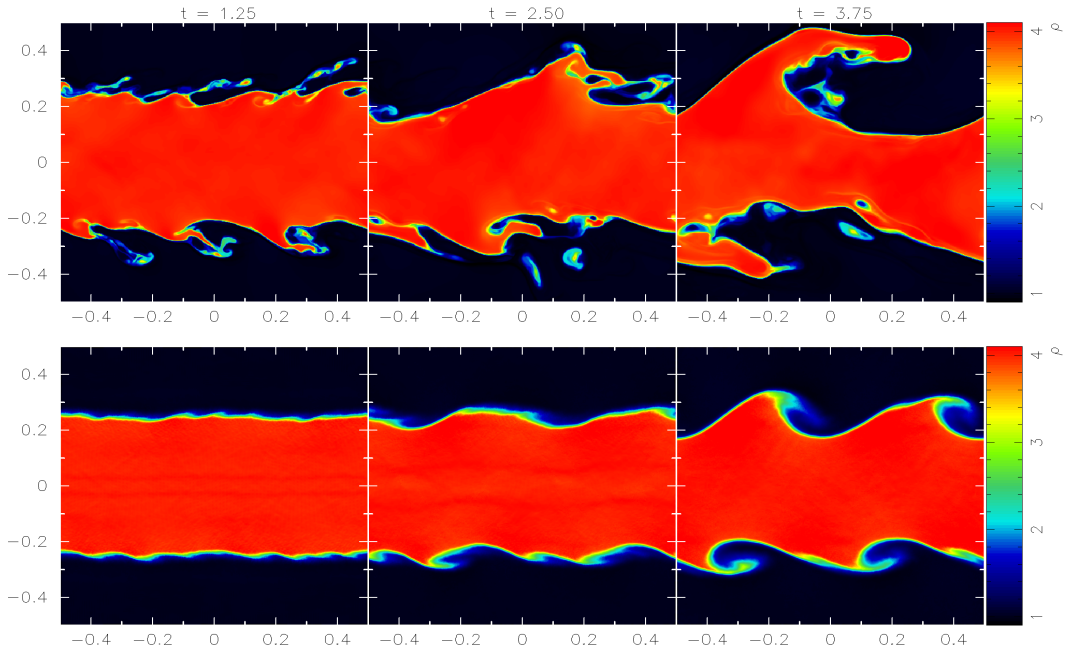

Fig. 3.29: Density results for the magnetized KHI test produced by the ATHENA grid code (upper row) and GCMHD+ (lower row) at $t = 1.25$ (left column), $t = 2.50$ (centre column) and $t = 3.75$ (right column). For both codes, comparison with Fig. 3.6 demonstrates that the magnetic field suppresses the growth of small-scale instabilities.

and so, to obtain the density contrast, we place 512×256 particles in the high density region and 256×128 particles in the low density region. The regions are in pressure equilibrium $P_h = P_l = 2.5$ and we assume $\gamma = 5/3$. Particles in the high density region have a velocity $\mathbf{v}_h = (-0.5, 0.0, 0.0)$ and those in the low density have a velocity $\mathbf{v}_l = (0.5, 0.0, 0.0)$. Sinusoidal perturbations are added to the y velocity component of the form $v_y(x_i) = \delta v_y \sin(\lambda 2\pi x_i)$, where $\delta v_y = 0.01$ and $\lambda = 1.0$. An initially homogeneous magnetic field $\mathbf{B} = (0.129, 0.0, 0.0)$ is applied across the simulation. As there is no analytic solution for this test we compare to a reference result provided by the ATHENA code.

We evolve this initial set up until $t = 3.75$ and a comparison of the results produced by our implementation and the ATHENA code at $t = 1.25, 2.50$ and 3.75 are shown in Fig. 3.29. Comparison of the reference result with the reference result in Fig. 3.6 clearly demonstrates that the addition of a magnetic field to the system significantly reduces the development of small-scale instabilities. The result produced by our implementation also shows that the magnetic

field reduces small-scale perturbations. However, the instability again takes longer to develop in the result produced by GCMHD+ in comparison to the result produced by the ATHENA code.

3.3 Summary

In this chapter we have presented a suite of idealized test simulations that thoroughly tested our numerical method for solving the fluid equations and the equations of magnetohydrodynamics. We have compared the results our implementation produced with analytic solutions and reference results produced by other numerical techniques. We have demonstrated the strengths and weaknesses of our code and how our additional algorithms help to overcome the numerical issues that arise when a magnetic field is added to the fluid. We have used the ideal test cases to explain why we have chosen the particular values of the free parameters that exist in our implementation.

We tested our code's ability to reliably solve the equations of fluid dynamics and correctly capture discontinuities in the fluid. Using a one dimensional shock tube test and a three dimensional blast wave test, we demonstrated that the code correctly captures both small and large discontinuities and reliably produces accurate pre- and post-shock fluid quantities. We then presented results to a self-similar collapse test with both gas and dark matter and demonstrated that the code's result tended towards the analytic solution as the resolution increased. SPH codes traditionally struggle to resolve and regulate mixing instabilities and we presented our implementation's result to the Kelvin-Helmholtz instability test and showed that while our code is capable of resolving the instability, it develops at a significantly slower rate in comparison to a grid based reference result.

The introduction of a magnetic field to the fluid enables a myriad of additional structures to develop at discontinuities in the fluid values. We ran a thorough range of one dimensional magnetic shock tubes that tested our code's ability to handle shock and rarefaction waves of different speeds, contact discontinuities, rotational discontinuities, compact features and switch-on and switch-off features. Our implementation reproduced all of the features present

in the reference results and is capable of capturing all of the different structures. We tested our two proposed resistivity switches and found that the PM05 switch produces less post shock oscillation, with the advantage that the value of $\alpha^B_{\min}$ could be increased to further suppress this oscillation.

We then looked at multi-dimensional tests of the code. The divergence advection test was used to show how the resistivity and cleaning schemes work to minimize the violation of the solenoidal condition of the magnetic field. The fast rotor test was used to provide a qualitative and quantitative comparison between our implementation's result and the ATHENA reference result, with the code producing excellent agreement with the grid-based method. We used the compressible Orszag-Tang vortex test to demonstrate that our code's result tends to the reference result with increasing resolution. It was used to compare how the resistivity switches track the increasingly more complicated shock fronts and apply resistivity to them. We found that the TP13 switch more accurately tracked the shocks, but applied too much resistivity and smoothed out some features. The reduction in the numerical divergence error of the magnetic field produced by the hyperbolic cleaning scheme was tested using the Orszag-Tang vortex and it was found that, even in this more stringent test, the scheme produced at least an order of magnitude reduction in the divergence error.

We then tested our code's ability to capture strong shocks in a magnetically dominated regime using the magnetic blast wave test. Our implementation correctly captured the suppression of the shock perpendicular to the magnetic field and is free from the numerical artefacts present in the grid-based reference result. This test demonstrated that choosing a value of $\hat{\beta}$ less than one can lead to numerical artefacts in the result. Finally, we used a magnetized KHI test to examine whether our code captures mixing instabilities in a magnetic medium. We found that our code did resolve the instability, but that its growth is significantly slower than the result produced by a grid-based method.

Overall, our code reliably produces results to this range of test problems, was capable of handling all of the structures that develop due to discontinu-

ities in the magnetized fluid quantities and was able to suppress the growth of numerical artefacts, such as the tensile instability and the divergence of the magnetic field. This gives us the confidence that our smoothed particle magnetohydrodynamics implementation, GCMHD+, produces robust and reliable results and that the results it produces to astrophysical problems are reliable.

Chapter 4

Evolution of a Seed Field due to Structure Formation

In the theory of hierarchical structure formation, gas and dark matter initially collapse to form stars and galaxies. These first objects then coalesce to form groups of galaxies, which then merge with other groups to form clusters of galaxies. Galaxy clusters are the largest virialized systems in the universe and their properties and their formation have been studied via observations. These observations show that between the galaxies of a cluster is the ICM, a tenuous low-density gas that fills the volume of the cluster. The ICM is expected to be turbulent, due to mergers and the accretion of smaller objects, and this has been confirmed by observations (Schuecker et al. 2004).

The magnetic fields that are observed in large-scale structures at the current epoch, regardless of their generation mechanism, would have been significantly altered by the formation of structure. As the resistive timescale of large-scale structure is significantly longer than the current age of the Universe, any seed field is effectively frozen into the gas and collapses with it. The shocks and turbulence induced by the hierarchical formation of a structure will amplify a seed field, redistribute it throughout the volume of the structure and erase any information about its origin. Therefore, to be able to say anything about the origins of the magnetic fields observed in large-scale systems the evolution of a seed magnetic field due to the formation of structure must first be understood. Numerical simulations that can accurately model

the formation of structure and reliably capture the evolution of a seed field are a tractable, and perhaps the only practical approach to furthering our understanding of the origins of large-scale magnetic fields.

4.1 Santa Barbara Cluster

The Santa Barbara galaxy cluster simulation is an idealized simulation that has become a standard test of common cosmological hydrodynamics codes (Frenk et al. 1999). From the initial conditions, a galaxy cluster forms in a flat cold dark matter (CDM) Universe. It uses the assumed cosmological parameter values of mean density of $\Omega = 1$, a Hubble constant of $H_0 = 50\,\mathrm{kms}^{-1}\mathrm{Mpc}^{-1}$, current rms line mass fluctuations in a radius of 16 Mpc of $\sigma_8 = 0.9$ and a baryon density, as a function of the critical density, of $\Omega_b = 0.1$. Although these parameters differ from those measured by current experiments (see Planck Collaboration et al. 2013; Hinshaw et al. 2013), we use these cosmological parameters to ensure a fair comparison between the performance of our code and other numerical codes. The primordial density fluctuation spectrum is assumed to have a spectral index of $n_s = 1$ and a shape parameter $\Gamma = 0.25$. In a sphere of comoving radius 32 Mpc a 3σ density perturbation is centred on the origin at a redshift of $z = 20$. In our set-up the gas particles each have a mass of $7.8 \times 10^8\,\mathrm{M}_\odot$ and the DM particles each have a mass of $7.8 \times 10^9\,\mathrm{M}_\odot$. We embed a magnetic field of 1×10^{-11} G in the gas particles and ensure that it is initially divergence free by orientating it only in the x-direction. We evolve this initial set-up to the current epoch at $z = 0$ using GCMHD+ and a galaxy cluster of mass $1.16 \times 10^{15}\,\mathrm{M}_\odot$ forms. For this simulation we do not use the hyperbolic cleaning scheme and use the PM05 resistivity switch.

This simulation tests our implementation's ability to capture the formation of structure and we used it to examine the impact of our artificial conductivity scheme by either including it or turning it off. Additionally, we tested the impact of our choice of minimum applied resistivity for the PM05 resistivity switch. (The parameters for each simulation are shown in Table 4.1).

The hydrodynamic properties of the cluster at $z = 0.0$ are shown in Fig.

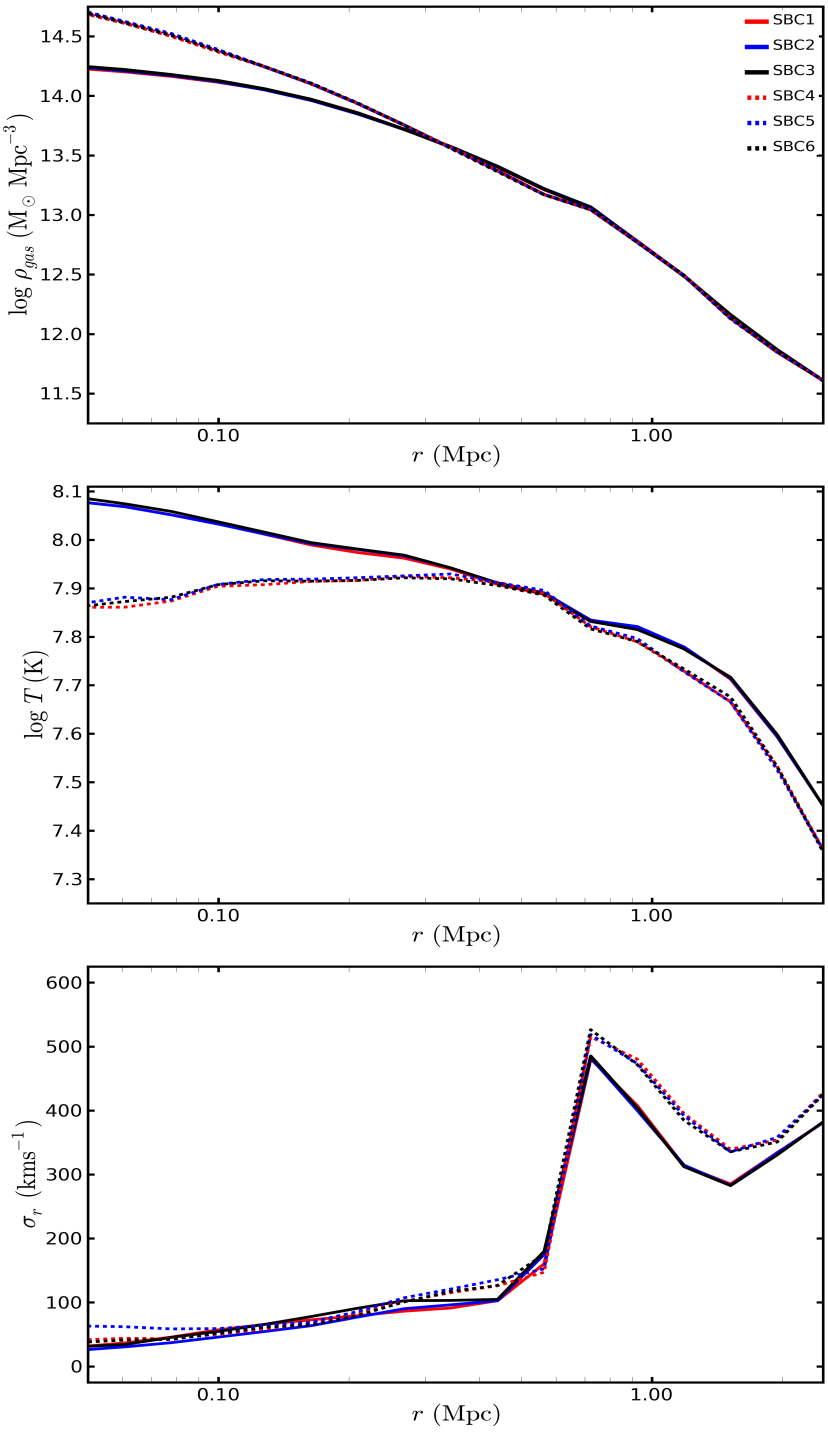

Fig. 4.1: Density (top panel), temperature (center panel) and velocity dispersion (bottom panel) radial profiles for the Santa Barbara galaxy cluster simulation. The inclusion of artificial conductivity alters the central density and temperature profiles of the cluster, with those including conductivity showing good agreement with other numerical schemes. The magnetic field scheme has no effect on the hydrodynamic properties. (See Table 4.1 for the different implementations)

Simulation	$\eta_{\rm min}$	Artificial Conductivity
SBC1	0.0	ON
SBC2	0.005	ON
SBC3	0.05	ON
SBC4	0.0	OFF
SBC5	0.005	OFF
SBC6	0.05	OFF

Table 4.1: Summary of the different implementations used to evolved the initial conditions of the Santa Barbara galaxy cluster test. We run half with artificial conductivity, half of them without conductivity and vary the minimum level of resistivity applied.

4.1. The density, temperature and velocity dispersion radial profiles of the simulated clusters demonstrate the impact of the artificial conductivity scheme. Those with artificial conductivity have a lower density core and higher central temperature in comparison to those without artificial conductivity. The figure shows that the choice of minimum applied resistivity has negligible impact on the hydrodynamic parameters of the cluster. This is expected, as the magnetic energy density is orders of magnitude smaller than the kinetic energy and so it, and any numerical scheme associated with it, should have negligible impact on the overall cluster formation. The radial profiles of the hydrodynamic properties of the clusters with artificial conductivity show good agreement with the results of other SPH implementations and those of the grid codes (Frenk et al. 1999), with the central gas density peaking at $2 \times 10^{14}\,{\rm M}_{\odot}\,{\rm Mpc}^{-3}$ and the central temperature of $10^{8}\,{\rm K}$.

The magnetic parameters of the clusters at $z = 0.0$ are shown in Fig. 4.2. The magnetic field amplitude as a function of radius is shown in the top panel. It can be seen that the final amplitude of the magnetic field is dependent on the level of minimum artificial resistivity enforced on the simulation. Clusters with an increased minimum resistivity show a lower final field amplitude throughout the cluster volume and the difference between enforcing $\alpha^{B}_{\rm min} = 0.0$ and $\alpha^{B}_{\rm min} = 0.05$ on the central field amplitude is approximately four orders of magnitude. This strong dependence on the minimum level of resistivity was

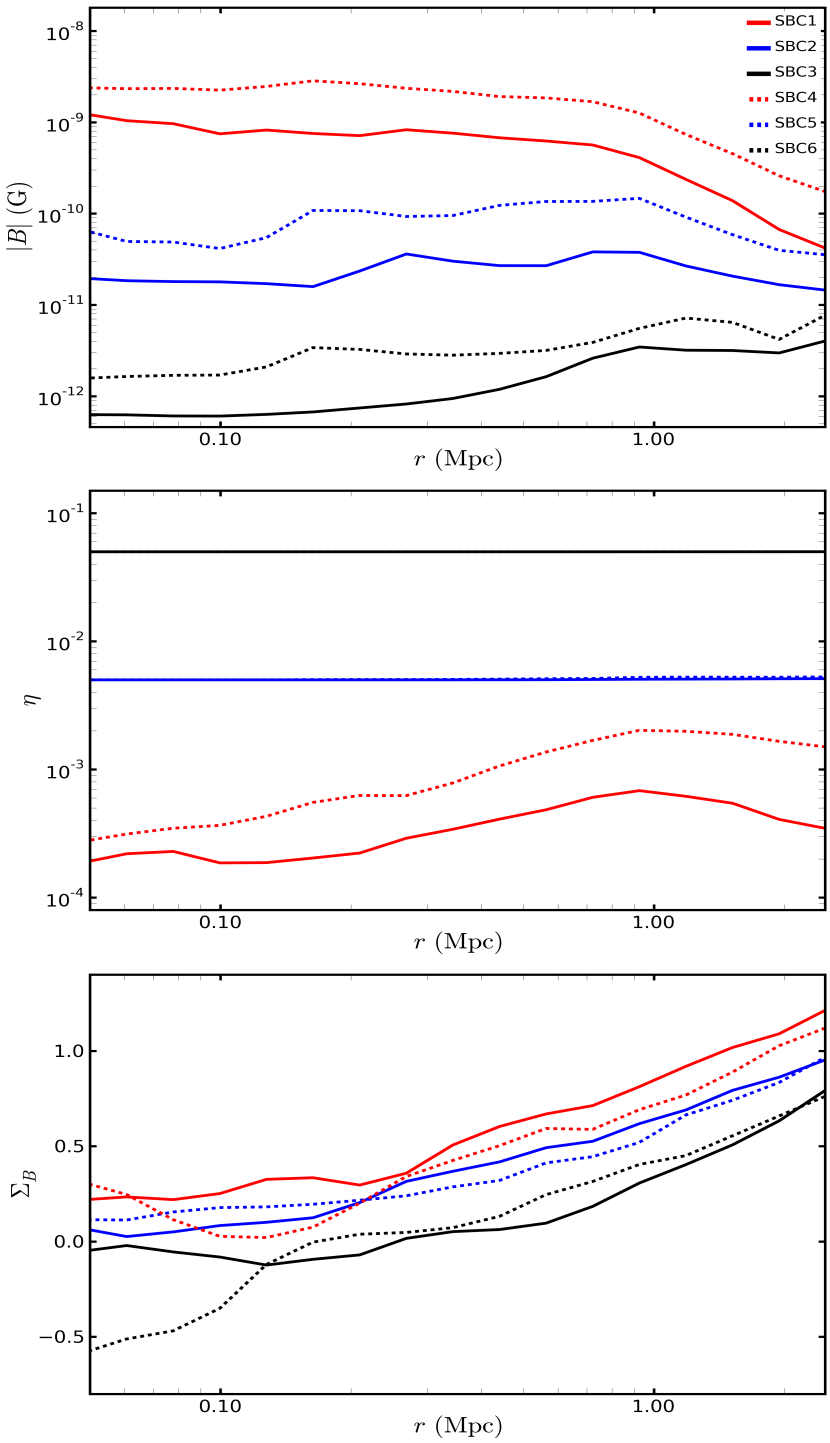

Fig. 4.2: Magnetic field amplitude (top panel), applied resistivity (center panel) and divergence error (bottom panel) radial profiles for the Santa Barbara galaxy cluster simulation. The strength of the minimum applied resistivity has a significant impact on the amplitude of the magnetic field at $z = 0.0$. (We note that the resistivity is in simulation units).

also found in the simulations of Dolag and Stasyszyn (2009). The higher density and less smoothed density and velocity profiles of the clusters simulated without artificial conductivity result in a stronger magnetic field in comparison to the cluster with artificial conductivity and the same minimum resistivity. Although none of the simulations reach the observed micro-Gauss amplitude, due to the limited resolution of the simulations, those with no minimum applied resistivity produce a magnetic field profile in agreement with the profiles observed using RM measurements (Bonafede et al. 2010; Feretti et al. 2012).

The middle panel of Fig. 4.2 shows the average resistivity applied, in simulation units, throughout the cluster volume as a function of radius. The clusters simulated without a minimum resistivity, i.e. $\alpha^B_{\rm min} = 0.0$, produce a resistivity value, averaged over the entire cluster volume, of $\alpha^B = 9.3 \times 10^{-4}$ and $\alpha^B = 3.4 \times 10^{-4}$, without and with conductivity respectively. The impact of accretion on the applied resistivity can be seen at $r \geq 1\,{\rm Mpc}$, where the resistivity increases due to the infall of material. Those simulations which enforce a minimum level of applied resistivity show negligible variation over the cluster volume, demonstrating that they are too strong for cosmological simulations. Due to the critical choice of $\alpha^B_{\rm min}$ for the performance of the PM05 switch in cosmological simulations, we set the fiducial value to $\alpha^B_{\rm min} = 0.0$ and all results presented in this thesis use this value unless otherwise stated.

The divergence error, Σ_B, radial profile is shown in the bottom panel of Fig. 4.2. Although the initial magnetic field was divergence free, the integration of the MHD equations has led to the build up of numerical divergence over the course of the simulations. Those simulations with an enforced minimum level of resistivity show a slight decrease in the divergence error, but the effect is small. Therefore, the application of artificial resistivity does reduce the divergence error, but the error is as large as the amplitude of the magnetic field.

Fig. 4.3 shows the Fourier power spectrum of B_x, B_y, and B_z for a cubic box of length $2R_{\rm vir}$ centred on the galaxy cluster in simulation SBC1 at $z = 0.0$. Despite the initial seed magnetic field being oriented entirely in the x-direction, there is similar power at all scales for all three coordinate directions of the

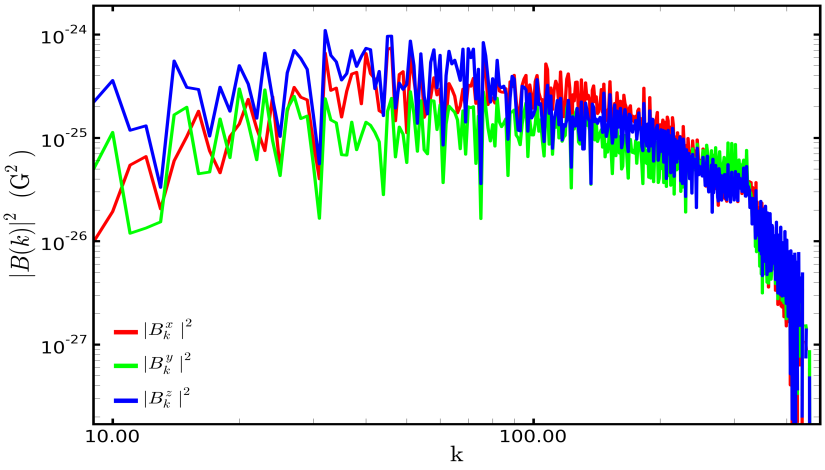

Fig. 4.3: Power spectrum of the x, y and z magnetic field components for the Santa Barbara galaxy cluster simulation, where the scale is normalized by the virial radius. Although initially orientated only in the x-direction, by the final redshift there is equal power at all scales in all three magnetic field components. Hence, the cluster magnetic field at $z = 0.0$ is independent of the initial spectral properties.

cluster magnetic field at the final redshift. The mixing and turbulence induced by merging events and the accretion of gas during the formation of the cluster redistributes the initial seed field, hence the final magnetic field loses the memory of the initial spectral properties of the seed magnetic field. The Santa Barbara cluster simulation demonstrates that our code can capture the dynamics of structure formation. However, to examine in greater detail how the formation history and mass of a galaxy cluster influences the evolution of a seed magnetic field, we must generate more complex initial conditions.

4.2 Generating Initial Conditions

The Santa Barbara cluster simulation is an idealized, low resolution test simulation of the formation of a galaxy cluster. To more accurately model how a seed field evolves due to the formation of structure, we require higher resolution simulations that produce galaxy clusters with a range of masses and formation histories. For the generation of the initial conditions we assume a flat ΛCDM cosmological model. The parameters of this model were taken from the WMAP five year data release, such that $H_0 = 72\,\mathrm{kms}^{-1}\mathrm{Mpc}^{-1}$,

Simulation	$M_{\rm vir}$ ($\times 10^{14}\,{\rm M}_{\odot}$)	$R_{\rm vir}$ (Mpc)	T ($\times 10^{7}\,{\rm K}$)	Last Significant Merger (z)
GC01	4.41	1.98	3.08	1.29
GC02	7.16	2.32	3.46	1.07
GC03	3.62	1.85	2.63	0.57
GC04	8.22	2.43	4.29	0.78
GC05	1.03	1.22	1.01	0.89
GC06	5.64	2.14	3.05	0.14
GC07	8.46	2.46	4.28	0.20
GC08	18.70	3.20	5.45	0.96
GC09	7.56	2.36	4.00	1.26
GC10	1.51	1.44	1.26	1.41

Table 4.2: Virial mass, virial radius, average temperature and the redshift of the last major merging event for the galaxy clusters that form in simulations GC01-10.

$\Omega_m = 0.26$, $\Omega_b = 0.044$, $\sigma_8 = 0.8$ and $n_s = 0.96$ (Komatsu et al. 2009). Using the GRAFIC2 code (Bertschinger 2001), we set up ten spherical cosmological volumes of comoving radius 200 Mpc with 64 DM particles evenly spaced over this radius at a redshift of $z = 30$. Each volume has white noise density perturbations applied to it, which will collapse to form structure.

The initial setup was evolved to $z = 0.0$ and the largest DM halo within a radius 75 Mpc from the centre of the box was selected using a *friend-of-friend* algorithm and its virial radius, $R_{\rm vir}$, calculated. Each DM particle that fell within $8 \times R_{\rm vir}$ of the centre of mass of the identified halo was then replaced at $z = 30$ by 64 DM particles. These particles had the same total volume as the initial particle's volume and their masses summed to the mass of the initial particle, ensuring that the same density was achieved. Additional higher frequency perturbations, drawn from the same white noise, were then added to the power spectrum in this region. As the region is sampled with an increased number of particles, the simulation has a greater mass and force resolution enabling it to capture the formation of the halo in greater detail. The volume was then resimulated.

At $z = 0.0$, the most massive halo in the higher resolution region was identified. The DM particles that fell within $4 \times R_{\rm vir}$ of the centre of mass of the halo were identified, ensuring that no lower resolution particles were present. These particles were then replaced in the initial conditions by 8 DM particles of lower mass, occupying the same volume, and further higher frequency perturbations were added. At this stage the initial volume of the highest resolution region was iteratively run and lower resolution particles identified and replaced to ensure that the most massive halo was free from lower resolution particles out to at least $2 \times R_{\rm vir}$. This ensures that the halos are free from any spurious forces and heating effects that can occur when a higher mass particle is present. We performed this iterative process for all simulation volumes to produce "zoomed" initial conditions for the formation of ten galaxy clusters.

The highest resolution DM particles each had a mass of $6.20 \times 10^8\,{\rm M}_\odot$ and a smoothing length of $h = 13.5\,{\rm kpc}$. To these initial conditions gas particles were added to the highest resolution region, with the same number gas particles as high resolution DM particles. The gas particles each had a mass of $1.26 \times 10^8\,{\rm M}_\odot$ and a smoothing length of $h = 8.1\,{\rm kpc}$. The gas particles were embedded with a magnetic field of $10^{-11}\,{\rm G}$, orientated in the x-direction only to ensure that it was divergence free. The resulting initial conditions produce ten simulations of the formation of a galaxy cluster. At $z = 0.0$, the clusters have a range of masses and different formation histories and these are summarized in Table 4.2, where a significant merger is defined as one where the mass of the smaller halo is at least a third of the larger halo.

4.3 Reliably Evolving a Seed Magnetic Field

As demonstrated with the Santa Barbara cluster simulation, while our implementation can accurately follow the formation of structures, the choice of numerical scheme can have a significant impact on the evolution of the magnetic field during structure formation. Reliably resolving discontinuities is critical to the amplification of the magnetic field and, therefore, the choice of artificial resistivity switch will affect the evolution of the magnetic field.

SPMHD fails to maintain the solenoidal constraint of the magnetic field and the use of the hyperbolic cleaning scheme to control the build up of numerical divergence of the magnetic field will effect the evolution of the magnetic field from its initial seed to the final field that permeates the large-scale structure.

To examine how our choice of numerical scheme effects the development of the magnetic field we use the initial conditions of simulation GC10. We then evolve these initial conditions to the current epoch at $z = 0.0$ using six different configurations of our code. The first implementation is a 'control' with the artificial resistivity and hyperbolic cleaning schemes turned off. The next three implementations all make use of the artificial resistivity scheme, but not the cleaning scheme. The first of these uses the PM05 switch to control the application of resistivity, 'PM05' implementation, and the second uses the TP13 switch, 'TP13' implementation. The 'constant' implementation uses a constant, fixed low level of artificial resistivity, $\eta = 10^{-3}$, throughout the simulation volume. This has been used by several authors when studying large-scale magnetic fields (Bonafede et al. 2011; Beck et al. 2013). The 'cleaned' implementation uses the hyperbolic cleaning scheme, but turns off the artificial resistivity scheme. Finally, our 'full' implementation uses the hyperbolic cleaning scheme and the artificial resistivity scheme, with the PM05 switch to target the application of the resistivity.

A density slice through the simulated galaxy cluster at $z = 0.0$ can be seen in Fig. 4.4 for all six configurations. Qualitatively, the choice of numerical MHD scheme has a negligible impact on the global dynamical and thermodynamical properties of the cluster. However, the choice of MHD scheme has a significant impact on the properties of the magnetic field permeating the cluster volume, as shown in Fig. 4.5. The amplitude of the magnetic field varies by orders of magnitude between the schemes, peaking at $1\,\mu$G in the centre of the 'control' implementation, which has no resistivity and no cleaning, to less than 10^{-10} G throughout the cluster in the 'TP13' implementation. The majority of the different numerical schemes produce a magnetic field with an amplitude between $10^{-7} - 10^{-9}$ G. Additionally, the choice of numerical scheme affects the topology of the magnetic field. Those simulations without

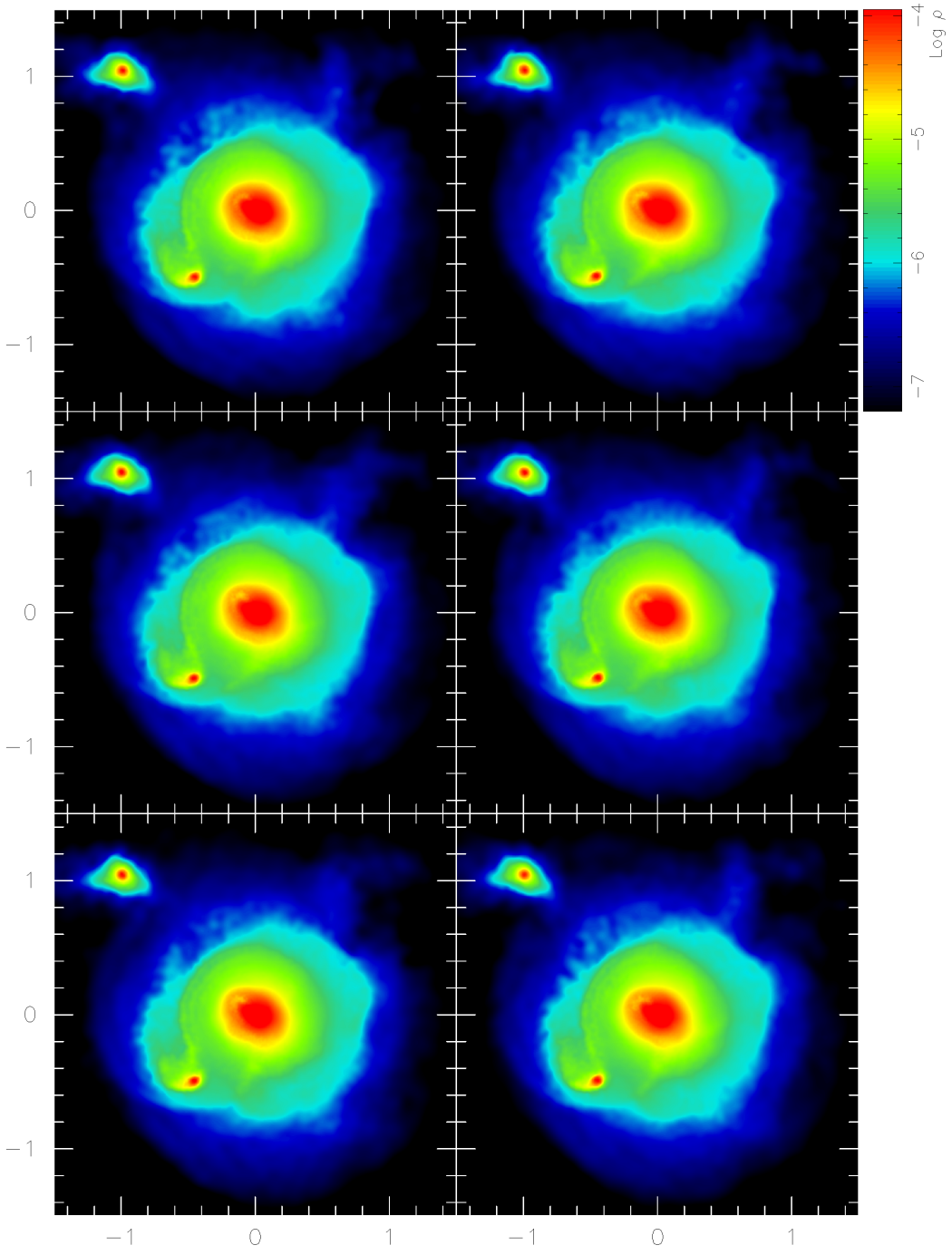

Fig. 4.4: Density slices, $3R_{\rm vir} \times 3R_{\rm vir}$ in size, through the xy plane of the galaxy cluster that forms in simulation GC10 for the 'control' (top left), 'constant' (top right), 'PM05' (center left), 'TP13' (center right), 'cleaned' (bottom left) and 'full' (bottom right) implementations. The global properties of the galaxy cluster are unaffected by the choice of MHD numerical scheme.

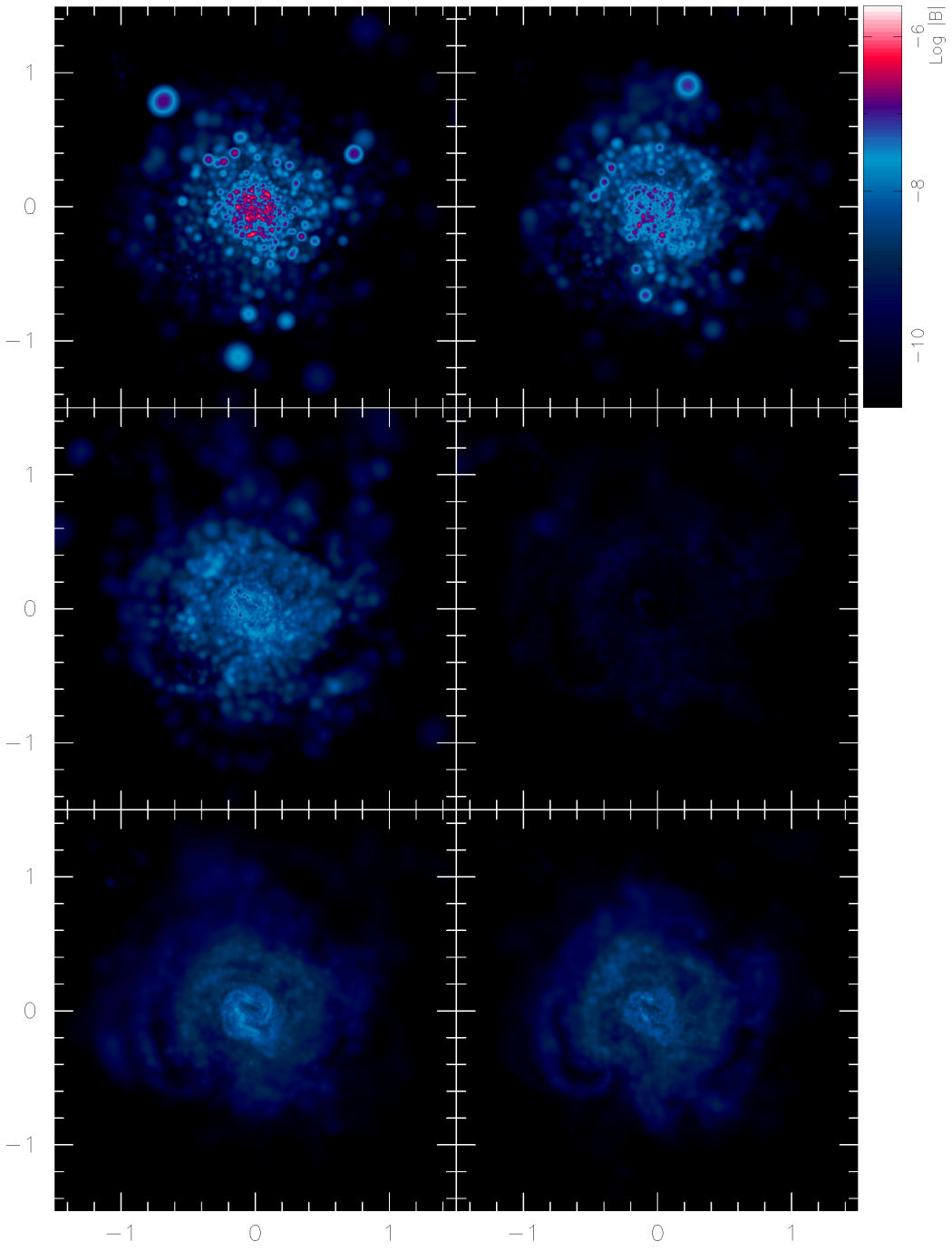

Fig. 4.5: Magnetic field amplitude slices, $3R_{\rm vir} \times 3R_{\rm vir}$ in size, through the xy plane of the galaxy cluster that forms in simulation GC10 for the same implementations as Fig. 4.4. The TP13 resistivity switch applies resistivity too strongly in cosmological simulations. Failure to minimize the violation of the solenoidal condition of the magnetic field leads to a unphysical clumpy patchwork magnetic field distribution.

the hyperbolic cleaning scheme produce a magnetic field that has rapid spatial variations, with regions of high amplitude magnetic field, associated with regions of high divergence error, surrounded by significantly weaker magnetic fields. Those including the cleaning scheme produce a magnetic field that is more gradual in its spatial variations.

To enable a more quantitative comparison of the impact of the different numerical schemes on the magnetic field of the cluster we radially bin the simulated clusters at $z = 0.0$. The radial profile of the magnetic field amplitude is shown in upper panel of Fig. 4.6. Excluding the 'TP13' implementation, all of the simulated clusters have a centrally peaking radial profile that declines steeply with radius, which is in good agreement with the magnetic field radial profiles of observed galaxy clusters (Feretti et al. 2012). The 'TP13' implementation shows a uniform field amplitude throughout the cluster. The inclusion of artificial resistivity, switches to control the application of resistivity and the hyperbolic cleaning lead to significant reductions in the amplitude of the central cluster magnetic field.

The middle panel of Fig. 4.6 shows the radial profile of the applied resistivity for those implementations that use the artificial resistivity scheme. The different switches used to control the application of the resistivity produce similar radial profiles, peaking where material is being accreted at the edge of the cluster and varying by an order of magnitude throughout the cluster volume. In section 4.1 we showed that the amplitude of the magnetic field is very sensitive to the level of applied resistivity, consequently, when following the evolution of a seed magnetic field, it is important to include a switch to target the application of resistivity. A constant level of applied resistivity is either too weak where it is required or too strong where it is not, leading to the incorrect evolution of the seed field. The TP13 resistivity switch applies twice as much resistivity at $z = 0.0$ compared to the PM05 switch, and significantly more at earlier epochs. This increase in applied resistivity leads to the uniform radial field profile and the amplitude of the magnetic field being five orders of magnitude weaker than the observed μG magnetic field amplitude (Carilli and Taylor 2002). Therefore, the TP13 resistivity switch applies too

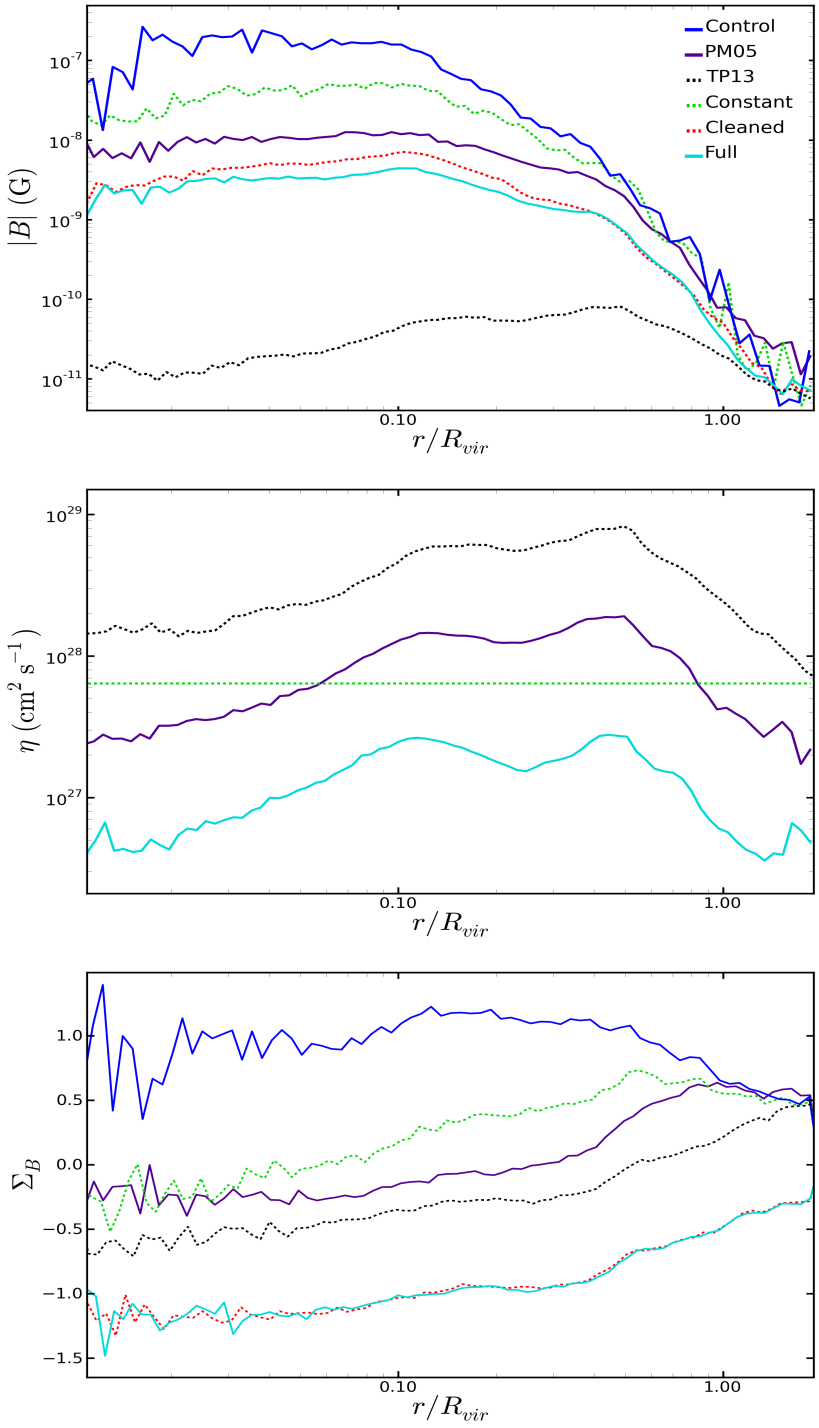

Fig. 4.6: Magnetic field amplitude (top panel), applied resistivity (center panel) and divergence error (bottom panel) radial profiles of the simulated galaxy cluster GC10 for the six different implementations. The magnetic field amplitude is very sensitive to the numerical scheme and the hyperbolic cleaning scheme produces an order of magnitude reduction in the divergence error.

much resistivity and is not appropriate for cosmological simulations.

The divergence error radial profiles of the simulated clusters are shown in the bottom panel of Fig. 4.6. The numerical divergence of the magnetic field is ten times the magnitude of the magnetic field amplitude in the 'control' implementation. The inclusion of resistivity, targeted or not, reduces the build up of divergent magnetic field and its magnitude is approximately equal to the magnetic field amplitude. However, the inclusion of the hyperbolic cleaning scheme significantly suppresses the build up of numerical divergence. This results in the magnitude of the numerical divergence of the magnetic field being on a few percent of the physical magnetic field throughout the simulated cluster volume.

The importance of suppressing the violation of the solenoidal condition can be seen by comparing simulations with and without the hyperbolic cleaning scheme. The only difference between the 'control' implementation and the 'cleaned' implementation is the inclusion of the cleaning scheme. However, the 'control' implementation produces a central magnetic field amplitude of 1×10^{-7} G, but the 'cleaned' implementation produces a central magnetic field amplitude of 2×10^{-9} G. Therefore, the significantly larger numerical divergence of the magnetic field of the 'control' implementation produces approximately a two order of magnitude increase in the central magnetic field amplitude of the cluster. Comparison of the 'PM05' implementation and the 'full' implementation shows that the inclusion of the hyperbolic cleaning scheme leads to an order of magnitude reduction in the level of applied resistivity. Using equation 2.73, this demonstrates that the divergence of the magnetic field, which is an artefact of the chosen numerical scheme, is driving the application of the resistivity. The final magnetic field amplitude and profile is very sensitive to the level of applied resistivity. Therefore, to accurately follow the evolution of a seed magnetic field due to the formation of structure it is critical to minimize the violation of the solenoidal constraint and this is currently best achieved in SPMHD by the inclusion of a hyperbolic cleaning scheme.

4.3.1 Magnetic Field Evolution with Redshift

To examine how the different numerical implementations produce very different magnetic field amplitudes in the final cluster volume we trace the evolution of the magnetic field with redshift for all of our implementations. To follow the evolution of the magnetic field we track the most massive proto-cluster halo back to $z = 3.0$. At each snapshot that the simulation produces we calculate the virial mass of the halo, the magnetic energy density per unit volume of the halo and the average divergence error of the particles that fall inside the virial radius of the cluster. These three values are plotted as a function of $\log_{10}(1 + z)$ in Fig. 4.7.

The virial mass of the clusters show that, in addition to steadily accreting mass from $z = 3.0$ to $z = 0.0$, the cluster undergoes several mergers during its formation, at 0.58 ($z = 2.80$), 0.41 ($z = 2.58$) and a smaller merging event at 0.21 ($z = 0.62$). At late times, $z < 0.5$, the cluster accretes several small objects. Although these merger events do lead to jumps in the magnetic energy per unit volume of the cluster, they are features in the trend of increasing magnetic energy with time, or decreasing redshift, and they are not the dominant amplification mechanism during the evolution of the magnetic field with time. However, the merging events and accretion of smaller objects will induce turbulence and mixing in the cluster volume. These motions are the dominant cause of the magnetic field amplification and so the formation of structure provides the energy for the dynamo mechanism.

There is a direct correlation between the average divergence error of the particles inside the cluster and the gradient of the increasing magnetic energy density with time. From equation (1.27), it is clear that if $\nabla \cdot \mathbf{B} \neq 0$ an additional term should be present in the induction equation. With this additional term the change in the magnetic field with time is now dependent on both the physical magnetic field and the numerical divergence of the magnetic field, which is unphysical. Hence, the amplification of magnetic field, and the final field amplitude, is dependent on the physical field and the unphysical divergence of the field. Therefore, to obtain the true evolution of a seed magnetic field due to the formation of structure any violation of the solenoidal

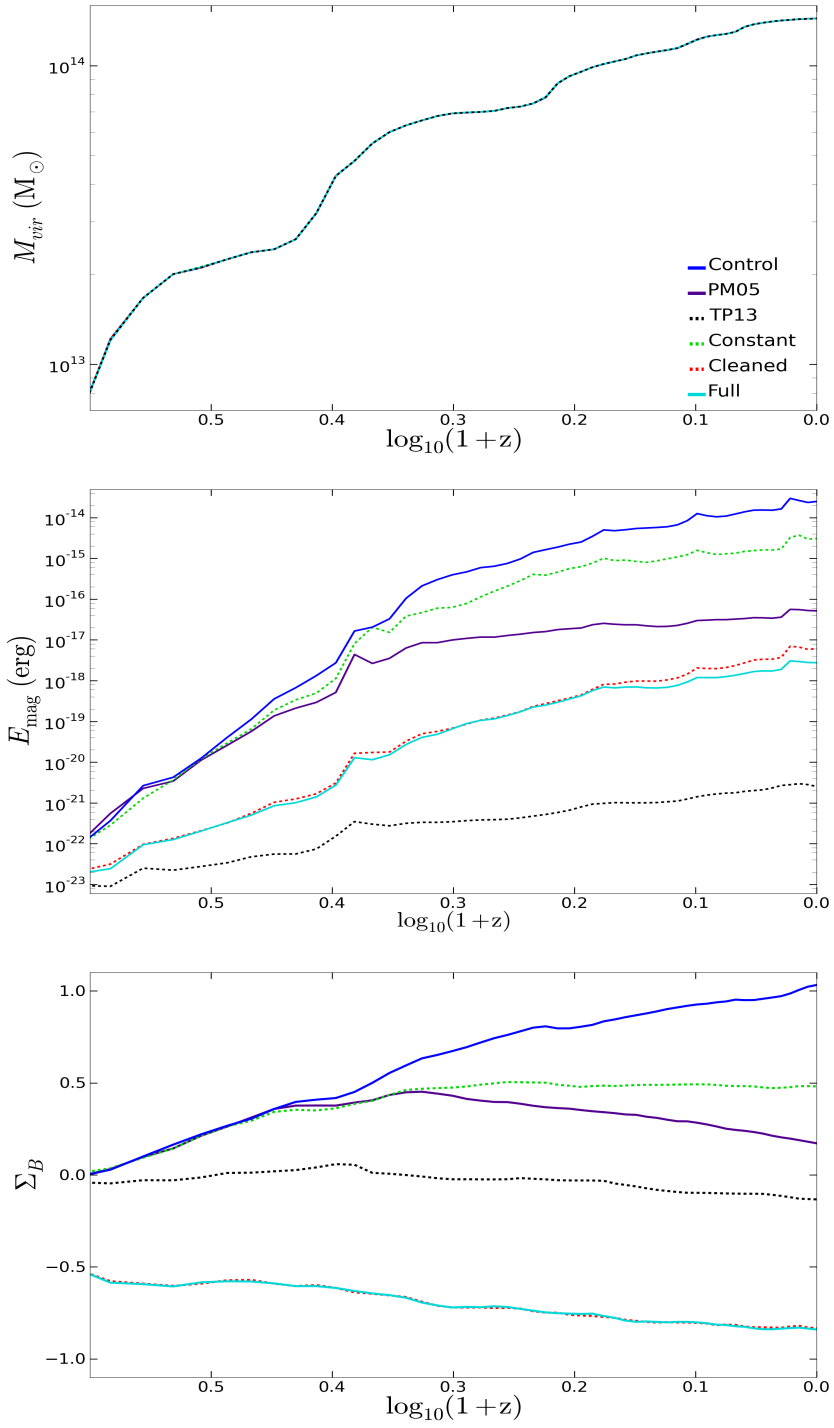

Fig. 4.7: The evolution of the virial mass (top panel), total magnetic energy (center panel) and average divergence error (bottom panel) of the cluster with redshift. Those clusters without the hyperbolic cleaning scheme show an increased slope of magnetic energy growth as there is significantly more unphysical field amplification, along with amplification of the physical magnetic field, throughout the growth of the cluster.

constraint must be minimized. Therefore, to obtain a more correct amplitude for a seed field amplified by the formation of structure any violation of the solenoidal constraint must be minimized.

To investigate the impact of the formation history of the cluster and the final cluster mass on the evolution of the seed magnetic field, our numerical scheme uses the PM05 resistivity switch to resolve discontinuities in the magnetic field and the hyperbolic cleaning scheme to minimize the violation of the solenoidal condition of the magnetic field.

4.4 The impact of Cluster Mass & Formation History

To investigate the impact of the formation history of the cluster and the mass of the cluster on the evolution of a seed magnetic field we used GCMHD+, with the PM05 resistivity switch and hyperbolic cleaning scheme, to evolve the ten zoomed initial conditions, produced using the GRAFIC2 code (see section 4.2), from $z = 30.0$ to $z = 0.0$. Each of the initial conditions has different random density perturbations added to it so that each cluster that forms has a different formation history and a different mass at $z = 0.0$. Fig. 4.8 shows the magnetic field amplitude, the level of applied resistivity and the divergence error as a function of radius at $z = 0.0$ for all ten clusters. To enable a comparison between the clusters, the radius has been normalized by the virial radius of each cluster.

The magnetic field amplitude and radial profiles are similar for all ten simulated galaxy clusters. They have a cored radial profile that peaks in amplitude between $(0.3 - 1) \times 10^{-8}$ G. There is a peak in the simulated cluster GC08 at $r/R_{\rm vir} > 1.00$ as this cluster is about to undergo a major merging event with an object that is half the virial mass of the cluster and the magnetic field of this object is significantly altering its outer radial profile. All ten simulated clusters show a similar radial profile for the average level of resistivity as a function of radius. We convert the applied resistivity to physical units to allow comparison with other work, such as Bonafede et al. (2011). They show a fairly flat resistivity strength that peaks slightly just before the virial radius and drops off rapidly outside the cluster volume. Although our scheme

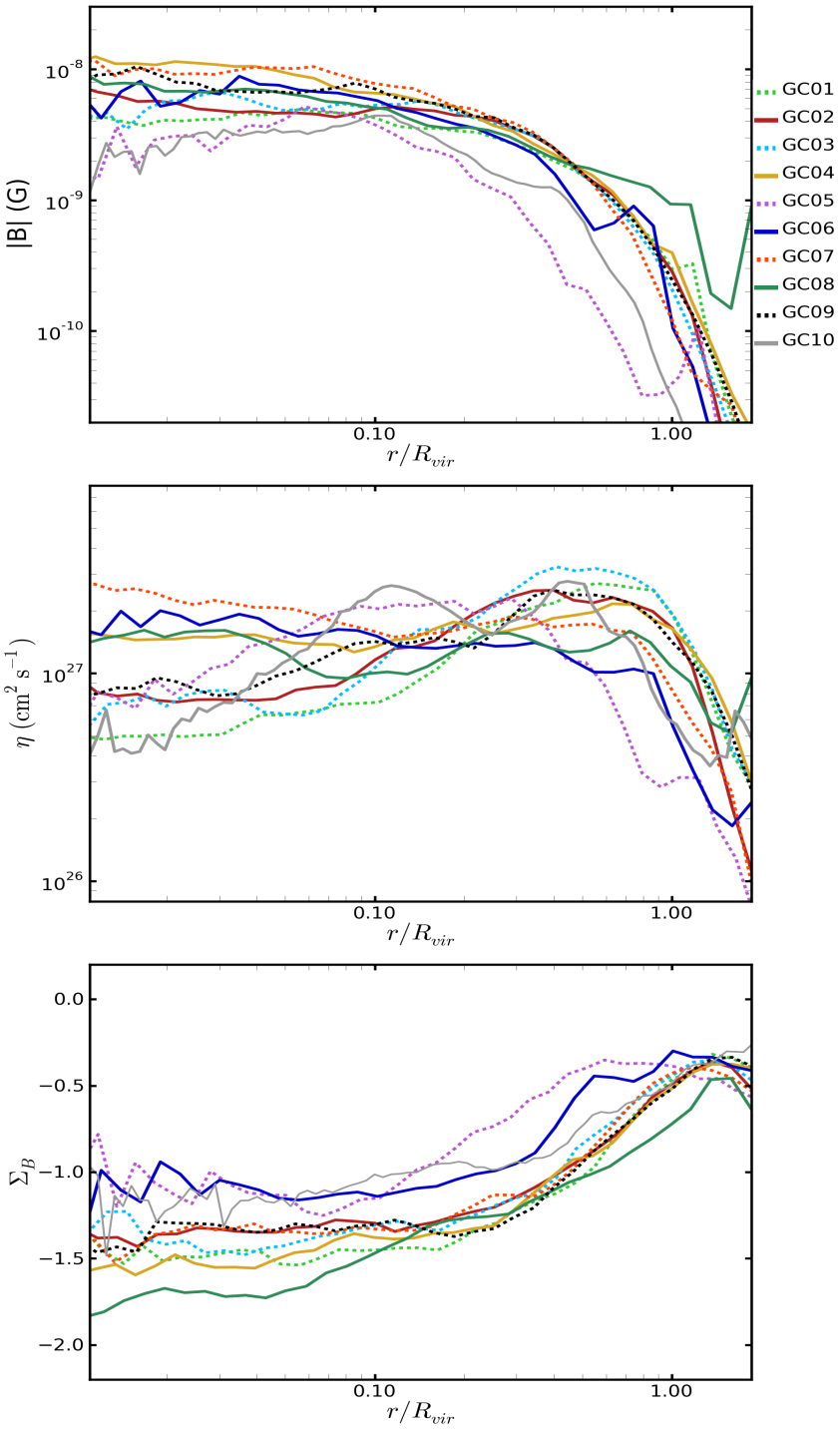

Fig. 4.8: Magnetic field amplitude (top panel), applied resistivity (center panel) and divergence error (bottom panel) radial profiles for simulated galaxy clusters GC01-GC10. Regardless of viral mass or formation history of the cluster all simulations produce a magnetic field of $(0.3 - 1.0) \times 10^{-8}$ G. The hyperbolic cleaning scheme and artificial resistivity scheme combine to keep the divergence error below 10% throughout the majority of the cluster volumes.

is not physically motivated, it is interesting that the strength of the applied resistivity shows good agreement with the turbulent resistivity value derived by Bonafede et al. (2011). All of the simulated clusters show a similar divergence error radial profile. The cleaning scheme keeps the average divergence error below 10% throughout the central region of the cluster and the average error increases in the outskirts of the cluster volume.

There is no discernible trend with either final cluster mass or the formation history of the cluster. Clusters GC07 and GC09 have a similar mass, but very different formation histories. Cluster GC09 undergoes one major merging event at $z = 1.15$ during its formation, slowly accreting matter instead, and cluster GC07 undergoes four significant merging events, the last of which occurred at $z = 0.67$. However, their final magnetic field amplitudes and radial profiles are very similar. The clusters range in mass by more than an order of magnitude, but the central amplitude of the magnetic field shows a very weak trend with mass. The magnetic fields of many clusters peak at 10^{-8} G, and these clusters are not the most massive.

The observations of the magnetic fields that inhabit the ICM of galaxy clusters show typical magnetic field amplitudes of $1-10\,\mu$G (Carilli and Taylor 2002). Our simulated galaxy clusters, independent of mass and merger history, produce magnetic fields with an amplitude of $(0.3 - 1) \times 10^{-8}$ G. This discrepancy occurs because of the resolution of our simulations. Galaxy clusters are turbulent due to their formation and X-ray observations of the Coma cluster have shown scale-invariant pressure fluctuations down to approximately 20 kpc (Schuecker et al. 2004), below which there were insufficient photons to produce a reliable measurement. Rotation measure observations of the Coma cluster have shown a minimum length scale of 2 kpc (Bonafede et al. 2010). Our simulations have a smoothing length of 8 kpc and fluctuations in the fluid quantities approaching this length scale or smaller are smoothed out and lost.

Fig. 4.9 shows the local velocity and magnetic energy density power spectrums of a cubic volume, with a length equal to the virial radius, for all ten simulated galaxy clusters. To allow a comparison between the clusters the virial radii have been normalized to unity. To obtain a measure of the local

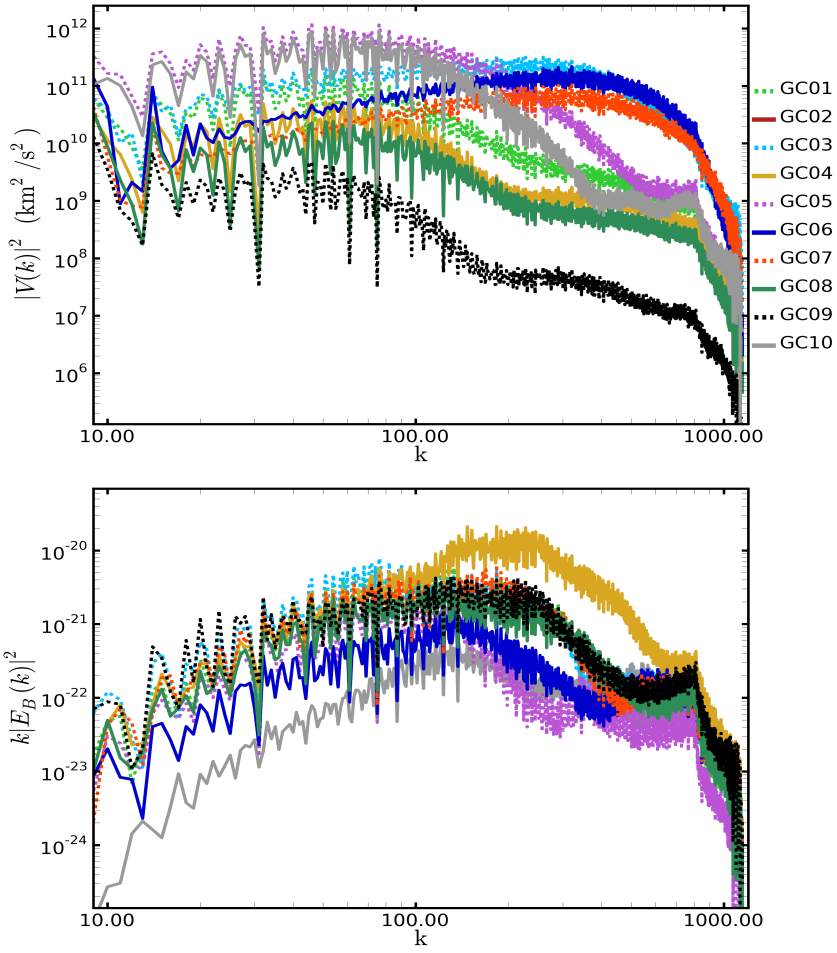

Fig. 4.9: Power spectrums of the local velocity (top panel) and magnetic energy density (bottom panel) for the clusters that form in simulations GC01-GC10, where the scale is normalized by the virial radius of the cluster. Those clusters that have not recently undergone a merging event show a broken power law velocity spectrum that cuts off at the resolution scale of the simulations. The magnetic energy also cuts off at the resolution scale of the simulations.

velocity of the particles, with respect to the bulk velocity cluster, we first smoothed the particle to a regular grid and found the average velocity. We then found the particles local velocity via $\delta \mathbf{v}_i \simeq (\mathbf{v}_i - \mathbf{v}_{\rm cell})^2$. The majority of the simulated clusters show a broken power law local velocity spectrums, indicating that, once sufficiently inside the cluster volume, scale-free turbulent motions dominate before the resolution limit of the simulations causes a cut-off. However, some clusters, such as GC03, GC06 and GC07, do not show this power law, but these clusters have recently undergone a merging

event that has disturbed the local velocity distributions. The magnetic energy spectrum shows a broken power law distribution at small scales. At the resolution limit of the simulations all of the galaxy clusters show cut-off and beyond it the power drops very rapidly. This cut-off at small scales is a result of the smoothing out of fluctuations on scales below the resolution limit of the simulations. The smoothing out of small velocity fluctuations limits the amplification of the magnetic field. The induction equation demonstrates that the motion of the fluid amplifies the magnetic field and the smaller turbulent motions fluctuate more rapidly. Therefore, the small-scale motions produce more amplification of the magnetic field compared to the large-scale motions. To reproduce the observed magnetic field amplitude in the ICM of galaxy clusters will require simulations of higher resolution.

4.5 Higher Resolution Galaxy Cluster

The resolution limit of the simulations leads to the smoothing out of small-scale velocity structures that would otherwise lead to additional amplification of the seed magnetic field during the formation of structure. To produce a higher resolution simulation we started with the GC10 initial conditions. At the second stage of refinement we replaced every DM particle that fell within $4 \times R_{\rm vir}$ with 64 lower mass particles, as opposed to 8 previously, occupying the same volume at the initial redshift of the simulation. Gas particles were added to the highest resolution region, with the same number gas particles as high resolution DM particles. This simulation contained 9.5×10^6 gas particles, each with a mass of $1.57 \times 10^7\,{\rm M}_\odot$ and a smoothing length of $h = 3.9\,{\rm kpc}$. The highest resolution DM particles had a mass of $7.8 \times 10^7\,{\rm M}_\odot$ and a smoothing length of $h = 6.8\,{\rm kpc}$.

The gas particles were embedded with an initially homogeneous magnetic field, which had an amplitude of $10^{-11}\,{\rm G}$. The field was orientated entirely in the x-direction to ensure that it was divergence free. We labeled this simulation HR10.

We evolved these initial conditions to the current epoch using GCMHD+ and a $1.51 \times 10^{14}\,{\rm M}_\odot$ galaxy cluster forms. Two implementations were used, the

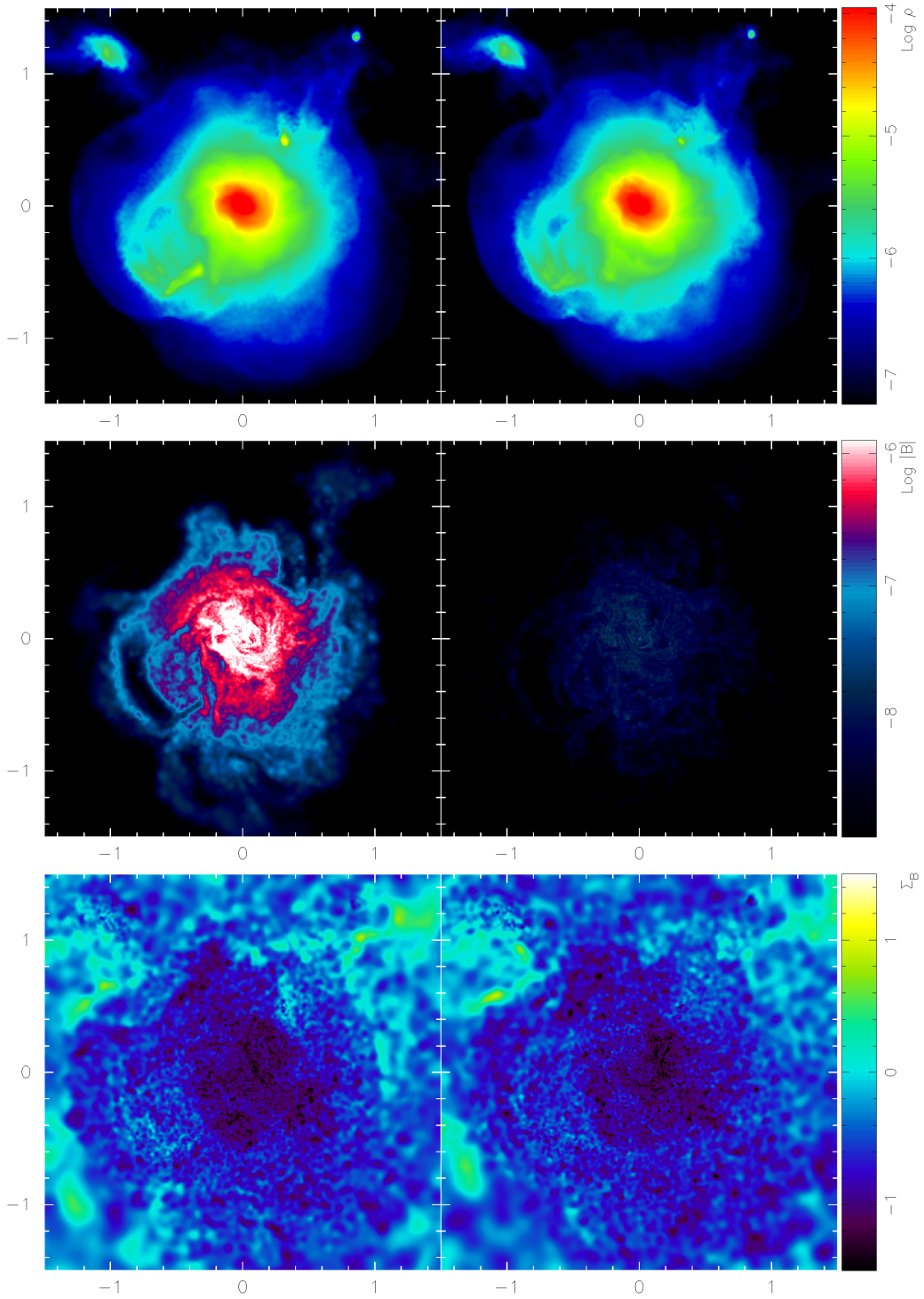

Fig. 4.10: Density (top row), magnetic field amplitude (central row) and divergence error (bottom row) slices, $3R_{\rm vir} \times 3R_{\rm vir}$ in size, through the xy plane of the galaxy cluster that forms in simulation HR10 for the 'cleaned' (left column) and 'full' (right column) implementations. At higher resolution the PM05 resistivity switch applies resistivity too strongly, leading to a suppression of the magnetic field amplitude.

'cleaned' implementation, including the hyperbolic divergence cleaning scheme and without resistivity, and the 'full' implementation, including both the cleaning scheme and the artificial resistivity scheme with the PM05 switch. Density, magnetic field amplitude and divergence error slices through the centre of both simulated clusters are shown in Fig. 4.10. The density slice demonstrates that the magnetic field, and associated numerical schemes, have negligible impact on the global properties of the cluster.

The hyperbolic cleaning scheme controls the divergence error so that the magnitude of the numerical divergence of the magnetic field is maintained at a few percent of the total amplitude of the magnetic field throughout the cluster volume. By minimizing the divergence error a more reliable amplification of the initial seed field is obtained. The amplitude of the magnetic field is significantly different between the two numerical implementations and the only difference between them is use of the artificial resistivity scheme. The 'cleaned' implementation produces a cluster with a central magnetic field amplitude of $1.5\,\mu$G, while the 'full' implementation produces a cluster with a central magnetic field amplitude of $0.016\,\mu$G. This is a significant difference from the lower resolution simulations where these two schemes produced similar values for the central amplitude of the magnetic field. As shown in equation 2.67 in section 2.5.4, the resistivity scheme works via the difference in total magnetic field at particle i and particle j. At this higher resolution, smaller scale fluctuations in the fluid quantities, such as the velocity and the magnetic field, are resolved and these fluctuations in the magnetic field cause the artificial resistivity scheme to increase the level of applied resistivity on average throughout the cluster volume.

Fig. 4.11 shows the radially averaged applied resistivity in the galaxy cluster for simulations HR10 and GC10 run with the 'full' implementation. The increase in resolution leads to an order of magnitude increase in the level of applied resistivity throughout the cluster volume. This increase in applied resistivity leads to a significant decrease in the amplitude of the magnetic field inhabiting the ICM. Therefore, we find that neither the PM05 nor the TP13 resistivity switches are suitable for MHD cosmological simulations of structure

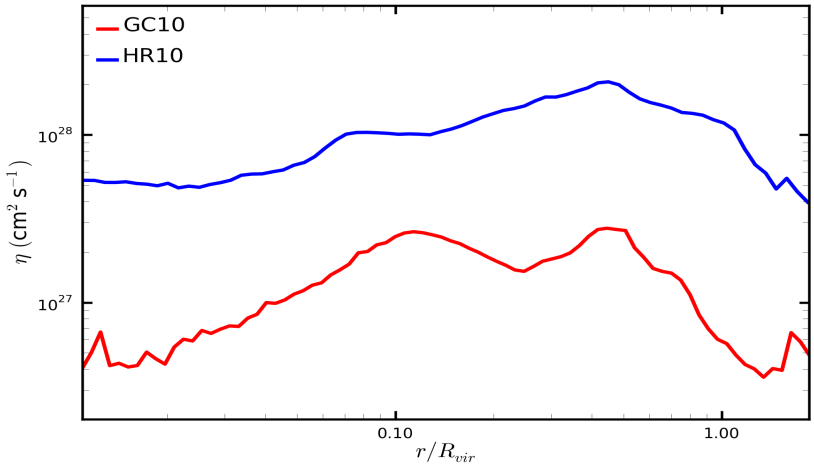

Fig. 4.11: Applied resistivity radial profiles for simulations GC10 and HR10 run using the 'full' implementation. The increase in resolution leads to an order of magnitude increase in the level of applied resistivity.

formation as they apply resistivity too strongly and this results in a significant decrease of the amplitude of the magnetic field.

In simulations of this kind it can be argued that an artificial resistivity scheme is not required. The resistive timescale of a galaxy cluster is significantly greater than the age of the Universe and so physically it can be neglected. Resistivity is artificially included in the simulations to ensure that any discontinuity in the magnetic field is smoothed out and sufficiently resolved. However, the initial seed magnetic field is free of discontinuities and there are no sources or sinks of magnetic field during the evolution of the initial set up. Due to the magnetic field being frozen into the fluid, any discontinuities that arise in the magnetic field must be associated with discontinuities in other fluid quantities, such as density. These discontinuities will be smoothed out and resolved by other schemes, such as artificial viscosity. Therefore, artificial resistivity is not required in these simulations.

The higher resolution simulation, run with the 'cleaned' implementation, shows that a primordial seed magnetic field is capable of reproducing the μG amplitude magnetic fields observed to fill the ICM of galaxy clusters. Fig. 4.12 shows the magnetic field amplitude and divergence error radial profiles of the higher resolution run. The magnetic field profile of the 'cleaned'

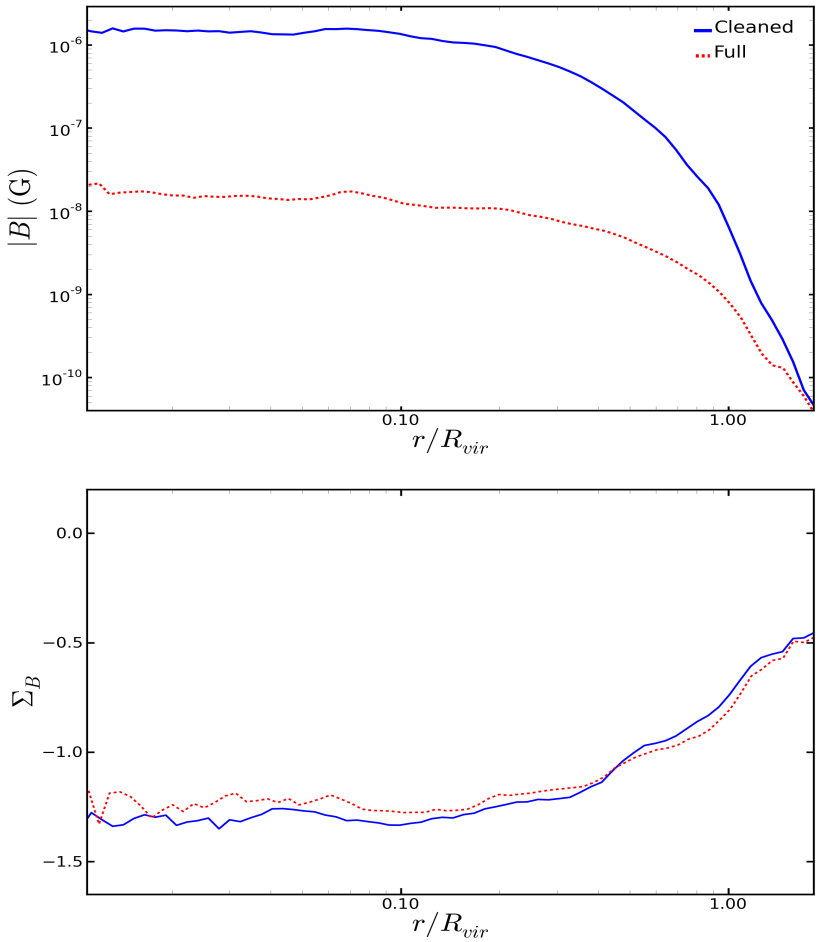

Fig. 4.12: Magnetic field amplitude (top panel) and divergence error (bottom panel) radial profiles for the higher resolution HR10 cluster simulation run with the 'cleaned' (blue solid) and 'full' (red dashed) implementations. The applied resistivity is too strong reducing the central magnetic field amplitude.

implementation shows good agreement with the radial profiles observed in galaxy clusters (Bonafede et al. 2010; Feretti et al. 2012). The divergence error profile shows that the numerical divergence of the magnetic field is kept to a few percent of the amplitude of the magnetic field throughout the cluster volume. In addition to the amplitude and profile of the magnetic field, there are a number of additional observable quantities that can be produced from the simulations and compared to observations of galaxy clusters.

4.6 Comparing with the Observations

Early X-ray observations showed that galaxy clusters were associated with spatially extended X-ray sources. The interpretation of these observations is that the ICM is filled with very hot, but low-density gas. The gravitational collapse of primordial material to form the structure of the Universe converts gravitational energy into kinetic energy, which is converted to thermal energy mainly by shocks. This collapse heats the gas of the ICM to $10^7 - 10^8\,\mathrm{K}$ (Kravtsov and Borgani 2012). At these temperatures the primary cooling mechanism of the free electrons in the ICM is thermal bremsstrahlung, which occurs when free electrons collide with ions. Due to their temperature, cooling via thermal bremsstrahlung results in the emission of X-ray photons.

The extended X-ray emission from galaxy clusters, which is observable, can be calculated for simulated galaxy clusters. Assuming that the dominant emission mechanism is thermal bremsstrahlung and the cluster has a metallicity of zero, the thermal X-ray intensity along our line of sight, l, through the simulated cluster volume is given in c.g.s gaussian units by

$$I_X = 1.4 \times 10^{-27} \int n_e^2 T_e^{1/2} dl \,, \tag{4.1}$$

where n_e is the electron number density and T_e is the electron temperature in K. Hence, the X-ray flux of the cluster is given by $F_X = \pi I_X$. To ensure that only fully ionized particles contribute to the X-ray flux, we include only particles whose temperature is higher than $5 \times 10^5\,\mathrm{K}$.

Observations of galaxy cluster at radio wavelengths show that they have diffuse emission that is not associated with any individual source (Carilli and Taylor 2002). Due to its spectral index, this radio emission is interpreted to be synchrotron emission from relativistic electrons. The extended nature of the emission, and assuming the minimum energy condition, shows that the ICM must be filled with micro-gauss magnetic fields. Under the assumption that the energy density of the relativistic electron is a power law distribution, the total synchrotron power, P, emitted at a frequency, ω, can be calculated for the simulated cluster via

$$P(\omega) = \frac{\sqrt{3} e^3 C B_\perp}{2\pi m_\mathrm{e} c^2 (p+1)} \Gamma\left(\frac{p}{4} + \frac{19}{12}\right) \Gamma\left(\frac{p}{4} - \frac{1}{12}\right) \left(\frac{m_\mathrm{e} c \omega}{3 e B_\perp}\right)^{-\frac{(p-1)}{2}} \,, \tag{4.2}$$

where e is the electron charge, $m_{\rm e}$ is the mass of the electron, c is the speed of light, $B_{\perp}$ is the magnetic field perpendicular to the line of sight and Γ is the gamma function (Rybicki and Lightman 1979). We calculate all of the parameters in cgs units. Under the assumption that the electrons are freshly accelerated, the spectral index of their power law distribution is $p = 2.2$. We calculate the synchrotron power of each particle at a frequency of $\omega = 1.4 \times 10^9\,\mathrm{Hz}$. The power emitted is normalized by C, which is dependent on the energy density of the relativistic electron. However, the simulations provide no information about the distribution of non-thermal particle species, such as relativistic electrons. Therefore, to calculate the synchrotron power emitted by the simulated galaxy cluster we must make an assumption about the energy distribution of the relativistic electrons.

The number density of relativistic electrons, $n_{\rm e}$, can be approximated by a power law

$$n_{\rm e}(E)dE = CE^{-p}dE = Cm_{\rm E}c^2\gamma^{-p}dE\,, \tag{4.3}$$

where $\gamma = (1 - \mathbf{v}_{\rm e}^2/c^2)^{-1/2}$ is the Lorentz factor and $\mathbf{v}_{\rm e}$ is the velocity of the electrons. Assuming this power law form for the number density, the energy density of the relativistic electrons can be calculated via

$$\varepsilon_{\rm re} = \int_1^{\infty} C(\gamma - 1)m_{\rm e}c^2\gamma^{-p}d\gamma\,, \tag{4.4}$$

where $\varepsilon_{\rm re}$ is the energy density of the relativistic electrons. Integrating this equation we come to a solution for the normalization constant, C, of equation (4.2) of the form

$$C = \frac{0.24 \times \varepsilon_{\rm re}}{m_{\rm e}c^2}\,. \tag{4.5}$$

Therefore, the assumption about the energy density of the relativistic electrons is critical to the strength of the radio emission from the simulated galaxy cluster. The observed similarities between the extended X-ray and radio emission of galaxy clusters show that the thermal and relativistic electron populations are intrinsically linked. Therefore, we could assume that the energy density of the relativistic electrons is simply some fraction of the thermal electron energy density. We set the energy density of the relativistic electrons equal to $\varepsilon_{\rm re} = 0.01\varepsilon_{\rm th}$, similar to Geng et al. (2012). An alternative method for

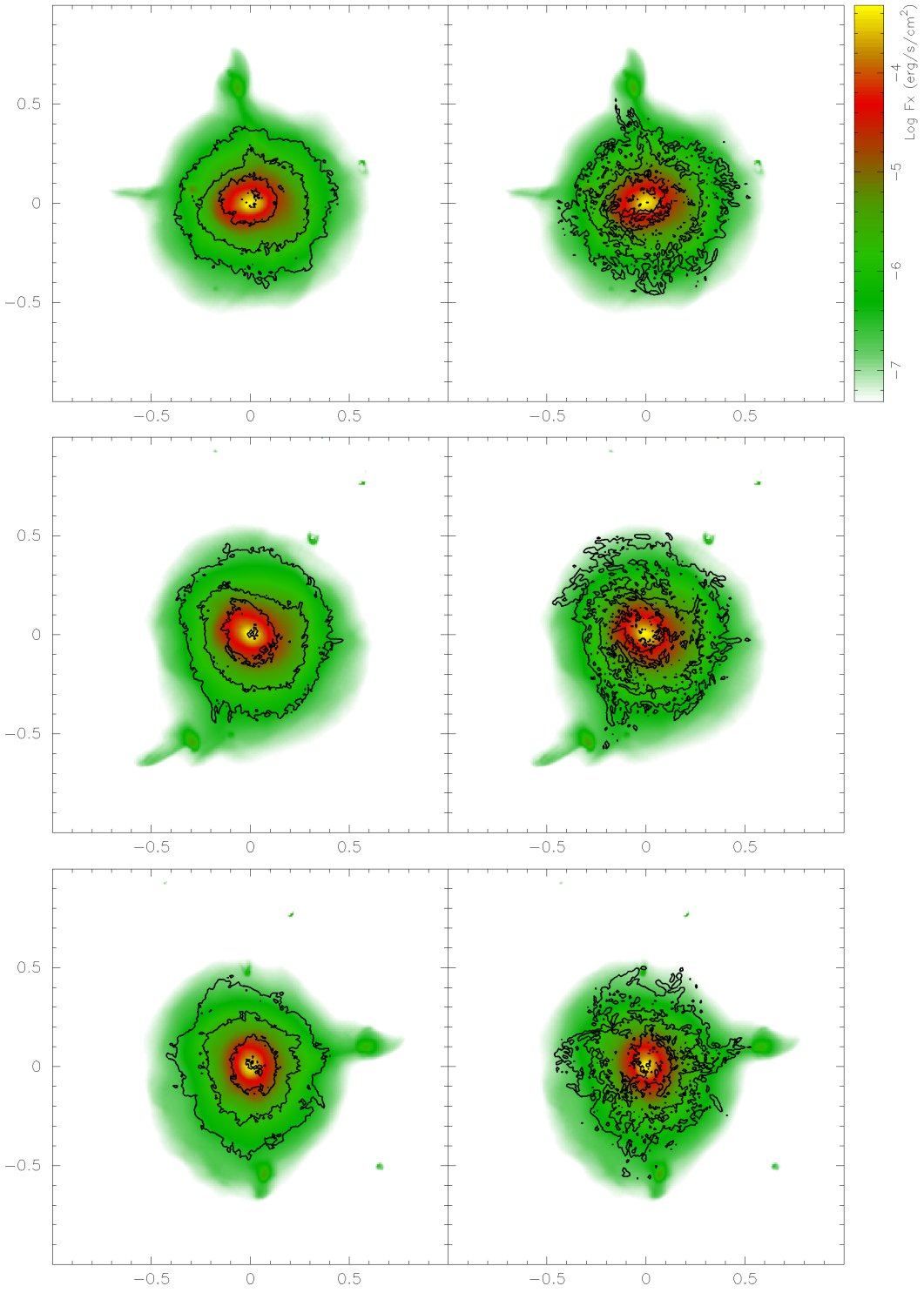

Fig. 4.13: Line of sight X-ray and radio fluxes in the xy (top row), xz (middle row) and yz (bottom row) planes for cluster HR10, run with the 'cleaned' implementation, assuming $\varepsilon_{\rm re} = 0.01\varepsilon_{\rm th}$ (left column) and $\varepsilon_{\rm re} = \varepsilon_{\rm B}$ (right column). The planes are $2R_{\rm vir} \times 2R_{\rm vir}$ and centred on the cluster. The contours define radio flux of $10^{-2}, 10^{-3}, 10^{-4}, 10^{-5}$ mJy.

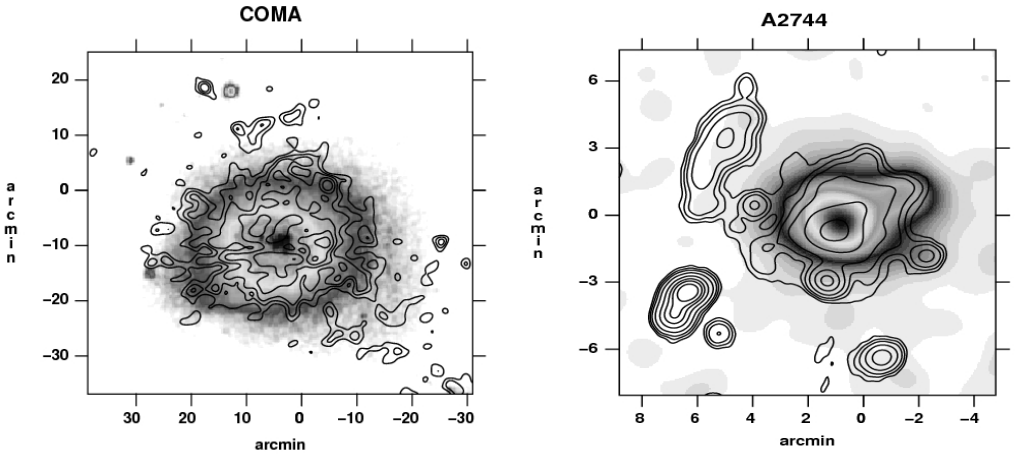

Fig. 4.14: X-ray (greyscale) and radio (contours) morphologies of the galaxies clusters Coma (left) and A2744 (right). There is qualitative agreement between the X-ray and radio fluxes of the observed clusters, which is seen in the simulated clusters. Image credit: Govoni et al. (2001)

estimating the energy density of the relativistic electrons is to make use of the minimum energy condition. This assumption is used when making observations of magnetic fields in galactic systems and has been shown to be valid for our own galaxy. Under this condition the relativistic electrons have the same energy density as the magnetic field so that the normalization of the synchrotron power can be calculated using $\varepsilon_{\rm re} = \varepsilon_{\rm B} = |\mathbf{B}|^2/8\pi$. For simulation HR10 evolved using the 'cleaned' implementation of GCMHD+, we calculate the X-ray flux, using equation (4.1), and the synchrotron power emitted by each particle, using equation (4.2), in the xy, xz and yz planes. We calculate the normalization of the synchrotron power using both assumptions and compare the results.

Fig. 4.13 shows the line of sight X-ray and radio fluxes of simulation HR10. Regardless of the assumption made about the energy density of the relativistic electrons the morphology of the X-ray emission and the morphology of the radio emission are qualitatively very similar and both centred on the centre of mass of the cluster. The X-ray and radio fluxes of the simulated galaxy cluster are of the same order of magnitude as the fluxes observed from galaxy clusters in the Universe (Govoni et al. 2001) and their morphology is

similar, see Fig. 4.14. The radio emission calculated assuming that the energy density of the relativistic electrons is equal to the magnetic energy density shows significantly more small scale features than the radio emission calculated assuming the relativistic electron energy density is a fraction of the thermal electron energy density. This is due to the assumptions used to calculate the radio emission leading to the differing dependence on the magnetic field, which has significantly more small-scale structure compared to the temperature and density.

To provide a quantitative comparison between the X-ray and radio fluxes, and the assumptions used to calculate them, we lay a 256×256 grid over the images and calculate the X-ray and radio fluxes for each pixel. We then plot the radio flux of each pixel as a function of its X-ray flux, similar to the pixel-by-pixel analysis of Govoni et al. (2001), and the result is shown in Fig. 4.15. Both methods of estimating the energy density of the relativistic electrons for the radio flux produce a linear power law relation with the X-ray flux of the cluster, but with significantly more scatter in the $\varepsilon_{\rm re} = \varepsilon_{\rm B}$ plot. The larger amount of scatter is due to the increased amount of small scale structure in the radio flux. A linear fit to the radio flux, calculated assuming $\varepsilon_{\rm re} = 0.01\varepsilon_{\rm th}$, for the xy, xz and yz planes produces a slope value of $b = 0.78, 0.67$ and 0.72 respectively. The linear power law relation found by comparing the X-ray and radio fluxes of the simulated cluster agrees with the values found by Govoni et al. (2001) for the four galaxy clusters they observed. We note that we do not fit the very brightest X-ray pixels as the relation is clearly no longer linear for these pixels. This is a numerical effect, our simulations are adiabatic in nature and the very centre of the galaxy cluster becomes overly dense compared to observed clusters. Due to the X-ray flux's dependence on $n_{\rm e}$ this causes the central pixels to become very bright in X-rays.

Another observation that we can calculate for simulation HR10, run with the 'cleaned' implementation, is the RM of the cluster and the dispersion of the RM. To calculate the RM maps in the xy, xz and yz planes of the cluster we first smooth the particles onto a $256 \times 256 \times 256$ cubic grid of length $2 \times R_{\rm vir}$, which is centred on the centre of mass of the cluster. We then calculate the

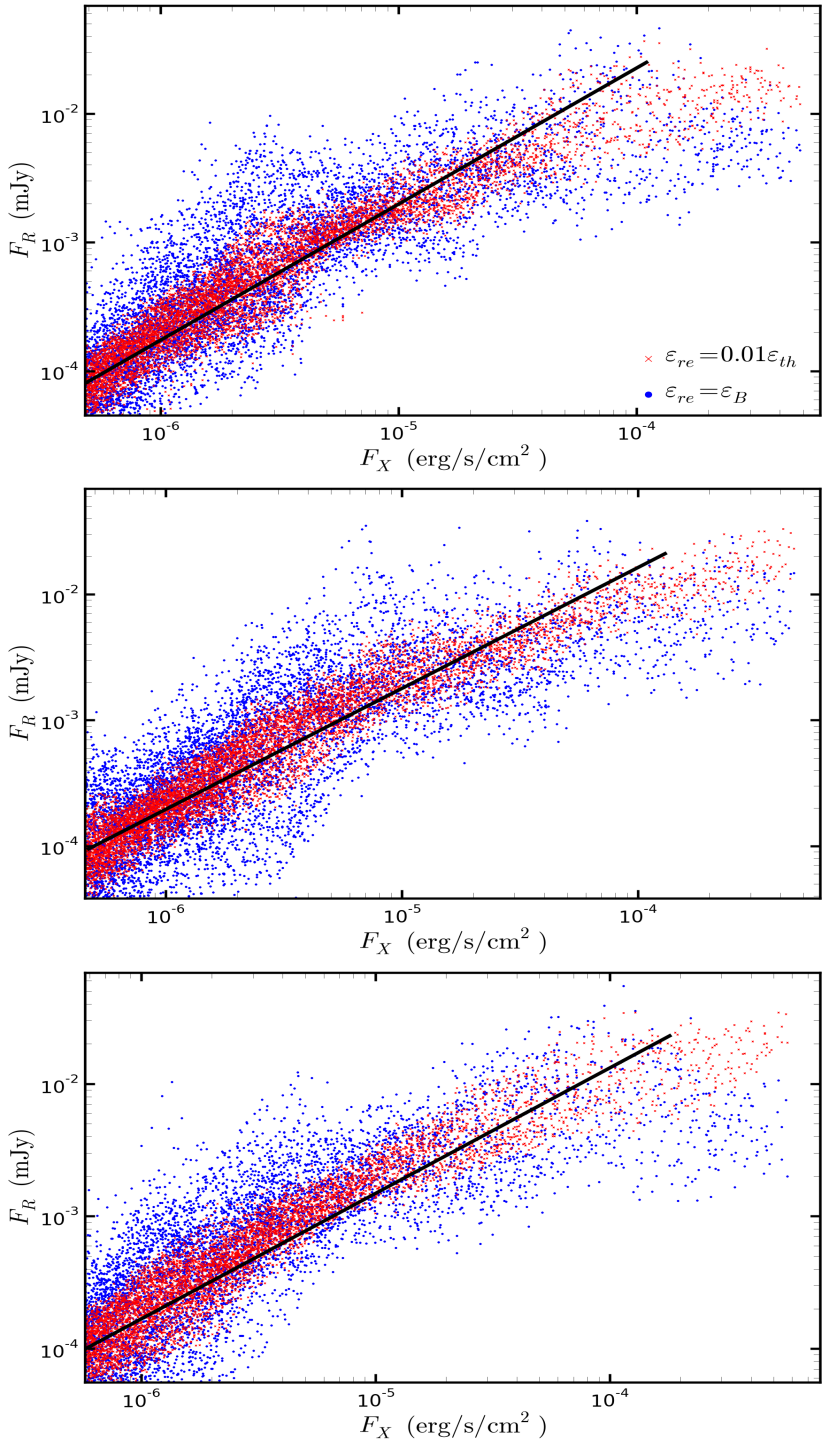

Fig. 4.15: Radio pixel flux as a function X-ray pixel flux for the xy (top panel), xz (middle panel) and yz (bottom panel) planes of cluster HR10. The red crosses show the radio flux calculated assuming $\varepsilon_{\rm re} = 0.01\varepsilon_{\rm th}$, while the blue points show the flux calculated assuming $\varepsilon_{\rm re} = \varepsilon_{\rm B}$. The fit (black line) to the red crosses produces a linear power law slope for all three planes.

density, temperature and magnetic field components for each cell. This enables us to calculate the RM along the third axis for each pixel in the map, i.e. for the xy map pixels we sum the RM along the z-direction, using equation (1.16).

The left column of Fig. 4.16 shows the xy, xz and yz RM maps of the galaxy cluster. They show that the cluster magnetic field is a patchwork of magnetic fields coherent on scales of a few kpc, which is in good agreement with the observed magnetic field coherence length of galaxy clusters. The right column shows the radial profile of the dispersion of the RM distribution, σ_{RM}, for the xy, xz and yz planes. The σ_{RM} shows the small scale fluctuations in the magnetic field and, due to the large number of fluctuations, is a more statistically stable measure of the variation of the magnetic field. The simulated cluster produces σ_{RM} profiles that are in reasonable agreement with the σ_{RM} profiles observed in galaxy clusters (Clarke et al. 2001).

4.7 Implications

We have shown that a primordial seed magnetic field, with an initial amplitude below the constraints placed by observations of the early Universe, is capable of being amplified to the observed μG amplitude observed in galaxy clusters. The magnetic field fills the volume of the cluster and simulated magnetic field has the same radial profile as magnetic fields observed in the ICM of galaxy clusters. The initial seed field evolves due to the formation of structure and produces a magnetic field at the current epoch that is able to reproduce the observed X-ray and radio flux morphologies of a galaxy cluster. Pixel-by-pixel analysis of the fluxes produces an approximately linear power law relation between them, in agreement with observations of several galaxy clusters (see Govoni et al. 2004). Additionally, we calculated the rotation measure map of the simulated cluster and found that is able to reproduce the observed RM structure and the correct RM magnitude.

Therefore, our simulations have shown that a primordial magnetogenesis mechanism is a viable way of magnetizing the large-scale structure of the Universe. This has implications for the observations of large-scale magnetic fields. Primordial magnetic fields are generated in the early Universe prior to re-

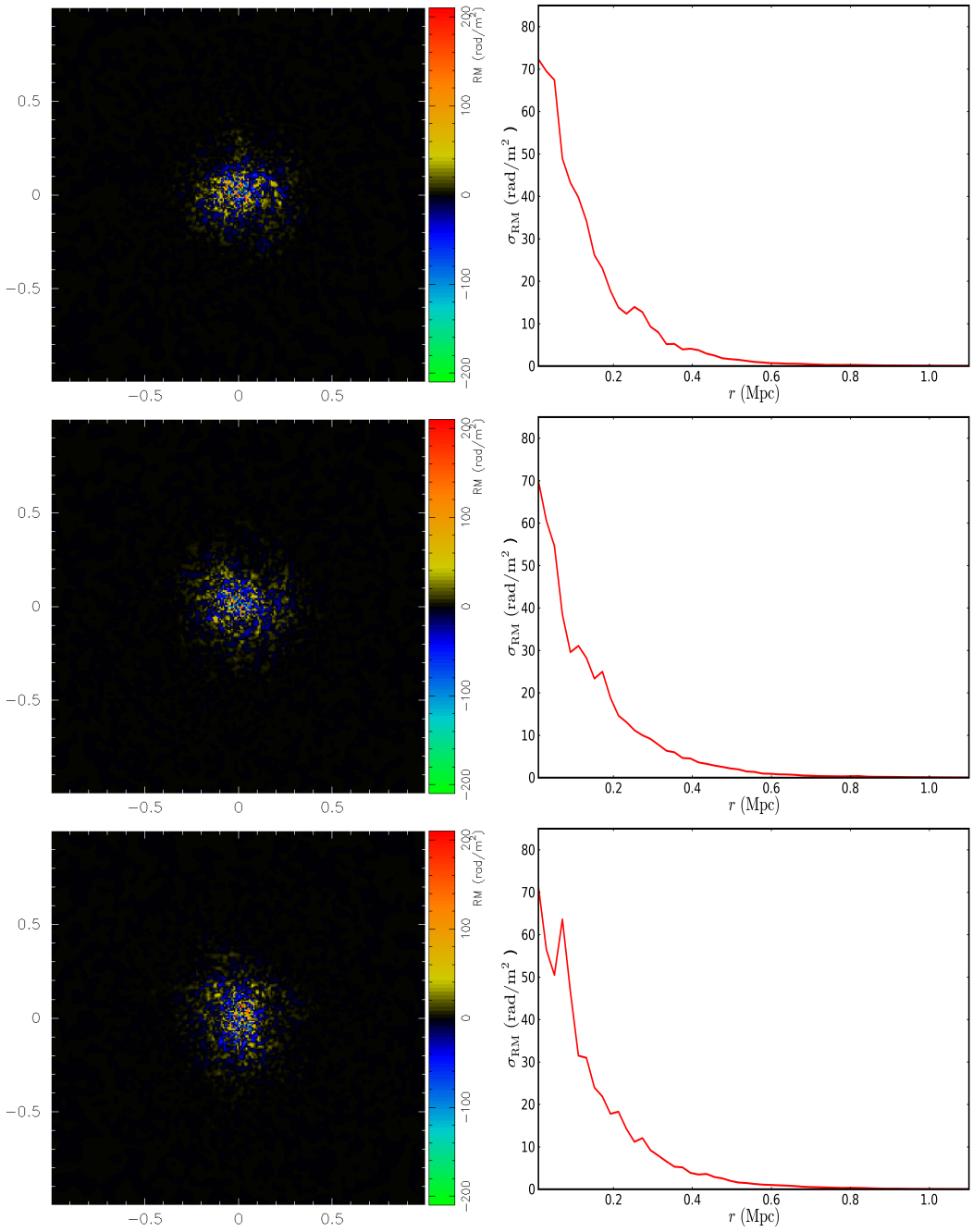

Fig. 4.16: RM maps (left column), $2R_{\rm vir} \times 2R_{\rm vir}$ in size, and $\sigma_{\rm RM}$ radial profiles (right column) for the xy (top row), xz (middle row) and yz (bottom row) planes of the galaxy cluster in simulation HR10. The cluster produces RM maps and σ_{RM} profiles that agree with the observations of galaxy clusters.

combination and magnetic fields that inhabit cosmological voids are relatively unaffected by the formation of structure. Therefore, detailed observations of void magnetic fields are a window into the conditions and properties of the early Universe. Additionally, a large number of primordial magnetogenesis mechanisms require physics beyond the standard model to generate magnetic fields of non-negligible amplitude. Hence, observations of magnetic fields on the very largest scales would provide insight into new physics.

A primordial magnetogenesis mechanism fills the entire observable volume of the Universe with a magnetic field. Therefore, processes that are sensitive to the presence of a magnetic field will be altered. A primordial magnetic field will impact the star formation history of the Universe and the generation of cosmic rays in the Universe. With magnetic fields filling the structure of the Universe, cosmic rays, the majority of which are protons, will propagate differently through the magnetized structures, effecting the cosmic ray flux that is observed on Earth.

4.8 Summary

In this section we have investigated the evolution of a seed magnetic field due to the formation of structure in the Universe. First, we verified our code's ability to capture the structural evolution of the Universe, in particular cluster formation. We used the idealized initial conditions of the Santa Barbara test to simulate the formation of a galaxy cluster with a seed magnetic field embedded in the gas particles. We compared our results for the hydrodynamic parameters of the cluster, such as density and temperature profiles, to the results produced by other numerical codes (in particular Hydra, P^3M-SPH,TVD and SAMR). These simulations demonstrated that our code correctly captures the formation of structure when the artificial conductivity scheme is included. Using these idealized initial conditions we showed that the amplitude of the magnetic field is very sensitive to the minimum level of resistivity applied to the simulation and that the initial conditions of the magnetic field do not affect the final magnetic field in the cluster.

We then presented how we generated initial conditions for cosmological

simulations of the formation of a galaxy cluster. We started with a DM sphere of comoving radius 200 Mpc and selected the most massive halo that formed. Particles that fell within a set distance, $8R_{\rm vir}$ for example, were then replaced by a greater number of particles with lower mass to refine the simulation of the formation of the selected halo. This process was repeated to produce high resolution "zoomed" initial conditions for the formation of ten galaxy clusters with different virial masses and different formation histories.

We then used one of the initial conditions to examine the impact of our numerical scheme on the evolution of the magnetic field, from initial seed to final field that permeates the ICM of the simulated galaxy cluster. Numerical schemes that failed to control the violation of the solenoidal condition, $\nabla \cdot \mathbf{B} = 0$, produced a magnetic field amplitude that was orders of magnitude greater than those that employed a scheme to minimize the violation of the condition, such as a hyperbolic cleaning scheme. Therefore, controlling the divergence error was found to be vital to reliably capturing the evolution of a seed magnetic field. The choice of resistivity switch was investigated and it was found that the TP13 resistivity switch too strongly applies resistivity and damps the amplitude of the cluster magnetic field.

The ten initial conditions were then evolved using the chosen numerical scheme to investigate the impact of cluster mass and formation history on the amplitude of the magnetic field inhabiting the ICM. No correlation with mass or formation history was found and all of the simulated clusters reached $(0.3 - 1) \times 10^{-8}$ G. By examining the power spectra of velocity and magnetic field of the simulations it was found that the resolution of the simulation was limiting the amplitude of the final magnetic field. Increasing the resolution of the simulation we found that the use of the PM05 resistivity switch suppressed the amplitude of the magnetic field and that resistivity may not be required for simulations with no sinks or sources of magnetic field. It was found that a primordial seed magnetic field of 10^{-11} G can be amplified to the observed micro-gauss amplitude by the formation of a galaxy cluster.

The high resolution simulation run with the hyperbolic cleaning scheme, but without an artificial resistivity scheme, was then used to reproduce observ-

able quantities of the cluster. We calculated the X-ray and radio fluxes of the simulated cluster and found that, regardless of the normalization of the radio emission, the morphologies of the fluxes are qualitatively similar to each other, as observed in galaxy clusters. The fluxes were then evaluated pixel-by-pixel and a linear power law relation between them was found for the simulated cluster, agreeing with the relation observed in galaxy clusters. The RM map of the simulated cluster was then calculated and the RM found agreed with the observed RM of galaxy clusters. The implications of a primordial seed field reproducing all of the observable quantities and being a viable seeding mechanism of the large-scale structure of the Universe were then discussed.

Chapter 5

Magnetic fields in Spiral Galaxies

A galactic magnetic field was first proposed to explain the cosmic ray population of the Milky Way (Alfvén 1949) and first observed at the same time via the polarization of star light (Hall 1949; Hiltner 1949). The magnetic field of the Milky Way has been measured using the rotation measure (RM) of pulsars and was found to have a bisymmetric spiral structure with an amplitude of $1.8 \pm 0.3\,\mu$G (Han and Qiao 1994). The magnetic field of external galaxies can be studied via their radio continuum emission. The total intensity of the synchrotron emission gives the amplitude of the total magnetic field and its linearly polarized intensity reveals the amplitude and structure of the magnetic field in the plane of the sky. The RM of sources behind and embedded within the galaxy provide an estimate of the magnetic field along the line of sight. Therefore, it is possible to measure the total amplitude and 3D topology of magnetic fields in nearby galaxies. For spiral galaxies, the average observed total magnetic field strength is $9 \pm 3\,\mu$G, with the strength increasing up to $25\,\mu$G inside spiral arms (see Niklas 1995). Observations of face-on galaxies reveal that the magnetic field follows the optical spiral pattern and edge-on galaxies show a plane parallel magnetic field. For a review of galactic magnetic fields see Krause (2014).

The current theory for the origin of magnetic fields in spiral galaxies is that they are generated and maintained by two dynamo mechanisms working at two different scales. The "small-scale" dynamo is powered by the turbulent motions generated by the formation of the protogalactic halo and supernovae.

This turbulent dynamo is capable of amplifying an initial seed field to a few μG, coherent on 100 pc scales, on a timescale of $\sim 10^8$ yr (Arshakian et al. 2009). This provides the seed for the "large-scale" dynamo that orders the magnetic field into structures that are coherent on the scale of the galaxy, on a timescale of $\sim 10^9$yrs (Arshakian et al. 2011). The origin of the initial seed field for the small-scale dynamo is unknown and could be of primordial origin or generated via plasma physics during the formation of the first structures.

Observations of linearly polarized emission from face-on spiral galaxies show that they have magnetic spiral arms that are analogous to their gaseous spiral arms, but offset such that they trail the gaseous arms in the sense of galactic rotation (Patrikeev et al. 2007; Beck 2007). It has been argued that this would be expected for spiral arms that are formed by density waves, producing spiral shocks in the galaxy (Fletcher 2010). However, spiral density wave theory (Lin and Shu 1964) has recently been questioned, as numerical simulations have shown that spiral arms are transient features instead of stable structures (Sellwood 2011; Wada et al. 2011; Grand et al. 2012). These transient structures are believed to by driven by local instabilities in the disc, which disperse on timescales of 100 Myr. However, current simulations of the formation of transient spiral arms do not included magnetism and the relationship between transient gaseous arms and magnetic arms is unknown. In addition, the energy density of the galactic magnetic field is comparable to the turbulent energy density and may impact on star formation, and hence the dynamical properties of the spiral arms.

5.1 Isolated disc galaxy set-up

As a pilot study we simulate an isolated disc galaxy with properties similar to those of M33. Due to its proximity, the magnetic field of M33 has been studied in high resolution (Fletcher et al. 2000; Tabatabaei et al. 2008; Li and Henning 2011). In terms of numerical practicality, due to the lower mass of M33 compared to more massive disc galaxies, such as the Milky Way, we can achieve a higher mass resolution simulation for the same number of particles.

The simulations assume a Λ-dominated cold dark matter cosmological

model, with parameters of $\Omega_b = 0.049$, $\Omega_m = 0.313$, $\Omega_\Lambda = 1 - \Omega_m$ and $H_0 = 67.4\,\mathrm{km\,s^{-1}\,Mpc^{-1}}$ (Planck Collaboration et al. 2013). Without losing generality we use a fixed DM halo potential. This avoids complicating the evolution of the baryonic and stellar discs, as a live DM halo will introduce additional effects such as numerical scattering and heating. When the DM resolution is too coarse, a live DM halo can even act as perturbing masses that disturb the baryonic disc (D'Onghia et al. 2013). Therefore, a fixed DM potential enables us to focus on the impact of the magnetic field in the disc of the galaxy. We use the standard Navarro-Frenk-White (NFW) DM halo density profile (Navarro et al. 1997), which takes the form

$$\rho_{\mathrm{DM}} = \frac{3H_0^2}{8\pi G}\frac{\Omega_m - \Omega_b}{\Omega_m}\frac{\rho_c}{cx(1+cx)^2}\,, \tag{5.1}$$

where

$$c = \frac{r_{200}}{r_s}\,, \tag{5.2}$$

$$x = \frac{r}{r_{200}}\,, \tag{5.3}$$

and

$$r_{200} = 1.63 \times 10^{-2}\left(\frac{M_{200}}{h^{-1}\mathrm{M}_\odot}\right)^{1/3} h^{-1}\,\mathrm{kpc}\,. \tag{5.4}$$

The characteristic density of the profile is ρ_c, r is the distance from the centre of the halo and r_s is the scale radius. We set the total halo mass such that $M_{200} = 4.9 \times 10^{11}\,\mathrm{M}_\odot$ and the concentration parameter to be $c = 12$.

To the fixed DM potential we add a stellar disc that has an exponential surface density profile that takes the form

$$\rho_{\mathrm{d},*} = \frac{M_{\mathrm{d},*}}{4\pi z_{\mathrm{d},*} R_{\mathrm{d},*}^2}\mathrm{sech}^2\left(\frac{z}{z_{\mathrm{d},*}}\right)\exp\left(-\frac{R}{R_{\mathrm{d},*}}\right)\,, \tag{5.5}$$

where $M_{\mathrm{d},*}$ is the mass of the stellar disc, $R_{\mathrm{d},*}$ is the scale length of the disc and $z_{\mathrm{d},*}$ is the disc scale height. The galaxy is orientated such that the disc is parallel to the xy plane and is centred on the coordinate origin.

For all simulations we set the stellar disc parameters to $M_{\mathrm{d},*} = 4.0 \times 10^9\,\mathrm{M}_\odot$, $R_{\mathrm{d},*} = 1.4\,\mathrm{kpc}$ and $z_{\mathrm{d},*} = 0.175\,\mathrm{kpc}$. In a similar manner to the stellar disc, we add a gas disc that follows the same exponential density profile

with $M_{\mathrm{d},g} = 2.0 \times 10^9\,\mathrm{M}_\odot$, $R_{\mathrm{d},g} = 4.0\,\mathrm{kpc}$ and $z_{\mathrm{d},g} = 1.0\,\mathrm{kpc}$. As cooling and radiative feedback are not included, we are in principle free to choose the parameters of the gas disc. The stellar and gas discs contained $400,000$ and $200,000$ particles respectively, resulting in a mass of $1 \times 10^4\,\mathrm{M}_\odot$ for all particles. This initial set-up was evolved for 1 Gyr to allow the galaxy to relax and to dissipate any numerical artefacts that may have been present in the initial set-up. The gas particles were then embedded with a μG amplitude magnetic field, orientated in the x-direction only to ensure that it was initially divergence free. Our focus is the impact of including a magnetic field on the evolution of the structure of the galaxy and so we ignore additional physical processes, such as star formation, radiative cooling and feedback, that will introduce additional complications. This set-up was initially used to test the stability of our numerical scheme.

5.2 Producing a stable numerical scheme

We evolved the relaxed isolated galaxy set-up, embedded with a magnetic field, for 1 Gyr using GCMHD+. Artificial viscosity and artificial conductivity, as presented in section 2.3, were included. The artificial resistivity scheme was included and used the PM05 switch with $\alpha^B_{\mathrm{min}} = 0.0$. The growth of numerical divergence of the magnetic field was suppressed by including the hyperbolic cleaning scheme with $\sigma = 1.0$. However, it was found that this implementation of GCMHD+ was not stable for isolated galaxy simulations.

Fig. 5.1 shows four snapshots of the density of the gas disc from 0.11 Gyrs to 0.17 Gyrs. During this period of evolution the gas disc is ripped apart and after this time no further spiral structure forms. The gas disc is ripped apart due to our choice of numerical scheme. Fig. 5.2 shows the divergence error of galaxy for the same four snapshots. Before the gas disc begins to be disrupted at 0.15 Gyrs the divergence error begins to fluctuate, first dropping and then growing very rapidly. The rapid growth of the numerical divergence leads to a rapid growth in the amplitude of the magnetic field. The magnetic field is link to the gas via the Lorentz force term in the momentum equation and by the artificial resistivity scheme, which heats the gas when it dissipates magnetic

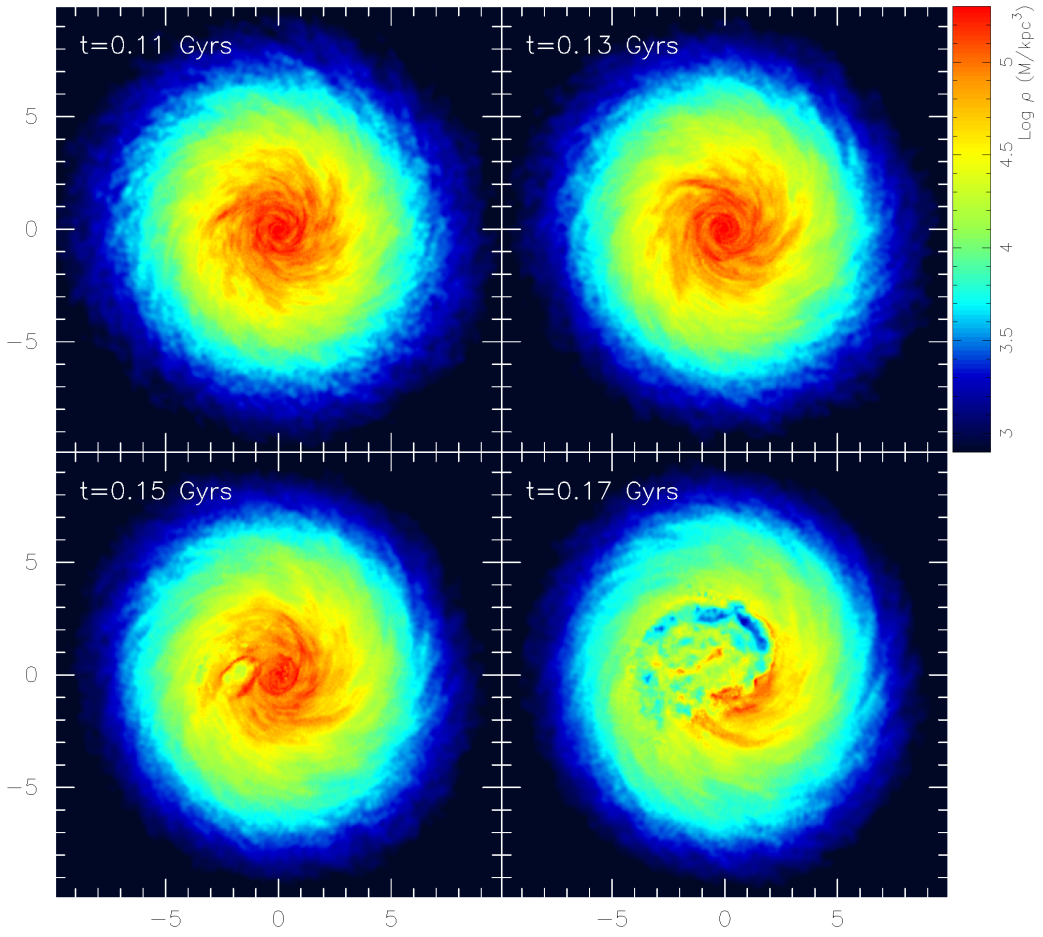

Fig. 5.1: Snapshots of the density of the gas disc of the galaxy at $t = 0.11, 0.13, 0.15$ and $0.17\,\mathrm{Gyr}$. The gas disc begins to be ripped apart at $0.15\,\mathrm{Gyr}$, after which spiral structures no longer form.

energy. Therefore, the rapid growth of the magnetic field and its resulting back-reaction rips the gas disc apart. The cause of the rapid growth of the divergence error is the use of the hyperbolic cleaning scheme and the gas disc is destroyed regardless of the resistivity switch used, the initial magnetic field orientation or the initial amplitude of the magnetic field.

A solution to this problem is to simply run the simulations without the hyperbolic cleaning scheme. However, this allows the numerical divergence of the magnetic field to grow as the simulation runs. This is undesirable as it may produce spurious forces, will lead to incorrect amplification of the magnetic field and cause the artificial resistivity scheme to apply too much resistivity to

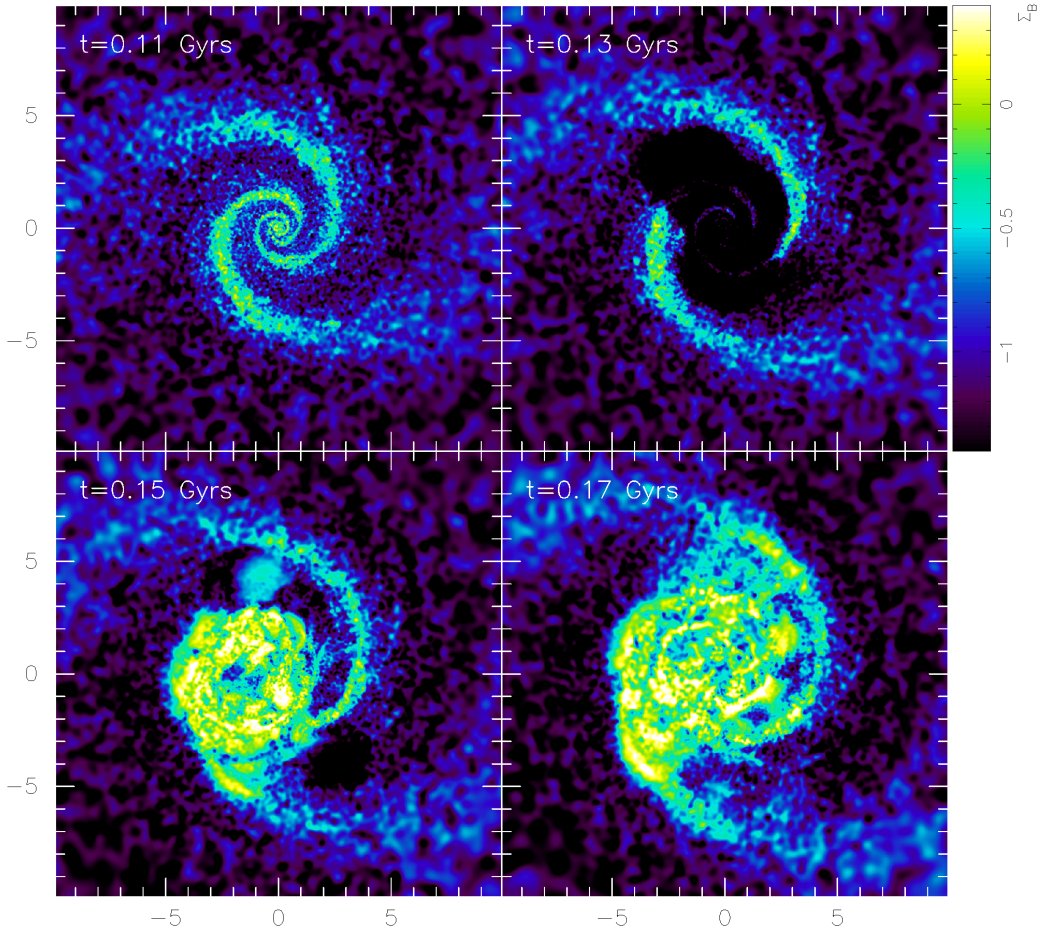

Fig. 5.2: Snapshots of the divergence error of the gas disc of the galaxy at $t = 0.11, 0.13, 0.15$ and $0.17\,\mathrm{Gyr}$. The divergence of the magnetic field fluctuates and then grows rapidly, ripping apart the gas disc of the galaxy.

the simulation, as demonstrated in Chapters 3 and 4. A compromise between the full unstable cleaning scheme and no cleaning scheme is to limit the change in the magnetic field that the cleaning scheme can introduce. Using equation (2.87), we limit the change in the magnetic field produced by the cleaning scheme to less than half of the change produced by the induction equation (2.56) at each time step for each particle. The disadvantage of this approach is that numerical divergence of the magnetic field is removed at a slower rate, compared to the unlimited cleaning scheme, resulting in a higher numerical divergence on average. However, it prevents the exponential growth of the divergence of the magnetic field, which results in the disc of the galaxy being

ripped apart, and produces a reduction in the divergence error compared to a numerical scheme that completely excludes the hyperbolic cleaning scheme.

5.3 Initial magnetic field

To examine the impact of the large-scale rotation of the galaxy on the magnetic field, we embedded the gas particles of three isolated galaxy set-ups with magnetic fields of amplitude 0.01 μG, 0.1 μG and 1 μG respectively, all initially orientated in the x-direction only. These initial set-ups were then evolved for 1 Gyr using GCMHD+ with the artificial resistivity scheme, using the PM05 switch, and the limited hyperbolic cleaning scheme. Fig. 5.3 shows a 10 kpc $\times$ 10 kpc snapshot, centred on the galaxy, of the stellar and gas discs of these three simulations 0.33 Gyr after the introduction of the magnetic field.

In agreement with previous work published in the literature, we find that the spiral structure of the galaxy is transient in nature. Spiral arms form and dissipate as we evolve the initial set-up on timescales of $\sim$ 100 Myr. The stellar discs of all three galaxies are unaffected by the amplitude of the applied magnetic field and are visually similar in all three simulations. However, the introduction of the magnetic field alters the structures that have formed in the gas disc. As the initial amplitude of the magnetic field increases the structure that forms in the gas disc of the galaxy becomes more tightly wound. Additionally, in the simulation that initially has a 1.0 μG amplitude magnetic field large diffuse spiral structures can be seen extending outwards from the galaxy and this is not seen in the simulations with a weaker initial magnetic field.

Fig. 5.4 shows a 10 kpc $\times$ 10 kpc snapshot, centred on the galaxy, of the magnetic field amplitude of the simulated galaxies at 0.33 Gyr. The kinetic energy of the large-scale rotation of the galaxies is orders of magnitude greater than the energy density of the magnetic field and so the field is effectively frozen into the gas. Therefore, as seen in all of the simulations, the rotation of the galaxy winds the initial field and produces a spiral patterned magnetic field, with large-scale reversals, that is coherent on the scale of the galaxy. However, the motion produces no significant amplification of the mag-

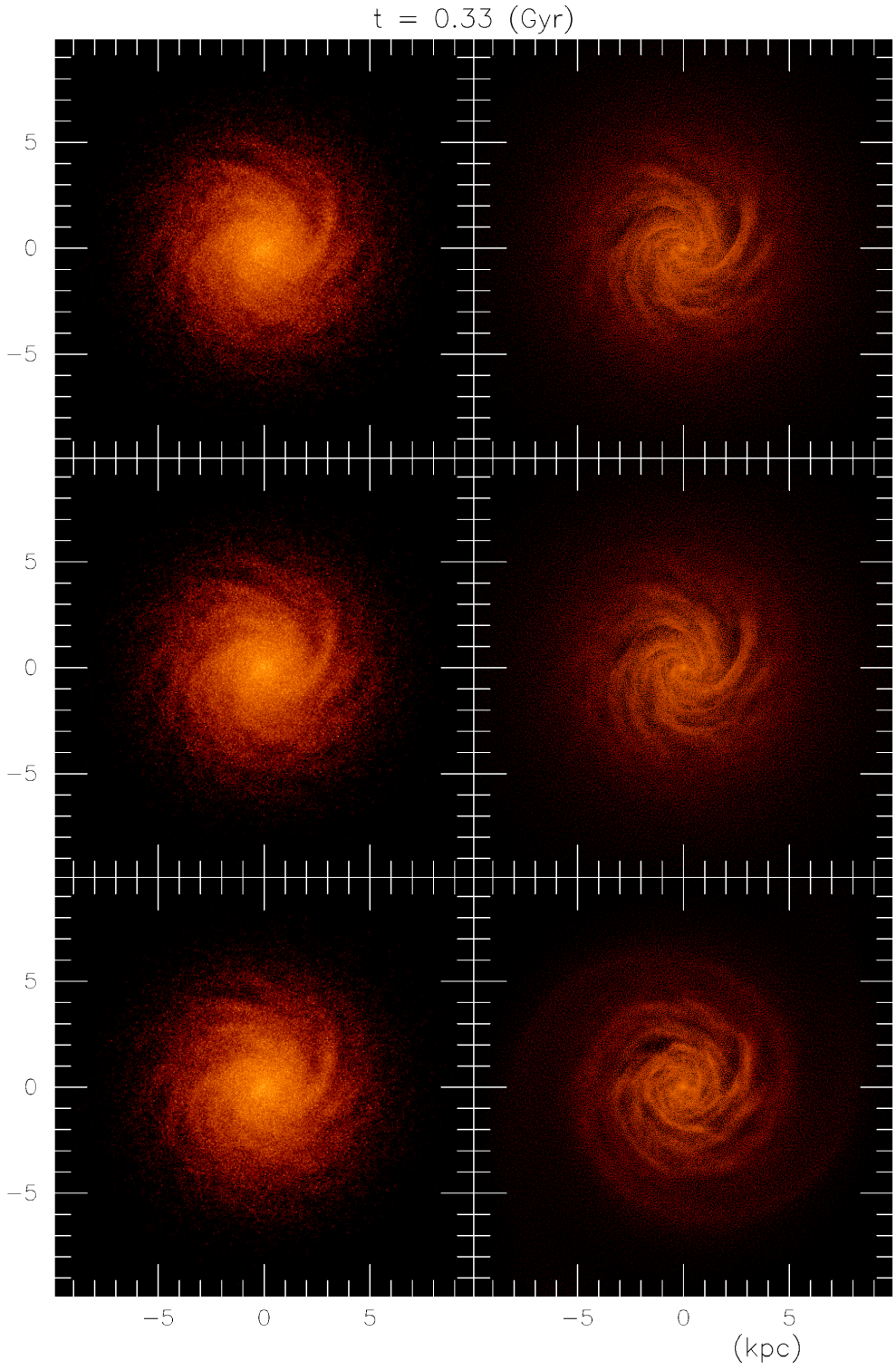

Fig. 5.3: Plots of the stellar particles (left column) and gas particles (right column) of the galaxy at $t = 0.33\,\mathrm{Gyr}$ with an initial magnetic field of $0.01\,\mu\mathrm{G}$ (top row), $0.1\,\mu\mathrm{G}$ (middle row), $1.0\,\mu\mathrm{G}$ (bottom row). As the magnetic field increases to micro-gauss strength the structures in the gas disc of the galaxy begin to wind more.

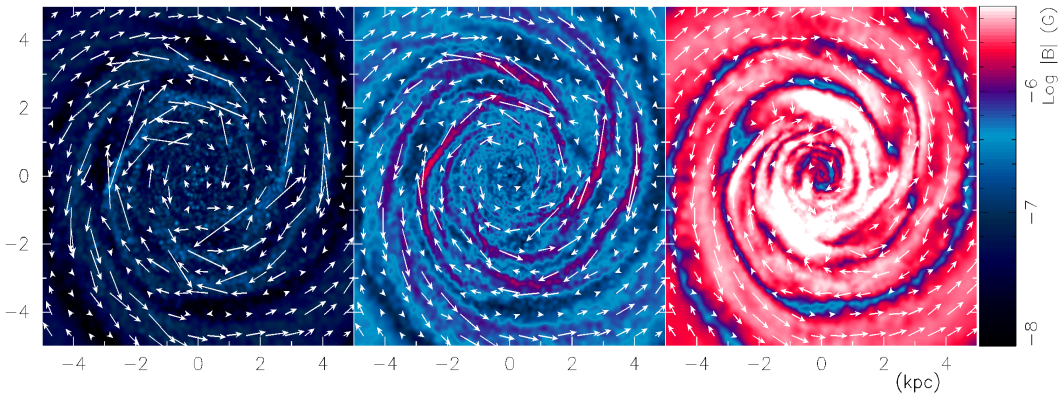

Fig. 5.4: Amplitude of the galactic magnetic after $t = 0.33\,\mathrm{Gyr}$ of evolution for the simulations with an initial magnetic field strength of $0.01\,\mu\mathrm{G}$ (left panel), $0.1\,\mu\mathrm{G}$ (centre panel) and $1.0\,\mu\mathrm{G}$ (right panel). The arrows denote the strength and direction of the magnetic field in the xy plane, normalized by the initial magnetic field strength.

netic field. The simulations began with a magnetic field amplitude of $0.01\,\mu\mathrm{G}$, $0.1\,\mu\mathrm{G}$ and $1\,\mu\mathrm{G}$ and after $1\,\mathrm{Gyr}$ of evolution have an average field amplitude of $0.06\,\mu\mathrm{G}$, $0.47\,\mu\mathrm{G}$ and $4.32\,\mu\mathrm{G}$, respectively. The formation of spiral structure leads to a local enhancement of the magnetic field amplitude, due to material condensing at localized instabilities. When a spiral arm dissipates the magnetic field amplitude reduces back down as the material diffuses. By comparing Fig. 5.3 and 5.4, it can be seen that the enhancement of magnetic field aligns exactly with the gaseous spiral arms.

To examine the impact of the initial orientation of the magnetic field we set up an additional isolated galaxy where the gas particles are embedded with a $1\,\mu\mathrm{G}$ amplitude magnetic field orientated in the z-direction. This set-up was evolved for $1\,\mathrm{Gyr}$ using the same numerical implementation of GCMHD+. Fig. 5.5 shows the galactic magnetic field after $1\,\mathrm{Gyr}$ of evolution and it is compared to the simulation with a $1\,\mathrm{Gyr}$ magnetic field orientated in the x-direction. There is a clear difference between two initial orientations of the magnetic field. An initially z-direction orientated magnetic field is beginning to be rotated into the plane of the galaxy by the large-scale rotational motion, but the field is not primarily located in the plane of the galaxy after $1\,\mathrm{Gyr}$. This is contradictory to the observations of galactic magnetic fields (Fletcher et al.

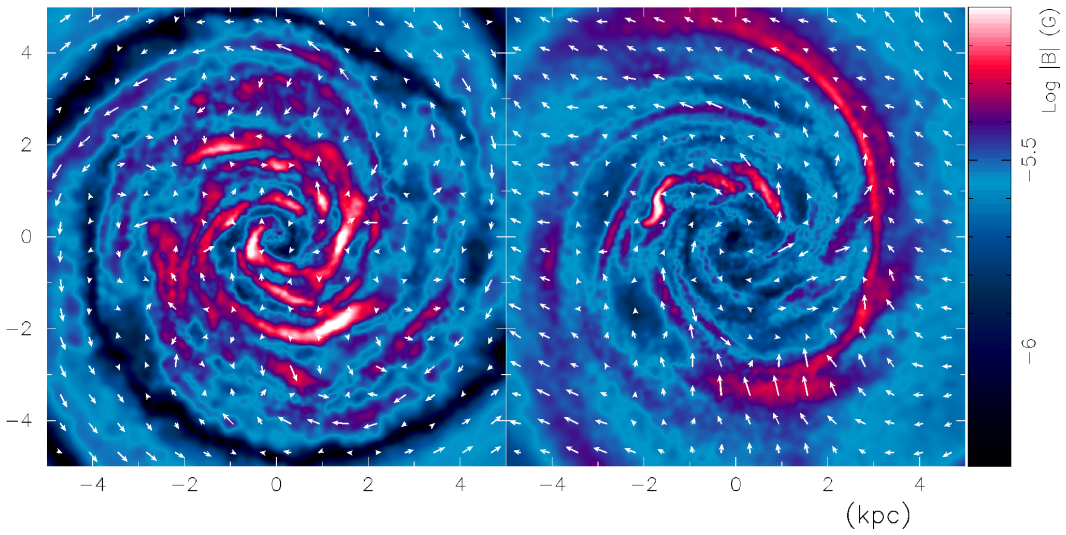

Fig. 5.5: Comparison of the magnetic field strength at $t = 1.0\,\mathrm{Gyr}$ for simulations with the magnetic field initially orientated in the x-direction (left panel) and z-direction (right panel). The white arrows denote the strength and direction of the magnetic field in the xy plane of the galaxy.

2011; Beck 2012; Tabatabaei et al. 2013) and it is likely that a longer period of evolution would result in a galaxy where the magnetic field is primarily orientated in the plane of the disc.

5.4 Magnetic fields and Spiral Structure

To examine the impact of the galactic magnetic field on the formation of spiral structure in the galaxy we must look at the formation of spiral arms over an extended time period. As the stellar disc is more massive than the gas disc of the galaxy it will have a dominant influence on the local dynamics in the disc of the galaxy. It has been shown that in lower resolution simulations that the spiral structure of the galaxy can disappear after only a few galactic rotations (Sellwood and Carlberg 1984). This occurs because the spiral structure of the disc scatters stars and increases the velocity dispersion of the stellar disc. The increase in the velocity dispersion produces an increase in the Toomre's Q value of the stellar disc (Toomre 1964), making it more stable against local instabilities. As spiral arms in simulations are believed to form from local instabilities in the disc, the heating of the stellar disc results in the loss of

spiral structure in the galaxy. However, this effect has been shown to be a numerical artefact of the resolution of the simulations, as increasing the resolution has been shown to produce galaxies that have a transient spiral structure for in excess of 10 Gyr (Fujii et al. 2011). Therefore, to ensure that we suppress the long term artificial heating of the disc and obtain a reliable spiral structure we increase the resolution of the simulations, such that the stellar disc contains 4×10^6 star particles, the gas disc contains 2×10^6 gas particles and each particle has a mass of $1 \times 10^3\,\mathrm{M}_\odot$.

The initial set-up was again relaxed to allow any numerical artefacts to dissipate and the resulting spiral galaxy was used as the base of two simulations. The first simulation was kept as a purely hydrodynamic simulation and was evolved using a GCMHD+ implementation that neglected the MHD scheme. The second simulation was embedded with a $1\,\mu$G magnetic field, orientated in the x-direction only to ensure that it was initially divergence free. This simulation was then evolved using a GCMHD+ implementation with artificial resistivity, using the PM05 switch, and the limited cleaning scheme. Both simulations were evolved for 1 Gyr. A comparison of the evolution of these two simulations allows the impact of the magnetic field on the formation of spiral structure to be investigated.

Snapshots of the formation and dissipation of the same spiral arm in the two simulations, without and with a galactic magnetic field, are shown in Fig. 5.6 and Fig. 5.7 respectively. A comparison of the stellar particles at all four snapshots shows that the magnetic field has negligible effect of the formation of the stellar spiral arm. This result is expected as the stars do not feel the influence of the magnetic field directly, i.e. the Lorentz force, and there is no star formation in these simulations. However, the structure of the gas disc is altered by the inclusion of the magnetic field. The gaseous spiral arms are more sharply defined and there is less material in the inter-arm regions of the simulation that includes a magnetic field. As seen in the lower resolution simulations, the increase in density due to the formation of a spiral arm produces an enhancement in the magnetic field. This leads to a arm of magnetic field, aligned exactly with the gaseous spiral arm, that is significantly

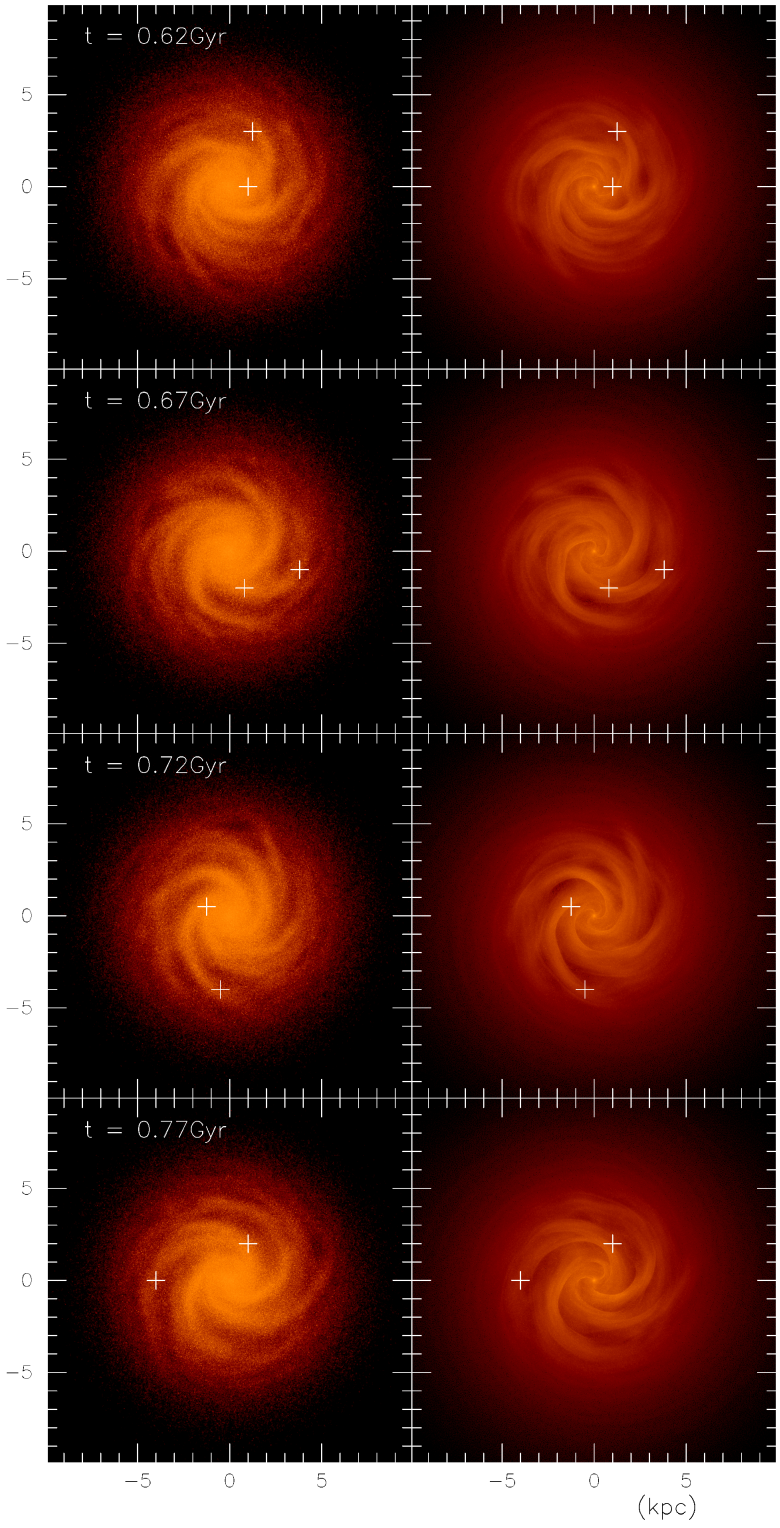

Fig. 5.6: Snapshots at $t = 0.62$, 0.67, 0.72 and 0.77 Gyr of the stellar (left column) and gas (right column) discs of the galaxy simulated without a magnetic field. The white crosses mark the spiral arm that forms and then dissipates in the 150 Myr that the snapshots cover.

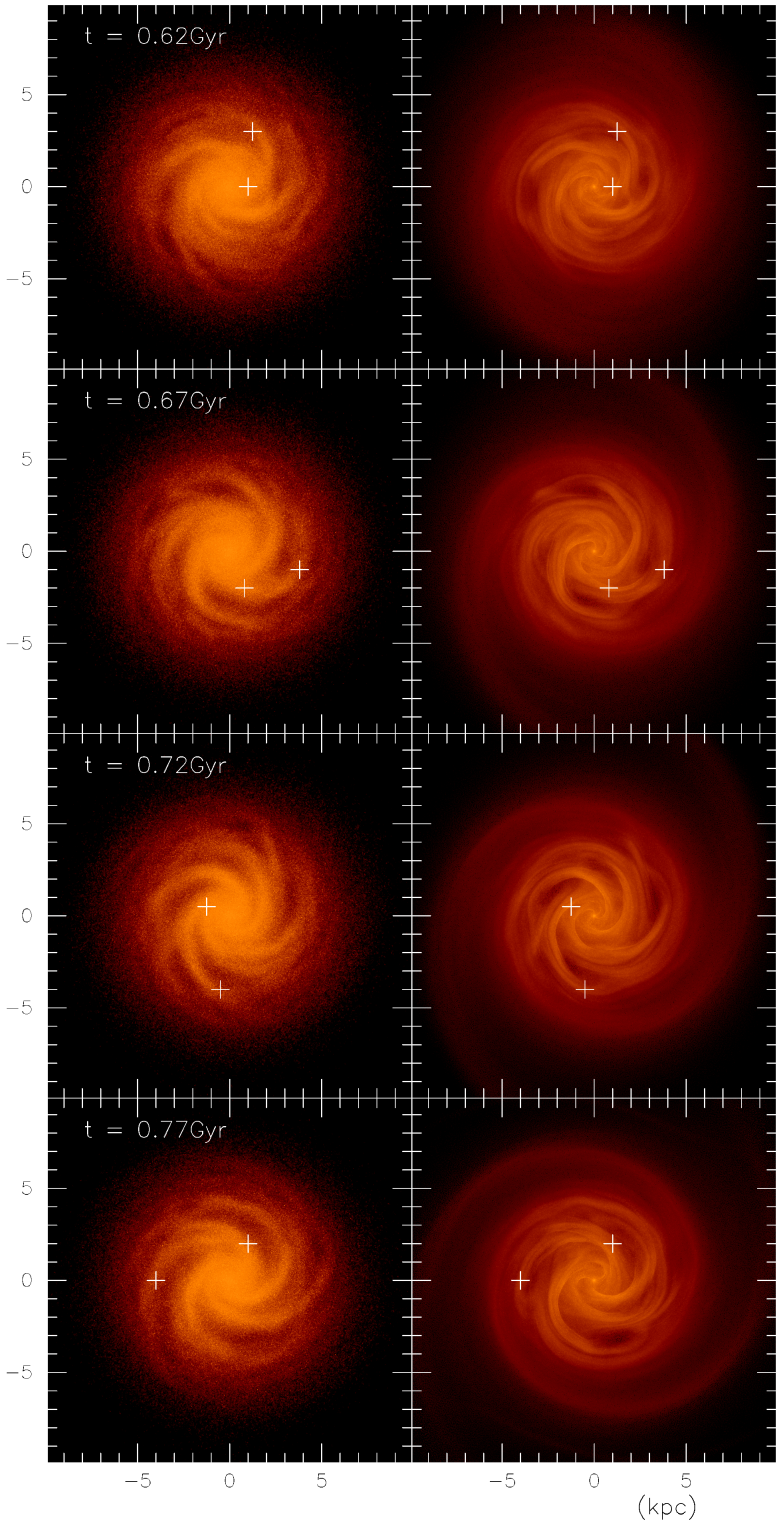

Fig. 5.7: The same as Fig. 5.6, but for the galaxy simulated with a magnetic field. The inclusion of the magnetic field produces more defined spiral arms and the inter-arms regions to be less dense.

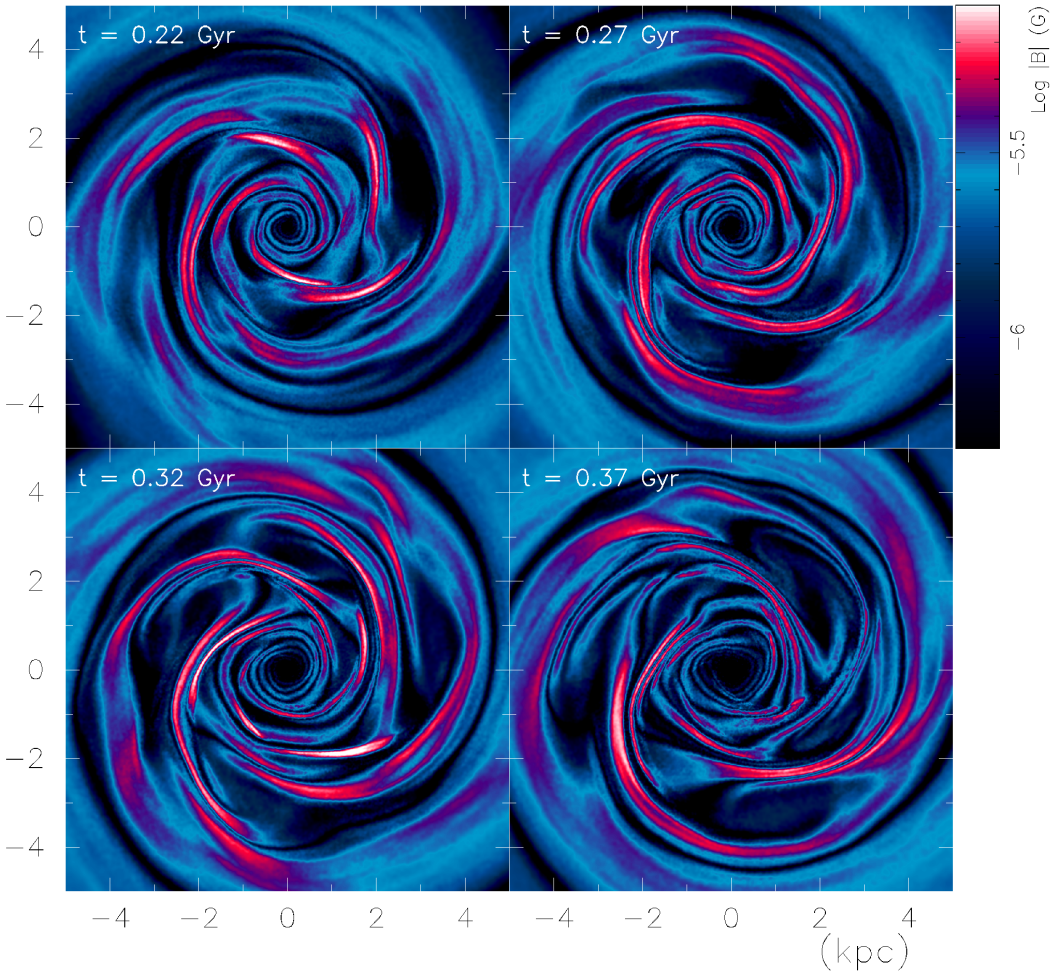

Fig. 5.8: Snapshots of the magnetic field strength at $t = 0.62$, 0.67, 0.72 and 0.77 Gyr of the simulated galaxy. The formation of spiral structure leads to amplification of the magnetic field and it dissipation weakens the field.

higher in amplitude compared to the ambient magnetic field of the galaxy. The magnetic tension force helps to prevent material that has fallen into the spiral arm from dissipating into the inter-arm region. This results in slightly more dense spiral structure of the galaxy compared to the purely hydrodynamical simulation.

The high resolution simulations produce a galaxy that has a magnetic field with a spiral structure and is primarily orientated in the plane of the galaxy, which is in agreement with the observations. The formation of spiral structure amplifies the magnetic field from an ambient μG amplitude to $\sim 20\mu$G, which is in reasonable agreement with the observations of nearby spiral galaxies.

However, the simulations do not agree entirely with the observations. In the simulations the formation of the spiral arm leads to the formation of a coherent magnetic arm that is exactly aligned with it. However, observations show that magnetic arms appear to be offset from the gaseous spiral arms. Additionally, the magnetic fields observed in spiral arms appear to be turbulent, but the simulation produces a coherent magnetic field in the spiral structure. Both of these discrepancies with the observations suggest that our model for the galaxy is too simplistic.

In the simulations we have neglected star formation and supernovae feedback so that the impact of the magnetic field could be isolated. Spiral arms in observed galaxies are associated with a burst of star formation. This star formation will then be associated with a number of supernovae events that will occur in the spiral arm. The outflows from these supernovae will produce turbulent motions in the gas of the spiral arms. The onset of turbulence will lead to a loss of coherence of the magnetic field and it will appear turbulent inside the spiral arms. The inclusion of supernovae feedback may also explain the observed offset of magnetic and gaseous spiral arms. The magnetic arms have been observed via linearly polarized synchrotron emission, which requires the magnetic field to be coherent. Including supernovae feedback will disrupt the coherence of the magnetic field in the spiral arms. Therefore, the most coherent magnetic field, and strongest linearly polarized emission, in the galaxy would reside in the interarm regions and an offset would be observed between the gas and magnetic spiral arms. Therefore, any future work should include additional schemes to deal with sub-resolution physics, such as the formation of stars, supernovae feedback and radiative cooling of the gas.

5.5 Summary

In this chapter we have looked at the interplay between the formation of transient spiral structure in a disc galaxy, similar in nature to M33, and the large-scale magnetic field of the galaxy. We detailed the set-up of our isolated galaxy, including a static DM halo, stellar and gas disc with an exponential profile and the initial magnetic field configuration. We then demonstrated

that our numerical scheme was unstable and that the cause of this instability was the hyperbolic cleaning scheme. This can be overcome by introducing a limiter that prevents the hyperbolic cleaning scheme from becoming the dominant term in the induction equation.

We showed that the large-scale rotation of the galaxy orders the magnetic field in the plane of the galaxy, but that there is little amplification of the initial seed field. The addition of a sufficiently strong magnetic field causes the spiral structure of the gas disc to become more tightly wound and denser. It was demonstrated that the formation of a spiral arms results in an increase of the magnetic field amplitude to $\sim 20\,\mu$G, in agreement with the observations of spiral galaxies. We then discussed where the simulations match the observations and where they disagree. It was argued that inclusion of additional physical processes that occurs at sub-resolution scales may bring the simulations more inline with the observations.

Chapter 6

Conclusions and Future Directions

In this thesis we developed an SPMHD code, GCMHD+, to study the magnetic fields of the largest structures in the Universe. We presented a review of the SPMHD numerical method. The discrete conservation equations were derived self-consistently from a variational principle. Schemes, such as artificial viscosity, conductivity and resistivity, were presented that allow discontinuities in the fluid quantities to be resolved and correctly captured. Additionally, schemes were presented that help to overcome some of the technical challenges that the addition of a magnetic field to the fluid introduces, such as the tensile instability and maintaining the solenoidal condition of the magnetic field. How to time-step this system of equations was also presented.

We then tested our numerical implementation with a thorough range of idealized test cases that have been used to validate other numerical MHD methods. The results were compared to analytical solutions, where available, and the results produced by a grid based MHD scheme. Our implementation produced reliable results for all of the test cases, although it struggled to capture the development speed of the mixing instability. We used the test cases to demonstrate the impact of the additional schemes and that they are required to produce reliable results. The results of the test cases were used to justify our choices for the free parameters that exist in the numerical implementation.

We then used GCMHD+ to study how a primordial seed magnetic field evolves as a galaxy cluster forms. It was shown that our implementation reliably captures the formation of structure. By varying the numerical scheme,

we demonstrated that if the numerical divergence of the magnetic field is allowed to grow it will dominate the evolution of the seed magnetic field. This results in a final magnetic field amplitude that is two orders of magnitude greater than the field amplitude in a simulation where the divergence is minimized. The amplitude and radial profile of the cluster magnetic field shows no trend with the mass or formation history of the cluster. If the resolution of the simulation is sufficient to resolve small enough scales, we showed that the formation of structure is sufficient to amplify a primordial seed magnetic field, with an amplitude below current upper limits, to the μG level observed in galaxy clusters at the current epoch. It was then demonstrated that this magnetic field was capable of reproducing other observations such as the linear power law relation between the X-ray and radio fluxes of a galaxy cluster and the $\sigma_{\rm RM}$ radial profile.

Finally, we used GCMHD+ to examine the impact of the transient spiral structure of an isolated disc galaxy on its magnetic field. We found that our numerical implementation becomes unstable due to the hyperbolic cleaning scheme causing rapid growth in the divergence of the magnetic field. This can be overcome by limiting the change in the magnetic field the cleaning scheme can introduce. It was shown that the global rotation of the galaxy leads to a spiral magnetic field structure with large-scale reversals of the magnetic field. We found that the magnetic field has a negligible impact on the formation of stellar spiral arms. However, the gaseous spiral arms are denser and more tightly wound when a magnetic field is present. If star formation is included in the simulations this may lead to the magnetic field influencing the formation of spiral structures in the galaxy.

6.1 Future work

As the observations of magnetic fields in astrophysical systems has increased they have been shown to be increasingly important to the behaviour of these systems. The origin and impact of the magnetic fields that inhabit the large-scale structure of the cosmic web is not well understood. However, observing facilities that are beginning to take data, such as LOFAR and MWA, and

those currently under development, i.e. SKA, will provide a wealth of higher sensitivity and greater resolution data on the magnetic fields of large-scale structure. Therefore, future work should be targeted at improving the theoretical understanding of large-scale magnetic fields in order to fully utilize the future observational data.

6.1.1 Examining other magnetogenesis mechanisms

We have shown that a primordial seed magnetic field is a viable option for magnetizing the ICM of a galaxy cluster and that it can reproduce the related observable quantities, such as RMs and radio flux. However, there are other proposed mechanisms for seeding the large-scale structure of the Universe with magnetic fields. As the Universe evolves to the current epoch many of these mechanisms may produce a significant contribution to the magnetization of large-scale structures. To fully utilize observations that future facilities will make, the contribution each mechanism makes to the magnetization of large-scale structure must be understood.

Due to the complex interactions between any seed field and the formation of structure, numerical simulations are the most promising method for examining the contributions of the different magnetogenesis mechanisms. The seed fields produced by radiation drag and the Biermann battery mechanism can be derived and additional terms can be included in the induction equation to act as sources of magnetic field in cosmological simulations of structure formation. The magnetic fields ejected by galaxies and AGN during the formation of structure can be modeled as a component of the sub-grid models used to include them in simulations. These sub-grid models can be constrained by observations, such as those of radio loud AGN.

By looking individually at each mechanism the dominant mechanisms for seeding large-scale structure with magnetic fields can be identified. Additionally, this would allow an examination of the impact of magnetic fields produced by mechanisms on the formation of structure. Comparing the predicted emission from simulations that have different magnetogenesis mechanisms with the observations of large-scale magnetic fields from current and future facilities will enhance our understanding of the origin of the largest magnetic fields in the

Universe and their impact on the structures they inhabit.

6.1.2 Magnetization of Filaments and Voids

The observations of magnetic fields in the large-scale structure of the Universe have reached the level of galaxy clusters. Due to material being more diffuse and magnetic fields being weaker in larger scale structures, such as cosmological voids and filaments, it is very difficult to directly detect synchrotron emission and reliably establish RMs from such structures with sensitivity of current observing facilities. This restriction in the observational capability has led to the theory of large-scale magnetogenesis being focused on explaining and reproducing the observations of magnetism in galaxy clusters. As shown in the simulations in Chapter 4, the formation processes of a galaxy cluster erases any memory of the initial seed as the magnetic field evolves to what is observed at the current epoch. There are a range of magnetogenesis mechanisms that have been suggested and studies have shown that they can reproduce the observed properties of the magnetic fields that permeate the ICM (see Dolag and Stasyszyn 2009; Donnert et al. 2009; Xu et al. 2012; Stasyszyn et al. 2013).

Although these mechanisms can produce similar magnetic fields in the ICM of a galaxy cluster, they will seed the cosmic web of structure in very different manners. If the primary magnetogenesis mechanism is primordial in nature then it will seed the entire Universe with magnetism, but if the primary mechanism is AGN then only the nodes of the cosmic web will show substantial magnetic fields. It was noted in (Donnert et al. 2009) that the galactic wind model used to magnetize the galaxy cluster left the surrounding medium significantly less magnetized compared to simulations using a primordial seed field. Running detailed cosmological MHD simulations of the formation of a cosmological filament with different magnetogenesis mechanisms will produce filaments with different magnetic field amplitudes and topologies.

From these simulations the synchrotron emission and RM structure of the cosmic web can be predicted for different magnetogenesis mechanisms. Future radio facilities, such as the SKA, are expected to be able to detect radio emission from the cosmic web. Therefore, comparison of the predictions from

simulations with the observations of the cosmic web will allow magnetogenesis mechanisms to be ruled out and provide a clearer picture of the origin of magnetic fields in large-scale structure.

6.1.3 Non-thermal electrons, high-energy cosmic rays and cosmic magnetism

The magnetic fields permeating the large-scale structure of the Universe are primarily observed by the synchrotron emission and RMs they induce. Synchrotron emission and a component of the RM are produced by the presence of a non-thermal electron population. However, the simulations presented here and the vast majority of cosmological simulations provide no information on non-thermal particle populations. Therefore, when making emission predictions from the simulations, assumptions have to be made about the energy density distribution of non-thermal particle populations. For example, to calculate the radio power of the cluster in Chapter 4 it was assumed that all the electrons were freshly shock accelerated.

A superior approach to these assumptions would be to use a sub-grid model to follow the evolution of the non-thermal particle populations, including electrons and high-energy charged cosmic ray particles, in the simulation. A non-thermal particle population can be evolved by solving the transport equation at all particles in the simulation at each time-step. Additionally, non-thermal particles can be injected into the simulation by supernovae and AGN. Using an algorithm to track the strength and propagation of shock fronts through the simulation, e.g. Pfrommer et al. (2006) and Skillman et al. (2008), the generation and re-acceleration of non-thermal particles due to shocks can be modeled. By tracking the time since the particle last encountered a shock the spectral index and energy density distribution of the non-thermal particle populations at each point can be evolved to take energy losses into account.

Self-consistently evolving a non-thermal particle population, such as relativistic electrons, would produce more accurate emission predictions from the simulations and would provide additional information about the emission, such as its predicted spectral index. Knowledge of both the thermal and non-thermal particle populations would facilitate the embedding of a polarized

radiative transfer code within the simulations. This would provide accurate RM and polarized emission predictions from the simulations. Additionally, non-thermal particles will exert an additional pressure (Vazza et al. 2014) and they will produce turbulence that will amplify any magnetic fields present (Brüggen 2013), which is currently neglected in many simulations. Both of these contributions should be included in cosmological simulations to produce a more reliable evolution of the magnetic field during the formation of structure.

6.1.4 Improving the numerical method

This work has shown that SPMHD can be used to reliably follow the evolution of a seed magnetic field in cosmological simulations of structure formation and be used to study how the formation of spiral structure in a galaxy affects the galactic magnetic field. However, there are significant issues with the particle method of solving the equations of magnetohydrodynamics. Its biggest issue is the failure to maintain the solenoidal condition of the magnetic field, $\nabla \cdot \mathbf{B} = 0$. Currently, ad-hoc additions to the method are required to suppress the growth of the numerical divergence of the magnetic field and to minimize any unphysical effects due to its non-zero value. In addition, the particle method still struggles to correctly resolve mixing instabilities such as the Kelvin-Helmholtz instability. Controlling the divergence of the magnetic field and resolving mixing instabilities are both important for reliably evolving a seed magnetic field during the formation of structure.

Recently codes have been developed that generate an unstructured mesh via the Voronoi tessellation of set of points and then solve the equations of hydrodynamics via the mesh (Springel 2010; Heß and Springel 2010). The points are allowed to move with local flow and so these are Lagrangian formulations of continuum hydrodynamics. This approach does not suffer from mixing problems inherent to SPH. Grid codes use the constrained transport method (Evans and Hawley 1988) to maintain the solenoidal condition of the magnetic field to machine precision and it has recently been shown that this technique can be extended to unstructured Voronoi meshes (Mocz et al. 2014). Therefore, the numerical implementation could be improved by using the par-

ticles to generate an unstructured mesh at each time step and then solving the MHD equations over this mesh. This would guarantee to suppress the numerical divergence of the magnetic field to machine precision and would remove the need for ad-hoc additions that may have undesirable and unknown side effects.

Appendix A

Derivation of the Biermann battery

In section 1.4.1 the induction equation, (1.28), was derived from Maxwell's equations, assuming that Ohm's law took the form $\mathbf{J} = \sigma[\mathbf{E} + (\mathbf{v} \times \mathbf{B})/c]$. This produced an equation for the rate of change of the magnetic field that was dependant on initial magnetic field and had no sources of magnetic field. However, the assumed form of Ohm's law was too simplistic. To obtain the correct description of the plasma the Boltzmann equation is required. This is an equation for the evolution, with time, of a particle's distribution function, f, and takes the form

$$\frac{\partial f}{\partial t} + \mathbf{w}\nabla \cdot f + \frac{\mathbf{F}}{m}\frac{\partial f}{\partial \mathbf{w}} = \left.\frac{\partial f}{\partial t}\right|_{\text{col}}, \tag{A.1}$$

where $\mathbf{w}$ is the particles velocity, $\mathbf{F}$ is an externally applied force, m is the particle mass and $(\partial f/\partial t)_{\text{col}}$ is the change in f due to collisions between particles. The function, f, is the density of particles in the phase space and is a function of position, velocity and time. For an electron, if $f = n_e m_e \mathbf{w}_e$ and the Lorentz force is applied as an external force, equation A.1 becomes

$$\frac{\partial(n_e m_e \mathbf{w}_e)}{\partial t} + \nabla \cdot (n_e m_e \mathbf{w}_e \mathbf{w}_e) + \frac{q(\mathbf{E} + \frac{1}{c}(\mathbf{w}_e \times \mathbf{B}))}{m_e}\frac{\partial(n_e m_e \mathbf{w}_e)}{\partial \mathbf{w}} = \left.\frac{\partial(n_e m_e \mathbf{w}_e)}{\partial t}\right|_{\text{col}}, \tag{A.2}$$

where q is the charge of the electron, $\mathbf{E}$ is the electric field and $\mathbf{B}$ is the magnetic field. The first term of this equation can be rewritten such that

$$n_e m_e \frac{\partial \mathbf{w}_e}{\partial t} + \mathbf{w}_e \frac{\partial(n_e m_e)}{\partial t} + \nabla \cdot (n_e m_e \mathbf{w}_e \mathbf{w}_e) + q\left(\mathbf{E} + \frac{1}{c}(\mathbf{w}_e \times \mathbf{B})\right)\frac{\partial(n_e \mathbf{w}_e)}{\partial \mathbf{w}} = \left.\frac{\partial(n_e m_e \mathbf{w}_e)}{\partial t}\right|_{\text{col}}. \tag{A.3}$$

The velocity in the second term on the left hand side can be split into a mean bulk velocity, $\mathbf{v}_e$, and a random velocity component, $\mathbf{u}_e$, such that $\mathbf{w}_e = \mathbf{v}_e + \mathbf{u}_e$ and

$$n_e m_e \frac{\partial \mathbf{w}_e}{\partial t} + \mathbf{w}_e \frac{\partial (n_e m_e)}{\partial t} + \nabla \cdot (n_e m_e \mathbf{v}_e \mathbf{v}_e) + \nabla \cdot (n_e m_e \mathbf{u}_e \mathbf{u}_e) + q\left(\mathbf{E} + \frac{1}{c}(\mathbf{w}_e \times \mathbf{B})\right) \frac{\partial (n_e \mathbf{w}_e)}{\partial \mathbf{w}} = -n_e m_e \left.\frac{\partial \mathbf{w}_e}{\partial t}\right|_{\text{col}} . \quad \text{(A.4)}$$

For an isotropic distribution of random velocities, this equation can be rearranged to obtain

$$n_e m_e \frac{\partial \mathbf{w}_e}{\partial t} + \mathbf{w}_e \frac{\partial (n_e m_e)}{\partial t} + n_e m_e \mathbf{v}_e \cdot \nabla \mathbf{v}_e + \mathbf{v}_e \nabla \cdot (n_e m_e \mathbf{v}_e) + \nabla P_e + e n_e \left(\mathbf{E} + \frac{1}{c}(\mathbf{v}_e \times \mathbf{B})\right) = -n_e m_e \frac{\mathbf{v}_e - \mathbf{v}_i}{\tau_{ei}} , \quad \text{(A.5)}$$

where $\mathbf{v}_i$ is the velocity of the ions in the plasma and τ_{ei} is the collisional time between the ions and the electrons. The second and fourth terms form a continuity equation and are equal to zero. Assuming $n_e = n_i$ and using the total current density, $\mathbf{j} = e(n_i v_i - n_e v_e)/c$, produces

$$\frac{m_e}{e}\left(\frac{\partial \mathbf{v}_e}{\partial t} + \mathbf{v}_e \cdot \nabla \mathbf{v}_e\right) + \frac{1}{e n_e} \nabla P_e + \left(\mathbf{E} + \frac{1}{c}(\mathbf{v}_e \times \mathbf{B})\right) = \eta \mathbf{j} , \quad \text{(A.6)}$$

where $\eta = m_e c / \tau_{ei} n_e e^2$ is the resistivity of the medium. Neglecting the the electron momentum as it is small and rearranging for $\mathbf{E}$

$$\mathbf{E} = -\frac{1}{e n_e} \nabla P_e - \frac{1}{c}(\mathbf{v}_e \times \mathbf{B}) + \eta \mathbf{j} . \quad \text{(A.7)}$$

This can now be substituted into Faraday's law, equation (1.23), to produce the equation for the rate of change of $\mathbf{B}$ with time

$$\nabla \times \left(-\frac{1}{e n_e} \nabla P_e - \frac{1}{c}(\mathbf{v}_e \times \mathbf{B}) + \eta \mathbf{j}\right) = -\frac{1}{c}\frac{\partial \mathbf{B}}{\partial t} , \quad \text{(A.8)}$$

$$\frac{\partial \mathbf{B}}{\partial t} = \nabla \times (\mathbf{v}_e \times \mathbf{B}) + \frac{c}{e n_e^2} \nabla n_e \times \nabla P_e - c\eta \nabla \times \mathbf{j} . \quad \text{(A.9)}$$

Using $\mathbf{j} = (\nabla \times \mathbf{B})/c$ and vector identities yields the induction equation, but with an additional source term that is not dependant on the magnetic field

$$\frac{\partial \mathbf{B}}{\partial t} = (\mathbf{B} \cdot \nabla)\mathbf{v}_e - \mathbf{B}(\nabla \cdot \mathbf{v}_e) + \frac{c}{e n_e^2} \nabla n_e \times \nabla P_e - \eta \nabla^2 \mathbf{B} . \quad \text{(A.10)}$$

Under the assumption that the plasma is in thermal equilibrium this equation becomes computationally calculable. This removes the need to calculate the electron density and pressure for each particle in the simulation and allows the use of the standard SPH density and pressure instead

$$\frac{P_e}{n_e} = \frac{P}{n(1+\chi)} = \frac{mP}{\rho(1+\chi)}\,, \tag{A.11}$$

where χ is the ionization fraction. Therefore, the source term takes the form

$$\left(\frac{\partial \mathbf{B}}{\partial t}\right)^{\text{batt}} = \frac{mc}{e(1+\chi)}\frac{\nabla\rho \times \nabla P}{\rho^2}\,, \tag{A.12}$$

and more commonly known as the Biermann battery mechanism. Using this additional term in the induction equation, simulations that initial start with no magnetic field will generate a magnetic field via the cross of pressure and density gradients.

Appendix B

Calculating Gravity via a Tree Code

The self gravity of a fluid is a long range N body interaction. This kind of problem can be represented as a solution to N 2nd order differential equations, where the velocities and positions of the particles, as a function of time, give the global macroscopic properties of the fluid. The range of the interaction means that it will significantly interact with many particles and so a particle's interaction with every other particle must be considered. This leads to a particle-particle calculation of order $O(N^2)$, which limits the number of particles which can be simulated to a relatively small amount. A way to get reduce the computational time required to calculated a long range interaction is to use a hierarchical tree code, first developed by Barnes and Hut (1986).

The octagonal tree code works by enclosing the whole system in a box. If this box contains more than one particle it will divide into boxes with a length, width and depth equal to half the original box, for a 2-D example see Fig B.1. The 3D system is now contained in 8 cells. Each of these cells is then analysed in turn for the number of particles present in it. If the number present is greater than one it will also divide in to 8 cells with half the dimensions of the parent. This process is continued until each cell contains either one or zero particles. This allows the tree method to automatically adjusts itself to the distribution of the particles in the system. A galaxy cluster simulation will have a steep gradient in the middle and this is accounted for by the tree method. The division of space is the book keeping structure of the code, with the simulation cell as the root of the tree. If the cell contains daughter cells

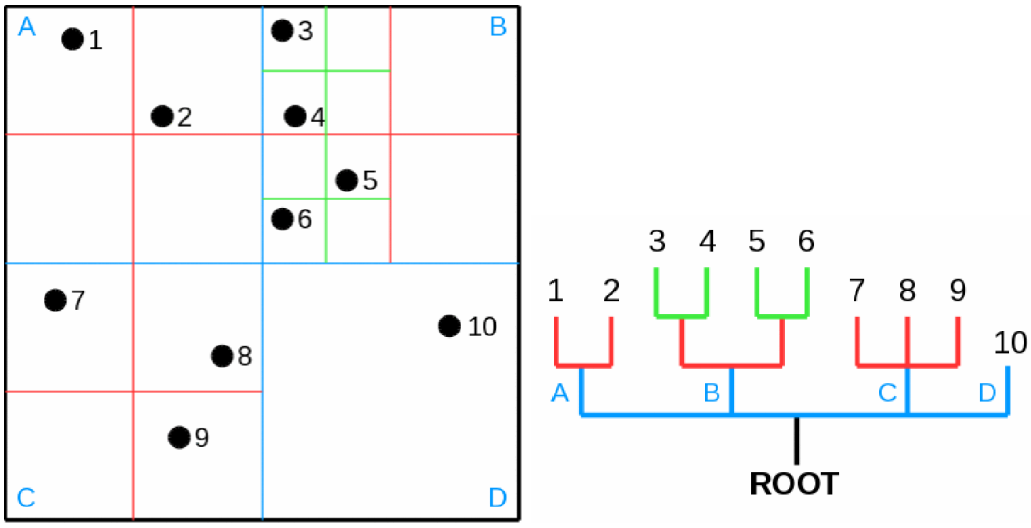

Fig. B.1: The left panel shows how a 2D system is split into cells containing only one particle per cell. The root cell is divided into 4 daughter cells; A, B, C and D as it contains more than 1 particle. Each of these is the inspected and A, B and C are labelled twigs and further divided. Cell D only contains one particle and so is labelled as a leaf. The right panel shows the resulting tree that develops by splitting the system in such a way.

it is labelled as a twig, while cells with one particle present in it is labelled a leaf. Cells containing zero particles are ignored, reducing any time spent on empty space. Each leaf has an identifier, a pointer to the parent cell and a label attached to it. The label contains all of the physical quantities, e.g. mass or position, associated with the particle contained within it. The root of the tree has an identifier as a twig and the number of non-empty daughters associated with it. Twigs have the same information as the root attached to them plus a pointer to the parent cell.

The calculation time of such a tree can be estimated by the number of divisions to reach a cell. The average volume of a cell is the volume of the simulation over the number of particles present in it. The average length of a cell is given by $(V^{\frac{1}{3}}/2)$ and so

$$\left(\frac{1}{n}\right)^{1/3} = \left(\frac{1}{2}\right)^{x} . \tag{B.1}$$

This means that the height of a tree, x, is of order $log_2(N^{\frac{1}{3}})$. This can be

approximated to

$$log_2(N^{\frac{1}{3}}) = \frac{1}{3log_2} log(N) \simeq log(N)\,. \tag{B.2}$$

For a system of N particles the time required to compute the gravitational interaction of the system is of order $O(N\log(N))$.

The labels of each leaf define the physical quantities associated to the particle present in its cell. The physical quantities associated to each twig, e.g. sum of mass, centre of mass, etc, can then be calculated from the twigs and leaves attached to it. The twig can then be treated as a pseudo-particle, which can be used to define larger pseudo-particles at the next level of the tree. This allows the information to propagate backwards through the tree to the root. This can used as a check to see if the tree is producing the correct mass for the system. When the force calculation on a particle is carried out, near particles are still directly summed over, but remote particles are included via the use of these pseudo-particles. Therefore, the calculation still retains the advantages of particle-particle calculations, while reducing the overall calculation time. In saving this time no resolution is lost or geometric constraint imposed on the system, as it is achieved via approximations to the potential. As long as these approximation errors are of similar magnitude to the numerical errors (round off, truncation and discreteness errors) then this potential should produce accurate results.

The tree structure distinguishes close particles from distant ones without the need to calculate the distance. Whether a particle interacts directly with another particle or as a constituent of a pseudoparticle is a flexible choice. The size of the current twig or leaf is compared with the distance from the particle by the relation

$$\frac{S}{d} \leq \theta\,, \tag{B.3}$$

where S is the size of the current node, d is the distance from the particle and θ is the tolerance parameter. If this relation is fulfilled by the node then its internal structure is ignored and the force is calculated using the twig properties. The value of θ chosen is a compromise and depends on the simulation being run. In the limit of $\theta = 0$ all particles individually contributed

to the force calculation and it takes on order $O(N^2)$ to compute. As $\theta \to \infty$ spatial resolution is lost and the force calculation is very fast but has low accuracy. The choice of θ depends on the problem, but a choice of $\theta \sim 0.1 \to 1$ proves to be a practical one in most cases.

The grouping of particles to speed up the calculation leads to a loss of information about the spatial distribution of the particles, causing an error in the potential. This information can be recovered using a multipole expansion of the force on a particle due to a pseudo-particle:

$$\begin{aligned} F(R - r_i) \simeq F(R) \quad & -r_i \nabla F(R) \quad + \tfrac{1}{2} r_i r_i \nabla\nabla F(R) \quad + \cdots , \\ [\text{Monopole} \quad & + \text{Dipole} \quad + \text{Quadrupole} \quad + \cdots] , \end{aligned} \tag{B.4}$$

where R is the vector from the centre of mass of the pseudo-particle to the particle and r_i is the vector from the centre of the pseudo-particle to its individual particle constituents. At a high enough order this will contain the total information on the particle distribution. This expansion is done from the highest level of the tree to the root. For dynamical simulations, i.e. time evolving, good accuracy is obtained by including dipole and quadrupole moments. This means that the root contains a 2nd order expansion of the system. Including moments produces a bigger increase in accuracy than reducing θ. The truncation error from this series increases monotonically with θ, which suggests a practical upper limit of $\theta = 1$ for any simulation. The expansion becomes economical for systems where $N \geq 10^4 - 10^5$. Dynamical systems recalculate the tree structure every time step. The creation of the structure is only a few percent of the run time for $\theta \leq 1$. This ensures that the whole system is enclosed by the root cell.

Appendix C

MHD shock tube test parameters

Test	N_L	ρ_L	V_L	B_L	P_L	N_R	ρ_R	V_R	B_R	P_R
1A	540	1.0	(10.0,0.0,0.0)	$(5.0,5.0,0.0)/(4\pi)^{0.5}$	20.0	540	1.0	$(-10.0,0.0,0.0)$	$(5.0,5.0,0.0)/(4\pi)^{0.5}$	1.0
1B	1000	1.0	(0.0,0.0,0.0)	$(3.0,5.0,0.0)/(4\pi)^{0.5}$	1.0	100	0.1	(0.0,0.0,0.0)	$(3.0,2.0,0.0)/(4\pi)^{0.5}$	10.0
2A	540	1.08	(1.2,0.01,0.5)	$(2.0,3.6,2.0)/(4\pi)^{0.5}$	0.95	500	1.0	(0.0,0.0,0.0)	$(2.0,4.0,2.0)/(4\pi)^{0.5}$	1.0
2B	1000	1.0	(0.0,0.0,0.0)	$(3.0,6.0,0.0)/(4\pi)^{0.5}$	1.0	100	0.1	(0.0,2.0,1.0)	$(3.0,1.0,0.0)/(4\pi)^{0.5}$	10.0
3A	550	0.1	(50.0,0.0,0.0)	$-(0.0,1.0,2.0)/(4\pi)^{0.5}$	0.4	550	0.1	(0.0,0.0,0.0)	$(0.0,1.0,2.0)/(4\pi)^{0.5}$	0.2
3B	550	1.0	$(-1.0,0.0,0.0)$	(0.0,1.0,0.0)	1.0	550	1.0	(1.0,0.0,0.0)	(0.0,1.0,0.0)	1.0
4A	1000	1.0	(0.0,0.0,0.0)	(1.0,1.0,0.0)	1.0	200	0.2	(0.0,0.0,0.0)	(1.0,0.0,0.0)	0.1
4B	400	0.4	$(-0.67,0.98,0.0)$	(1.3,0.0025,0.0)	0.53	1000	1.0	(0.0,0.0,0.0)	(1.3,1.0,0.0)	1.0
4C	650	0.65	$(0.67,-0.26,0.0)$	(0.75,0.55,0.0)	0.5	1000	1.0	$(0.4,-0.94,0.0)$	(0.75,0.0,0.0)	0.75
4D	1000	1.0	(0.0,0.0,0.0)	(0.7,0.0,0.0)	1.0	300	0.3	(0.0,0.0,1.0)	(0.7,1.0,0.0)	0.2
5A	960	1.0	(0.0,0.0,0.0)	(0.75,1.0,0.0)	1.0	120	0.125	(0.0,0.0,0.0)	$(0.75,-1.0,0.0)$	0.1

Table C.1: Summary of the initial conditions for the 1D MHD shock tube tests presented in section 3.2.1, where N is the number of particles, ρ is the density, V is the 3D velocity structure, B is the 3D magnetic field structure and P is the pressure. L and R denote the left and right halves of the simulation.

Bibliography

Abramowski, A., Acero, F., Aharonian, F. and et al. (H.E.S.S. collaboration) (2012), Measurement of the extragalactic background light imprint on the spectra of the brightest blazars observed with H.E.S.S., *A&A* **550**, A4.

Agertz, O., Moore, B., J., S., Potter, D., Miniati, F., Read, J., Mayer, L., Gawryszczak, A., Kravtsov, A., Nordlund, Å., Pearce, F., Quilis, V., Rudd, D., Springel, V., Stone, J., Tasker, E., Teyssier, R., Wadsley, J. and Walder, R. (2007), Fundamental differences between SPH and grid methods, *MNRAS* **380**, 963–978.

Alfvén, H. (1949), On the Solar Origin of Cosmic Radiation, *Physical Review* **75**, 1732–1735.

Aloisio, A., Bacci, C., Bao, K. Z., Barone, F., Bartoli, B., Bernardini, P., Bleve, C., Branchini, P., Bussino, S., Calloni, E. and et al. (2001), The ARGO-YBJ experiment in Tibet, *Nuovo Cimento C Geophysics Space Physics C* **24**, 739.

Arshakian, T. G., Beck, R., Krause, M. and Sokoloff, D. (2009), Evolution of magnetic fields in galaxies and future observational tests with the Square Kilometre Array, *A&A* **494**, 21–32.

Arshakian, T. G., Stepanov, R., Beck, R., Krause, M. and Sokoloff, D. (2011), Modeling the total and polarized emission in evolving galaxies: "Spotty" magnetic structures, *Astronomische Nachrichten* **332**, 524–536.

Atwood, W. B., Abdo, A. A., Ackermann, M., Althouse, W., Anderson, B., Axelsson, M., Baldini, L., Ballet, J., Band, D. L., Barbiellini, G. and et al. (2009), The Large Area Telescope on the Fermi Gamma-Ray Space Telescope Mission, *ApJ* **697**, 1071–1102.

Balsara, D. S. (1995), von Neumann stability analysis of smooth particle hydrodynamics – suggestions for optimal algorithms, *J. Comp. Phys.* **121**, 357–372.

Barnes, D. J., Kawata, D. and Wu, K. (2012), Cosmological simulations using GCMHD+, *MNRAS* **420**, 3195–3212.

Barnes, J. and Hut, P. (1986), A hierarchical O(N log N) force-calculation algorithm, *Nature* **324**, 446–449.

Barrow, J. D., Ferreira, P. G. and Silk, J. (1997), Constraints on a Primordial Magnetic Field, *Physical Review Letters* **78**, 3610–3613.

Beck, A. M., Dolag, K., Lesch, H. and Kronberg, P. P. (2013), Strong magnetic fields and large rotation measures in protogalaxies from supernova seeding, *MNRAS* **435**, 3575–3586.

Beck, R. (1982), The magnetic field in M31, *A&A* **106**, 121–132.

Beck, R. (2002), The Role of Magnetic Fields in Spiral Galaxies, *arXiv:0212288* .

Beck, R. (2007), Magnetism in the spiral galaxy NGC 6946: magnetic arms, depolarization rings, dynamo modes, and helical fields, *A&A* **470**, 539–556.

Beck, R. (2012), Magnetic fields in Galaxies, *Space Sci. Rev.* **166**, 215–230.

Beck, R. and Hoernes, P. (1996), Magnetic spiral arms in the galaxy NGC6946, *Nature* **379**, 47–49.

Bennett, C. L., Bay, M., Halpern, M., Hinshaw, G., Jackson, C., Jarosik, N., Kogut, A., Limon, M., Meyer, S. S., Page, L., Spergel, D. N., Tucker, G. S., Wilkinson, D. T., Wollack, E. and Wright, E. L. (2003), The Microwave Anisotropy Probe Mission, *ApJ* **583**, 1–23.

Benz, W. (1990), *Smoothed Particle Hydrodynamics - A review*, Kluwer, pp.269–288.

Bernet, M. L., Miniati, F., Lilly, S. J., Kronberg, P. P. and Dessauges-Zavadsky, M. (2008), Strong magnetic fields in normal galaxies at high redshift, *Nature* **454**, 302–304.

Bertschinger, E. (1985), Self-similar secondary infall and accretion in an Einstein-de Sitter universe, *ApJS* **58**, 39–65.

Bertschinger, E. (2001), Multiscale Gaussian Random Fields and Their Application to Cosmological Simulations, *ApJS* **137**, 1–20.

Biermann, L. (1950), Über den Ursprung der Magnetfelder auf Sternen und im interstellaren Raum (miteinem Anhang von A. Schlüter), *Zeitschrift Naturforschung Teil A* **5**, 65.

Bonafede, A., Dolag, K., Stasyszyn, F., Murante, G. and Borgani, S. (2011), A non-ideal magnetohydrodynamic GADGET: simulating massive galaxy clusters, *MNRAS* **418**, 2234–2250.

Bonafede, A., Feretti, L., Murgia, M., Govoni, F., Giovannini, G., Dallacasa, D., Dolag, K. and Taylor, G. B. (2010), The Coma cluster magnetic field from Faraday rotation measures, *A&A* **513**, 30–50.

Bonvin, C., Durrer, R. and Maartens, R. (2014), Can primordial magnetic fields be the origin of the BICEP2 data?, *ArXiv e-prints* .

Børve, S., Omang, M. and Trulsen, J. (2001), Regularized Smoothed Particle Hydrodynamics: A New Approach to Simulating Magnetohydrodynamic Shocks, *ApJ* **561**, 82–93.

Børve, S., Omang, M. and Trulsen, J. (2004), Two-dimensional MHD Smoothed Particle Hydrodynamics Stability Analysis, *ApJS* **153**, 447–462.

Børve, S., Omang, M. and Trulsen, J. (2006), Mulitdimensional MHD Shock Tests of Regularized Smoothef Particle Hydrodynamics, *ApJ* **652**, 1306–1317.

Brackbill, J. U. and Barnes, D. C. (1980), The effect of nonzero product of magnetic gradient and B on the numerical solution of the magnetohydrodynamic equations, *J. Comp. Phys.* **35**, 426–430.

Brentjens, M. A. and de Bruyn, A. G. (2005), Faraday rotation measure synthesis, *A&A* **441**, 1217–1228.

Brookshaw, L. (1985), A method of calculating radiative heat diffusion in particle simulations, *Proceedings of the Astronomical Society of Australia* **6**, 207–210.

Brown, S. and Rudnick, L. (2011), Diffuse radio emission in/around the Coma cluster: beyond simple accretion, *MNRAS* **412**, 2–12.

Brüggen, M. (2013), Magnetic field amplification by cosmic ray-driven turbulence - I. Isotropic CR diffusion, *MNRAS* **436**, 294–303.

Burn, B. J. (1966), On the depolarization of discrete radio sources by Faraday dispersion, *MNRAS* **133**, 67–83.

Byleveld, S. E. and Pongracic, H. (1996), The influence of magnetic fields on star formation, *PASA* **13**, 71–74.

Carilli, C. L. and Taylor, G. B. (2002), Cluster Magnetic Fields, *ARA&A* **40**, 319–348.

Clarke, T. E., Kronberg, P. P. and Böbringer, H. (2001), A New Radio-X-Ray Probe of Galaxy Cluster Magnetic Fields, *ApJ* **547**, L111–L114.

Csikor, F., Fodor, Z. and Heitger, J. (1998), The strength of the electroweak phase transition at $m_H \tilde{}$ 80 GeV, *Physics Letters B* **441**, 354–362.

Cullen, L. and Dehnen, W. (2010), Inviscid smoothed particle hydrodynamics, *MNRAS* **408**, 669–683.

Davis, Jr., L. and Greenstein, J. L. (1951), The Polarization of Starlight by Aligned Dust Grains, *ApJ* **114**, 206.

de Forcrand, P. and Philipsen, O. (2003), QCD phase diagram for small densities from simulations at imaginary μ, *Nuclear Physics B Proceedings Supplements* **119**, 535–537.

Dedner, A., Kemm, F., Krönew, D., Munz, C. D., Schnitzer, T. and Wesenberg, M. (2002), Hyperbolic Divergence Cleaning for the MHD Equations, *J. Comp. Phys.* **175**, 645–673.

Dehnen, W. and Aly, H. (2012), Improving convergence in smoothed particle hydrodynamics simulations without pairing instability, *MNRAS* **425**, 1068–1082.

Dolag, K., Bartelmann, M. and Lesch, H. (1999), SPH simulations of magnetic fields in galaxy clusters, *A&A* **348**, 351–363.

Dolag, K. and Stasyszyn, F. (2009), An MHD GADGET for cosmological simulations, *MNRAS* **398**, 1678–1697.

D'Onghia, E., Vogelsberger, M. and Hernquist, L. (2013), Self-perpetuating Spiral Arms in Disk Galaxies, *ApJ* **766**, 34–47.

Donnert, J., Dolag, K., Lesch, H. and Müller, E. (2009), Cluster magnetic fields from galactic outflows, *MNRAS* **392**, 1008–1021.

Duric, N. (1990), Equipartition - Fact or Fiction, *IAU Symposium* **140**, 235–236.

Durrer, R. (2007), Cosmic magnetic fields and the CMB, *New A Rev.* **51**, 275–280.

Durrer, R. and Neronov, A. (2013), Cosmological magnetic fields: their generation, evolution and observation, *A&A Rev.* **21**, 62–170.

Durrer, R., Kahniashvilli, T. and Yates, A. (1998), Microwave background anisotropies from Alfvén waves, *Phys. Rev. D* **58**, 123–141.

Eckart, C. (1960), Variation Principles of Hydrodynamics, *Physics of Fluids* **3**, 421–427.

Evans, C. R. and Hawley, J. F. (1988), Simulation of magnetohydrodynamic flows - A constrained transport method, *ApJ* **332**, 659–677.

Feretti, L., Giovannini, G., Govoni, F. and Murgia, M. (2012), Clusters of galaxies: observational properties of the diffuse radio emission, *A&A Rev.* **20**, 54–113.

Fillmore, J. A. and Goldreich, P. (1984), Self-similar gravitational collapse in an expanding universe, *ApJ* **281**, 1–8.

Fletcher, A. (2010), Magnetic fields in Nearby Galaxies, *in Astronomical Society of the Pacific Conference Series*, Vol. 438, pp.197–210.

Fletcher, A., Beck, R., Berkhuijsen, A. M. and Shukurov, A. (2000), The regular magnetic fields of M31 and M33, from radio polarisation observations, *in Proceedings 232. WE-Heraeus Seminar*, pp.201–204.

Fletcher, A., Beck, R., Shukurov, A., Berkhuijsen, E. M. and Horellou, C. (2011), Magnetic fields and spiral arms in the galaxy M51, *MNRAS* **412**, 2396–2416.

Frenk, C. S., White, S. D. M., Bode, P., Bond, J. R., Bryan, G. L., Cen, R., Couchman, H. M. P., Evrard, A. E., Gnedin, N., Jenkins, A., Khokhlov, A. M., Klypin, A., Navarro, J. F., Norman, M. L., Ostriker, J. P., Owen, J. M., Pearce, F. R., Pen, U.-L., Steinmetz, M., Thomas, P. A., Villumsen, J. V., Wadsley, J. W., Warren, M. S., Xu, G. and Yepes, G. (1999), The Santa Barbara Cluster Comparison Project: A Comparison of Cosmological Hydrodynamics Solutions, *ApJ* **525**, 554–582.

Fujii, M. S., Baba, J., Saitoh, T. R., Makino, J., Kokubo, E. and Wada, K. (2011), The Dynamics of Spiral Arms in Pure Stellar Disks, *ApJ* **730**, 109–122.

Fulk, D. A. and Quinn, D. W. (1996), An analysis of 1-D Smoothed Particle Hydrodynamic Kernels, *J. Comp. Phys.* **126**, 165–180.

Geng, A., Beck, A. M., Dolag, K., Bürzle, F., Beck, M. C., Kotarba, H. and Nielaba, P. (2012), Synthetic X-ray and radio maps for two different models of Stephan's Quintet, *MNRAS* **426**, 3160–3177.

Gingold, R. A. and Monaghan, J. J. (1977), SPH elastic dynamics, *Computer methods in applied mechanics and engineering* **190**, 6641–6662.

Gould, R. J. and Schréder, G. (1966), Opacity of the Universe to High-Energy Photons, *Physical Review Letters* **16**, 252–254.

Govoni, F., Enßlin, T. A., Feretti, L. and Giovannini, G. (2001), A comparison of radio and X-ray morphologies of four clusters of galaxies containing radio halos., *A&A* **369**, 441–449.

Govoni, F., Markevitch, M., Vikhlinin, A., van Speybroeck, L., Feretti, L. and Giovannini, G. (2004), Chandra Temperature Maps for Galaxy Clusters with Radio Halos, *ApJ* **605**, 695–708.

Grand, J. J., Kawata, D. and Cropper, M. (2012), The dynamics of stars around spiral arms, *MNRAS* **421**, 1529–1538.

Grasso, D. and Rubinstein, H. R. (2001), Magnetic fields in the early Universe, *Phys. Rep.* **348**, 163–266.

Greenstein, G. (1969), Primordial Helium Production in "Magnetic" Cosmologies, *Nature* **223**, 938–939.

Gregori, G., Ravasio, A., Murphy, C. D., Schaar, K., Baird, A., Bell, A. R., Benuzzi-Mounaix, A., Bingham, R., Constantin, C., Drake, R. P., Edwards, M., Everson, E. T., Gregory, C. D., Kuramitsu, Y., Lau, W., Mithen, J., Niemann, C., Park, H.-S., Remington, B. A., Reville, B., Robinson, A. P. L., Ryutov, D. D., Sakawa, Y., Yang, S., Woolsey, N. C., Koenig, M. and Miniati, F. (2012), Generation of scaled protogalactic seed magnetic fields in laser-produced shock waves, *Nature* **481**, 480–483.

Grojean, C., Servant, G. and Wells, J. D. (2005), First-order electroweak phase transition in the standard model with a low cutoff, *Phys. Rev. D* **71**, 036001.

Habe, A., Uchida, Y., Ikeuchi, S. and Pudritz, R. E. (1991), Triggering the collapse of self-gravitating clouds by torsional Alfven waves, *PASJ* **43**, 703–718.

Hale, G. E. (1908), On the Probable Existence of a Magnetic Field in Sun-Spots, *ApJ* **28**, 315.

Hall, J. S. (1949), Observations of the Polarized Light from Stars, *Science* **109**, 166–167.

Han, J. L. and Qiao, G. J. (1994), The magnetic field in the disk of our Galaxy, *A&A* **288**, 759–772.

Hanasz, M., Wóltański, D. and Kowalik, K. (2009), Global Galactic Dynamo Driven by Cosmic Rays and Exploding Magnetized Stars, *ApJ* **607**, L155–L159.

Henyey, F. S. (1982), Canonical construction of a Hamiltonian for dissipation-free magnetohydrodynamics, *Phys. Rev. A* **26**, 480–483.

Herquist, L. and Katz, N. (1989), TREESPH - A unification of SPH with the hierarchical tree method, *ApJS* **70**, 419–446.

Heß, S. and Springel, V. (2010), Particle hydrodynamics with tessellation techniques, *MNRAS* **406**, 2289–2311.

Hiltner, W. A. (1949), Polarization of Light from Distant Stars by Interstellar Medium, *Science* **109**, 165.

Hinshaw, G., Larson, D., Komatsu, E., Spergel, D. N., Bennett, C. L., Dunkley, J., Nolta, M. R., Halpern, M., Hill, R. S., Odegard, N., Page, L., Smith, K. M., Weiland, J. L., Gold, B., Jarosik, N., Kogut, A., Limon, M., Meyer, S. S., Tucker, G. S., Wollack, E. and Wright, E. L. (2013), Nine-year Wilkinson Microwave Anisotropy Probe (WMAP) Observations: Cosmological Parameter Results, *ApJS* **208**, 19–43.

Hoang, T. and Lazarian, A. (2008), Radiative torque alignment: essential physical processes, *MNRAS* **388**, 117–143.

Hosking (2002), The Role of Magnetic Fields in Star Formation, PhD thesis, Cardiff University, UK.

Huber, S. J. and Konstandin, T. (2008), Gravitational wave production by collisions: more bubbles, *J. Cosmology Astropart. Phys.* **9**, 22.

Huber, S. J., Konstandin, T., Prokopec, T. and Schmidt, M. G. (2007), Baryogenesis in the MSSM, nMSSM and NMSSM, *Nuclear Physics A* **785**, 206–209.

Ichiki, K., Takahashi, K., Ohno, H., Hanayama, H. and Sugiyama, N. (2006), Cosmological Magnetic Field: A Fossil of Density Perturbations in the Early Universe, *Science* **311**, 827–829.

Ichiki, K., Takahashi, K., Sugiyama, N., Hanayama, H. and Ohno, H. (2007), Generation of Large-Scale Magnetic Fields from Primordial Density Fluctuations, *Modern Physics Letters A* **22**, 2091–2098.

Jain, R. K. and Sloth, M. S. (2012), Consistency relation for cosmic magnetic fields, *Phys. Rev. D* **86**, 123528.

Jones, C. A. (2011), Planetary Magnetic Fields and Fluid Dynamos, *Annual Review of Fluid Mechanics* **43**, 583–614.

Kahniashvili, T., Tevzadze, A. G., Brandenburg, A. and Neronov, A. (2013), Evolution of primordial magnetic fields from phase transitions, *Phys. Rev. D* **86**, 083007.

Kandus, A., Kunze, K. E. and Tsagas, C. G. (2011), Primordial magnetogenesis, *Phys. Rep.* **505**, 1–58.

Kawata, D. and Gibson, B. K. (2003), GCD+: anew chemodynamical approach to modelling supernovae and chemical enrichment in elliptical galaxies, *MNRAS* **340**, 908–922.

Kawata, D., Okamoto, T., Gibson, B. K., Barnes, D. J. and Cen, R. (2013), Calibrating an updated smoothed particle hydrodynamics scheme with GCD+, *MNRAS* **428**, 1968–1979.

Kazes, I., Troland, T. H. and Crutcher, R. M. (1991), Zeeman splitting of H I toward high velocity clouds and NGC 1275, *A&A* **245**, L17–L19.

Kim, S.-H. and Martin, P. G. (1995), The size distribution of interstellar dust particles as determined from polarization: Spheroids, *ApJ* **444**, 293–305.

Kneiske, T. M. (2008), Gamma-Ray Background: A Review, *Chinese Journal of Astronomy and Astrophysics Supplement* **8**, 219–225.

Knight, T. M. (2013), Smoothed particle magnetohydrodynamics for the solar corona, PhD thesis, Aberystwyth University, Aberystwyth, Wales.

Komatsu, E., Dunkley, J., Nolta, M. R., Bennett, C. L., Gold, B., Hinshaw, G., Jarosik, N., Larson, D., Limon, M., Page, L., Spergel, D. N., Halpern, M., Hill, R. S., Kogut, A., Meyer, S. S., Tucker, G. S., Weiland, J. L., Wollack, E. and Wright, E. L. (2009), Five-Year Wilkinson Microwave Anisotropy Probe Observations: Cosmological Interpretation, *ApJS* **180**, 330–376.

Kovac, J. M., Leitch, E. M., Pryke, C., Carlstrom, J. E., Halverson, N. W. and Holzapfel, W. L. (2002), Detection of polarization in the cosmic microwave background using DASI, *Nature* **420**, 772–787.

Krause, M. (2014), Magnetic fields and halos in spiral galaxies, *ArXiv e-prints* .

Kravtsov, A. V. and Borgani, S. (2012), Formation of Galaxy Clusters, *ARA&A* **50**, 353–409.

Kulsrud, R. M. (2011), A Critical Review of Galactic Dynamos, *ARA&A* **37**, 37–64.

Kunze, K. E. (2010), Large scale magnetic fields from gravitationally coupled electrodynamics, *Phys. Rev. D* **81**, 043526.

Langer, M., Aghanim, N. and Puget, J. L. (2005), Magnetic fields from reionisation, *A&A* **443**, 367–372.

Langer, M., Puget, J. L. and Aghanim, N. (2003), Cosmological magnetogenesis driven by radiation pressure, *Phys. Rev. D* **67**, 043505.

Lazarian, A. (1997), Gold Alignment and Internal Dissipation, *ApJ* **483**, 296.

Lesch, H. and Chiba, M. (1995), Protogalactic evolution and magnetic fields, *A&A* **297**, 305–310.

Li, H. B. and Henning, T. (2011), The alignment of molecular cloud magnetic fields with the spiral arms in M33, *Nature* **479**, 499–501.

Lin, C. C. and Shu, F. H. (1964), On the Spiral Structure of Disk Galaxies, *ApJ* **140**, 646–655.

Londrillo, P. and Del Zanna, L. (2000), High-Order Upwind Schemes for Multidimensional Magnetohydrodynamics, *ApJ* **530**, 508–524.

Lucy, L. B. (1977), A numerical approach to the testing of the fission hypothesis, *MNRAS* **82**, 1013–1024.

Mac Low, M., Klessen, R., Burkert, A. and Smith, M. (1999), Decay Timescales of MHD Turbulence in Molecular Clouds, pp.256–260.

Mao, S. A., McClure-Griffiths, N. M., Gaensler, B. M., Brown, J. C., van Eck, C. L., Haverkorn, M., Kronberg, P. P., Still, J. M., Shukurov, A. and Taylor, A. R. (2012), New Constraints on the Galactic Halo Magnetic Field Using Rotation Measures of Extragalactic Sources towards the Outer Galaxy, *ApJ* **755**, 21–35.

Martin, J. and Yokoyama, J. (2008), Generation of large scale magnetic fields in single-field inflation, *J. Cosmology Astropart. Phys.* **1**, 25–57.

Matese, J. J. and O'Connell, R. F. (1969), Neutron Beta Decay in a Uniform Constant Magnetic Field, *Physical Review* **180**, 1289–1292.

Meglicki, Z. (1994), Verification and accuracy of smoothed particle magnetohydrodynamics, *Computer Physics Communications* **81**, 91–104.

Mocz, P., Vogelsberger, M. and Hernquist, L. (2014), A constrained transport scheme for MHD on unstructured static and moving meshes, *MNRAS* **442**, 43–55.

Monaghan, J. J. (1992), Smoothed Particle Hydrodynamics, *ARA&A* **30**, 543–574.

Monaghan, J. J. (1997), SPH and Riemann Solvers, *J. Comp. Phys.* **136**, 298–307.

Monaghan, J. J. (2000), SPH without a Tensile Instatbility, *J. Comp. Phys.* **159**, 290–311.

Monaghan, J. J. (2005), Smoothed particle hydrodynamics, *Rep. Prog. Phys.* **68**, 1703–1759.

Monaghan, J. J. and Lattanzio, J. C. (1985), A refined particle method for astrophysical problems, *A&A* **149**, 135–143.

Monaghan, J. J. and Price, D. (2001), Variational principles for relativistic smoothed particle hydrodynamics, *MNRAS* **328**, 381–392.

Morris, J. P. (1996), Analysis of smoothed particle hydrodynamics with applications, PhD thesis, Monash University, Melbourne, Australia.

Morris, J. P. and Monaghan, J. J. (1997), A Switch to Reduce SPH Viscosity, *J. Comp. Phys.* **136**, 41–50.

Murray, J., Wadsley, J. and Bond, J. R. (1996), MHD with SPH: application to the high redshift IGM, *Bulletin of the American Astronomical Society* **28**, 1413.

Navarro, J. F., Frenk, C. S. and White, S. D. M. (1997), A Universal Density Profile from Hierarchical Clustering, *ApJ* **490**, 493–508.

Navarro, J. F. and White, S. D. M. (1993), Simulations of Dissipative Galaxy Formation in Hierarchically Clustering Universes - Part One - Tests of the Code, *MNRAS* **265**, 271–300.

Neronov, A. and Vovk, I. (2010), Evidence for Strong Extragalactic Magnetic Fields from Fermi Observations of TeV Blazars, *Science* **328**, 73–75.

Neronov, A., Semikoz, D., Kachelriess, M., Ostapchenko, S. and Elyiv, A. (2010), Degree-scale GeV "Jets" from Active and Dead TeV Blazars, *ApJ* **719**, L130–L133.

Neumann, J. and Richtmyer, R. D. (1950), A Method for the Numerical Calculation of Hydrodynamic Shocks, *Journal of Applied Physics* **21**, 232–237.

Newcomb, W. A. (1962), Lagrangian and Hamiltonian methods in magnetohydrodynamics, *Nucl. Fusion Suppl.* **2**, 451–463.

Niklas, S. (1995), Ph.D. thesis, PhD thesis, University of Bonn.

Noh, W. F. (1987), Errors for calculations of strong shocks using an artificial viscosity and an artificial heat flux, *J. Comp. Phys.* **72**, 78–120.

Oppeneer, P. M. (1984), Variational principle for ideal MHD, *Physics Letters A* **104**, 207–211.

Orszag, S. A. and Tang, C. M. (1979), Small-scale structure of two-dimensional magnetohydrodynamic turbulence, *Journal of Fluid Mechanics* **90**, 129–143.

Ossendrijver, M. (2003), The solar dynamo, *A&A Rev.* **11**, 287–367.

Pakmor, R., Bauer, A. and Springel, V. (2011), Magnetohydrodynamics of an unstructured moving grid, *MNRAS* **418**, 1392–1401.

Paoletti, D. and Finelli, F. (2011), CMB constraints on a stochastic background of primordial magnetic fields, *Phys. Rev. D* **83**, 341–353.

Patrikeev, I., Fletcher, A., Stepanov, R., Beck, R., Berkhuijsen, E. M., Frick, P. and Horellou, C. (2007), Analysis of spiral arms using anisotropic wavelets: gas, dust and magnetic fields in M 51, *A&A* **458**, 441–452.

Pfrommer, C., Springel, V., Enßlin, T. A. and Jubelgas, M. (2006), Detecting shock waves in cosmological smoothed particle hydrodynamics simulations, *MNRAS* **367**, 113–131.

Phillips, G. J. (1985), Fragmentation in collapsing magnetic gas clouds - Non-uniform initial fields, *Proceedings of the Astronomical Society of Australia* **6**, 205–207.

Planck Collaboration, Ade, P. A. R., Aghanim, N., Armitage-Caplan, C., Arnaud, M., Ashdown, M., Atrio-Barandela, F., Aumont, J., Baccigalupi,

C., Banday, A. J. and et al. (2013), Planck 2013 results. XVI. Cosmological parameters, *ArXiv e-prints* .

Powell, K. G., Roe, P. L., Linde, T. J., Gombosi, T. I. and De Zeeuw, D. L. (1999), A Solution-Adaptive Upwind Scheme for Ideal Magnetohydrodynamics, *J. Comp. Phys.* **154**, 284–309.

Price, D. (2008), Modelling discontinuities and Kelvin Helmholtz instabilities in SPH, *J. Comp. Phys.* **227**, 10040–10057.

Price, D. and Monaghan, J. J. (2004a), Smoothed Particle Magnetohydrodynamics - I. Algorithm and tests in one dimension, *MNRAS* **348**, 123–138.

Price, D. and Monaghan, J. J. (2004b), Smoothed Particle Magnetohydrodynamics - II. Variational principles and variable smoothing length terms, *MNRAS* **348**, 123–138.

Price, D. and Monaghan, J. J. (2005), Smoothed Particle Magnetohydrodynamics - III. Multidimensional tests and the $\nabla \cdot B = 0$ constraint, *MNRAS* **364**, 384–406.

Price, D. J. (2004), Magnetic fields in Astrophysics, PhD thesis, Institute of Astronomy, Madingley Rd, Cambridge, CB2 0HA.

Price, D. J. (2010), Smoothed Particle Magnetohydrodynamics - IV. Using the vector potential, *MNRAS* **401**, 1475–1499.

Price, D. J. (2012), Smoothed particle hydrodynamics and magnetohydrodynamics, *J. Comp. Phys.* **231**, 759–794.

Price, D. J. and Monaghan, J. J. (2012), An energy-conserving formalism for adaptive gravitational force softening in smoothed particle hydrodynamics and N-body codes, *MNRAS* **374**, 1347–1358.

Ratra, B. (1992), Cosmological 'seed' magnetic field from inflation, *ApJ* **391**, L1–L4.

Read, J. I. and Hayfield, T. (2012), SPHS: smoothed particle hydrodynamics with a higher order dissipation switch, *MNRAS* **422**, 3037–3055.

Read, J. I., Hayfield, T. and Agertz, O. (2010), Resolving mixing in smoothed particle hydrodynamics, *MNRAS* **405**, 1513–1530.

Reid, M. J. and Silverstein, E. M. (1990), OH masers and the Galactic magnetic field, *ApJ* **361**, 483–486.

Richtmyer, R. D. and Morton, K. W. (1967), *Difference methods for initial-value problems*, 2nd edition, New York: Interscience.

Robertson, B. E., Kravtsov, A. V., Gnedin, N. Y., Abel, T. and Rudd, D. H. (2010), Computational Eulerian hydrodynamics and Galilean invariance, *MNRAS* **401**, 2463–2476.

Rosswog, S. (2009), Astrophysical smoothed particle hydrodynamics, *New A Rev.* **53**, 78–104.

Rosswog, S. and Price, D. (2007), MAGMA: a three-dimensional, Lagrangian magnetohydrodynamics code for merger applications, *MNRAS* **379**, 915–931.

Rybicki, G. B. and Lightman, A. P. (1979), *Radiative processes in astrophysics*, New York, Wiley-Interscience, Chapter 6, pp.167–191.

Ryu, D. and Jones, T. W. (1995), Numerical magnetohydrodynamics in astrophysics: Algorithm and tests for one-dimensional flow, *ApJ* **442**, 228–258.

Saitoh, T. and Makino, J. (2009), A Necessary Condition for Individual Time Steps in SPH Simulations, *ApJ* **697**, L99–L102.

Saitoh, T. and Makino, J. (2010), FAST: A Fully Asynchronous Split Time-integrator for a Self-Gravitating Fluid, *PASJ* **62**, 301–314.

Schleicher, D. R. G., Banerjee, R. and Klessen, R. S. (2009), Influence of Primordial Magnetic Fields on 21cm Emission, *ApJ* **692**, 236–245.

Schleicher, D. R. G. and Miniati, F. (2011), Primordial magnetic field constraints from the end of reionization, *MNRAS* **418**, L143–L147.

Schuecker, P., Finoguenov, A., Miniati, F., Böhringer, H. and Briel, U. G. (2004), Probing turbulence in the Coma galaxy cluster, *A&A* **426**, 387–397.

Schwarz, D. J. and Stuke, M. (2009), Lepton asymmetry and the cosmic QCD transition, *J. Cosmology Astropart. Phys.* **11**, 25.

Sedov, L. (1959), *Similarity and Dimensional Methods in Mechanics*, New York: Academic Press.

Sellwood, J. A. (2011), The lifetimes of spiral patterns in disc galaxies, *MNRAS* **410**, 1637–1646.

Sellwood, J. A. and Carlberg, R. G. (1984), Spiral instabilities provoked by accretion and star formation, *ApJ* **282**, 61–74.

Sethi, S. K. and Subramanian, K. (2005), Primordial magnetic fields in the post-recombination era and early reionization, *MNRAS* **356**, 778–788.

Skillman, S. W., O'Shea, B. W., Hallman, E. J., Burns, J. O. and Norman, M. L. (2008), Cosmological Shocks in Adaptive Mesh Refinement Simulations and the Acceleration of Cosmic Rays, *ApJ* **689**, 1063–1077.

Sod, G. A. (1978), A survey of several finite difference methods for systems of nonlinear hyperbolic conservation laws, *J. Comp. Phys.* **27**, 1–31.

Sokoloff, D. D., Bykov, A. A., Shukurov, A., Berkhuijsen, E. M., Beck, R. and Poezd, A. D. (1998), Depolarization and Faraday effects in galaxies, *MNRAS* **299**, 189–206.

Spitzer, L. (1962), *Physics of Fully Ionized Gases*, 2nd edition, New York: Interscience.

Springel, V. (2010), E pur si muove: Galilean-invariant cosmological hydrodynamical simulations on a moving mesh, *MNRAS* **401**, 791–851.

Springel, V. and Hernquist, L. (2002), Cosmological smoothed particle hydrodynamics simulations: the entropy equation, *MNRAS* **333**, 649–664.

Springel, V., Yoshida, N. and White, S. D. M. (2001), GADGET: a code for collisionless and gas dynamical cosmological simulations, *New A* **6**, 79–117.

Stasyszyn, F. A., Dolag, K. and Beck, A. M. (2013), A divergence-cleaning scheme for cosmological SPMHD simulations, *MNRAS* **428**, 13–27.

Stern, D. P. (1970), Euler Potentials, *American Journal of Physics* **38**, 494–501.

Stone, J. M., Gardiner, T. A., Teuben, P., Hawley, J. F. and Simon, J. B. (2008), Athena: A New Code for Astrophysical MHD, *ApJS* **178**, 137–177.

Subramanian, K. (2010), Magnetic fields in the early Universe, *Astronomische Nachrichten* **331**, 110–120.

Tabatabaei, F. S., Berkhuijsen, E. M., Frick, P., Beck, R. and Schinnerer, E. (2013), Multi-scale radio-infrared correlations in M31 and M33: The role of magnetic fields and star formation, *A&A* **557**, A129–A142.

Tabatabaei, F. S., Krause, M., Fletcher, A. and Beck, R. (2008), High-resolution radio continuum survey of M33. III. Magnetic fields, *A&A* **490**, 1005–1017.

Takahashi, K., Mori, M., Ichiki, K., Inoue, S. and Takami, H. (2013), Lower Bounds on Magnetic Fields in Intergalactic Voids from Long-term GeV-TeV Light Curves of the Blazar Mrk 421, *ApJ* **771**, L42–L47.

Tang, Y. W., Ho, P. T. P., Girart, J. M., Rao, R., Koch, P. and Lai, S. P. (2009), Evolution of Magnetic Fields in High Mass Star Formation: Sub-millimeter Array Dust Polarization Image of the Ultracompact H II Region G5.89-0.39, *ApJ* **695**, 1399–1412.

Tashiro, H. and Sugiyama, N. (2011), Sunyaev-Zeldovich power spectrum produced by primordial magnetic fields, *MNRAS* **411**, 1284–1292.

Tauber, J. A., Mandolesi, N., Puget, J.-L., Banos, T., Bersanelli, M., Bouchet, F. R., Butler, R. C., Charra, J., Crone, G., Dodsworth, J. and et al. (2010), Planck pre-launch status: The Planck mission, *A&A* **520**, A1–A22.

Tavecchio, F., Ghisellini, G., Bonnoli, G. and Foschini, L. (2011), Extreme TeV blazars and the intergalactic magnetic field, *MNRAS* **414**, 3566–3576.

Toomre, A. (1964), On the gravitational stability of a disk of stars, *ApJ* **139**, 1217–1238.

Tóth, G. (2000), The $\nabla \cdot B = 0$ Constraint in Shock-Capturing Magnetohydrodynamics Codes, *J. Comp. Phys.* **161**, 605–652.

Tricco, T. and Price, D. (2012), Constrained hyperbolic divergence cleaning for smoothed particle magnetohydrodynamics, *J. Comp. Phys.* **231**, 7214–7236.

Tricco, T. and Price, D. (2013a), A switch for Artificial Resistivity and Other Dissipation Terms, *ArXiv e-print* .

Tricco, T. and Price, D. (2013b), A switch to reduce resistivity in smoothed particle magnetohydrodynamics, *MNRAS* **436**, 2810–2817.

Turner, M. S. and Widrow, L. M. (1988), Inflation-produced, large-scale magnetic fields, *Phys. Rev. D* **37**, 2743–2754.

Vazza, F., Gheller, C. and Brüggen, M. (2014), Simulations of cosmic rays in large-scale structures: numerical and physical effects, *MNRAS* **439**, 2662–2677.

Verschuur, G. L. (1995), Zeeman Effect Observations of H i Emission Profiles. II. Results of an Attempt to Confirm Previous Claims of Field Detections, *ApJ* **451**, 645.

Wada, K., Baba, J. and Saitoh, T. R. (2011), Interplay between Stellar Spirals and the Interstellar Medium in Galactic Disks, *ApJ* **735**, 1–9.

Widrow, L. M. (2002), Origin of galactic and extragalactic magnetic fields, *Reviews of Modern Physics* **74**, 775–823.

Xu, H., Govoni, F., Murgia, M., Li, H., Collins, D. C., Norman, M. L., Cen, R., Feretti, L. and Giovannini, G. (2012), Comparisons of Cosmological Magnetohydrodynamic Galaxy Cluster Simulations to Radio Observations, *ApJ* **759**, 40–76.

Xu, H., Li, H., Collins, D. C., Li, S. and Norman, M. L. (2010), Evolution and Distribution of Magnetic Fields from Active Galactic Nuclei in Galaxy Clusters. I. The Effect of Injection Energy and Redshift, *ApJS* **725**, 2152–2165.